

HARVARD UNIVERSITY  
Graduate School of Arts and Sciences



DISSERTATION ACCEPTANCE CERTIFICATE

The undersigned, appointed by the  
Department of Physics  
have examined a dissertation entitled

Synthetic Physiology: Manipulating and measuring biological pattern  
formation with light

presented by Harold Michael McNamara

candidate for the degree of Doctor of Philosophy and hereby  
certify that it is worthy of acceptance.

Signature Adam E. Cohen

Typed name: Professor Adam Cohen, Chair

Signature L. Mahadevan

Typed name: Professor L. Mahadevan

Signature Olivier Pourquie

Typed name: Professor Olivier Pourquie

Signature Nicholas Bellono

Typed name: Professor Nicholas Bellono

Date: September 3, 2019



# Synthetic Physiology: Manipulating and measuring biological pattern formation with light

A DISSERTATION PRESENTED  
BY  
HAROLD MICHAEL McNAMARA  
TO  
THE DEPARTMENT OF PHYSICS

IN PARTIAL FULFILLMENT OF THE REQUIREMENTS  
FOR THE DEGREE OF  
DOCTOR OF PHILOSOPHY  
IN THE SUBJECT OF  
PHYSICS

HARVARD UNIVERSITY  
CAMBRIDGE, MASSACHUSETTS  
SEPTEMBER 2019

©2019 – HAROLD MICHAEL McNAMARA  
ALL RIGHTS RESERVED.

## Synthetic Physiology: Manipulating and measuring biological pattern formation with light

### ABSTRACT

Multicellular tissues and organisms execute complex physiological functions through precise spatiotemporal coordination of their constituent cells. Cells achieve this coordination through long-range intercellular communication pathways – for example, electrical signaling synchronizes the beating heart, and biochemical morphogen signals organize the developing embryo. It is an outstanding challenge in quantitative biology to develop mathematical models (borrowing from e.g. control theory or statistical physics) that explain how robust pattern formation emerges from these long-range interactions. It is generally challenging to connect theoretical models to experimental demonstrations due to the difficulty of manipulating and measuring physiological dynamics in complex tissues.

The emergence of optogenetic tools has opened new opportunities in experimental biology. By placing signaling pathways under the control of light, one can leverage methods from optical physics in order to pattern biological signals with precise agility in space and time. By combining these tools with complementary optical methods for mapping resultant patterns with high spatial resolution, one can create high-dimensional biological interfaces in order to study pattern formation. Optogenetic tools have achieved widespread adoption in the study of the brain, but they have only begun to be extended to study biological pattern formation in other contexts like the developing embryo.

The first portion of this thesis presents ‘synthetic electrophysiology’, a new framework for studying bioelectrical pattern formation. By deploying all-optical electrophysiology in engineered tissues with designed electrical components, we study electrical tissues as dynamical systems. In tissues comprised of synthetic excitable cells, we show that geometry is a fundamental determinant of stability and chaos in biological pacemakers, and we show that excitable cells can be composed into bioelectric circuits capable of primitive information processing and memory. We also show that electrically bistable tissues can form reaction-diffusion patterns of electrical domains which undergo phase transitions via spontaneous symmetry breaking. These previously unobserved classes of stable electrical patterns suggest a potential role for electrophysiology during embryonic development. This strategy of ‘bioelectrical engineering’ can articulate subtle aspects of electrophysiological patterning that may be obscured by the complexity of the embryo *in vivo*.

The latter portion of this thesis describes progress towards developing tools for optical manipulation and measurement of spatial patterns of gene expression. The ability to spatially pattern morphogen signals in the embryo, and to map the complete transcriptional response of a system to a given signal, could enable the pressure-testing of mutually consistent morphogen models which

classical methods cannot disambiguate. First, we describe a new optogenetic platform for patterning the Nodal morphogen signal in the zebrafish embryo. By fusing the Nodal receptors *acvr1b/acvr2b* to the photoassociating domain pair *CRY2/CIB1*, we convert blue photons into Nodal morphogens. Deploying these reagents in a platform for patterning illumination in dozens of embryos in parallel enables us to systematically study the spatiotemporal requirements of Nodal signaling. We next discuss a new platform for using photochemical patterning of DNA barcodes to layer spatial information onto droplet microfluidics-based single cell RNA sequencing (scRNAseq) methods. By attaching these DNA ‘zipcodes’ as barcoded features on the cell surface, we can introduce spatial information onto scRNAseq while retaining the single-cell discretization and full-transcriptome depth of droplet methods. Combining optogenetic morphogen patterning with spatially resolved transcriptomics may enable more powerful studies of how the embryo processes morphogen patterns as dynamical signals.

We conclude by discussing future prospects for this strategy of ‘synthetic physiology’ to unveil quantitative physical principles which underlie the robustness and reliability of biological patterning.

# Contents

0	INTRODUCTION	1
1	BACKGROUND	6
1.1	Pattern formation in the embryo . . . . .	6
1.2	Electrophysiological patterning . . . . .	12
1.3	New optical tools for probing biological complexity . . . . .	20
2	SYNTHETIC ELECTRICALLY EXCITABLE TISSUES WITH OPTICAL CONTROL AND READOUT	30
2.1	Motivation . . . . .	31
2.2	Excitable cells with a bidirectional optical interface . . . . .	33
2.3	Ring oscillators and bioelectric memories in patterned OS-HEK cells . . . . .	37
2.4	Biophysical characterization of Optopatch Spiking HEK cells . . . . .	40
2.5	Optically defined ring oscillator . . . . .	45
2.6	Conclusions . . . . .	46
2.7	Methodology . . . . .	49
2.8	Publication information . . . . .	56
2.9	Contributions . . . . .	57
3	GEOMETRY DETERMINES STABILITY AND CHAOS IN BIOELECTRIC PACEMAKERS	58
3.1	Motivation . . . . .	59
3.2	iOS-HEK cells show alternans and arrhythmias . . . . .	63
3.3	Geometry dependent instabilities in iOS-HEK cells . . . . .	65
3.4	A Hodgkin-Huxley model captures iOS-HEK dynamics . . . . .	69
3.5	Mapping the transition between the near field and far field response . . . . .	72
3.6	Second-degree conduction block in iOS-HEK cells . . . . .	73
3.7	Geometry dependent instabilities in human iPSC cardiomyocytes . . . . .	74
3.8	Scaling properties of electrical instabilities . . . . .	76
3.9	Conclusions . . . . .	81
3.10	Methodology . . . . .	82
3.11	Publication information . . . . .	93

3.12	Contributions . . . . .	93
4	BIOELECTRIC DOMAINS, PHASE TRANSITIONS, AND SIGNALING VIA DOMAIN WALL MIGRATION	95
4.1	Motivation . . . . .	96
4.2	Bistable membrane voltages . . . . .	98
4.3	Bioelectrical domains in extended tissues . . . . .	102
4.4	Noise-induced breakup of discrete bioelectric domains in a continuous tissue . . .	109
4.5	Electrical bistability and hysteresis during myogenesis . . . . .	112
4.6	Conclusions . . . . .	115
4.7	Methodology . . . . .	119
4.8	Publication information . . . . .	129
4.9	Contributions . . . . .	129
5	SPATIOTEMPORAL CONTROL OF EMBRYONIC DEVELOPMENT USING OPTO-NODAL	131
5.1	Motivation . . . . .	132
5.2	OptoNodal: Controlling a morphogen pathway with light . . . . .	137
5.3	A platform for perturbing and imaging dozens of embryos in parallel . . . . .	140
5.4	Optical induction of germ layer fate within the vertebrate embryo . . . . .	144
5.5	Optical rescue of embryonic development . . . . .	146
5.6	Outlook . . . . .	149
5.7	Contributions . . . . .	153
6	SPATIALLY-RESOLVED SINGLE CELL TRANSCRIPTOMICS THROUGH PHOTOCHEMICAL BARCODING	154
6.1	Motivation . . . . .	155
6.2	Photochemical patterning of DNA zipcodes . . . . .	157
6.3	Sequencing zipcodes . . . . .	162
6.4	Outlook . . . . .	166
6.5	Contributions . . . . .	169
7	CONCLUSION	170
	REFERENCES	198

# Listing of figures

1	Strategy and motivation for the synthetic physiology approach. . . . .	4
1.1	Positional information and reaction-diffusion models of patterning. . . . .	10
1.2	Example classifications of neurons in the Izhikevich framework. . . . .	18
1.3	All-optical electrophysiology. . . . .	24
1.4	Diversity of photoassociating domain applications. . . . .	27
2.1	Optopatch spiking HEK (OS-HEK) cells enable optical stimulation and optical read-out of electrical waves in confluent monolayers . . . . .	35
2.2	Microscope design for imaging OS-HEK cultures . . . . .	36
2.3	Ring oscillators in annular OS-HEK cell cultures . . . . .	38
2.4	Optical control of conduction velocity with static illumination . . . . .	39
2.5	Characterizing wave propagation in OS-HEK cell cultures . . . . .	41
2.6	Action potential dynamics during a periodic wave train . . . . .	42
2.7	Optically triggered wave propagation around an optically defined corner . . . . .	44
2.8	Dynamic optical tuning of OS-HEK cell oscillators . . . . .	45
3.1	Isradipine renders Optopatch-Spiking HEK cells susceptible to arrhythmia . . . . .	64
3.2	Stability of spiking in iOS-HEKs cells depends on sample geometry and location of pacing . . . . .	66
3.3	Replicates of geometry-depending instabilities in iOS-HEKs . . . . .	68
3.4	A Hodgkin-Huxley model recapitulates the effect of geometry on spike dynamics . . . . .	71
3.5	Mapping the transition from near field to far field dynamics . . . . .	73
3.6	Curvature-induced second-degree conduction block in iOS-HEK cell tracks . . . . .	74
3.7	Geometry-dependent arrhythmias in cultured human iPSC-derived cardiomyocytes (hiPSC-CM) . . . . .	75
3.8	Geometry dependent instabilities in different numerical models of excitable cells . . . . .	77
3.9	Scaling properties of instabilities in iOS-HEK cells . . . . .	78
3.10	Effect of gap junction coupling on dynamics in Hodgkin-Huxley simulations of iOS-HEK cells . . . . .	79

4.1	Biochemical and bioelectrical pattern formation . . . . .	97
4.2	Electrophysiological bistability in an engineered cell line . . . . .	100
4.3	Electrophysiological characterization of bi-HEK cells . . . . .	101
4.4	Bioelectric domain walls in an engineered cell line . . . . .	104
4.5	Balance of ionic currents determines velocity of domain wall motion in homogeneous tissues . . . . .	105
4.6	Bioelectrical domain wall formation in eight distinct islands . . . . .	107
4.7	Stability of bioelectrical domain walls . . . . .	108
4.8	Gap junction blockers convert 2-D behavior in an island to an ensemble of independent 0-D systems . . . . .	109
4.9	Effect of noisy gene expression on domain wall properties . . . . .	110
4.10	Spatially correlated variability in $K_{ir2.1}$ expression drives breakup of tissues into discrete domains . . . . .	111
4.11	Bioelectric domain wall propagation in stem cell-derived myocytes . . . . .	113
4.12	Electrophysiological phenotypes in immature isolated myocytes . . . . .	114
4.13	Gap junction coupling in confluent cultures of immature myocytes . . . . .	116
5.1	Overview of Nodal signaling pathway . . . . .	133
5.2	Feedbacks in nodal signaling . . . . .	135
5.3	Controlling Nodal signaling with light . . . . .	139
5.4	A platform for high-throughput optical patterning of embryos . . . . .	142
5.5	Painting cell fate in the vertebrate embryo . . . . .	145
5.6	Stochastic aspects of the endodermal decision . . . . .	146
5.7	Testing the spatiotemporal demands of Nodal patterning with optogenetics 1: signal magnitude . . . . .	148
5.8	Testing the spatiotemporal demands of Nodal patterning with optogenetics 2: signal extent . . . . .	149
5.9	Rescue of overall body plan with OptoNodal2 . . . . .	150
5.10	Testing for nonlinearities in the mesendoderm decision . . . . .	150
5.11	Design criteria of the Nodal signal . . . . .	151
5.12	Playing arbitrary developmental programs with light . . . . .	152
6.1	Photochemical barcoding design and strategy . . . . .	158
6.2	Patterning DNA barcodes using sequential photo-click chemistries . . . . .	160
6.3	Protocol optimization for photochemical barcoding . . . . .	162
6.4	Demonstration of photochemical labeling in brain tissue . . . . .	163
6.5	Sequencing zipcodes . . . . .	164
6.6	Applications of photochemical zipcoding . . . . .	167
7.1	Voltage as a morphogen . . . . .	172
7.2	Using light to study developmental decisions as dynamical systems . . . . .	173

TO MY PARENTS.

# Acknowledgments

IT TAKES A VILLAGE to raise a PhD candidate, and I consider myself extremely fortunate to have had the support of so many brilliant and kind people throughout my life who have helped me complete this journey (both when it was a figurative journey of the mind, and when it was a literal journey that took me far ashore).

My colleagues in the Cohen Lab created a truly special scientific environment which I will always remember fondly. It was a privilege to work in the company of world-class experts in classical electrophysiology, protein engineering, ultrafast optics, neuroscience (either in zebrafish or in mice), membrane mechanics, etc (the list goes on...) all under the same roof. I learned and benefited from everyone with whom I overlapped in the group, and will follow their careers with great interest. For a representative but incomplete sampling: Daan Brinks shepherded me into the lab as a bug-eyed rotation student and helped teach me how to patch clamp and approach experimental biology as a physicist. Kit Werley and Hongkang Zhang helped to initiate the synthetic electrophysiology project which ended up proving extremely fruitful. My PhD ‘siblings’ Sami Farhi, Vicente Parot, and Linlin Fan made for a wonderful cohort of friends who each brought their own scientific aesthetic to the lab. Over the last year of pushing through to the finish, Urs Böhm and Amanda Klaeger were a constant source of good office banter and cheer. Technical support at various points from Vaibhav Joshi, Katherine Williams, Melinda Lee, Shahinoor Begum, and Hanan Dahche helped me accomplish much more than I would have been able to do alone.

Throughout my PhD, Adam’s mentorship was essential to both any specific technical successes I had as well as to my overall scientific growth. I am extremely grateful that he gave me the independence and freedom to explore science as a ‘free-range’ grad student. Sometimes these explorations broke new ground, and sometimes they ended up as dead ends – the countless hours Adam invested in me helped me to learn how to tell the difference between the two. I am not sure there is another group where I could have traversed from physics to electrophysiology, then to developmental biology, then to RNA sequencing method development, all in a single lab. Whatever successes I ever manage to achieve in science, they will be indebted to Adam’s mentorship during my PhD.

Speaking of wanderings – I was also extremely fortunate to join with so many collaborators to tackle interesting interdisciplinary problems. I am extremely grateful that Nate Lord wandered into our lab one day looking for a collaborator to study zebrafish morphogens. Working with Nate and with Alex Schier was my gateway to the amazing world of embryology, and I am also indebted to

Nate for teaching me everything I know about development. Later in my PhD I was fortunate to work with Olivier Pourquié and Ziad Al Tanoury on muscle development. Their openness to our sometimes unconventional ideas has made me encouraged that our approach can make a real contribution to developmental biology. In our synthetic electrophysiology project, I was lucky to work with Stephanie Dodson and Björn Sandstede to increase the mathematical sophistication of our dynamical models. I am also grateful to Michael Levin, Joshua Finkelstein, and the Allen Discovery Center at Tufts University for intellectually provocative conversations and for building a community around the study of electrophysiology in the embryo. I am grateful to L. Mahadevan and to Alex Schier for sitting on my oral qualifying examination committee, and to Maha, Olivier, and Nick Bellono for sitting on my dissertation defense committee.

I am lucky that I was able to do my PhD in Somerville/Cambridge/Boston surrounded by so many friends from all over the world – not just from Harvard, but also from undergrad at Yale, from Cambridge (the original one) and Dublin, and from my hometown in Pittsburgh (including my siblings!). Whether at trivia nights, pickup basketball/volleyball, or during late night Super Smash Bros. marathons, I was fortunate to enjoy the company of such eclectic and entertaining people for so many years.

I am grateful to Blaire for supporting me and for appreciating my drive to do this, even when it meant I was distracted or stressed or otherwise less present than I might have been, and for reminding me to balance my life when I needed to take a breather. Spending time with her and with our cats Gatsby and Sesame lent a rhythm to my life that did not depend on whether or not my experiments worked that day.

Finally, I am so lucky to have parents who have always believed in me and supported me unconditionally, whatever choices I made or paths I pursued. Whether these choices were practical or self-indulgent, and whether they took me to Cambridge or to Cairo. I hope I can eventually honor the privilege you have given me by paying it forward, in one way or another.

# 0

## Introduction

One of the most fundamental challenges in biology is understanding how complex networks of biological parts interact to generate the diverse forms and functions we observe in nature. To what extent can compact mathematical principles explain processes like embryonic development? Can we exploit these principles in order to solve important technological problems?

Dissecting any such principles is challenging due the notorious complexity of biological systems. Biological complexity manifests across a range of spatial and temporal scales: from biochemical sig-

naling pathways within a single cell, to cells communicating within an organism, to whole organisms interacting in an ecosystem, biological systems in general feature networks of components with nonlinear and dynamic interactions. One strategy to navigate this complexity is to articulate the complete details of a given system of interest. This approach may be described as the “reductionist” or “top-down” approach, and it represents the major viewpoint in modern biological research. For example, one might characterize the transcriptional profile of every cell within a tissue or organism, along with the protein structure corresponding to each translated gene, and then use the information to generate an “atlas” of where these cell types and proteins are present in a given system of interest.

With the advent of modern molecular biology and next-generation sequencing, the reductionist approach has been remarkably successful in articulating biological complexity with increasingly granular resolution. For example, with droplet microfluidics-enabled single cell RNA profiling, it is routine to characterize expression of  $10^4$  genes within  $10^5$  cells in a single pooled measurement. This project frequently carries the assumption that a complete list of biological parts will constitute a complete understanding of a given system. This assumption, however, begs a corresponding complete description of how these parts interact across scales of biological organization. The presence of myriad concomitant processes within intact biological systems poses a challenge to articulating these interactions via a classical reductionist approach. Thus while we now have an excellent descriptive understanding of cell types within model organisms, we have a comparatively limited understanding of how these cell types interact to form organized systems.

A complementary approach to study complex systems is the “constructivist” or “bottom-up” approach. Rather than studying a complete, intact system, one can assemble components one by one to study interactions in simpler reduced systems. While this approach may not preserve the full details of a system of interest, it has two important advantages. First, reduced systems can highlight or even isolate particular features of a system, making the interpretation of interactions more straight-

forward. Second, the constructivist approach can elucidate collective phenomena that emerge at different scales of biological organization. As PW Anderson famously observed, “more is different”<sup>7</sup>: interactions between simple components can give rise to new emergent properties which do not manifest in isolation. By building bottom-up systems out of defined components, one might characterize emergent properties with a rigor that is not accessible in full biological systems.

While the constructivist approach is common in the physical sciences (and in condensed matter physics in particular), it has not been commonly adopted in the biological sciences. An important exception is the foundational work in characterizing biochemical signaling pathways by studying interactions between biomolecules via *in vitro* reconstitutions. At higher order scales of biological complexity – for example, at the level of cells interacting to form tissues and organisms - the constructivist approach has largely been impractical. Adopting this framework would require means to assemble defined biological components, as well as means to both observe and perturb these components with spatiotemporal precision.

A convergence of technical developments is poised to open higher-order hierarchies of biological complexity to this bottom-up paradigm. Synthetic biology has matured as a field and now offers the means to assemble engineered biological components with designed properties. The fluorescence microscopy revolution has developed sophisticated tools for observing complex biological dynamics, including expression of reporter genes, second messenger molecules (calcium, cyclic nucleotides), and electrical signals carried by the membrane potential. Finally, new optogenetic tools enable the expression of light-sensitive protein based actuators for complementary control of these biological signaling dynamics in genetically defined cell types. Combining optogenetic tools with modern optical instrumentation enables the creation of high-dimensional biological interfaces with up to 1 million inputs and outputs. Whereas the development of synthetic biology enabled a constructivist approach to study signaling within single cells, pairing synthetic biology with optogenetics enables the extension of bottom-up biology into the multicellular domain.

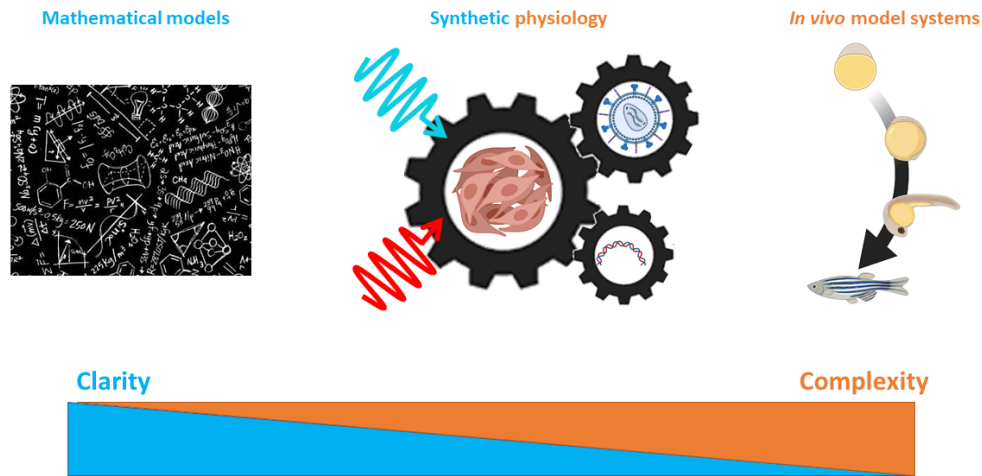


**Figure 1: Strategy and motivation for the synthetic physiology approach.** While mathematical models offer clarity and rigorous precision, they rely on simplifying assumptions regarding physiological systems and components. Conversely, *in vivo* preparations recapitulate the full complexity of biology, but are challenging to measure and interpret. By building new experimental systems out of biological components, and by manipulating them with precise optical techniques, we seek to bridge the rigor of mathematical models and the biological fidelity of *in vivo* systems.

This strategy of ‘synthetic physiology’ represents a new route to study biological complexity from the bottom-up. This thesis describes efforts to develop and deploy this strategy across a range of systems, with a particular interest in discovering mathematical principles underlying embryonic development. Chapter 1 provides relevant background and historical context on embryonic development, electrophysiology, and optogenetics for readers with backgrounds outside any of these fields (this material is likely dispensable to readers familiar with the state of the art). Next, chapters 2, 3, and 4 constitute a coherent unit describing the application of synthetic biology and optogenetics to study electrophysiological pattern formation. By introducing ion channels into electrically inert biological cells, we can create synthetic cells with designed electrical properties. Expression of light-gated ion channels offers the means to perturb these cells with light, and the expression of ge-

netically encoded or small molecule voltage indicators allows for the direct visualization of electrical patterns. By building bioelectric systems from the bottom up, one can isolate aspects of electrical pattern formation that might be obscured by the complexity of intact biological systems. Chapter 2 demonstrates this method to engineer bioelectric ‘circuits’ capable of wave propagation and basic information processing. Chapter 3 extends this approach to study stability and chaos in the context of biological pacemakers. Chapter 4 demonstrates the formation of stable electrical reaction-diffusion domains via spontaneous symmetry breaking in bistable tissues. This new class of electrical patterns may point to a role for voltage in coordinating embryonic development.

The remainder of this thesis describes the development of analogous tools for studying biochemical and genetic pattern formation. Chapter 5 details development and preliminary application of an optogenetic platform for manipulating and measuring biochemical morphogen signals during development of the zebrafish embryo. While it has long been appreciated that patterns of signaling proteins are essential to organizing embryonic development, it is challenging to manipulate these patterns using conventional means. By placing Nodal signaling under optical control, we can explore how spatiotemporal aspects of this signal organize early cell fate decisions and morphogenesis. Finally, Chapter 6 describes preliminary efforts to develop a complementary method to read out genetic patterns using spatially-resolved single-cell sequencing via photochemical barcoding.

This thesis concludes by discussing future prospects and avenues for using light to study biological self-organization.

# 1

## Background

### I.I PATTERN FORMATION IN THE EMBRYO

#### I.I.I HISTORICAL BACKGROUND

The embryo is a remarkable example of a self-organizing system. During human development, a single zygote must reliably execute waves of cell division, migration, and differentiation in order to assemble a complex organism containing over  $10^{13}$  cells<sup>187</sup>, each residing in its appropriate loca-

tion within the body plan and expressing the correct combination of the  $10^4$  genes in its genome. Biological cells make for noisy components, yet embryos succeed in robustly assembling their target morphology. Variations on this developmental programming contribute to the vast diversity of forms and functions we observe in nature.

The first evidence that embryos could organize themselves was reported in the late 19th century. Hans Driesch showed that cells of the early sea urchin embryo could be separated, with each generating a full adult organism<sup>85</sup>. Perhaps the most famous foundational work of early embryology was that of Spemann and Mangold in the 1920s. Working with salamander embryos, they showed that grafting a set of cells sampled from a particular location (the blastopore lip) at a particular time (gastrulation) of development into another salamander led to the organization of an ectopic secondary body axis in the grafted host.<sup>245</sup> This work established the concept of the ‘organizer’ within the field of embryology, and revealed the first evidence that cells of the embryo contain the programming necessary to instruct formation of complex tissues and morphologies. The concept of the organizer has since been shown to generalize beyond salamanders into numerous other species, including chickens, zebrafish, and humans.<sup>11,180</sup>

We now understand that organizers and indeed many other parts of the embryo function via long-range intercellular signaling pathways – i.e. via ‘morphogens’. The term morphogen was first introduced in Alan Turing’s seminal 1952 paper, where he demonstrated that chemical reactions amongst components (morphogens) with different diffusion coefficients could give rise to time-stationary modes of finite wavelength via a spontaneous symmetry breaking.<sup>260</sup> This ‘reaction-diffusion’ model of morphogenesis has been profoundly influential, and has inspired sustained efforts to identify and characterize signaling molecules which could act as Turing’s morphogens.

There are several families of biomolecules which can function as morphogens. Many of the best characterized morphogens belong to families of secreted proteins which bind extracellular receptor complexes, which can in turn activate downstream signaling pathways which ultimately lead to the

transcription of target genes. For example: in Transforming Growth Factor Beta (TGF $\beta$ ) superfamily morphogen pathways (Nodal/Activin; Bone Morphogenic Proteins, or BMPs), a TGF $\beta$  ligand binds and activates complex of type 1 and type 2 serine/threonine kinase receptors expressed on the cell surface.<sup>181</sup> The activated receptor complex then phosphorylates a Smad-family transcription factor. The phosphorylated Smad (pSmad) can then translocate to the nucleus and activate target genes of its associated pathway. The Fibroblast Growth Factor (FGF) pathway involves a similar scheme, in which FGF family ligands bind receptor tyrosine kinase domains which in turn activate target intracellular signaling pathways (e.g. RAS-MAPK).<sup>213</sup> Another family of morphogens is the Hedgehog family; in mammals, Sonic Hedgehog (Shh) is the best characterized.<sup>38</sup> Shh ligand binds the receptor Patched-1; the ligand-bound Patched-1 can then disinhibit the activity of Smoothed, thereby permitting the activation of GLI target genes. The Wnt family of proteins is another class of proteins that signal by binding a Frizzled (Fz) family G-protein coupled receptor (GPCR), which in turn can associate with co-receptors. The direct action of Fz on Dishelved (Dsh) can then branch off into a variety of alternative Wnt pathways (the canonical pathway; the non-canonical planar cell polarity pathway; the Wnt/calcium pathway). Other intercellular signaling pathways involve more diverse mechanisms: for example, in the Notch pathway, both Notch receptors and ligands (e.g. Delta-like and Jagged in mammals) are membrane localized, therefore requiring direct cell-cell contact in order to signal via a 'handshake' mechanism.<sup>158</sup>

### 1.1.2 MODELS OF MORPHOGEN PATTERNING

Modern molecular biology has been extremely successful at articulating the molecular components and mechanisms through which cells can communicate long-range morphogenic information. Despite this success, there remain fundamental open questions about the function of morphogen signals in the embryo. What are the dynamical principles through which these signals organize cell fate decisions, and how can perturbations to these signals generate the diversity of forms and

functions we see in nature? Indeed, many canonical morphogens were first identified in *Drosophila melanogaster*, yet orthologs of these same signaling pathways are also crucial for instructing the very different mammalian body plan. How precisely do morphogen signals work?

One proposal is the ‘positional information’ model, pioneered by Lewis Wolpert<sup>274</sup>. In this picture, gradients of morphogen signals establish coordinate systems within the embryo via their local concentration. By sensing these local concentrations, cells can interpret their position within the embryo and then compare them against threshold values in order to make cell fate decisions. This picture describes a mechanism through which cells make autonomous decisions based on external cues (which may be maternally defined). The positional information model provides an intuitive explanation for the preponderance of morphogen gradients within the embryo, and an explanation for how these gradients could organize cell-fate decisions. However, one implication of this model is that developmental programs should be exquisitely sensitive to the local concentration of morphogen molecules. The ability of embryonic development to tolerate fluctuations, as well as the presence of feedback decoration in many morphogen pathways, suggest that positional information is not a complete description of how morphogens instruct the embryo.

An alternative model is provided by Turing’s reaction-diffusion model<sup>260</sup>, in which spatial patterns emerge not from exogenously pre-patterned signals but rather from spontaneous symmetry breakings in active matter. This model differs from the positional information model in two important respects. First, it does not require the invocation of exogenous pre-patterns. Patterns of morphogens can emerge not just from initial conditions, but rather emerge from the intrinsic dynamics of tissues and embryos. Second, decisions amongst cells are not cell-autonomous. Instead, spatial coupling via morphogen secretion enables communication between cells and the potential for compensatory mechanisms that account for deviations from default patterns. While these features could explain the robustness of embryonic development in the presence of fluctuations, conclusively demonstrating a reaction-diffusion process *in vivo* is extremely challenging experimentally.

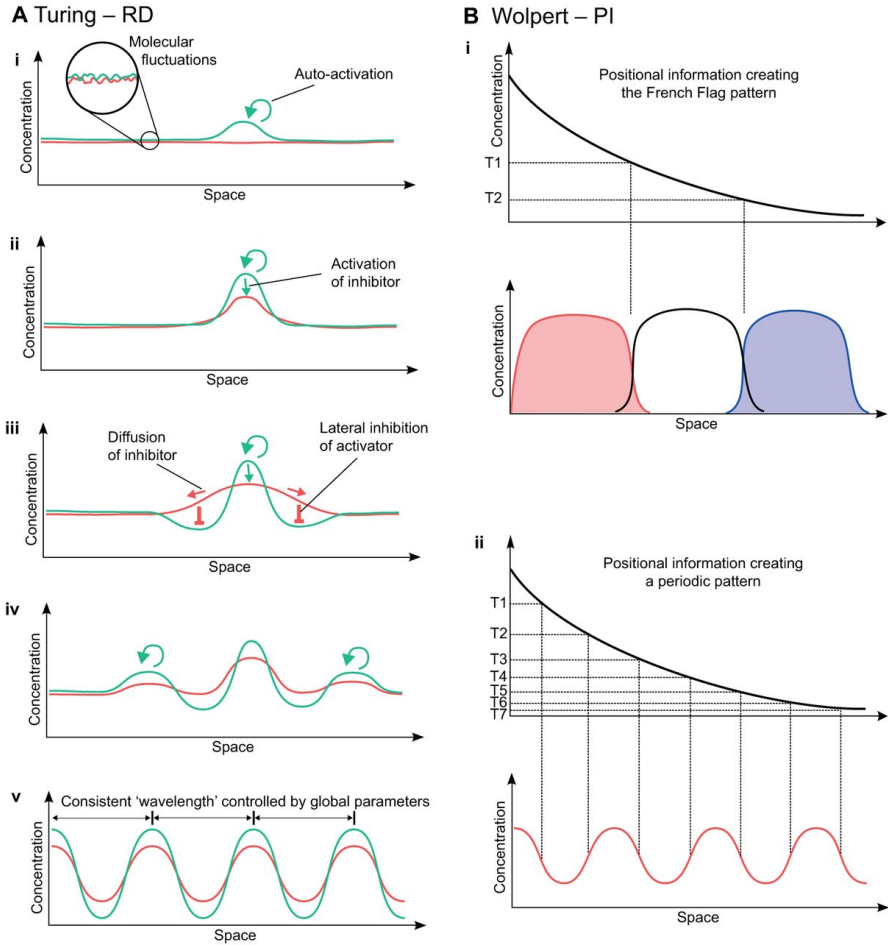


**Figure 1.1: Positional information and reaction-diffusion models of patterning.** Figure adapted directly from Green and Sharpe.<sup>107</sup> A) Pattern formation in a reaction-diffusion system. i) Noise in initial conditions induces a spontaneous symmetry breaking in which local feedbacks can amplify both activators and inhibitors (ii) of signaling. If the system parameters are tuned appropriately, these dynamics can generate spatial patterns with finite wavelengths, i.e. Turing patterns (iv-v). B) Pattern formation through positional information. An analog gradient encodes information via its local concentration, which can yield either classical 'French flag' germ layer patterns (i) or Turing-like patterns (ii) through combinatorial thresholding.

### 1.1.3 ORGANIZING THE EMBRYO

How much development programming relies on external cues, and how much is capable of being self-organized by embryonic cells? Recent experimental advances have demonstrated that collections of stem cells can recapitulate a significant degree of developmental programming *ex vivo* in the absence of external instructions. In one study, a human embryo was maintained *ex utero* for up to 14 days without maternal signaling.<sup>70</sup> Another showed that two-dimensional ‘microcolonies’ of human embryonic stem cells self-organize into germ layers, recapitulating an early stage of embryonic development outside of the embryo.<sup>266</sup> Yet another study demonstrated that, under specific culture conditions, three-dimensional aggregates of induced pluripotent stem cells can grow and organize into ‘brain organoids’ which recapitulate a remarkable degree of the complexity found in the adult brain, including canonical markers for forebrain, prefrontal cortex, and hippocampus.<sup>163</sup> These milestones demonstrate that apparently simple *in vitro* systems contain the programming necessary to execute at least some aspects of embryonic development and organogenesis.

In the setting of the complex embryo, positional information and reaction-diffusion patterning models are not mutually exclusive hypotheses.<sup>107</sup> Indeed, we know that maternally deposited pre-patterns are crucial for embryonic development<sup>280</sup>, and that active feedbacks within these same pathways can stabilize patterns in the presence of challenges during embryonic development.<sup>232</sup> The temporal components of morphogen signals also can play a role in instructing developmental decisions.<sup>136</sup> A source of a diffusible signal will not only establish a gradient of local concentration, but also results in a gradient of arrival times for this signal to surrounding cells.

Disambiguating the role of these various features of a morphogen is extremely challenging with traditional methods – for example, injecting purified morphogen ligands will not only alter a pre-pattern, but will also activate feedbacks and generate gradients of signals in both space and in time. More precise spatiotemporal perturbations are required in order to articulate the dynamical princi-

ples that coordinate morphogen signaling pathways.

## 1.2 ELECTROPHYSIOLOGICAL PATTERNING

### 1.2.1 HISTORICAL CONTEXT: BIOELECTRIC PATTERNING IN THE HEART

Biochemical morphogens are not the only signals that cells use to communicate. Indeed, electrical patterns were among the first physiological dynamics to be characterized. In the 18th century, Luigi Galvani famously identified bioelectricity as a medium for biological signaling when he demonstrated that an external voltage could cause contraction of skeletal muscles.<sup>99</sup> It took an additional century to establish bioelectric patterns as the mechanism for regulating cardiac pacing.<sup>243</sup> Walter Gaskell showed in 1886 that lesioning muscle fibers connecting the atria and ventricles could block excitation of the ventricles, but did not affect atrial pacing, thereby establishing the sinus venosus as the cardiac pacemaker. Building on previous anatomic work from Purkinje, His, and Tawara, Martin Flack and Arthur Keith identified the sinus node where the heartbeat originates in 1907.<sup>148</sup> The concurrent invention of the electrocardiogram by Einthoven firmly established electrical dynamics as the mechanistic basis for regulating a stable, sinus cardiac rhythm.<sup>81</sup> The surface electrocardiogram remains a standard of clinical care to this day.

At a cellular level, it is now well understood that the cardiac physiology is coordinated by action potentials – stereotyped, nonlinear excitations in individual cardiomyocytes. Electrical depolarization of the plasma membrane activates voltage-gated calcium channels, leading to a subsequent calcium influx. Intracellular ryanodine receptors can generate additional calcium-induced calcium release from intracellular calcium stores in the sarcoplasmic reticulum.<sup>37</sup> In cardiomyocytes, calcium binding to troponin causes sliding of filaments and contraction of myocyte cells, squeezing the chambers of the heart and providing the mechanical pressure to eject blood into circulation.<sup>82</sup>

While the heart typically supports a regular ‘sinus’ rhythm associated with healthy cardiac phys-

iology, perturbations to the heart can disrupt this rhythm and drive transitions into irregular and even chaotic regimes. This irregularity can have both a spatial and a temporal aspect. For example, cardiac excitations can develop re-entrant patterns, in which an excitation fails to terminate, but circles back to re-initiate activity during the usual refractory period of the cardiac cycle.<sup>228,9</sup> A mechanistic basis for re-entrant waves was established by George Mines in the beginning of the 20th century, when he showed that explanted rings of cardiac tissue could support sustained oscillations after an excitation.<sup>189</sup> *In vivo*, local defects (e.g. regions of reduced or blocked conduction velocity) can similarly act as geometric generators of re-entrant spiral waves.

George Mines also showed that when the size of explanted rings of cardiac tissue is reduced, the temporal pattern of excitations undergoes a period-doubling bifurcation from a regular sinus rhythm to an alternating pattern of large and small excitations. If a given excitation circles back around the ring before the origin can fully recover, the next excitation is reduced in magnitude. The reduced magnitude wave then allows more time for the tissue to recover, leading to a full excitation on the subsequent cycle. This alternating pattern of large and small excitations – now referred to as ‘alternans’ - adds a temporal dimension to cardiac arrhythmias. Clinical electrocardiogram recordings can similarly show a transition to cardiac alternans under increasing pace rate in the setting of disease.<sup>12</sup>

The spatiotemporal pattern of electrical signaling in the heart is, quite literally, a matter of life and death. There is therefore considerable interest in developing a rigorous understanding of the conditions that determine stability, instability, and the emergence of chaos in the cardiac bioelectric pattern. Perturbations in a wide variety of parameters, some genetic (which species? variants of ion channels? expression levels of ion channels?), some biophysical (size of heart? geometry? conduction velocity? pace rate?), and some biochemical (concentration of cardioactive drugs? Levels of modulatory hormones?) could cause drastic differences in physiology. Mapping these dynamical regimes is extremely challenging *in vivo*. While some coarse perturbations can be made (e.g. genetic

knockout models; addition of cardiac drugs), we cannot explore the complete parameter space of the heart in its intact physiological setting.

Mathematical modeling provides an alternative approach to the study of electrical patterning and stability. Broadly, mathematical models of the heart occupy a continuum which ranges from biophysically fidelitous models to reduced models, in which some molecular details of the heart are coarse-grained. The former camp have their lineage in the work of Hodgkin and Huxley<sup>121</sup> – for example, the Noble model is a direct adaptation of Hodgkin-Huxley with parameters based on recordings from Purkinje fibers.<sup>205</sup> Recent work has extended these models to include explicit contributions from the myriad different ion channel subtypes expressed in different flavors of cardiac myocytes.<sup>209,252,253</sup> As the precision of these models increases, fitting unique parameter sets to experimental data becomes increasingly complex,<sup>112</sup> posing a challenge to the extrapolation and generalization of the predictions which they generate. On the other hand, in reduced models, a minimal set of coarse-grained variables is used to capture the salient qualitative dynamics. For example, the Aliev-Panfilov model<sup>4</sup> (based on the FitzHugh-Nagumo neural model<sup>94</sup>) is a two-variable model in which all slow ion channel kinetics are coarse-grained into a single recovery variable. An autoregressive model of cardiac dynamics has also been developed to study cardiac stability without explicitly modeling the membrane potential.<sup>287</sup> When choosing models across this continuum of complexity, one faces a general tradeoff between the degree with which one can describe a specific system with particular molecular components and the degree to which one can generalize predictions.

It remains an outstanding challenge to connect the complexity of *in vivo* measurements with the mathematical rigor of theoretical models. Experiments performed in engineered tissues offer a means to make contact between these two fields: to make experimental measurements in biological cells in which each molecular component is known and can be modeled explicitly.

### 1.2.2 HISTORICAL CONTEXT: BIOELECTRICAL PATTERNING IN THE BRAIN

The brain is the other organ which most famously relies on complex electrical pattern formation for its healthy function. Electrical signals from brain tissues were reported early as 1875<sup>249</sup>, but the relative complexity of neural electrical patterns made these observations challenging to interpret. Concurrent to the foundational electrophysiological work of the late 19th and early 20th centuries, Ramon y Cajal was establishing the foundations of neuroscience with his pioneering anatomical characterization of the brain.<sup>229,171</sup> By establishing that the dense meshwork of the brain was in fact compartmentalized into individual cells, he established the neuron as the fundamental unit of the brain.

This new ‘neuron theory’ was ultimately connected with electrophysiology of the brain by the work of Hodgkin and Huxley, published in 1952.<sup>121</sup> By making direct electrical contact with the squid giant axon, they developed a quantitative model for how feedbacks within voltage-gated ion channels sitting within the plasma membrane can cause transient excitations (action potentials, or ‘spikes’) in response to a stimulus. Patterns of spikes can govern communication between cells via coupling between voltage and neurotransmitter release. Transmission of neurotransmitters across synapses then governs the electrical patterns of a downstream cell, and so on. The electrical signals which one can record from the brain ultimately reflect patterns of electrical firing between complex networks of neurons.

Coordinated electrical signaling is essential to neurophysiology across many scales. At the level of individual neurons, complex morphological structures may cause the electrical signal to be compartmentalized between different regions of a cell (e.g., a given dendrite may sit at a different voltage than its soma<sup>276</sup>). At the level of small networks of neurons, synchronization between different cell types (e.g. inhibitory and excitatory) can underlie elemental computations and circuit functions (‘microcircuits’).<sup>150,154,177</sup> At a coarser-grained level, the flow information between anatomically

specialized brain regions allows for the parallel processing and eventual synthesis of multimodal information.<sup>262,258</sup> Different temporal patterns of activity are also thought to synchronize electrical activity within the brain across a range of timescales.<sup>34,35,39</sup> The synchronization of electrical signaling in the brain can also be pathological: for example, in the context of epilepsy.<sup>134</sup>

The tremendous progress of electrophysiology over the past half century has proceeded through the expansion and continued application of electrode-based experimental technique. The patch clamp remains the gold standard for single-cell electrophysiology: by forming a direct electrical contact with a cell, one can either record the voltage response of a cell in a given context (‘current clamp’) or use feedback electronics to measure the current response of a cell at a given voltage set-point (‘voltage clamp’).

Patch clamp methods have improved in sophistication considerably since the work of Hodgkin and Huxley and enabled the application of the method in more challenging and sensitive preparations.<sup>218</sup> However, this technique is particularly difficult to scale beyond a single cell due to the requirement for one patch electrode per cell. To observe larger ensembles of cells, arrays of electrodes can be placed in the extracellular space to record from any cell within its neighborhood. These multielectrode arrays come in a variety of formats, and are capable of measuring both shared common-mode activity (local field potentials, LFP) as well as individual spikes by sorting signals based on their timing and waveform on different electrodes. Extracellular electrode recordings have led to many seminal discoveries in neuroscience<sup>97,211</sup>, and new versions of the technology can record from up to 700 single units simultaneously during complex behavioral paradigms.<sup>138</sup> However, they have relatively limited spatial resolution (set by the physical size of individual electrodes) and are unable to associate electrical recordings with genetically defined cell types without augmentation from other techniques.

Classifying the diversity of electrophysiological patterns found within the brain is a challenging task. At the single-cell level, considerable progress has been made towards identifying and character-

izing ‘cell types’ which occur in various circuit motifs and brain regions. This continues the project which Ramon y Cajal began, and in its modern incarnation it combines measures of cell morphology, electrophysiology, and gene expression to generate an ‘atlas’ of cell types within the brain. In recent years this effort has been turbo-charged by single-cell RNA sequencing methods that enable measurement of the full transcriptome between thousands of single cells in parallel.<sup>153,175</sup> This approach has made it routine to characterize the genetic diversity of entire brain regions in single shots, and some emerging techniques enable the addition of spatial information to these measurements.<sup>45,230</sup> However, these measurements are extremely challenging to relate to functional measurements of electrophysiology. How these complex patterns of gene expression determine the electrophysiological properties of single cells, and how these single cells are assembled into functional electrical circuits, remains largely unknown.

An alternative classification scheme could involve reducing the full complexity of neurons into coarse-grained functional categories. These reduced models can come in a variety of flavors: one example is the Izhikevich model.<sup>131</sup> While classifying neural patterns in this scheme neglects some biological complexity, it can still capture several key features of electrical patterning in a more compact format. This format may make it more tractable to explore how single-neuron properties assemble into functional microcircuit motifs.

In addition to being structured in time, it is also well established that electrical patterns in the brain can be structured in space. Imaging experiments across a range of modalities (fMRI, EEG, voltage sensitive dyes) have revealed that activity can be organized into mesoscopic brain regions: for example, into whisker-associated barrels of the rodent barrel cortex.<sup>250</sup> These patterns are typically explained as consequences of gross neuroanatomy which is assembled during embryonic development. As a complementary explanation, some theoretical models anticipate spatial patterns of neural activity arising from a spontaneous symmetry breaking in a nominally homogeneous system. For example, a model which coarse-grains firing rates and synaptic transmission and embeds

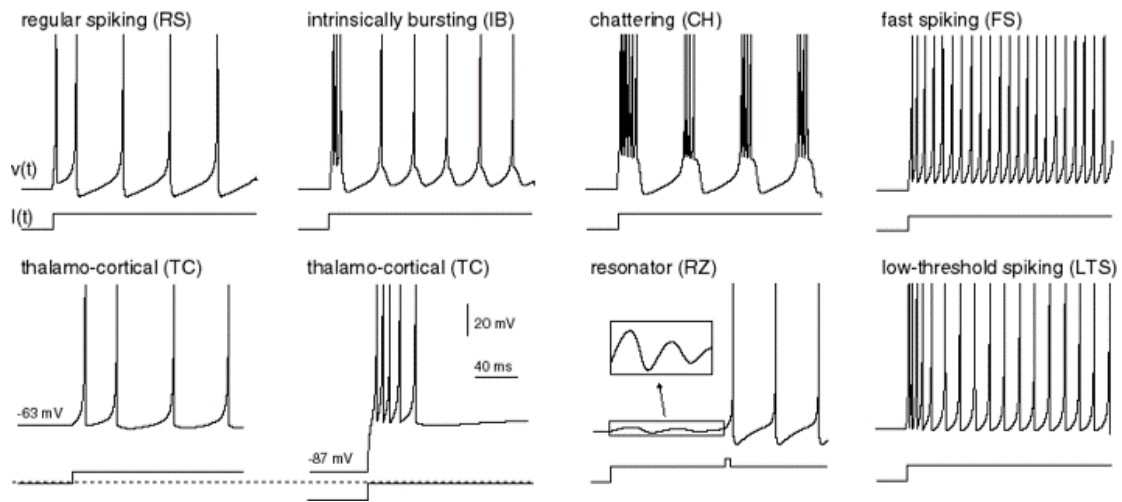


Figure 1.2: Example classifications of neurons in the Izhikevich framework. Adapted from Izhikevich.<sup>131</sup>

these dynamics in a ‘neural field’ can give rise to reaction-diffusion patterns such as waves and Turing patterns.<sup>57</sup> In general, it remains an open challenge to connect the diversity of temporal patterns observed at the single cell level to the complex spatiotemporal patterns which manifest in the intact brain.

### 1.2.3 UNCONVENTIONAL ELECTROPHYSIOLOGY ACROSS SCALES

Studies of electrophysiological signaling and pattern formation have focused almost exclusively on the heart and brain. Both cardiomyocytes and neurons share a common motif of electrical patterning: both cell types signal through transient action potentials on the order of milliseconds (in neurons) to hundreds of milliseconds (in cardiomyocytes). Electrical dynamics have also been well established in a handful of other systems – for example, in the pancreas<sup>13</sup>, in skeletal myocytes<sup>119</sup>, or in the electrogenic<sup>21</sup> and electroreceptive<sup>18,19</sup> organs of fish – all share this common motif of signaling through transient action potentials or oscillations.

Could electrical pattern formation coordinate biological functions on other spatiotemporal

scales? Action potentials are one particular class of reaction-diffusion patterns which are predicted by the Hodgkin-Huxley equations, but electrically coupled tissues could also in principle support time-stationary patterns that govern physiology on longer timescales – for example, on the timescales of embryonic development. Observing these patterns would be essentially infeasible using conventional electrode-based recording methods, as they would require stable intracellular recordings across multiple spatial locations over long time periods. It is conceivable that the comparative ease with which electrodes can detect action potentials has biased our understanding of electrophysiology towards spiking dynamics and away from other classes of patterns.

A number of recent studies have suggested that electrical patterning is essential for embryonic development in several systems.<sup>79,216,221</sup> For example: there is circumstantial evidence that electrophysiology may play a role in zebrafish skin pattern formation. Mutations in genes related to electrophysiology cause the zebrafish skin to develop other classes of reaction-diffusion like patterns besides the wildtype stripes: the jaguar mutation (Kir7.1)<sup>130</sup> and the leopard mutation (connexin41.8)<sup>267</sup> both cause spotted patterns to form. Zebrafish melanophores (one class of pigment cell) cultured *in vitro* show contact-dependent depolarization when contacting xanthophore cells (another pigment cell type).<sup>129</sup> Finally, optogenetic stimulation of melanophores was found to be sufficient to rearrange the skin pattern in wildtype fish into spot-like and labyrinthine patterns.<sup>10</sup> Collectively, the observations point to a role for long-term patterns of voltage to pattern developing tissues such as the zebrafish skin.

These observations provide compelling suggestions that voltage could play a role as a morphogen by organizing into patterns which are stable on the timescale of embryonic development. However, the complexity of *in vivo* systems poses a challenge to mechanistic interpretation. The developing embryo features signaling patterns across multiple modalities (e.g. voltage, biochemical signaling, mechanical rearrangement and cell migration) and scales which all happen concurrently. In order to establish a mechanistic basis for electrical signaling during embryonic development, one must

disentangle its role from the contributions of other signaling modalities. One strategy for navigating this complexity is to build reduced systems which demonstrate the essential physiology of interest *in vitro* in order to generate hypotheses of how it may manifest *in vivo*. In chapter 4 we will deploy this strategy to investigate the potential for stable electrical reaction-diffusion patterns to organize a developmental process.

### 1.3 NEW OPTICAL TOOLS FOR PROBING BIOLOGICAL COMPLEXITY

#### 1.3.1 MOTIVATION: LIMITATIONS OF CONVENTIONAL METHODS FOR STUDYING BIOLOGICAL PATTERN FORMATION

The aforementioned landmark experiments in biological pattern formation relied on experimental techniques with restricted precision in space and time. For example, transplant experiments in the early embryo require sampling cells from a particular location and developmental stage in a donor embryo, and transplanting them into a second staged location in a host embryo. Injections of purified morphogens also can only generate point sources of diffusible signals. Mutant studies perturb signaling pathways throughout the entire embryo for all of development; overexpression studies can realize some degree of spatiotemporal control using promoters associated with specific cell types,<sup>145,183</sup> but these strategies have restricted flexibility and are not feasible to apply to developmental signals in the early embryo (which are upstream of cell type specifications).

Classical electrophysiological experiments similarly rely on the use of an electrode placed either in direct contact or close proximity to the cells of interest. The spatial resolution of the method is therefore limited by the physical size of the stimulating or recording electrodes. While next-generation electrode technologies can enable the recording of hundreds of cells at once<sup>138</sup>, they cannot in general localize these cells with precision beyond the length scale set by the recording device. Moreover, standard algorithms for clustering units on multielectrode arrays rely on filtering high-frequency

spikes from background variation; slower changes in membrane potential cannot in general be assigned to individual cells. Spatial resolution in electrical stimulation is even more restricted: patch clamp measurements can stimulate individual cells, and extracellular electrodes can stimulate gross anatomical brain regions, but any intermediate scale of electrical stimulation is essentially infeasible. The limitations of standard electrophysiological recording techniques can therefore bias our understanding of electrical pattern formation in biology to the study of spiking cells; it is not clear that other forms of bioelectric patterning could be detected using conventional instrumentation.

### 1.3.2 DEVELOPMENT OF OPTOGENETICS

In order to study biochemical and bioelectric pattern formation across a more general range of spatiotemporal scales, new methods of interrogating pattern forming processes are needed. Light provides a generically powerful medium for interacting with biological systems. Optical physics has developed methods and instrumentation to manipulate light with extremely precise spatiotemporal resolution, and evolution (both natural and laboratory-directed) has yielded light-sensitive proteins that can perturb and report biological dynamics. By combining the heterologous expression of light-sensitive protein constructs with modern optical instrumentation, the ‘optogenetic’ strategy has opened new possibilities in experimental biology.

The proposal of using light to control biological dynamics, and electrical dynamics in the brain in particular, was proposed conceptually some time before it was realized practically – for example, by Francis Crick in 1979.<sup>222</sup> By the early 2000’s, progress towards this goal had been made by Gero Miesenböck and collaborators: both by the expression of *Drosophila* rhodopsin proteins (which are directly light-sensitive)<sup>285</sup> and by pairing of ionotropic receptors with photocaged ligands.<sup>286</sup> However, these instantiations all carried limitations, either of slow kinetics (with rhodopsins) or of the requirement of multiple components (in photocaging strategies). Contemporaneous work by Peter Hegemann and Ernst Bamberg characterized a microbial opsin protein in the green algae *Chlamy-*

*domonas reinhardtii* which produces a fast cation current in response to blue light stimulation.<sup>199</sup> Karl Deisseroth and Ed Boyden subsequently showed that the expression of this channelrhodopsin-2 (ChR2) protein in mammalian neurons enabled the precise control of neural spiking with light.<sup>25</sup>

The development of channelrhodopsin-2 as a molecular biological tool proved to be the harbinger of a movement within experimental neuroscience. Subsequent work has expanded the optogenetic toolkit to include proteins capable of inhibiting neuronal activity: for example, with the proton pump Archaelhodopsin-3<sup>51</sup>, with the chloride pump Halorhodopsin<sup>288</sup>, or with anion channelrhodopsins (GtACRs).<sup>176,105</sup> Other efforts have characterized or engineered new channelrhodopsins with altered spectral properties: for example, channelrhodopsins with red- or blue-shifted absorption spectra that facilitate combination with spectrally orthogonal actuators or fluorescent proteins.<sup>106,152,168</sup>

Channelrhodopsin and its microbial opsin cousins have provided a flexible toolkit to replace stimulating electrodes with light. Related efforts have developed genetically encoded indicators of biological dynamics to replace the recording electrode as well. The most prominent of these have been genetically encoded calcium indicators (GECIs), including GCaMP. By fusing circularly permuted versions of green fluorescent protein (cpEGFP) with the protein calmodulin and a calmodulin target sequence (derived from myosin light chain kinase), calcium-induced conformational changes will directly affect the fluorescence efficiency of the GFP fluorophore.<sup>201</sup> Because electrical spiking in neurons leads to an increase in the intracellular concentration of calcium, GCaMP allows for the optical readout of activity in genetically defined populations of neurons. Considerable effort since has improved the performance metrics of GCaMP, resulting in brighter<sup>254</sup>, faster<sup>46,66</sup>, and red-shifted GECIs.<sup>66</sup> By combining optogenetic actuators with spectrally orthogonal GECIs, several groups have realized all-optical neurophysiology in genetically defined cell populations.<sup>87,215</sup>

### 1.3.3 VOLTAGE IMAGING AND ALL-OPTICAL ELECTROPHYSIOLOGY

Paired optogenetic stimulation and calcium imaging has now established itself as a standard method of neuroscience. While this technique offers significant advantages in spatial resolution and genetic labeling when compared to electrode-based methods, it has the limitation of reading an indirect measure of electrical activity (calcium) rather than directly reading the voltage in target cells. Especially in systems where electrophysiological activity has been less well-characterized, and the correspondence of electrical signaling and calcium dynamics is not well understood, it may be challenging to relate calcium dynamics to underlying electrical patterning.

Genetically encoded voltage indicators (GEVIs) have recently been established as alternatives to GECIs.<sup>277</sup> Voltage imaging was first demonstrated with voltage-sensitive (or ‘potentiometric’) dyes (VSDs) which would partition across the cell membrane according to ratios predicted by the Nernst equation.<sup>44</sup> More recent work has developed VSDs which intercalate into the plasma membrane and whose fluorescence is directly modulated by voltage, enabling sub-millisecond kinetics;<sup>125</sup> however, these dyes still suffer from high background fluorescence (thus lower SNR) and phototoxicity in many applications.

In order to circumvent limitations of dye-based measurements, Adam Cohen’s laboratory set out to develop a protein-based voltage indicator which could be genetically encoded. One early prototype was based on the bacterial proteorhodopsin GPR, a light-driven proton pump.<sup>160</sup> In wild type GPR, light-driven proton transport generates a spectral shift in the protein through changes in the protonation of the Schiff base linking the retinal chromophore to the protein. By mutating the protein to reduce the strength with which protons are bound to this base, GPR can be ‘run in reverse’ to change color in response to physiological changes in membrane potential. This proteorhodopsin optical proton sensor (PROPS) enabled the optical recording of electrical activity in *E. coli*.<sup>160</sup> However, expression of PROPS in eukaryotic cells did not result in reliable localization to the plasma

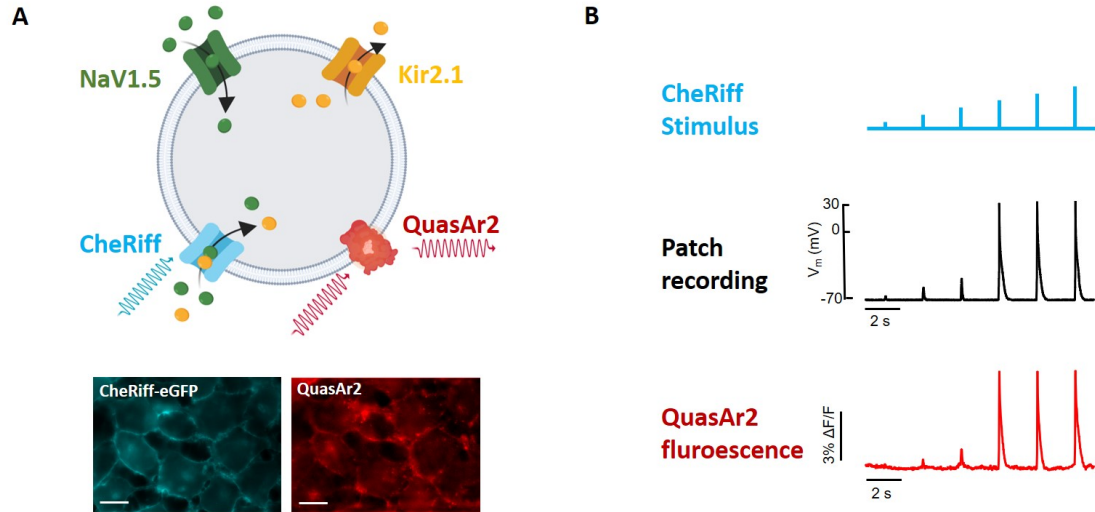


**Figure 1.3: All-optical electrophysiology.** A) Expressing a spectrally orthogonal channelrhodopsin and voltage indicator (e.g. CheRiff and QuasAr2) enables optical stimulation and readout of voltage. B) In response to a train of blue light pulses with increasing amplitude (top), the current clamp electrode recording (middle) and near-infrared fluorescence trace (bottom) both record spikes with tight correspondence. Scale bars = 20  $\mu\text{m}$ .

membrane.

An alternative sensor was developed based on the aforementioned Archaeorhodopsin-3 of *Halorubrum sodomense*.<sup>159</sup> Through a similar mechanism to PROPS, near-infrared fluorescence of Arch was able to report single-trial action potentials with high signal-to-noise ratio and submillisecond spatial resolution. Subsequent improvements to wild-type Arch (to eliminate native photocurrent and to improve kinetics and brightness) generated next-generation QuasArs (Quality superior to Arch). By combining these constructs with blue-shifted channelrhodopsins, the goal of all-optical electrophysiology was finally realized.<sup>120</sup>

Efforts continue to improve the performance of Arch-based voltage indicators: for example, by fusing them with fluorescent proteins or dyes to form FRET-based reporters<sup>1,104,293</sup> or by performing directed evolution screens to optimize properties like brightness and trafficking efficiency.<sup>219</sup> Improvements to Arch-based GEVIs have culminated with the recent demonstration of all-optical

electrophysiology in the mouse brain *in vivo*, including the hippocampus and layer 1 of the barrel cortex.<sup>2,86</sup>

By combining all-optical electrophysiological constructs with modern optical instrumentation, one can achieve a bioelectric interface with over 1 million inputs (e.g. from a digital micromirror array) and 1 million outputs (in high-speed CMOS camera), with diffraction limited (i.e. submicron) spatial resolution. Efforts continue to develop next-generation voltage indicators that enable new regimes of measurement: for example, indicators with a voltage-sensitive two-photon fluorescence signal. Voltage imaging will continue to change the landscape of contemporary neuroscience and neuroimaging.

#### 1.3.4 OPTOGENETIC TOOLS FOR CONTROLLING PROTEIN-PROTEIN INTERACTIONS

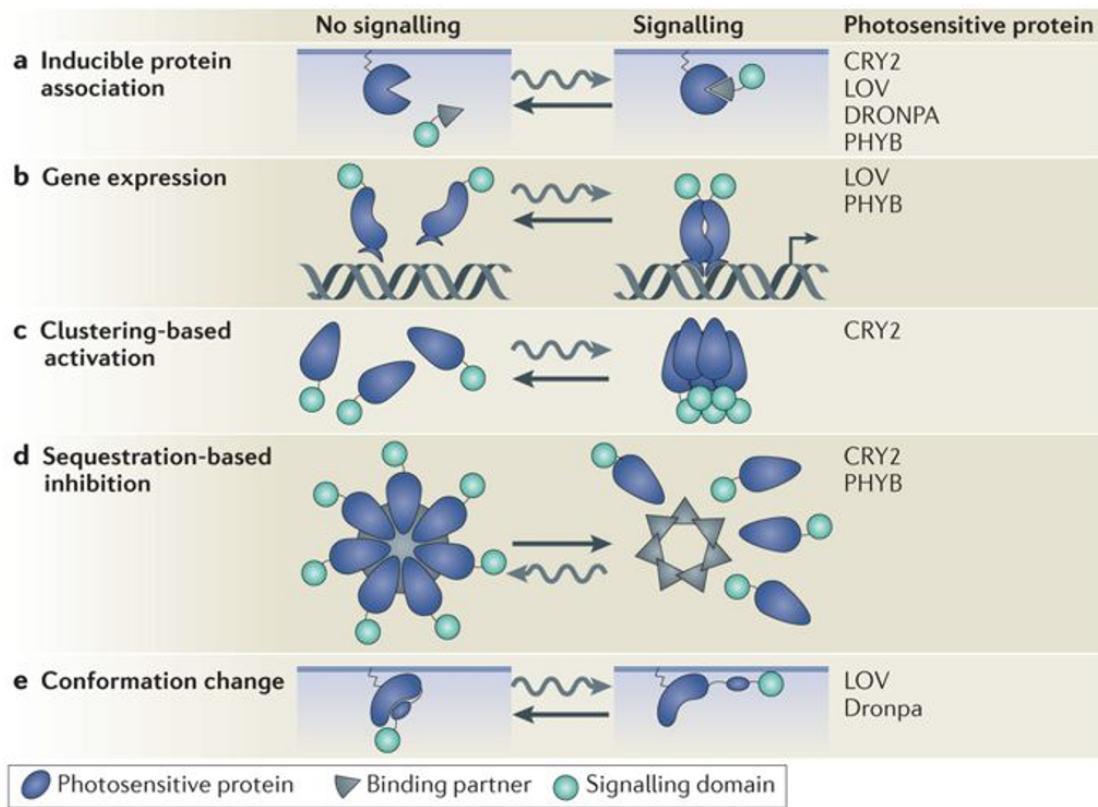
Perturbing biological dynamics with light is a generically powerful strategy with potential advantages beyond the scope of electrophysiology. Many biochemical signaling pathways proceed through the interaction of two proteins in the presence of a signal ligand: for example, the association of type 1 and type 2 TGF $\beta$  receptors in the presence of their associated ligand. If one could manipulate these interactions with light, then one could extend the optogenetic method beyond electrophysiology and neuroscience to more general classes of biological pattern formation.

Fortunately, nature has evolved a number of protein tools which associate or dissociate in response to light. The identified photoassociating domains (PADs) fall into several broad categories, most of which were originally characterized in *Arabidopsis thaliana*. The largest and most diverse category of PADs are the light-oxygen-voltage sensing domains (LOV domains).<sup>225</sup> LOV domains were first identified in *Arabidopsis* as effector domains within kinases that regulate phototropism.<sup>280</sup> Conformational changes mediated by a Flavin cofactor-dependent photocycle lead to redox signaling changes and downstream transduction of light into biochemical signaling. LOV domains have been found in a wide diversity of organisms (from *Arabidopsis* to microbes) and vary considerably in

photophysical kinetics and association topology. Another class of tools is based on the *Arabidopsis* cryptochrome CRY<sub>2</sub>, which endogenously binds CIB<sub>1</sub> when it is excited by blue light. The CRY<sub>2</sub>-CIB<sub>1</sub> system constitutes a powerful PAD with high dynamic range, quick kinetics (association and dissociation kinetics on the minute timescale), and two-photon sensitivity.<sup>149</sup> A third important PAD is derived from the phytochrome system of *Arabidopsis*: the protein phytochrome B (Phy) will, when bound to the chromophore phycocyanobilin (PCB), undergo conformational changes in response to absorption of red to near infrared light. Only one conformation binds the phytochrome interactor factor 6 (PIF), so Phy/PIF represents yet another PAD toolkit.<sup>257</sup>

Each PAD has potential advantages and disadvantages. Notably, PHY/PIF can be controlled by red light (LOV and CRY<sub>2</sub>/CIB<sub>1</sub> tools are blue light sensitive), making it in principle amenable to deep tissue applications or spectrally compatible combination with blue light-sensitive tools. Also, PHY/PIF can be bidirectionally driven, as red and near-infrared absorption drive opposing conformational changes. However, the reliance of PHY/PIF on PCB chromophore (which is not natively synthesized in animal cells) represents a dramatic limitation. Alternative bacterial phytochrome systems which instead utilize biliverdin chromophores (which are abundant in animals, including mammals) may offer an alternative platform which circumvents this limitation.<sup>139</sup> In general, the cryptochrome and LOV based constructs have been more heavily utilized and have spawned a series of engineered versions with faster kinetics, sensitivity, and predilection towards homo- or hetero-oligomerization.<sup>77,III,146</sup>

Adapting PADs into optogenetic tools is not yet a plug-and-play process: nuances in the structure and function of PADs may interfere with more complex aspects of tool function. For example, method demonstration of many PADs is typically achieved by fusing the two components to different fluorescent proteins, and targeting one subunit to the plasma membrane. Imaging of either fluorescent protein can show recruitment of the cytosolic component to the membrane in the presence of PAD photoexcitation. This kind of assay may not be sensitive to more stringent technical



Photosensitive protein	Turn-on speed	Turn-off speed ( $t_{1/2}$ )	Chromophore requirement	Compatible imaging wavelengths (nm)	$\lambda_{on}$ (nm)	$\lambda_{off}$ (nm)	Effector affinity
PHYB	Seconds	• Seconds (illuminated at 750nm) • Hours (dark reversion)	PCB; exogenous or synthesized in situ	$\leq 514$	650	750	• <100 nM (post 650nm) • >100 $\mu$ M (post 750nm)
CRY2	Seconds	5 minutes	Flavin; endogenous	$\geq 561$	405–488	NA	Not determined
LOV	Seconds	Tens of seconds to minutes	Flavin; endogenous	$\geq 514$	440–473	NA	• 1 $\mu$ M (dark) • 100 $\mu$ M (light)
Dronpa	Seconds	• Tens of seconds (illuminated at 390nm) • Tens of minutes (dark reversion)	None	$\geq 600$	390	490	• 10 $\mu$ M (post 490nm) • >100 $\mu$ M (post 390nm)

CRY2, CRYPTOCHROME 2; NA, not applicable; PHYB, PHYTOCHROME B; PIF, PHYTOCHROME INTERACTING FACTOR.

**Figure 1.4: Diversity of photoassociating domain applications.** Figure and table adapted from Tischer.<sup>255</sup> Photoassociating domains can be conjugated to target proteins in order to induce heterodimers, to localize proteins to a particular cellular compartment, to induce homo-oligomerized clusters, to sequester proteins, or to induce conformational changes. Bottom: photoassociating domains vary in their kinetics, affinities, and spectral properties.

requirements of PAD-based optogenetic tools: for example, if two subunits of a split enzyme need to complex in a particular orientation. Development of biochemically active optogenetic tools frequently involves screens among a diversity of PADs or design topologies (e.g. C- or N-terminus conjugation) in order to find a biochemically permissive structure.<sup>109</sup> While crystal structure-guided rational design can sometimes inform design strategies, this is not feasible with all PAD varieties. Improving the dynamic range, modularity, and spectral flexibility of PAD-based optogenetic tools remains an outstanding challenge.

### 1.3.5 PROSPECTS FOR OPTOGENETICS IN DEVELOPMENTAL BIOLOGY

Optogenetics has now been widely adopted as a core tool of modern neuroscience. The combination of spatiotemporal control and genetic specificity offered by optogenetics has enabled experimental progress towards disentangling the complexity of the brain that would be infeasible with conventional methods.

Applications of optogenetics in other complex biological systems are still emerging. The developing embryo is a particularly compelling candidate system: developmental programs rely on multiple spatiotemporally structured signals, and disentangling the specifications and tolerances of these signals is challenging with conventional tools. Many existing applications of optogenetics to embryology have leveraged the temporal precision of optical stimulation. For example, optogenetic stimulation of Nodal signaling throughout the zebrafish embryo was found to have effects on gene expression which were highly sensitive to the temporal period in which the pathway was active.<sup>235</sup> Similarly, optogenetic stimulation of Erk signaling in *Drosophila* has been used to explore how cellular responses depend on signaling dynamics independent of signal intensity.<sup>136</sup> Some coarse amount of spatial control can be achieved with widefield illumination by targeting one of the PAD components to a particular cellular compartment (e.g. the plasma membrane).<sup>30</sup> Another scale of spatial control can be achieved by patterning the stimulating illumination; this has been demonstrated in

*Drosophila* to control tissue folding via Rho activation,<sup>132</sup> and to probe the how embryonic lethality of ectopic Erk/Ras stimulation depends on the stimulus location.<sup>135</sup>

These applications demonstrate a proof of principle that optogenetic tools can manipulate embryonic development with spatiotemporal precision that would be infeasible using other techniques. An outstanding challenge is to extend this approach to articulate the design specifications of morphogen patterns in the embryo: which features of these signal are important for cell fate specification and embryonic development? And how do different signals interact to generate robust development outcomes out of noisy cellular components? Using light to illuminate the spatiotemporal constraints of morphogen patterning can establish optogenetics as a core methodology in the study of embryo, just as it has been established in the study of the brain.

# 2

## Synthetic electrically excitable tissues with optical control and readout

COMPLEX ELECTRICAL DYNAMICS in excitable tissues occur throughout biology, but the roles of individual ion channels can be difficult to determine due to the complex nonlinear interactions in native tissue. Here we ask whether we can engineer a tissue capable of basic information storage and

processing, where all functional components are known and well understood. We develop a cell line with 4 transgenic components: two to enable collective propagation of electrical waves, and two to enable optical perturbation and optical readout of membrane potential. We pattern the cell growth to define simple cellular ring oscillators that run stably for  $\sim 10^4$  cycles), and that can store data encoded in the direction of electrical circulation. Using patterned optogenetic stimulation, we probe the biophysical attributes of this synthetic excitable tissue in detail, including dispersion relations, curvature-dependent wavefront propagation, electrotonic coupling, and boundary effects. We then apply the biophysical characterization to develop an optically reconfigurable bioelectric oscillator. These results demonstrate the feasibility of engineering bioelectric tissues capable of complex information processing with optical input/output.

## 2.1 MOTIVATION

Electrical dynamics in the brain, heart, endometrium, and pancreas arise from complex interactions among a large number of electrically excitable cells. The task of deciphering the relations between ion channel dynamics, single-cell properties and tissue function is often daunting. A longstanding goal in synthetic biology is to design minimal systems that recreate aspects of naturally evolved variants.<sup>226</sup> By probing the necessity and sufficiency of individual components, this strategy can augment our understanding of more complex natural systems, and it can also point toward design principles for synthetic systems with novel behaviors and properties.

Most efforts within synthetic biology have focused on engineering intracellular networks to create basic functional elements such as oscillators<sup>83</sup>, registers<sup>100</sup>, and counters.<sup>96</sup> Multicellular interactions have the possibility to evince emergent dynamics not seen in individual cells.<sup>179</sup> Indeed, models of cellular automata have been a standard tool in theoretical explorations of complex networks. Excitable media have been shown theoretically capable of implementing complex computations<sup>3,61</sup>;

and light-sensitive Belousov-Zhabotinsky reactions have been experimentally used to implement rudimentary image transformations<sup>162</sup> and logical operations.<sup>69</sup> In the context of cardiac dynamics, simple models of coupled excitable cells show rich dynamics under periodic forcing, including period doubling and transitions to chaos in 1D<sup>102</sup> and 2D<sup>59</sup>, and spiral waves and wave breakup in 2D and 3D.<sup>144,143,270</sup> Experimental implementations of multicellular synthetic biological systems have remained challenging.<sup>179</sup>

Hsu and coworkers showed that two voltage-gated ion channels were sufficient to induce electrical spikes in otherwise electrically inexcitable tumor cells.<sup>124</sup> Kirkton and Bursac used a similar strategy to engineer an electrically spiking cell line which additionally supported nearest-neighbor coupling via a gap junction protein.<sup>151</sup> Our lab then engineered a spiking cell line in which a genetically encoded fluorescent voltage indicator enabled direct, dye-free visualization of electrical waves.<sup>217</sup>

While these systems constituted synthetic excitable tissues, their amenability to rigorous biophysical characterization and dynamical control was limited by a lack of spatiotemporal control over wave initiation. Spatially patterned optogenetic stimulation has been applied to study a variety of cardiac<sup>32</sup> and neuronal<sup>84</sup> preparations, but spectral crosstalk of most optogenetic actuators and voltage reporters prevented simultaneous perturbation and measurement of membrane potential. We recently developed a genetic construct, called ‘Optopatch’, which comprises a bicistronic vector for co-expression of a blue light-gated ion channel, CheRiff, and a red light-excited voltage indicator, QuasAr2.<sup>120</sup> Together, these two proteins enabled crosstalk-free optical stimulation and measurement of membrane voltage in cultured neurons. However, the low brightness of QuasAr2 posed an obstacle to imaging with field of view sufficiently wide to study collective multicellular dynamics.

Here we report a synthetic bioelectric tissue which supports simultaneous optical stimulation and readout of membrane voltage, and whose complex nonlinear dynamics enabled basic information storage and processing. The tissue comprised human embryonic kidney (HEK-293) cells expressing an inward rectifier potassium channel ( $K_{ir2.1}$ ), a voltage-gated sodium channel ( $Na_v1.5$ )

and the Optopatch genes. To interact with this tissue we developed an optical system engineered to combine high-precision patterned optogenetic stimulation with high sensitivity voltage imaging over a large field of view ( $5 \text{ mm} \times 1 \text{ mm}$ ).

This high level of control enabled biophysical characterization of the tissue at a previously unattainable level of detail and the creation of simple bioelectric circuits which could store and process information. Information storage was performed in bioelectric ring oscillators whose direction of circulation constituted a topologically stable binary bit. Information processing was achieved via optical steering, gating, and modulation of electrical wave propagation. The combination of rationally designed excitable cells with high-resolution optogenetic control opens the door to creation of increasingly complex bioelectrical systems. While the biophysics of ion channels limits the speeds of these systems to  $< 100 \text{ Hz}$ , the living substrate opens the possibility for novel sensing<sup>203</sup> and tissue engineering applications<sup>282</sup>, as well as fundamental studies of the biophysics of excitable tissues.

## 2.2 EXCITABLE CELLS WITH A BIDIRECTIONAL OPTICAL INTERFACE

HEK cells have a resting potential around  $-20 \text{ mV}$ , a membrane resistance  $> 500 \text{ M}\Omega$ <sup>27</sup>, and on their own are electrically inexcitable. We engineered a HEK cell line that stably expressed an inward rectifier potassium channel,  $K_{ir2.1}$ , and a voltage-gated sodium channel,  $Na_{v1.5}$  (Figure 2.1a). The  $K_{ir2.1}$  channels lowered the resting potential to  $-70 \text{ mV}$ , priming the  $Na_{v1.5}$  channels for activation. Upon depolarization to voltages greater than  $-50 \text{ mV}$ , the sodium channels activated, leading to a voltage spike. The  $Na_{v1.5}$  channels then inactivated and the  $K_{ir2.1}$  channels returned the membrane to its resting potential. To provide a bidirectional optical interface, we also stably expressed a blue light-activated channelrhodopsin, CheRiff (Figure 2.1b), and a red light excited fluorescent voltage indicator, QuasAr2 (Figure 2.1c), linked by a self-cleaving P2A peptide<sup>120</sup>. The HEK cells endogenously expressed a low level of gap junctions,<sup>33</sup> which provided nearest neighbor electrical coupling. We

called the engineered cell line Optopatch Spiking HEK cells (OS-HEK cells).

We characterized the cells via simultaneous manual patch clamp and fluorescence measurements, while stimulating with pulses of blue light of increasing intensity ( $\lambda_{\text{ex}} = 488 \text{ nm}$ , 6 pulses of 10 ms duration from 15 to 115 mW/cm<sup>2</sup>). At blue stimulus intensity  $\leq 60 \text{ mW/cm}^2$  cells showed small electrical depolarizations with magnitude proportional to illumination intensity. At blue stimulus intensity of 90 mW/cm<sup>2</sup>, cells spiked to +33 mV, close to the sodium reversal potential, and then gradually returned to baseline. Illumination at higher intensities did not lead to further increases in spike amplitude, a defining characteristic of action potentials. The QuasAr2 fluorescence closely followed the electrical recording, with an action potential amplitude of 6%  $\Delta F/F$ . These results established the feasibility of simultaneous optical stimulation and optical readout of electrical spikes in OS-HEK cells.

To probe collective dynamics, we developed a wide-field optical system for simultaneous imaging and stimulation. To achieve high optical sensitivity over a large field of view we used a large-aperture objective lens (Olympus MVX-2, 2x, NA 0.5), custom extra-large dichroic mirrors (60 × 85 mm), and a custom imaging path. Due to the low brightness of QuasAr2, it was necessary to illuminate the sample with high intensity red light (635 nm, 13 W/cm<sup>2</sup>) over the whole imaging area (5 mm × 1 mm). To avoid autofluorescence of the glass in the objective lens, the red light was brought into the sample through a custom fused silica prism coupled to the bottom of the sample via immersion oil (Figure 2.2).<sup>120</sup> The laser entered the sample just below the angle for total internal reflection at the glass-water interface, minimizing illumination of glass below or buffer above the cells. Fluorescence from the sample passed through the prism to the objective. Patterned blue illumination was provided by a digital micromirror device (DMD) with a resolution of 912 × 1140 pixels. Individual cells within a confluent monolayer ( $\sim 160,000 \text{ cells/cm}^2$ ) were resolvable via the fluorescence of CheRiff-eGFP (Figure 2.1e). The field of view comprised  $\sim 8000$  OS-HEK cells. At high cell densities we often observed spontaneous spiral waves of fluorescence propagating through the dish.

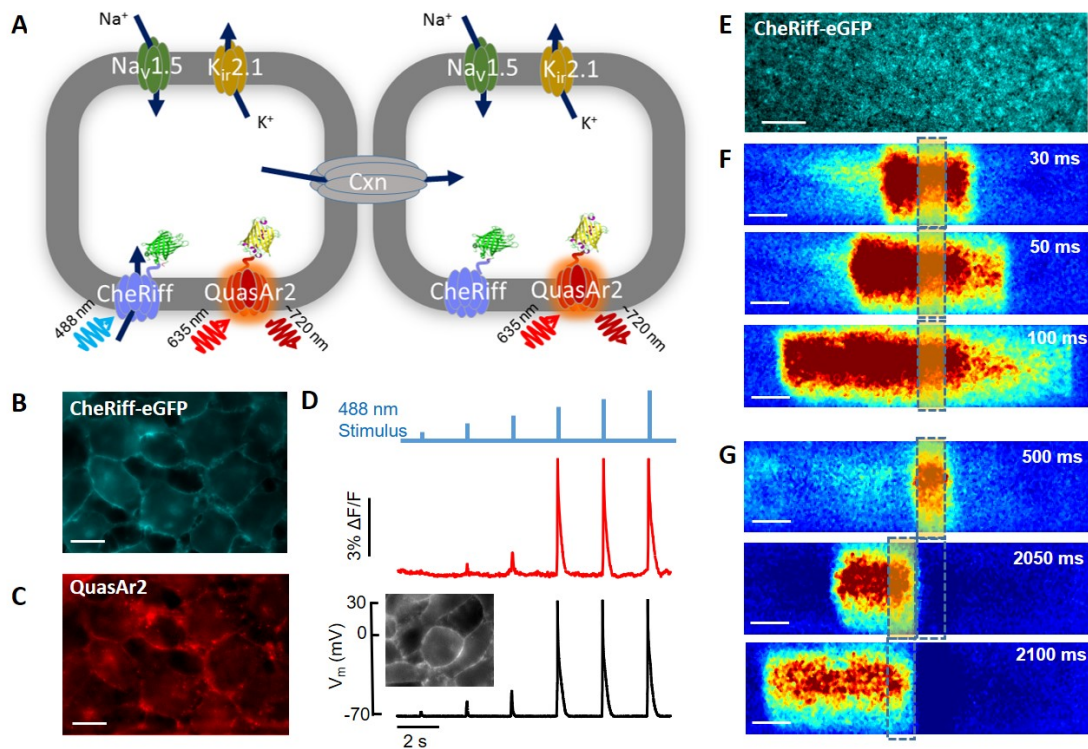


**Figure 2.1: Optopatch spiking HEK (OS-HEK) cells enable optical stimulation and optical readout of electrical waves in confluent monolayers.** A) Functional components of OS-HEK cells. Two transgenic ion channels ( $\text{Na}_v1.5$ ,  $\text{K}_i2.1$ ) imbue the cells with the ability to produce electrical spikes. Two optogenetic components (CheRiff and QuasAr2) provide optical input and output, respectively. Endogenous gap junctions provide electrical coupling between neighboring cells. B) Image of eGFP fluorescence in CheRiff-eGFP. C) Image of QuasAr2 fluorescence. Scale bars in B and C, 20  $\mu\text{m}$ . D) Simultaneous fluorescence recording (red,  $\lambda_{\text{exc}} = 635 \text{ nm}$ ,  $1 \text{ kW/cm}^2$ ,  $\lambda_{\text{em}} = 668 - 743 \text{ nm}$ ) and patch clamp measurements (black) during ramped optogenetic stimulation (blue). Inset: image of the recorded cell. E) Wide-field image of eGFP fluorescence in a confluent layer of OS-HEK cells. F) Images of QuasAr2 fluorescence showing wave propagation induced by a flash of blue light delivered to the dashed box. G) Directional waves are launched by inactivating a zone (top), and then stimulating an adjacent region (middle). Scale bars in E-G 500  $\mu\text{m}$ .

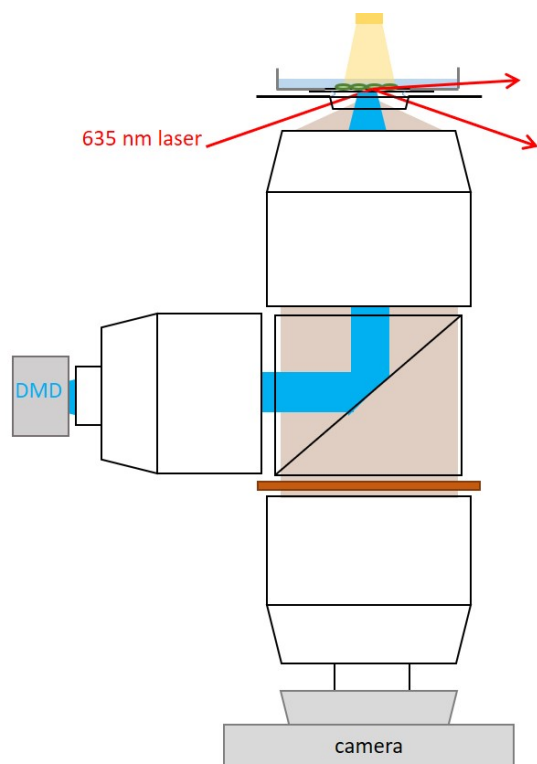


**Figure 2.2: Microscope design for imaging OS-HEK cultures.** A digital micromirror device is used to pattern blue light for structured CheRiff excitation. QuasAr2 fluorescence is imaged in a pseudo-TIRF configuration in order to minimize background autofluorescence from the ultrawidefield objective by coupling into immersion oil via a fused silica prism.<sup>120</sup>

We stimulated the sample with a bar of blue light ( $\lambda_{\text{ex}} = 488 \text{ nm}$ ,  $200 \text{ mW/cm}^2$ ,  $300 \mu\text{m} \times 1 \text{ mm}$ ,  $50 \text{ ms}$  duration) and recorded a movie of the ensuing changes in QuasAr2 fluorescence. An action potential wave propagated through the syncytium away from the bar at a velocity of  $2.3 \text{ cm/s}$ , (Figure 2.1f), establishing that a confluent layer of OS-HEK cells could support collective wave propagation, with optical input and output.

To launch unidirectional waves, we used the fact that static depolarization leads to inactivation of sodium channels. A bar-shaped region was illuminated with a long-lasting blue pulse ( $2 \text{ s}$ ,  $200 \text{ mW/cm}^2$ ). An adjacent bar was then illuminated with a brief blue pulse ( $50 \text{ ms}$ ,  $200 \text{ mW/cm}^2$ ). The resulting wave propagated unidirectionally away from the statically illuminated region (Figure 2.1g). A similar protocol has been used to launch directional waves in cardiac cell cultures.<sup>32</sup>

### 2.3 RING OSCILLATORS AND BIOELECTRIC MEMORIES IN PATTERNED OS-HEK CELLS

The capability of OS-HEK cells to support optically triggered wave propagation suggested that these cells might be configured as stable oscillators. We used soft lithography<sup>227</sup> to pattern the cell growth into annular patterns with diameters ranging from  $1$  to  $5 \text{ mm}$  (Figure 2.3a). We then used the illumination sequence of Figure 2.1g to launch unidirectional waves in these rings. Waves propagated stably in rings of diameter  $2$ ,  $3$ , and  $4 \text{ mm}$ , but in  $1 \text{ mm}$  diameter rings waves caught their tails and quenched.

Waves could be launched clockwise or counterclockwise, stopped with a bar of static illumination, and then relaunched in either direction (Figure 2.3b-d). The direction of wave propagation constituted a topologically stable bit of information. To explore the capabilities of this bioelectric memory, we wrote all four two-bit patterns of oscillation into two concentric rings. The handedness remained stable for  $> 2 \text{ hrs}$ , corresponding to  $\sim 10^4$  oscillation cycles (Figure 2.3e). Over  $2 \text{ hours}$  the oscillation frequency in the  $3 \text{ mm}$  diameter ring drifted by  $4.8\%$ , from  $2.37 \text{ Hz}$  to  $2.25 \text{ Hz}$ .

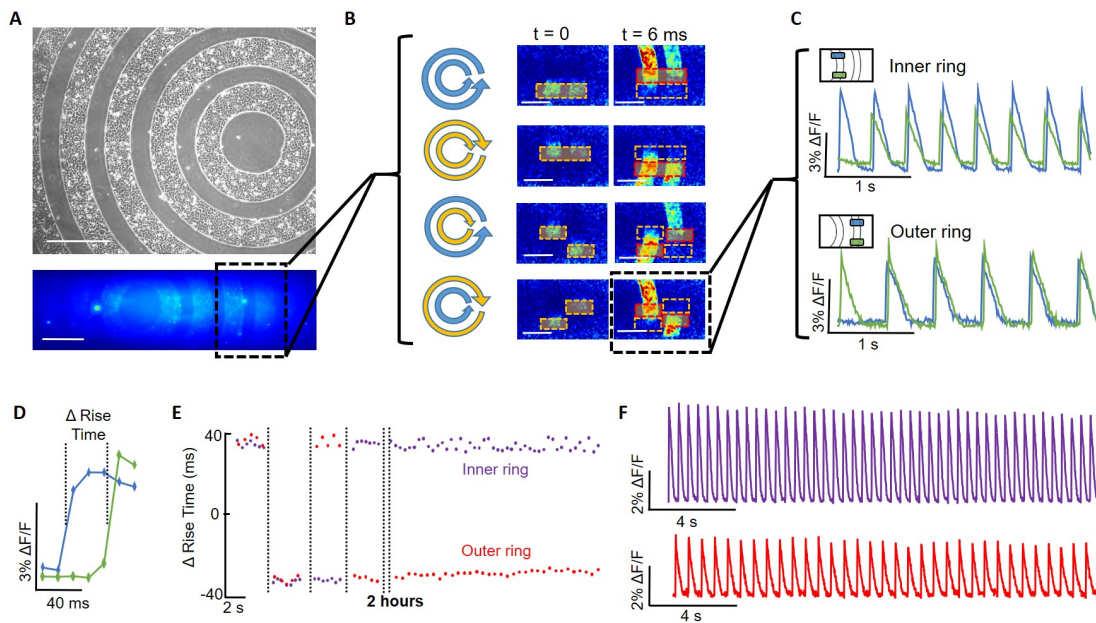


**Figure 2.3: Ring oscillators in annular OS-HEK cell cultures.** A) Top: transmitted light image of micropatterned rings of OS-HEK cells. Bottom: the fluorescence field of view was limited to a slice through the rings. B) Optical initiation of directional waves in the annular cultures. In two concentric rings, waves were launched sequentially in all four binary combinations of directions. Dashed boxes indicate the illumination sequences used to launch the waves. Scale bars in A and B 1 mm. C) Intensity patterns of QuasAr2 fluorescence after wave initiation. D) A slight time shift in the upstroke of the waves measured at different locations on the annulus indicated the direction of circulation. E) Writing of all four two-bit binary patterns. Red and purple dots indicate the direction of propagation in the outer and inner rings, respectively. The last pattern was left undisturbed at room temperature and continued to circulate for  $> 2$  hours. F) Oscillation patterns in regions of the inner and outer rings after 2 hours of continuous circulation, corresponding to  $\sim 10^4$  cycles.

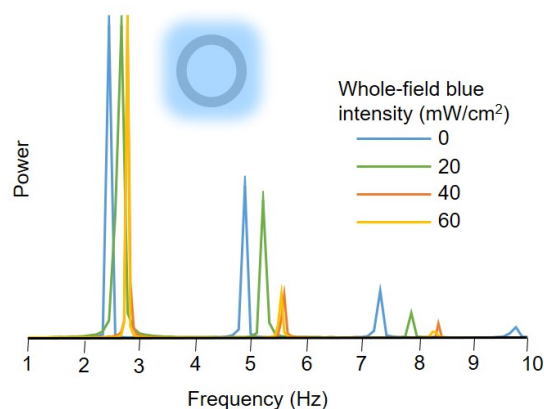


**Figure 2.4: Optical control of conduction velocity with static illumination.** A directional wave was launched in an annular ring of OS-HEK cells. The whole ring was then exposed to static blue illumination of gradually increasing intensity. The graph shows the power spectrum of the QuasAr2 fluorescence at a region along the ring. As the intensity of the background blue illumination increased, the oscillation frequency increased, up until a point after which the oscillation collapsed. This behavior is interpreted as activation of  $\text{Na}_v$  channels at modest depolarization leading to increased conduction velocity, followed by inactivation at strong depolarization.

As in any physical oscillator, long-term stability enabled us to detect subtle shifts in frequency, in this case arising from changes in conduction velocity. In principle, conduction velocity could be sensitive to any environmental or pharmacological perturbation which affected the ion channels or metabolism of the cells. Burton and coworkers found that conduction velocity in cultured cardiac myocytes could be increased by whole-field weak optogenetic stimulation.<sup>32</sup> We tested whether the same was true for OS-HEK cells. In a ring of diameter 3 mm, oscillations in the absence of blue illumination occurred at a frequency of 2.44 Hz and had a transform-limited spectral linewidth of 0.11 Hz in a 9 s measurement band. Whole-field illumination with dim blue light brought the cells closer to activation threshold and thereby led to faster conduction, up to a maximum 14% increase at 60 mW/cm<sup>2</sup> (Figure 2.4). Illumination above 60 mW/cm<sup>2</sup> quenched the oscillation. Transform-limited changes in oscillation frequency as small as 4.2% in a 10 s measurement window were readily detectable, suggesting possible biosensor applications for rings of OS-HEK cells.

## 2.4 BIOPHYSICAL CHARACTERIZATION OF OPTOPATCH SPIKING HEK CELLS

Wave propagation in excitable media is governed by the restitution properties of the individual units<sup>102,110</sup> the dispersion relation of the medium (dependence of conduction velocity on excitation rate)<sup>15</sup>, and the effect of curvature on wavefront velocity.<sup>36,275</sup> These parameters have previously been studied in cardiac tissue<sup>89</sup>, though until recently stimulation with physical electrodes imposed constraints on stimulus geometry. Patterned optogenetic stimulation combined with voltage imaging provided a facile measurement platform to characterize in detail these biophysical parameters in cultures of OS-HEK cells.

### 2.4.1 DISPERSION RELATIONS

In a periodically stimulated excitable medium, each wavefront propagates in the wake of the preceding wave. If the interval between waves is comparable to or shorter than the recovery time of the medium, conduction velocity and action potential duration depend on stimulus frequency. We measured the dispersion relations in a homogenous OS-HEK culture by launching periodic trains of ten waves with a bar-shaped stimulus (50 ms, 200 mW/cm<sup>2</sup>, 125  $\mu$ m  $\times$  6 mm), with repetition frequency from 0.5 to 4.0 Hz. For each wave, we characterized the conduction velocity (CV, Figure 2.5), and action potential duration (AP<sub>50</sub>, full-width at half-maximum, Figure 2.6). The spatial extent of the propagating depolarization was then given by  $L=AP_{50}\times CV$ . Between trains of different frequencies the sample was given 2 s to relax. We observed a weak decrease of conduction velocity with increasing frequency between 0.5 and 2.5 Hz (Figure 2.5a), and also a weak decrease of AP<sub>50</sub> over this frequency range (Figure 2.6). At stimulus frequencies > 2.5 Hz it was not possible to quantify wave propagation because the stimulus triggered reentrant spiral waves which interfered with smooth propagation of optically triggered waves.

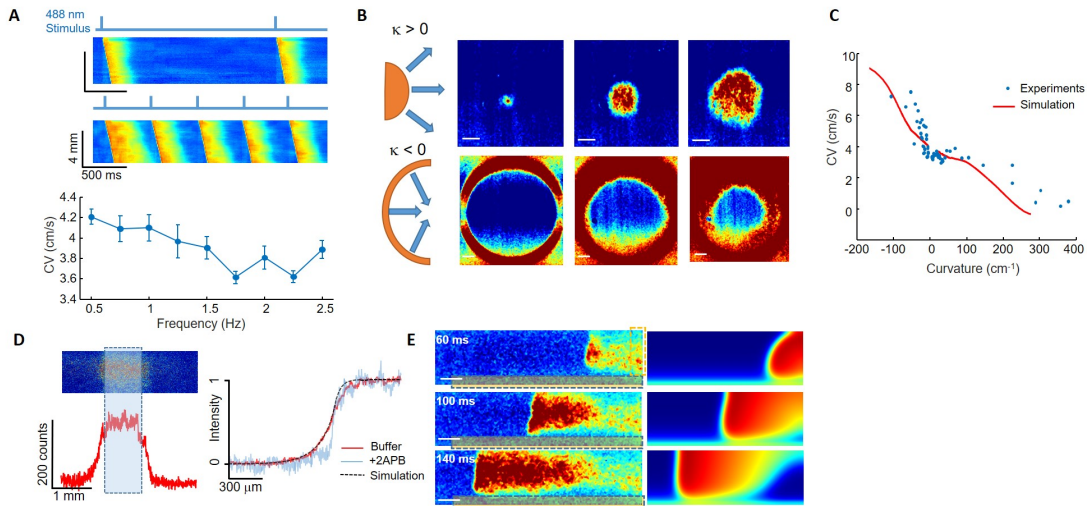


**Figure 2.5: Characterizing wave propagation in OS-HEK cell cultures.** A) Dispersion relation. Samples were stimulated with a vertical bar of blue light for 50 ms, 10 times in succession, with variable frequency. Movies of fluorescence were converted into kymographs by averaging parallel to the wavefront. Top: example kymographs recorded at 0.5 Hz and 2 Hz. Bottom: mean conduction velocity as a function of stimulus frequency. Error bars represent standard deviation of individual wave measurements within a train. B) Curvature-dependent conduction velocity. Waves were launched either outward from a small spot (top) or inward from an annular ring (bottom) to probe positive and negative curvatures, respectively. Scale bars 500  $\mu\text{m}$ . Successive panels separated by 10 ms. C) Scatter plot of conduction velocities as a function of curvature (blue points). Each point represents a single frame of a particular wave. Data were compiled across several trials with differing fields of view to accommodate both low and high curvatures ( $n = 10$  trials). Red: Numerical simulations based upon Aliev-Panfilov model. D) Static electrotonic coupling. Top: cells were illuminated with a bar of blue illumination of sufficient intensity ( $200 \text{ mW}/\text{cm}^2$ ) to saturate CheRiff photocurrent. Bottom: mean QuasAr2 intensity profile transverse to the bar of illumination. The CheRiff-induced depolarization spread laterally away from the illuminated zone. Right: Comparison of measured depolarization profile to a numerical fit based on the Aliev-Panfilov model with a coupling length of 300  $\mu\text{m}$ . A gap junction blocker (2-aminoethoxydiphenyl borate) suppressed the lateral spread of depolarization. E) Static illumination guides to propagation. Left: a wave was launched adjacent to a region of static illumination (indicated with dotted box on the bottom of the images). The wave propagated parallel to the boundary, with local inhibition adjacent to the boundary. Right: comparison to simulations of the Aliev-Panfilov model. Scale bars 500  $\mu\text{m}$ .

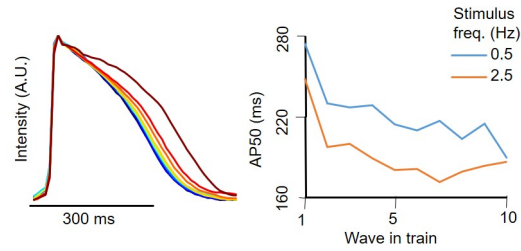


**Figure 2.6: Action potential dynamics during a periodic wave train.** Left: the first action potential after a rest interval was broader than subsequent action potentials. Here stimuli were delivered at 0.5 Hz. Right: Reduction in AP width as a function of stimulus number for stimuli at 0.5 and 2.5 Hz. In both cases, after 5 stimuli the AP50 reached steady state. Mean steady state AP width at 0.5 Hz was 208 ms, and at 2.5 Hz was 180 ms.

#### 2.4.2 CURVATURE-DEPENDENT VELOCITY

We quantified the effect of wavefront curvature,  $\kappa$ , on conduction velocity,  $CV$ , in OS-HEK monolayers by launching either circular outgoing waves ( $\kappa > 0$ ) or annular incoming waves ( $\kappa < 0$ ). High-speed (500 Hz) maps of the wavefronts revealed that  $CV$  depended sensitively on  $\kappa$  (Figure 2.5c). For a planar wavefront to be stable,  $CV$  must be a monotonically decreasing function of  $\kappa$ , consistent with our observations. We compared our observations to numerical simulations of the Aliev Panfilov model,<sup>4</sup> a simple two-variable description of an excitable medium. The simulations reproduced the qualitative features of the data, including an asymmetry between positive and negative curvatures. Due to the simplicity of the Aliev Panfilov model, precise agreement with experiment is not expected.

The liminal radius is the smallest stimulus radius that can initiate an outward propagating wave.<sup>169</sup> Applying a linear extrapolation of the positive-curvature data to  $CV = 0$  yielded a liminal radius of  $25 \mu\text{m}$ . Optically excited regions smaller than this radius are predicted to be unstable to spontaneous collapse, while larger regions are predicted to trigger an outward propagating wave. Consistent with this extrapolation, we experimentally observed that stimuli smaller than  $25 \mu\text{m}$  in radius failed to trigger outward waves, although large local variations in cell density on this size scale led to

considerable region-to-region variation. The liminal size is of clinical interest as it relates to the sensitivity of the myocardium to ectopic depolarization. Previous work has investigated this parameter in cardiac tissue by varying the diameter of the stimulating electrode<sup>169</sup> or optical fiber for optogenetic stimulation.<sup>283</sup>

### 2.4.3 OPTICALLY CONTROLLED BOUNDARY CONDITIONS

. We next explored the feasibility of using static illumination patterns to create inexcitable zones for the purpose of steering optically induced waves. Figure 2.1g shows that static illumination of a bar-shaped region created a barrier for propagating waves. We interpret this local loss of excitability as a consequence of depolarization-induced inactivation of  $\text{Na}_v1.5$  channels.

Since we sought to form patterns of high complexity, we next studied the spatial resolution with which we could optically modulate membrane potential. Static illumination of a bar-shaped region led to a steady-state depolarization which decayed to half its maximum at  $160\ \mu\text{m}$  beyond the edge of the illumination (Figure 2.5d). To verify that the observed broadening was due to electrical coupling (as opposed to optical scattering or imaging aberrations), we added a gap junction blocker, 2-aminoethoxydiphenyl borate (2-APB,  $5\ \mu\text{M}$ ). This drug prevented wave propagation and led to a step-like decrease in fluorescence at the edge of the static illuminated region (Figure 2.5d), confirming that the spread in fluorescence beyond the illuminated region was due to electrotonic coupling.

We compared our results to numerical simulations of the Aliev Panfilov model.<sup>4</sup> We determined the cell-cell coupling parameter in the model by fitting to the data on electrotonic spread of static depolarization (Figure 2.5d). This fit gave a dimensionless coupling length of  $\phi = 12.5$ , corresponding to  $\phi = 300\ \mu\text{m}$  in our experiments. This parameter set the spatial resolution with which patterns of static illumination could modulate the potential. One could imagine that the partially depolarized region adjacent to the static illumination could act as a pacemaker, shedding periodic waves into the unstimulated region. We found this not to be the case. No degree of static blue light stimulus

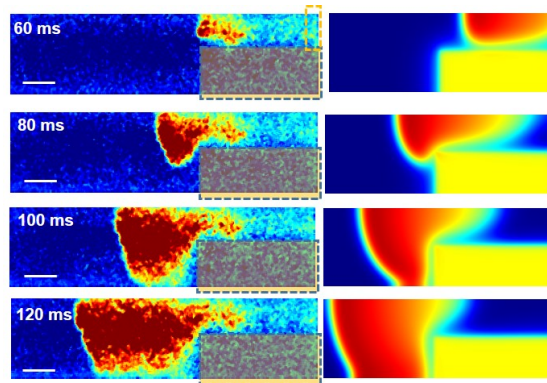


**Figure 2.7: Optically triggered wave propagation around an optically defined corner.** The region in the dashed box was subjected to static blue illumination, and a directional wave was launched from the top right, propagating to the left. The wave propagated rapidly around the optically defined corner. Left: experimental data. Right: Aliev Panfilov simulations. Scale bar 500  $\mu\text{m}$ .

induced periodic activity. We speculate that shift of  $\text{Na}_{\text{V}1.5}$  population to the slow inactivated state suppressed oscillations for any degree of static depolarization.<sup>291</sup>

We next used patterns of static illumination to guide wave propagation. We illuminated a bar of cells with static blue light, and then used a pulse of blue light to launch a wave propagating along this optical boundary. We observed a convex curved wavefront near the static interface (Figure 2.7). The wavefront was retarded immediately adjacent to the boundary, but then slightly advanced further out. As the wave propagated, the advanced region gradually spread outward from the boundary, until eventually the wave appeared to have a straight wavefront outside the boundary region.

We ascribe the nonmonotonic dependence of conduction velocity on distance from a depolarized boundary to the non-monotonic dependence of sodium channel activation on membrane voltage.<sup>101</sup> Large depolarizations (close to the optical boundary) inactivated sodium channels and hence slowed conduction. Modest depolarizations (further from the boundary) brought the sodium channels closer to the activation threshold and hence sped conduction. This qualitative picture is consistent with our prior observations that weak whole-field blue illumination accelerated wave propagation, while strong blue illumination suppressed wave propagation.

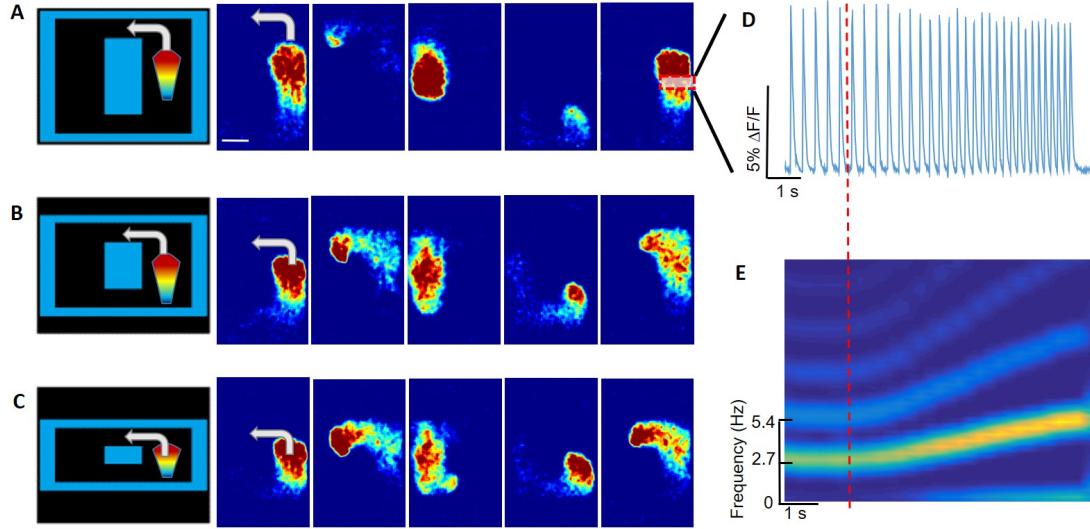


**Figure 2.8: Dynamic optical tuning of OS-HEK cell oscillators.** A-C) Circular wave motion in an optically defined rectangular track, defined by the pattern of blue illumination shown on the left. The boundaries were applied as a quasi-static illumination pattern, and then a directional wave was launched to initiate counterclockwise circulation. The top and bottom optical boundaries were then continuously shrunk during the recording. The apparent decrease in signal amplitude at the top and bottom of the largest pattern arose because the wave passed the edge of the fluorescence excitation spot. Scale bars 1 mm. Movies acquired at 100 Hz, successive panels separated by 8 – 10 frames. D) QuasAr2 fluorescence from the indicated region. As the vertical dimension of the track shrank, the oscillations sped up. E) Spectrogram of the data in (D) showing the increase in frequency with time.

We observed close correspondence to numerical simulations of the Aliev-Panfilov model using the coupling length determined by fit to the static depolarization profile. We reproduced propagation patterns both along a depolarized boundary (Figure 2.5e) and around a corner (Figure 2.7). We found that due to spread of inactivation near optical boundaries, optically defined channels had to be at least  $300 \mu\text{m}$  wide to support wave conduction.

## 2.5 OPTICALLY DEFINED RING OSCILLATOR

Finally, we sought to define a cellular circuit entirely optically. In contrast to physically patterned circuits, patterned illumination can be used to dynamically reconfigure circuit boundaries, enabling

new types of circuit function.

Starting with a homogeneous confluent culture of OS-HEK cells, we illuminated with static blue light to define the boundaries of a rectangular track (Figure 2.8a). We then optically launched a counterclockwise wave within the track. The wave circulated stably within the optically defined boundaries at constant frequency. We then dynamically changed the dimensions of the track, and observed a corresponding change in the oscillation frequency. Upon removing the optical boundaries, the wave expanded outward and dissipated at the edges of the dish. The spectrogram of the intensity trace demonstrates the expected increase of oscillator velocity as the circumference shrank (Figure 2.8c). These results demonstrate that one can use optical patterning to define dynamically reconfigurable boundary conditions in cultures of OS-HEK cells.

## 2.6 CONCLUSIONS

OS-HEK cells and the associated optical instrumentation provide a versatile platform for exploring emergent bioelectric phenomena in excitable tissues. The two heterologously expressed ion channels,  $\text{Na}_v1.5$  and  $\text{Kir} 2.1$ , combined with the endogenous gap junction protein, constitute a minimal system for sustaining collective electrical waves in vitro. The ability to define boundary conditions optically and to vary these conditions in real time opens the possibility to explore the effects of geometry on wave propagation phenomena with much greater precision and versatility than would be possible if physical cell patterning were required. For instance, measurements of conduction velocity vs. wavefront curvature (Fig. 2.5c) revealed a nonlinear dependence, indicating deviations from the linear eikonal approximation.<sup>147</sup> A similarly shaped dependence of velocity on wavefront curvature was previously observed in calcium waves within single isolated rat cardiomyocytes.<sup>275</sup> To our knowledge, our results constitute the most precise measurement of the influence of wavefront geometry on electrical conduction in a biological tissue. More than 100 years ago Mines considered

rings of cardiac tissue as a model for reentrant arrhythmias, and observed stabilization of reentrant waves at high stimulus rates.<sup>189</sup> More recent work has considered annular geometries in cardiac electrical conduction<sup>95,103</sup>, in cardiac calcium dynamics<sup>198</sup>, and in chemical reaction-diffusion systems.<sup>207</sup> In contrast to previous work in fixed geometries, our optical approach opens the door to exploring how reconfiguration of boundary conditions affects dynamics in a bioelectric medium. In principle, one could close the loop between optical readout of voltage and optical stimulation to provide spatiotemporal feedback in OS-HEK cells, an idea first discussed by Sakurai et al.<sup>236</sup>

Spiking HEK cells have previously been proposed as a model of cardiac tissue.<sup>151</sup> The quantitative data obtained here test the limits of this model and reveal instructive differences from real cardiac tissue. The relations of conduction velocity and AP<sub>50</sub> to beat rate determine the stability of wave propagation in the tissue.<sup>228,155</sup> If the slope of the restitution curve (AP<sub>50</sub> vs diastolic interval) exceeds 1, then under periodic pacing electrical alternans (alternating short and long beats) develops,<sup>206</sup> a phenomenon first characterized by Mines.<sup>188</sup> Guevara and coworkers showed that this transition can occur via a period-doubling bifurcation, and can eventually lead to chaotic dynamics.<sup>102,110</sup> Transitions to chaos may be involved in ventricular fibrillation and sudden cardiac death.<sup>269</sup>

In OS-HEK cells the conduction velocity and AP<sub>50</sub> were largely independent of stimulus frequency (and hence diastolic interval), up to a sharp cutoff frequency (Figs. 2.5a, 2.6). Neither alternans nor chaos were observed in the periodically paced OS-HEK cells, the physically patterned rings of OS-HEK cells, nor in the optically defined ring oscillator. To interpret this qualitative difference from cardiac tissue, we turn to the classic Noble model<sup>205</sup>, in which cardiac dynamics are described by three currents: voltage-gated sodium, inward rectifier potassium, and slow delayed rectifier potassium. OS-HEK cells lack the slow delayed rectifier potassium channel of the Noble model, and thus recover after each action potential within a time set by sodium channel re-priming, approximately 4 ms.<sup>265</sup> Thus each beat in OS-HEK cells is largely independent of preceding activity. The lack of

the slow delayed rectifier current in OS-HEK cells most likely explains the difference in dispersion relation between OS-HEK cells and cardiac tissue.

One could augment the OS-HEK cells in several ways to make them more “cardiac-like”. Expression of a slow KV channel, such as hERG, would provide a gradually recovering excitability after each action potential. A slow hyperpolarization-activated cation channel, such as an HCN channel, would lead to a gradual depolarizing “funny current” after each action potential, also gradually increasing excitability.<sup>51</sup> Finally, one could add a drug, such as amitriptyline, which slows the recovery of  $\text{Na}_v1.5$  from inactivation and may thus lead to slowly recovering excitability.<sup>264</sup> The OS-HEK system provides a platform for testing the sufficiency of these additional components to induce alternans and chaotic dynamics under rapid pacing. It will also be interesting to explore whether these modifications render the cells capable of driving oscillatory behavior under steady state optogenetic stimulation.

One could also augment the OS-HEK cells to implement more complex cellular logic. For instance, expression of A-type voltage-gated potassium channels should shorten the AP duration to resemble more closely a neuronal action potential. The correspondingly shorter AP wavelength would lead to a higher bit-rate in propagating wave trains. Expression of voltage-gated  $\text{Ca}^{2+}$  channels may introduce additional slow dynamics and memory effects, and provide a means to couple electrical dynamics to intracellular signaling cascades and ultimately to changes in gene expression.

Expression of ligand-gated ion channels could provide a sensitive chemical interface, whose activation would manifest as changes in wave dynamics. Activation of G-protein coupled receptors (GPCRs) can also couple to ion channel modulation<sup>67</sup> and thereby affect the function of OS-HEK cells. The ring oscillator geometry enables integration over thousands of oscillation cycles, facilitating detection of extremely subtle changes in oscillation frequency. Finally patterned cell growth of multiple engineered cell types in two and three dimensions<sup>256</sup> may enable formation of highly complex bioelectrically active synthetic tissues, with cells having differing electrophysiological properties

localized in different regions. An interesting avenue for future research will be to engineer cell lines to perform more complex bioelectrical computations.

## 2.7 METHODOLOGY

### 2.7.1 GENERATION OF OS-HEK CELL LINES

The pIRESpuro3-Nav1.5 plasmid was obtained from ChemCORE at Johns Hopkins University. The Nav1.5 expression was driven by a CMV promoter. The Optopatch construct contained coding sequences of CheRiff-eGFP and QuasAr2-mOrange, separated by a self-cleaving P2A peptide sequence. The Optopatch construct was cloned into a modified FCK lentivirus vector (mFCK), in which the original CaMKII promoter was replaced by a CMV promoter. The Kir2.1 cDNA was amplified from Addgene plasmid 32669 (pENTR-L5-Kir2.1-mCherry-L2) and cloned into pLX304 lentivirus vector that contained a blasticidin selection marker. The Kir2.1 expression was driven by a CMV promoter.

HEK293 cells were maintained in Dulbecco's Modified Eagle Medium (DMEM) with 10% fetal bovine serum, penicillin (100 U/mL), streptomycin (100 µg/mL) and were transfected with pIRESpuro3-Nav1.5 using TransIT-293 Transfection Reagent (Mirus Bio) following manufacturer instructions. 48 hrs after transfection, puromycin was added to a final concentration of 2 µg/mL. Cells were selected for 14 days to stabilize the expression of Nav1.5. Surviving cells were subsequently transduced by mFCK-Optopatch lentivirus. 10 days after infection, GFP positive cells were enriched by FACS sorting and were then transduced by pLX304-Kir2.1 lentivirus. 48 hrs after transduction, Kir2.1 expressing cells were selected by 5 µg/mL blasticidin. At the same time, 2 µg/mL puromycin was also included to ensure stable expression of Nav1.5. Cells were cultured for 14 days and then single cells were dispersed in wells of a 48 well plate. Monoclonal lines were screened using Optopatch to detect cells that showed robust optically induced and optically recorded action potentials. In

the selected Nav1.5/Optopatch/Kir2.1 monoclonal cell line (OS-HEK cells), action potentials were robustly triggered by blue laser stimulation and recorded by QuasAr2 fluorescence, with a SNR greater than 30.

### 2.7.2 CELL CULTURE

The selected OS-HEK cell line was grown in 10 cm tissue culture dishes in 10 mL DMEM-10 supplemented with 2  $\mu\text{g}/\text{mL}$  puromycin and 5  $\mu\text{g}/\text{mL}$  blasticidin until reaching approximately 80% confluence. Cells were then trypsinized and transferred to cryovials with 500,000 cells/vial in 10% dimethyl sulfoxide (DMSO) / 90% DMEM-10 medium, and frozen overnight at -80 C using an isopropyl alcohol freezing container (Thermo Scientific).

For functional experiments, OS-HEK cells were thawed and centrifuged at 300 g for 5 minutes to pellet cells and aspirate DMSO-containing medium. Cells were then resuspended and plated in 10 cm plastic tissue culture dishes in 10 mL DMEM-10 supplemented with 2  $\mu\text{g}/\text{mL}$  puromycin and 5  $\mu\text{g}/\text{mL}$  blasticidin. Following standard HEK cell culture convention, OS-HEK lines were maintained between 30% and 70% confluence, and were passaged (by trypsinizing, centrifuging, aspirating old media and resuspending in fresh media) at a 1:3 ratio once reaching 70% confluence. After thawing, a given line typically maintained functional performance (i.e. spiking under blue light stimulation) for approximately 7 passages, or 2 weeks. At longer times in culture, expression of Kir2.1 appeared to diminish, rendering the cells inexcitable.

For imaging and electrophysiology experiments, cells were passaged from 10 cm plastic dishes and replated on 35 mm coverslip-bottom dishes which had been pre-coated with 1:30 matrigel:Minimal Essential Media (MEM) in a central 10 mm well to allow for cell adhesion. For confluent layers, cells were plated at high density by delivering 500,000 cells in a 500  $\mu\text{L}$  DMEM-10 droplet in the central well, then left to settle for 1 hour before adding an additional 1.5 mL DMEM-10 to the dish. Cells were then transferred to the incubator for at least 3 hours before measurement. Electrophysiology

and single-cell imaging

Measurements were performed in Tyrode's solution, containing (in mM): 125 NaCl, 2 KCl, 2 CaCl<sub>2</sub>, 1 MgCl<sub>2</sub>, 10 HEPES, 30 glucose. The pH was adjusted to 7.3 with NaOH and the osmolality was adjusted to 305-310 mOsm with sucrose. Prior to measurements, 35 mm dishes were washed twice with 1 mL phosphate-buffered saline (PBS) to remove residual culture media, then filled with 2 mL Tyrode's solution. Filamented glass micropipettes (WPI) were pulled to a resistance of 5 – 10 MΩ and filled with internal solution containing (in mM): 140 KCl, 1 MgCl<sub>2</sub>, 10 EGTA, 10 HEPES, 3 Mg-ATP, pH adjusted to 7.3 with KOH.

Simultaneous patch clamp and QuasAr2 imaging experiments were performed on a home-built inverted microscope using a low-noise patch clamp amplifier (A-M Systems, Model 2400). Voltage traces were collected under  $i = 0$  current clamp mode. Blue light for optical stimulation (Coherent Obis) was modulated using an acousto-optic tunable filter (Gooch and Housego GH18A series). Red light for monitoring QuasAr2 fluorescence (Dragon Lasers M series, 635 nm) was modulated independently using a shutter. Fluorescence in the near-infrared was filtered using a dichroic mirror (quadband 405/488/532/635) and an emission filter (668 – 743 nm) and recorded using a scientific complementary metal-oxide semiconductor (CMOS) camera (Hamamatsu Orca Flash 4.2). Experiments were performed at ambient room temperature (25 °C).

### 2.7.3 ULTRAWIDE-FIELD IMAGING AND MICROSCOPY

Ultrawide-field imaging experiments were performed on a home-built inverted microscope modified from a design described previously (Figure 2.2).<sup>120</sup> In brief, this system provided a field of view of 5 mm × 5 mm, spatial resolution of 3 μm, and maximum frame rate of 1 kHz. Blue light for CheRiff excitation was produced by a 488 nm laser with 3 watt maximum power (Coherent Genesis MX) set to 1 watt output. Excitation intensity was modulated using an acousto-optic modulator (NEOS Technologies, AOB Model N45030-5-6.5) and spatially patterned using a digital micromirror de-

vice (DMD) (DLi4130, Digital Light innovations). Physical DMD pixels of linear dimension  $6.5 \mu\text{m}$  were demagnified 2x onto the sample plane for  $3.25 \mu\text{m}$  resolution. Red light for exciting QuasAr2 fluorescence was provided by six 500 mW lasers (Dragon Lasers M series, 635 nm). The lasers were first combined pairwise via half-wave plates and polarizing beamsplitters. The three resulting beams were then directed onto the sample via a custom fused silica prism interposed between the sample and the objective. The prism directed the beams to the sample at an angle close to total internal reflection at the glass-water interface, achieving an illumination intensity of  $13 \text{ W/cm}^2$  at the sample. The red illumination covered a field of view of  $5 \times 1 \text{ mm}$ . The size of the field of view was limited by available laser power and by concern over laser-induced heating of the sample for larger illuminated regions. Near-IR fluorescence emission was filtered using emission filters (Chroma ET665lp and Semrock quadband 336/510/581/703) and re-imaged onto a sCMOS camera (Hamamatsu Orca Flash 4.2).

To achieve accurate stimulation of user-selected regions on the sample, it was necessary to map DMD pixels onto camera pixels. First, a triangular test pattern was projected onto a spatially uniform fluorescence test target, and imaged on the camera. Then, an affine transformation matrix was produced to map DMD pixels to camera pixels. Desired blue stimulation patterns were then manually defined on images of the sample, and transformed back into DMD pixels using the registration matrix. Stacks of illumination pattern images were then pre-loaded into the DMD volatile memory. Custom LabView software provided trigger signals to synchronize modulation of the red and blue lasers, activation of patterns on the DMD, and camera triggers.

#### 2.7.4 CELL PATTERNING

To create physically defined ring oscillators (Figure 2.3), we adapted a published microcontact printing protocol<sup>227</sup> to define fibronectin patterns covalently bound to cytophobic polyacrylamide gels. In brief, patterns were designed in AutoCAD and printed on a mylar transparency (CAD Art Ser-

vices). The pattern was transferred to a layer of SU-8 3025 on a Si wafer via contact photolithography, followed by removal of un-exposed photoresist with SU-8 developer. The SU-8 master was then used as a template for casting a poly(dimethylsiloxane) (PDMS) stamp.

Coverslip-bottomed 35 mm dishes with 20 mm central wells (MatTek P35G-1.5-20-C.s) were coated with a layer of polyacrylamide gel functionalized with succinimide esters for covalent immobilization of patterned fibronectin. Glass coverslips were chemically activated by plasma cleaning and then incubated for 30 minutes in a nitrogen-purged glovebox with silane solution (v/v: 0.5% 3-methacryloxypropyltrimethoxysilane, 2% acetic acid, 97.5% anhydrous EtOH). Still in a nitrogen atmosphere, polyacrylamide gels (40:1 acrylamide:bisacrylamide) were polymerized on the activated glass (final W/V concentrations in pH 7 phosphate buffer: 8% acrylamide, 0.2% bisacrylamide, 0.1% tetramethylethylenediamine, 0.12% potassium persulfate; 1 mL/dish). The solution was doped with 4.2 mg/mL N-acryloxysuccinimide (acryl-NHS) to allow for covalent binding of fibronectin. Gels were polymerized under siliconized coverslips (Hampton Research, HR3-239) to ensure smooth top surfaces.

PDMS stamps were exposed to a solution of fibronectin (Yo Proteins 663, 0.05 mg/mL) for 30 min following by aspiration and drying in air for 10 min. Stamp patterns were then printed onto the NHS-functionalized acrylamide dishes. The NHS covalently bonded to the fibronectin, forming a stable cell-adherent pattern. Cells were deposited by gently pipetting a 500  $\mu$ L DMEM-10 droplet with 500,000 cells into the dish central well, leaving to settle at room temperature under a laminar flow hood for > 30 min. Unadhered cells were removed by gently aspirating the 500  $\mu$ L droplet, then gently adding 2 mL DMEM-10. This protocol yielded confluent patterns with high fidelity to the original template (Figure 2a).

### 2.7.5 ALIEV-PANFILOV SIMULATIONS

We simulated wave propagation in the OS-HEK cell cultures via the Aliev-Panfilov model.<sup>4</sup> The Aliev-Panfilov model treats the cell as a two-parameter nonlinear oscillator:

$$\frac{du}{dt} = ku(1 - u)(u - a) - uv + c + \phi \nabla^2 u \quad (2.1)$$

$$\frac{dv}{dt} = \varepsilon(u)(jv - v) \quad (2.2)$$

Where  $u$  is the external (i.e. excitation) parameter, and  $v$  is in the internal (i.e. recovery) parameter. Numerical integration was performed in MATLAB using the ode45 differential equation solver. To match simulations to single cell spike data, we chose excitation threshold, transmembrane current magnitude, and recovery factor. The parameter  $c$  corresponds to the optical drive, and is a function of space and of time (set to 1 when pixels are illuminated and to 0 when they are not). The parameter corresponds to the electrical coupling length of the syncytium, and was calibrated by matching the decay length for static depolarization. Nearest-neighbor electrical coupling was implemented using the MATLAB imfilter function with a discrete Laplacian filter and replicating boundary conditions. Display images correspond to simulations of on  $128 \times 32$  or  $128 \times 45$  grids of Aliev-Panfilov cells run over 4000 to 85000 time steps depending the complexity of the simulated optical stimulus.

Simulations of curvature dependent conduction velocity (Fig. 2.5c) were performed on a  $128 \times 128$  grid. Wavefronts were determined by the positions where the intensity crossed a threshold set to three quarters of the maximum intensity. Trajectories were measured from a 1-dimension slice taken across the grid midline, and the spatially discrete results were fit using the MATLAB fit function ('smoothingspline' fit type, with smoothing parameter = 0.8). Plots of wavefront radius as a

function of time were transformed into plots of conduction velocity as a function of curvature.

#### 2.7.6 IMAGE PROCESSING AND DATA ANALYSIS

All images were processed and analyzed using homemade MATLAB scripts. For single cell experiments (Figure 1), intensity traces were extracted by constructing a weight image based on the covariance of individual pixels with the recorded patch voltage, then using that image to weight contribution of individual pixels to the overall average intensity trace. This algorithm is described in detail in Referece<sup>159</sup>. For ultrawide-field experiments (Figures 2.3-2.8), movies were background-subtracted using an image of the red illumination beam profile, and smoothed using a median filter (using a  $3 \times 3$  pixel window) to preserve wavefront edges. Resulting movies were corrected for photobleaching at each pixel using a sliding minimum filter with a width of 150 samples. This procedure preserved spikes and spike shapes, but removed downward baseline drift. Wavefronts were defined by thresholding movies to identify the wavefront and then manually recording the wavefront coordinates. Some movies acquired over a large field of view were down-sampled using  $4 \times 4$  pixel binning to maintain reasonable file size. For dispersion analysis (Figure 2.5a), movies were binned at  $4 \times 4$  pixels, and then averaged over the vertical direction (i.e. parallel to the wavefront). The resulting kymographs were corrected for photobleaching as described above at each spatial position. The amplitude of the spikes at each coordinate was mapped to the range  $[0, 1]$ , thereby removing variable offsets and amplitudes due to heterogeneities in the culture. Rising and falling edges of each spike were detected using a half-maximum threshold followed by linear interpolation to achieve sub-frame time resolution.

Conduction velocities were calculated by measuring arrival time at two spatial locations 2 mm apart. Action potential full-width half max (AP<sub>50</sub>) was calculated by temporally aligning APs at each spatial location, averaging, and then fitting rising and falling times using linear interpolation. For analysis of curvature dependent velocity (Figure 3b), movies were mean subtracted and then

smoothed using a  $3 \times 3$  median filter, and then manually traced in ImageJ to determine wavefront diameter along the horizontal axis. Velocities were calculated by spline interpolation of the position of the wavefront as a function of time, and then taking the spline derivative at sample time points. Associated curvatures were taken as the inverse of the wavefront radius measured at that frame. Curvature-dependent velocity data were divided into piecewise linear regimes and then fit with straight lines using least-squares regression to determine the parameter  $\alpha$ .

For analysis of propagation in the ring oscillator (Figure 2.3), raw data were binned, corrected for the red laser illumination profile, and median filtered as described above. Intensity traces were computed from mean intensity within manually defined regions of interest. Fluorescence traces were corrected for photobleaching using a sliding minimum filter as described above. Spike rise times were detected with sub-frame precision using linear interpolation of samples before and after a half-maximum threshold (Figure 2.3d). Oscillator direction was determined by computing differences in rise times at adjacent regions of interest (Figure 2.3e). For the optically defined oscillator track (Figure 2.8), intensity traces were calculated from a horizontal region in which the boundary did not move during the experiment (Figure 2.8c). Power spectra (Figure 4d) were computed by taking short-time Fourier transforms (STFT) of these intensity traces.

## 2.8 PUBLICATION INFORMATION

A version of this chapter appeared previously as: McNamara, H.M., Zhang, H., Werley, C.A. and Cohen, A.E., 2016. Optically controlled oscillators in an engineered bioelectric tissue. *Physical Review X*, 6(3), p.031001.<sup>186</sup>

## 2.9 CONTRIBUTIONS

I designed, conducted, and analyzed experiments described in this chapter. Hongkang Zhang created the OS-HEK cell line. Kit Werley created the wide-field imaging system. Adam Cohen oversaw the research. Adam and I wrote the manuscript published based on this work.<sup>186</sup>

We also thank Miao-Ping Chien for help with cell patterning, and Katherine Williams and Melinda Lee for technical support. This work was supported by ONR grant N000141110-549, NIH grants 1-R01-EB012498-01 and New Innovator grant 1-DP2-OD007428, and the Howard Hughes Medical Institute.

# 3

## Geometry determines stability and chaos in bioelectric pacemakers

LITTLE IS KNOWN about how individual cells sense the macroscopic geometry of their tissue environment. Here we explore whether long-range electrical signaling can convey information on tissue geometry to individual cells. First, we studied an engineered electrically excitable cell line. Cells

grown in patterned islands of different shapes showed remarkably diverse firing patterns under otherwise identical conditions, including regular spiking, period-doubling alternans, and arrhythmic firing. A Hodgkin-Huxley numerical model quantitatively reproduced these effects, showing how the macroscopic geometry affected the single-cell electrophysiology via the influence of gap junction-mediated electrical coupling. Qualitatively similar geometry dependent dynamics were observed in human induced pluripotent stem cell (iPSC)-derived cardiomyocytes. The cardiac results urge caution in translating observations of arrhythmia *in vitro* to predictions *in vivo* where the tissue geometry is very different. We study how to extrapolate electrophysiological measurements between tissues with different geometries and different gap junction couplings.

### 3.1 MOTIVATION

Cells in multicellular organisms sense their location within tissues via diffusible molecules, contact interactions, and mechanical signals. Gap junction-mediated electrical signals can also, in principle, provide long-range positional cues<sup>248</sup>, though mechanistic details have been difficult to determine due to the simultaneous presence of, and interactions between, all of the above signaling modalities in physiological tissue. Furthermore, until recently, technical limitations prevented tissue-scale mapping of membrane voltage: point-wise measurements with patch pipettes were slow and laborious, and voltage-sensitive dyes lacked sensitivity and often mediated phototoxicity.

The electrophysiological properties of many types of isolated cells have been probed in great detail via patch clamp electrophysiology.<sup>118</sup> In tissues, cells form electrical connections with their neighbors via gap junction channels. One can then ask whether this coupling is a minor perturbation on the individual cells, or whether it fundamentally changes the dynamics. In condensed matter physics, the properties of a bulk solid can differ dramatically from those of its constituent atoms. Similarly, the emergent electrical properties of bulk tissue might differ dramatically from those of

individual cells. For instance, rearrangements of gap junctions in cardiac tissue, which only affect the cell-to-cell coupling, have been implicated in the onset of arrhythmia.<sup>137</sup>

One manifestation of long-range electrical coupling is that the electrical dynamics of a cell interior to a tissue could be influenced by remote boundaries. It has been well established that boundaries can influence paracrine signaling pathways<sup>266</sup>, but it remains an open question to what extent tissue geometry and topology influence electrical signaling. In the heart, structural defects can act as nuclei for arrhythmias<sup>231</sup>, but interpreting these effects is difficult due to the multiple interacting factors that govern dynamics, including electrical coupling between myocytes<sup>36,89,169</sup>, mechano-electrical feedbacks<sup>22,204</sup>, and differences in cell-autonomous properties of the individual myocytes between regions of the heart<sup>6,127,202</sup>. Subtle shifts in any of these parameters can cause discontinuous changes in dynamics, e.g. from a stable beat to a possibly fatal arrhythmia.

It is important to understand how long range electrical signaling can convey positional cues generally, and how these signals govern dynamical stability in excitable tissues. For spatially compact systems (i.e. characterized by a single membrane voltage), dynamics can often be described by autoregressive models in which the response to stimulus  $n + 1$  is a function of the response to stimulus  $n$ . Simple criteria then determine whether the fixed point corresponding to periodic dynamics is stable or unstable. Autoregressive models of this sort have been applied with good success to cardiac<sup>206</sup> and neuronal<sup>52,141</sup> dynamics. Recent theoretical work showed that conduction could dramatically alter the stability conditions.<sup>48,64</sup> However, the wide diversity of cardiac models, combined with uncertainty in model parameters, presents a challenge for comparison to experiments.<sup>53,64</sup> Only a few experiments have explicitly probed the roles of intercellular coupling in cardiac dynamics.<sup>28,29,234</sup> In complex cells such as cardiomyocytes, one typically cannot vary one parameter without affecting many others. For instance, growing human induced pluripotent stem cell-derived cardiomyocytes (hiPSC-CM) on different size islands affects<sup>272</sup>, which in turn can affect electrophysiology.

Uncertainties regarding the role of geometry in cardiac stability have an important practical implication: it has been widely claimed that if human induced pluripotent stem cell (iPSC)-derived cardiomyocytes (hiPSC-CM) can be made to show mature patterns of ion channel expression,<sup>76,223,281</sup> then *in vitro* cultures will be a useful substrate for studying arrhythmias.<sup>23,55,122,239</sup> This belief underpins a large-scale effort, called the Comprehensive in-vitro Proarrhythmia Assay (CiPA), sponsored by the U.S. Food and Drug Administration (FDA) to use hiPSC-CM as a substrate for evaluating pro-arrhythmia risks in candidate therapeutics. However, this approach would need further consideration if one finds that there are fundamental geometry-driven differences in stability between cultured cells and intact tissue, even when all voltage-dependent conductances are identical. To explore the role of geometry under controlled conditions, we engineered a synthetic excitable tissue where all elements were well understood. This synthetic approach has the further merit of being amenable to rigorous quantitative modeling. We previously introduced Optopatch Spiking Human Embryonic Kidney (OS-HEK) cells<sup>186</sup> as an engineered excitable cell type with an all-optical electrophysiological interface. HEK293 cells present a clean electrophysiological background, in that their membranes pass little current between -80 and +30 mV<sup>263</sup>, while an endogenous Na<sup>+</sup>/K<sup>+</sup> ATPase maintains steady cardiac-like transmembrane concentration gradients for these two cations (Sultan et al., 2008).<sup>247</sup> The cells were engineered to express just two voltage-dependent channels, the voltage-gated cardiac sodium channel, NaV<sub>1.5</sub>, and the inward rectifier potassium channel, K<sub>ir2.1</sub>. Expression of a channelrhodopsin, CheRiff, permitted optogenetic stimulation. CheRiff has a 4.5 ms opening time and a 16 ms closing time, and a reversal potential around 0 mV.<sup>120</sup> Membrane voltage was recorded optically, via either a far-red voltage-sensitive protein (QuasAr2<sup>120</sup>) or dye (BeRSTr<sup>125</sup>). Endogenous gap junction proteins introduced nearest-neighbor electrical coupling.<sup>186</sup> The individual components of the OS-HEK cells have previously been characterized in detail by manual patch clamp recordings.<sup>289</sup> When optogenetically stimulated, these cells produced single action potentials. When grown into a confluent syncytium, the endogenous gap junctions mediated

bulk propagation of electrical waves.<sup>186</sup>

The OS-HEK cells previously demonstrated many interesting attributes of excitable tissues, including wave conduction, curvature-dependent wavefront velocity, and re-entrant spiral waves.<sup>186</sup> Despite the dynamical similarity to cardiomyocytes, these cells bore little resemblance from a molecular perspective, lacking, for instance, voltage-gated Ca<sup>2+</sup> channels, calcium-induced calcium release, delayed rectifier potassium channels, and mechano-electrical feedbacks. We did not previously observe dynamical bifurcations (‘arrhythmias’) in OS-HEK cells, suggesting that a necessary ingredient was missing from our minimal model system.

We hypothesized that our previous failure to observe arrhythmia in the OS-HEK system was due to the absence of slowly recovering conductances that could provide memory from spike to spike (a necessary condition for arrhythmia in the simple autoregressive models). Upon repolarization after a spike, OS-HEK cell ion channels recovered fully within 4 ms, so each beat was independent of its predecessors. In contrast, in cardiomyocytes, delayed rectifier potassium channels gradually restore excitability after repolarization. The calcium channel blocker isradipine also causes slow state-dependent block in the NaV<sub>1.7</sub> and NaV<sub>1.5</sub> sodium channels, with a with a recovery time for NaV<sub>1.7</sub> of 200 ms at -100 mV.<sup>289</sup> We reasoned that in the presence of isradipine, the NaV<sub>1.5</sub> channels in OS-HEK cells would show a similar slow recovery after a beat, mimicking via a different ionic mechanism the slow recovery of cardiomyocytes after repolarization. We hypothesized that this slow recovery would be sufficient to support arrhythmic dynamics.

Here we describe isradipine-OS-HEK (iOS-HEK, where the ‘I’ stands for isradipine) cells, a synthetic bioelectric system which shows dynamical transitions between regimes of regular pacing, complex but repeating patterns, and irregular (non-repeating) dynamics as the drive frequency is increased. We explored in detail how these stability regimes were influenced by the macroscopic tissue geometry. Remarkably, we found that the transitions to complex and irregular patterns depended sensitively on the culture geometry. At a single pacing frequency, we simultaneously observed reg-

ular rhythms, alternating patterns, irregular dynamics, or depolarization block in islands that were identical in all respects except for their geometry. A biophysically detailed Hodgkin Huxley-style model captured these geometric effects. The iOS-HEK cells further showed second-degree conduction block in regions of high wavefront curvature, demonstrating sensitivity to two-dimensional geometric features. Finally, we show that similar geometry-dependent transitions occur in cultured human iPSC-derived cardiomyocytes.

Together our findings show that macroscopic tissue geometry is a fundamental determinant of bioelectrical dynamics, and not just a perturbation on the cell-autonomous behavior. We discuss which parameters are sensitive or insensitive to tissue geometry, and propose scaling relations that can be used to extrapolate across tissue geometries and across intercellular coupling strengths.

### 3.2 iOS-HEK CELLS SHOW ALTERNANS AND ARRHYTHMIAS

In a confluent monolayer of OS-HEK cells, we observed regular spiking when the cells were optogenetically paced at 4 Hz (10 ms pulses, 100 mW/cm<sup>2</sup>). Addition of isradipine (10  $\mu$ M) converted the spiking to an alternating rhythm between large and small spikes (i.e., ‘alternans’, Figure 3.1c), consistent with a previous report.<sup>289</sup> We refer to the OS-HEK cells with 10  $\mu$ M isradipine as iOS-HEK cells.

Using microcontact printing,<sup>227</sup> we patterned cell-adhesive fibronectin features onto cytophobic polyacrylamide surfaces. Features comprised square islands of linear size 100  $\mu$ m, 200  $\mu$ m and 500  $\mu$ m, as well as serpentine tracks of width 100, 200, 500  $\mu$ m and edge length of 1 mm and 5 mm. Overall track lengths were as long as 7 cm. Cell growth followed the printed patterns (Fig. 3.1b). We used a digital micromirror device (DMD) to target blue light stimulation to specific regions of the sample. In a change from previous studies on OS-HEK cells, we used the far red dye BeRST1<sup>125</sup> to report membrane voltage (Fig.3.1a). This dye had superior brightness to the protein-based reporter,

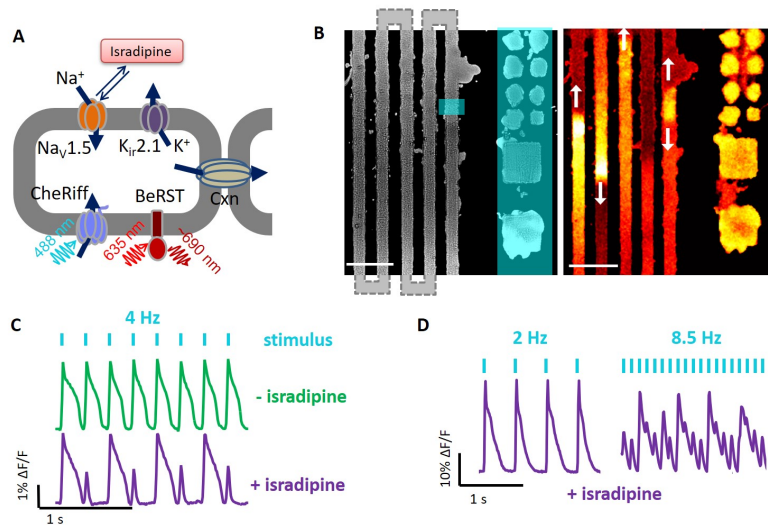


**Figure 3.1: Isradipine renders Optopatch-Spiking HEK cells susceptible to arrhythmia.** A) Molecular components of the synthetic excitable tissue. The voltage-gated sodium channel  $\text{Na}_v1.5$  and inward-rectifying potassium channel  $\text{K}_{ir}2.1$  are together sufficient to produce action potentials in response to a depolarizing stimulus. CheRiff is a blue-shifted channelrhodopsin which depolarizes the cells in response to blue light, and BeRST1 is a dye which reports voltage through changes in red fluorescence. Connexin channels (Cxn) introduce electrical coupling between neighboring cells. B) Left: microcontact printing defines patterns of cell growth. The vertical stripes connect in a serpentine pattern outside the field of view. Blue overlay shows regions of optogenetic stimulation. Zero-dimensional “islands” are tested alongside one-dimensional “tracks.” Right: single frame from a movie of BeRST1 fluorescence showing traveling waves in the track region. Scale bars 500  $\mu\text{m}$ . C) Fluorescence recordings of membrane voltage showing that isradipine (10  $\mu\text{M}$ ) induces alternans in OS-HEK cells paced at 4 Hz. D) At low pace frequency isradipine OS-HEK (iOS-HEK) cells beat periodically in synchrony with the pacing, but at high pace frequency the cells produce an irregular rhythm.

QuasAr2, had low toxicity and showed similar sensitivity to voltage. We recorded the voltage dynamics using a custom ultrawide-field ‘Firefly’ microscope.<sup>271</sup> Once on the microscope, cell cultures showed stable behavior for typically  $\sim 90$  min. All data presented here were acquired in  $< 60$  min.

Localized stimulation of the serpentine tracks induced propagating electrical waves. Optogenetically induced waves propagated with a typical conduction velocity of  $3.3$  cm/s, had an AP width at 50% repolarization of  $110$  ms, and thus had a depolarized action potential length,  $\lambda$ , of  $\lambda = 3.6$  mm. The fluorescence in the paced region of the track showed complex beat rate-dependent dynamics. At  $2$  Hz pacing, the cells spiked regularly and in phase with the drive (Fig. 3.1d, left). At  $8.5$  Hz pacing, the cells showed a complex and irregular fluorescence pattern, indicative of arrhythmia (Fig. 3.1d, right).

### 3.3 GEOMETRY DEPENDENT INSTABILITIES IN IOS-HEK CELLS

We characterized in detail the dependence of the electrical dynamics on local geometry. Cells were grown either in small square ‘islands’ or on adjacent linear ‘tracks’, and paced simultaneously in both geometries at frequencies between  $2$  and  $11$  Hz. The islands were paced with spatially homogeneous illumination, so cells across each island spiked synchronously and gap junction-mediated conduction did not contribute to the dynamics. We refer to these as zero-dimensional (0D) dynamics.

Tracks were stimulated in small regions ( $200$   $\mu\text{m}$  wide,  $100$   $\mu\text{m}$  long) to induce 1D propagating waves. We observed the response in both the directly stimulated region (near field) and in the conductively stimulated region (far field; Fig. 3.2a). Electrical waveforms stabilized to their far-field dynamics within a distance  $d \approx 0.05\lambda$  from the stimulus ( $d = 180$   $\mu\text{m}$  in our experiments), so we characterized the far-field dynamics at a distance  $750$   $\mu\text{m}$  from the stimulus. In the far-field, the waves propagated stably, reaching  $> 1$  cm from the stimulated zone. Island and track features were in-

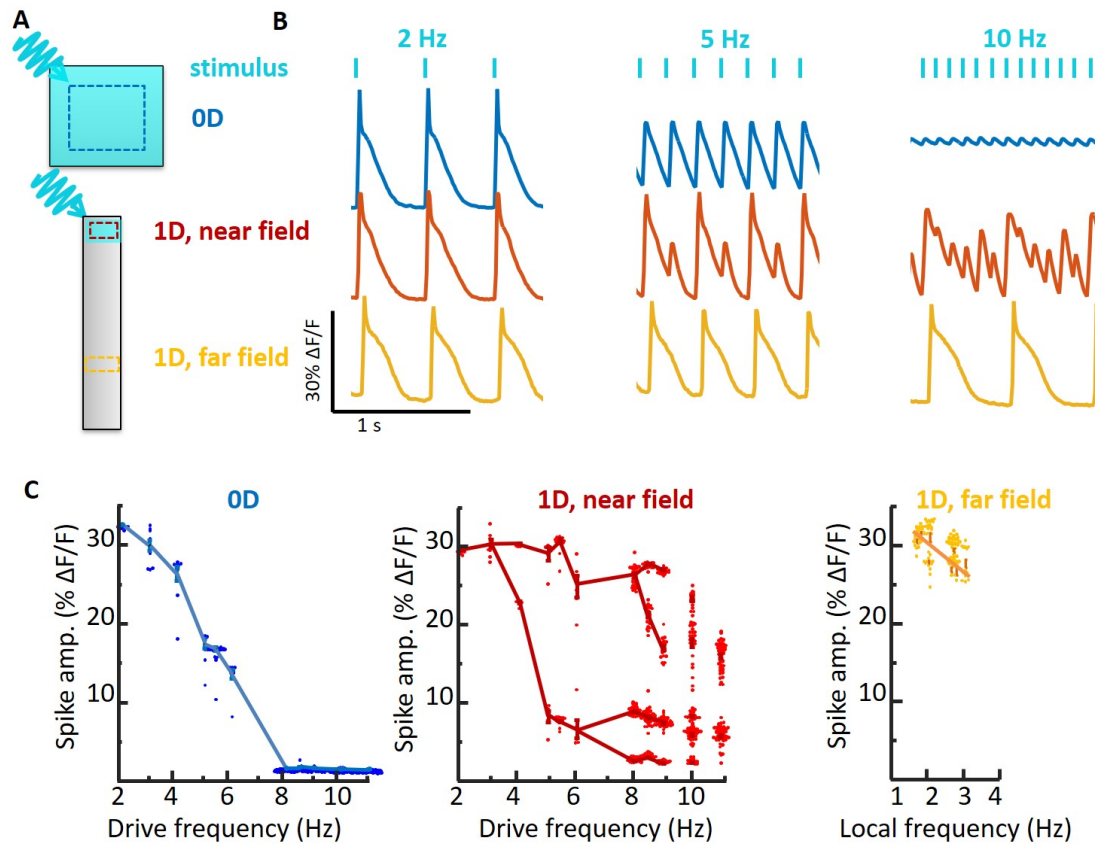


**Figure 3.2: Stability of spiking in iOS-HEKs cells depends on sample geometry and location of pacing.** A) Cell culture geometries, with locations of optogenetic stimulus shown in blue and regions of fluorescence voltage imaging shown with dotted lines. B) Simultaneously recorded electrical dynamics in OD, 1D near field, and 1D far field. At pacing frequencies of 5 and 10 Hz the cells showed different dynamics in the three regions. C) Geometry-dependent spike amplitude as a function of beat frequency. The plots for OD and 1D near field show spike amplitude as a function of pacing frequency. The plot for 1D far field shows spike amplitude as a function of local frequency, which can be a sub-harmonic of the pacing frequency. Fluorescence dynamics were recorded from regions of interest typically 100  $\mu\text{m}$  on a side, containing  $\sim 100$  cells. Due to the strong gap junction coupling between cells, the fluorescence waveforms of individual cells closely matched the local population average. For each stimulus frequency, the amplitudes of up to 100 spikes were displayed in a beeswarm plot. The lines are a guide to the eye connecting clusters of spikes with similar amplitudes. The data for all plots were recorded simultaneously from adjacent features in the same dish. Each plot represents a recording from a single feature. Similar dynamics were observed in  $n = 4$  OD features and  $n = 3$  1D features.

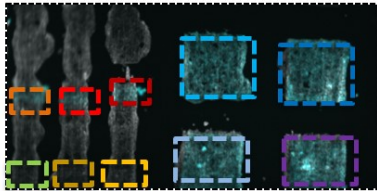
termixed within each dish, were seeded with the same stock of OS-HEK cells, and were measured simultaneously. Thus any differences in dynamics between regions could be ascribed to the island geometry.

At low pace frequencies ( $\leq 3$  Hz), all three regions spiked with a stable rhythm in synchrony with the pacing (Fig. 3.2b). To our surprise, at higher pace frequencies we observed dramatically different dynamics in the three regions (Fig. 3.3). The oD islands always produced regular electrical oscillations at the pace frequency. As the pace frequency increased, the amplitude of these oscillations diminished, up to 8 Hz, beyond which the responses were undetectable (Fig. 3.2c).

The iD near-field response developed a 1:1 alternans pattern at frequencies  $> 3$  Hz. Additional bifurcations arose at 6 Hz and 8 Hz. At 10 Hz the dynamics no longer showed any repeating pattern, suggesting a transition to irregular dynamics (Fig. 3.2).

Remarkably, the iD far-field showed no transitions to alternans or irregular dynamics (Fig. 3.2b). All spikes in the far-field had nearly equal amplitude and waveform. At pace frequencies between 3 and 6 Hz, only every other spike propagated to the far field, i.e. the local beat frequency was half the pace frequency. At higher pace frequencies, a smaller portion of spikes reached the far field. These spikes had irregular timing in the near-field but conducted at velocities which gradually evened out timing variations, such that the spiking appeared regular in the far-field, always at a frequency  $< 3$  Hz. The iD track acted as a filter which converted high-frequency arrhythmic spiking in the near-field into lower frequency rhythmic spiking in the far field. Together these experiments gave the unanticipated result that under regular pacing, iOS-HEK cells showed irregular dynamics only in the iD near-field, not in the oD or iD far-field regions.

A



B

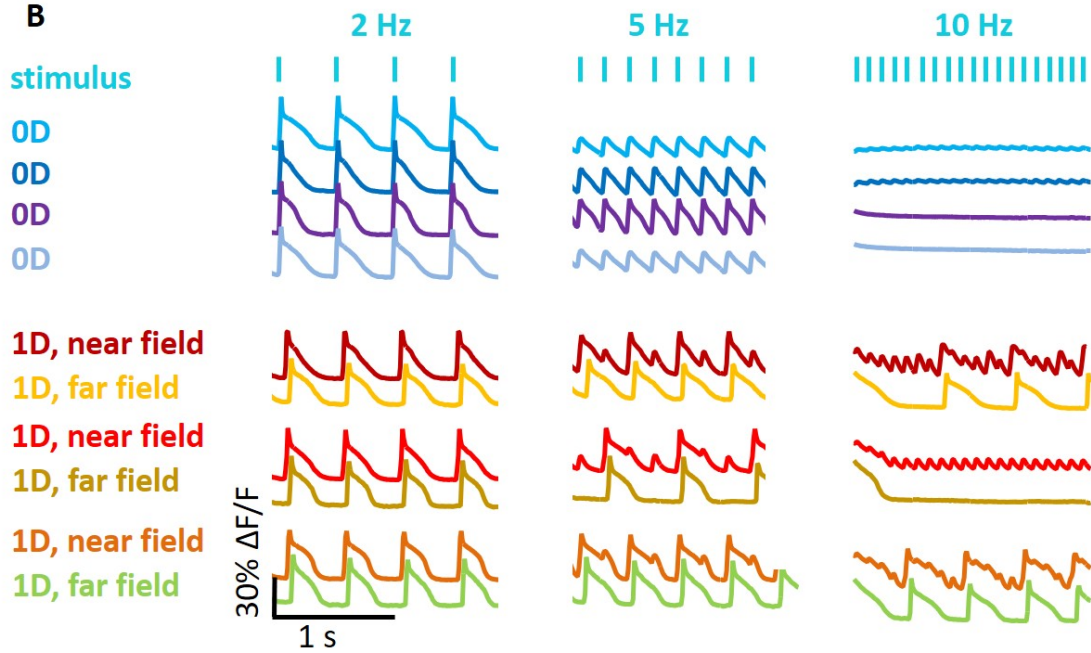


**Figure 3.3: Replicates of geometry-depending instabilities in iOS-HEKs.** A) In a single sample, 4 OD features and 3 1D figures (including both near and farfield measurements) were measured simultaneously across drive frequencies. B) In all OD samples, increasing drive rates showed a consistent attenuation of spike amplitude, transitioning into depolarization block. All 1D near-field samples showed arrhythmic transitions at higher beat frequencies, which were filtered into the far-field.

### 3.4 A HODGKIN-HUXLEY MODEL CAPTURES IOS-HEK DYNAMICS

We developed a conductance-based Hodgkin Huxley-type model to simulate the dynamics of iOS-HEK cells. The properties of  $\text{Na}_v1.5$ ,  $\text{K}_{ir2.1}$ , and channelrhodopsin  $\text{ChR2}$  are all well known, so we were able to constrain the model with a small number of free parameters (Fig. 3.4a). The sodium channel model comprised Hodgkin-Huxley activation and inactivation gates  $m$  and  $h$  with dynamics taken from the literature.<sup>252,253</sup> To capture the use-dependent block by isradipine, we introduced an additional slowly activating and slowly recovering gate,  $j$ . The  $\text{K}_{ir2.1}$  conductance was modeled as an instantaneous function of voltage, inferred from the shape of the action potential repolarization. The channelrhodopsin was modeled as a linear conductance with a 0 mV reversal potential, modulated in space and time by the blue light illumination. A diffusive term captured the nearest-neighbor gap junction coupling. The governing equation is:

$$C_m \frac{\partial V}{\partial t} = G_{cxn} \nabla^2 V - g_{Na} m^3 h (1-j) (V - E_{Na}) - g_{Kir}(V) (V - E_k) - g_{ChR}(x, t) (V - E_{ChR}) \quad (3.1)$$

where  $C_m$  is the membrane capacitance of a cell, and  $G_{cxn} = g_{cxn} \times l$  where  $g_{cxn}$  is the gap junction conductance between cells, and  $l$  is the linear dimension of a cell. The electrical diffusion coefficient is given by  $G_{cxn}/C_m$ . To simulate oD dynamics,  $g_{cxn}$  was set to zero. Eq. 3.1 represents a continuum model, which treats the domain as homogeneous tissue. In simulations, the cell discreteness is recovered by setting the spatial discretization equal to cell length.

The unknown parameters ( $C_m, g_{cxn}, g_{Kir}, g_{ChR}$ ) were determined by fitting to observed fluorescence waveforms, conduction velocities, and patch clamp measurements (described further under Methodology). The free parameters in the model enter in the dynamics of the isradipine variable,  $j$ ,

which was assumed to bind sodium channels in their open state with rate  $\alpha$ , and unbind with rate  $\mu$ :

$$\frac{dj}{dt} = \alpha m_{\infty}(1 - j) - \mu j \quad (3.2)$$

where  $m_{\infty}$  is the steady state value of the  $m$  gate. The kinetic parameters in Eq. 3.2 were chosen to fit the experimentally observed dynamical transitions.

Action potential waveforms were simulated in a oD geometry and in a linear 1D track comprising 2000 cells, with pacing delivered to 40 cells on one end. The near-field response was monitored in the paced zone, and the far-field response was monitored at a distance of 3 mm from the stimulus.

Simulated electrical waveforms (Fig. 3.4b) captured the main geometry and frequency-dependent features of the data. Specifically, the simulations in oD showed a smooth and monotonic decrease in spike amplitude with increasing pace frequency. At high pace frequencies, the baseline potential increased in both simulation and experiment, reflecting simultaneous  $\text{Na}_V$  channel inactivation and stimulus-driven depolarization relative to the  $\text{K}_{ir}$  reversal potential (i.e. depolarization block).

Simulations in the 1D near-field showed a series of frequency-dependent bifurcations that became increasingly irregular at high pace frequency. In the 1D far-field, these bifurcations were suppressed: spikes that propagated to the far-field had full amplitude, regular spacing, and were within the narrow band of frequencies that supported far-field propagation.

The simulated oD waveforms had greater amplitude than the experimental waves at high stimulus frequencies. This minor discrepancy traces to an overestimate of the strength of the channelrhodopsin drive. In all other circumstances, the strength of channelrhodopsin stimulation was not a critical parameter because the channelrhodopsin only served to raise the membrane voltage above threshold. But in the oD, high frequency case, the other ion channels were largely inactive, so the amplitude of the residual voltage fluctuations depended on the strength of the channelrhodopsin drive. Overall, these simulations confirmed that cells with identical conductances, paced at the same

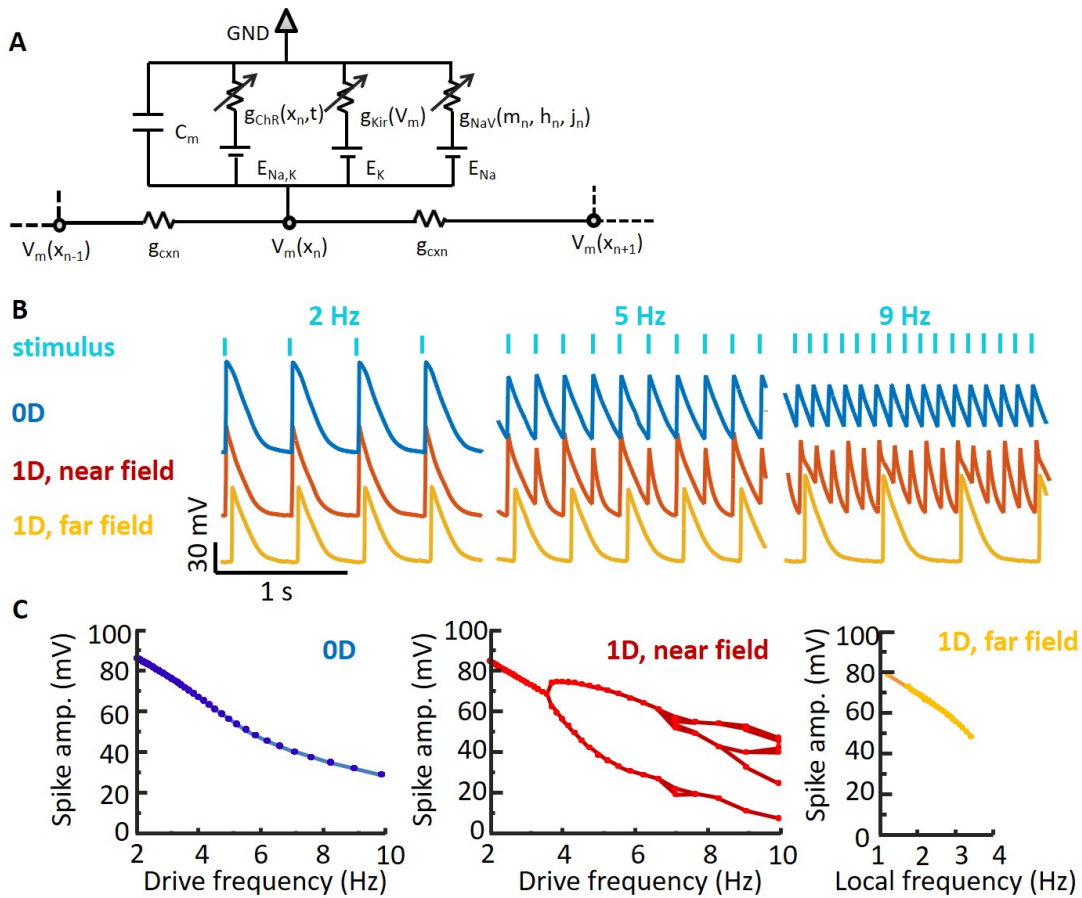


**Figure 3.4: A Hodgkin-Huxley model recapitulates the effect of geometry on spike dynamics.** A) Model schematic. Each cell has a channelrhodopsin (ChR), an inward-rectifier potassium channel ( $K_{ir}$  2.1) and a voltage-gated sodium channel ( $Na_V$  1.5). The  $Na_V$  is further gated by a state-dependent isradipine block. Neighboring cells are coupled via gap junctions. B) Simulated action potential waveforms in different geometries and pace frequencies (analogous to data in Fig. 3.2b). C) Simulated spike amplitude as a function of frequency for three geometries (analogous to data in Fig. 3.2c).

frequency, can show widely divergent behavior depending upon the geometry of the surrounding excitable tissue.

### 3.5 MAPPING THE TRANSITION BETWEEN THE NEAR FIELD AND FAR FIELD RESPONSE

We next investigated the transition from near-field to far-field behavior. How does alternans, or even irregular spiking, in the near-field lead to regular spiking in the far-field? We mapped the fluorescence dynamics of iD tracks as a function of distance from the stimulated zone, across a range of stimulus frequencies (Fig. 3.5a,b). There was a clear bifurcation in the ability of spikes to propagate into the far-field. Near-field spikes with amplitude lower than a critical threshold decayed as a function of distance, while spikes above this threshold grew to become propagating far-field spikes. Once in the far-field, spikes propagated stably for several cm, until reaching a break in the track. Spatially resolved simulations yielded similar results (Fig. 3.5d). The simulations showed that the conduction velocity of each far-field spike decreased as it approached the preceding spike such that irregularities spike spacing gradually evened out. The small dip in the amplitude of propagating spikes near the stimulated zone (Fig. 3.5c,d) was traced to a buildup of bound isradipine in cells subjected to rapid optogenetic stimulation.

At pace frequencies just above the transition to near-field alternans (experimentally observed between 3 and 4 Hz), one might expect period-doubling deviations from a regular spike train to arise slowly. We defined an alternans decay length,  $d$ , as the distance over which a near-field alternans beat decayed to 50% of its initial height (Fig. 3.5e). Simulations near the alternans transition indeed revealed a divergence in  $d$  near the critical frequency. At pace frequencies far above the critical frequency, the alternans decay length became a small fraction of the far-field action potential length,  $d \approx 0.04\lambda$  (Fig. 3.5f), consistent with experimental results (Fig. 3.5c).

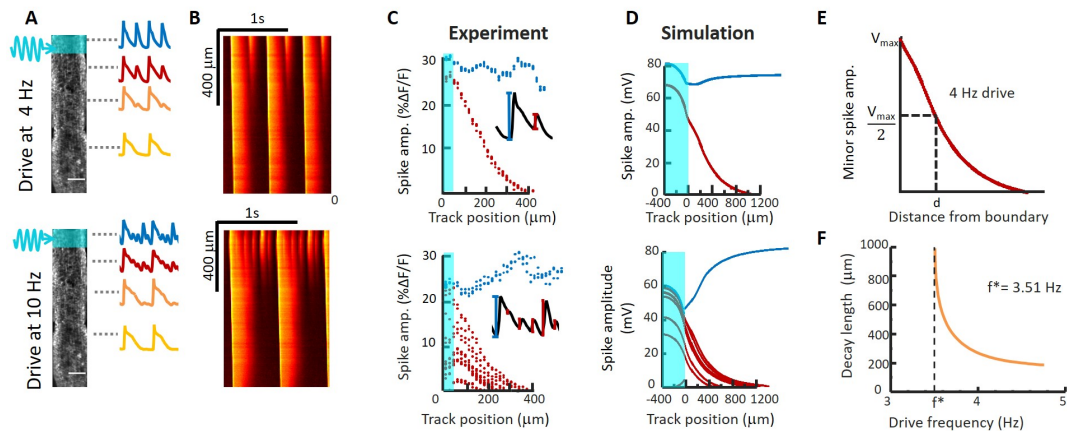


**Figure 3.5: Mapping the transition from near field to far field dynamics.** A) 1D tracks were stimulated at one end and action potential waveforms were recorded as a function of distance from the pacing stimulus. B) Kymographs showing electrical dynamics as a function of distance from the pacing stimulus. Some spikes decay in amplitude, while others grow in amplitude. C) Quantification of spike amplitude as a function of distance from the stimulus (shown in cyan). Spikes that reach the far field are shown in blue and spikes that decay are shown in red. D) Numerical simulations under conditions matched to the experiments. E) Definition of the spike decay length, corresponding to 50% loss of amplitude. F) Simulated decay length for near-field spikes as a function of pacing frequency. Below a critical frequency,  $f^*$ , all spikes reach the far field.

### 3.6 SECOND-DEGREE CONDUCTION BLOCK IN iOS-HEK CELLS

Conduction block and consequent arrhythmias can arise when a region of the heart acts as a partial barrier to conduction.<sup>242</sup> This effect can arise from spatial variations in either ion channel expression<sup>161</sup>, or gap junctional coupling.<sup>74</sup> We thus explored the effect of local defects on spike propagation in iOS-HEK cell tracks. In a serpentine track with sharp turns, we observed that stably propagating far-field waves sometimes failed at the turns (Fig. 3.6a). Furthermore, failures occurred in a regular temporal sequence, e.g. Fig. 3.6a shows a pattern that after the first few beats stabilized into a 3:2 block (3 upstream spikes triggered 2 downstream spikes). The waves developed a curved wavefront and slowed repolarization at the turns, a purely geometrical consequence of the increased electrotonic loading associated with bending a wavefront around a corner. Thus geometrical effects alone are sufficient to cause conduction block, even in a background of homogeneous ion channel

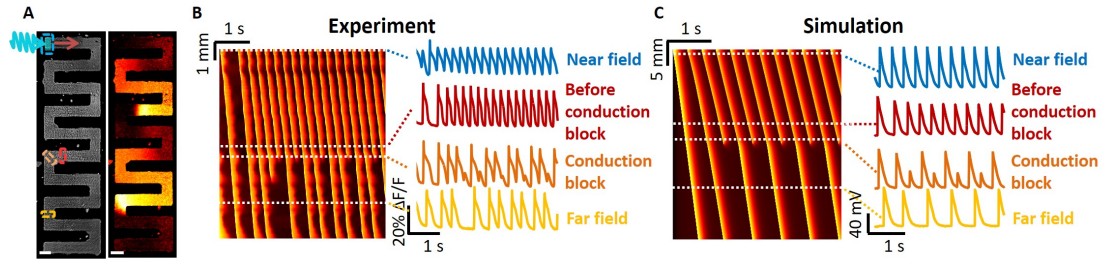


**Figure 3.6: Curvature-induced second-degree conduction block in iOS-HEK cell tracks.** A) Left: image of an iOS-HEK cell track showing stimulus region highlighted in cyan and regions of fluorescence monitoring shown with dashed rectangles. Right: single frame from an optical voltage recording showing two action potentials propagating through the track. Scale bars 200  $\mu\text{m}$ . B) Left: kymograph showing action potential propagation with a 4 Hz pacing frequency. The vertical axis represents contour coordinate along the track. All spikes conducted into the far-field, but conduction showed second-degree block at a corner where there was a slight defect in the pattern, corresponding to the red and orange rectangles. C) Numerical simulations of second-degree conduction block in a 1D track with a 10 cell zone of 3-fold reduced gap junctional coupling.

levels and gap junction strengths. A related effect has been reported in cultured cardiomyocytes, where a junction of a thin strand of cells to a large island showed unidirectional conduction block due to the inability of the thin strand to drive the large island.<sup>90</sup>

In our experiments, the conduction block was attributable to a 2D wavefront curvature effect. To capture this effect in computationally tractable 1D simulations, we simulated linear tracks in which a small region (10 cells) had a reduced gap junctional coupling. The simulated waves showed a 1:1 conduction block (Fig. 3.6c), qualitatively similar to that observed experimentally. These experiments and simulations show that local perturbations in the electrotonic coupling, are sufficient to lead to second-degree conduction block.

### 3.7 GEOMETRY DEPENDENT INSTABILITIES IN HUMAN iPSC CARDIOMYOCYTES

Finally, we explored whether the geometry-dependent effects observed in iOS-HEK cells also occurred in human iPSC-derived cardiomyocytes (hiPSC-CM).<sup>279</sup> Due to the significant commercial interest in using these cells as an *in vitro* model for cardiotoxicity testing<sup>31,55,122,142,194</sup>, the correspon-

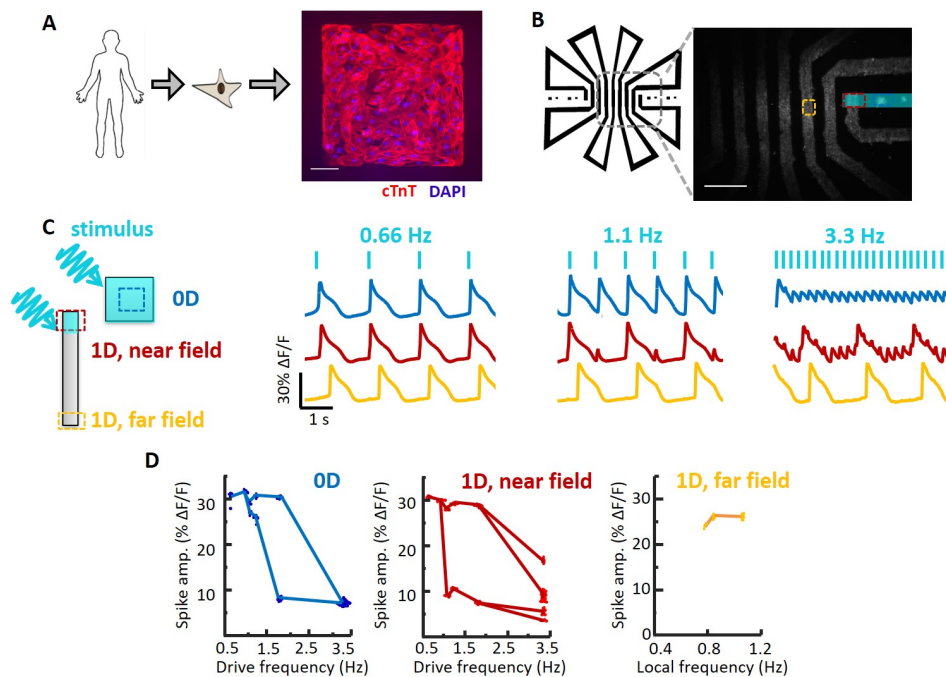


**Figure 3.7: Geometry-dependent arrhythmias in cultured human iPSC-derived cardiomyocytes (hiPSC-CM).** A) Image of hiPSC-CM grown on a patterned square island. Scale bar 100  $\mu\text{m}$ . B) Patterned hiPSC-CM cell growth in a set of OD islands and a long 1D track. The track geometry was designed to interpose long path lengths between returns to the field of view (2 cm between red and yellow regions of interest), to account for the high propagation speed of action potentials in hiPSC-CM compared to iOS-HEK cells. Scale bar 1 mm. C) Simultaneously recorded electrical dynamics in OD, 1D near field, and 1D far field. At elevated pacing frequencies the cells showed different dynamics in the three geometrical regimes. D) Quantification of the action potential height as a function of frequency in the three geometrical regimes.

dence (or lack of) between *in vitro* and *in vivo* arrhythmias has some practical importance.

We used microcontact printing to define side-by-side patterns of oD islands and iD tracks and then plated hiPSC-CM onto these patterns (Fig. 3.7b). CheRiff was expressed using a lentiviral vector to allow patterned blue light stimulation<sup>272</sup>, and BeRST1 was used to image changes in membrane potential. We optogenetically paced oD islands and iD tracks simultaneously across a range of frequencies with pulses of 50 ms duration. In the iD tracks, waves propagated with a conduction velocity of 7.2 cm/s and had an AP duration of 360 ms, corresponding to a depolarized action potential length of 2.6 cm.

As with the iOS-HEK cells, we observed that the dynamics depended strongly on the geometry (Fig. 3.7c). At high pace frequency (3.3 Hz), the oD islands showed small regular oscillations, the 1D near-field showed an erratic pattern of large beats with small oscillations superposed, and the 1D far-field only showed the large beats at a sub-harmonic of the pace frequency. As in the iOS-HEK cultures, the alternans beats decayed over a distance much less than the action potential length (decay length  $d = 535 \mu\text{m}$ , corresponding to  $d = 0.2 \lambda$ ). Thus the qualitative geometry-dependent behavior of the hiPSC-CM largely mirrored the behavior of the iOS-HEK cells.

The hiPSC-CM cells differed from the iOS-HEK cells in several important regards. First, the hiPSC-CM were spontaneously active, imposing a minimum on the optogenetic pace frequency. Second, the oD hiPSC-CM islands showed a transition to alternans (Fig. 3.7c,d) which disappeared at high drive frequencies (3 Hz). Third, the 1D bifurcation to alternans was continuous in the iOS-HEK cells but discontinuous in the hiPSC-CM. In iOS-HEK simulations, these last two differences can be captured simply by tuning the isradipine unbinding rate (Fig. 3.1b). Simulations of the Noble model also showed clear geometry-dependent differences in the onset of instabilities (Fig. 3.8c).<sup>205</sup> Finally, real cardiac tissue can support alternans in far-field traveling waves<sup>189</sup>, while both the iOS-HEK cells and the hiPSC-CM seemed only to support this phenomenon in the near field. Thus there remain important dynamical features of real cardiac tissue which appear not to be captured by either the iOS-HEK cells or the hiPSC-CM.

### 3.8 SCALING PROPERTIES OF ELECTRICAL INSTABILITIES

Given the importance of gap junction strength and sample geometry, it is interesting to ask whether one can scale both parameters to preserve the overall dynamics. Such scaling could be useful, for instance, in modeling *in vivo* cardiac dynamics in a cell culture system. We explored this question by systematically varying the gap junction strength in iOS-HEK simulations of a 1-D track (Fig.

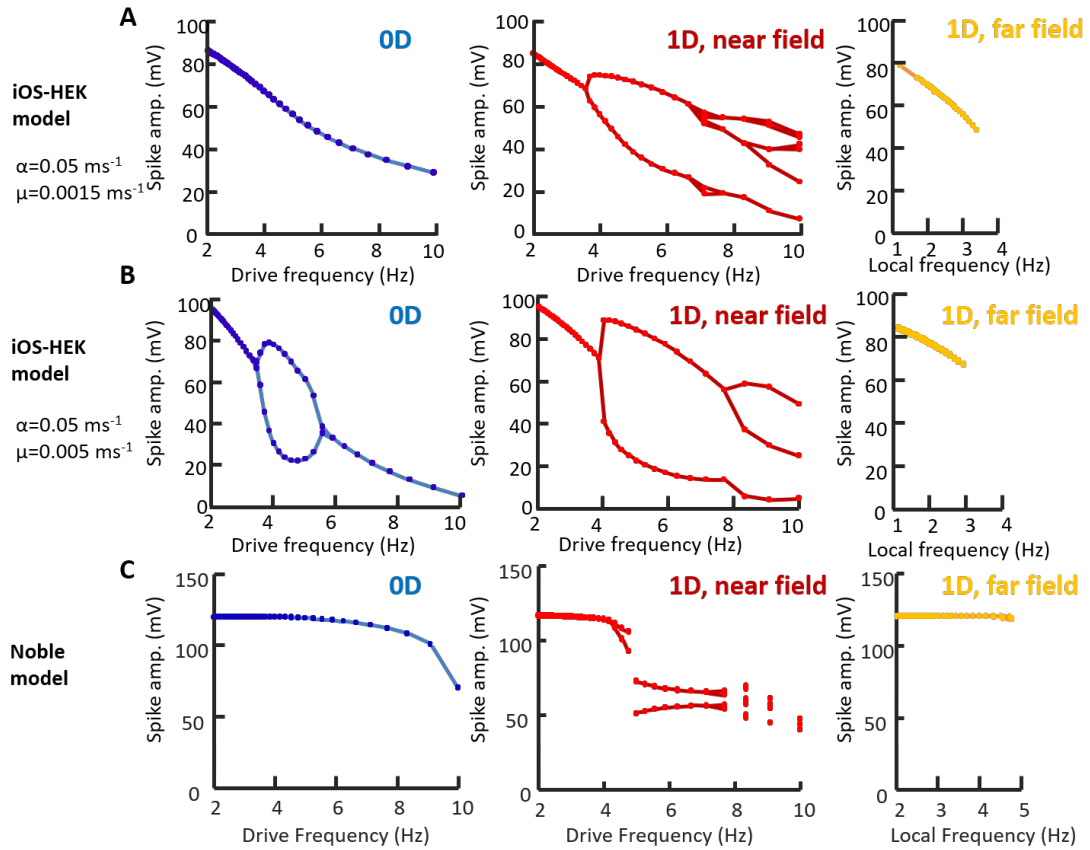


**Figure 3.8: Geometry dependent instabilities in different numerical models of excitable cells.** A) Hodgkin Huxley model of iOS-HEK cells (same as Fig. 3.4c, repeated here for comparison to other models). B) Same as (A) with artificially accelerated israpidine unbinding kinetics ( $\mu = 0.005 \text{ ms}^{-1}$ ). 0D features show alternans at intermediate drive frequencies. The 1D near field shows a discontinuous alternans transition. C) Simulation of the cardiac Noble model<sup>205</sup>, which also shows geometry-dependent changes in dynamics.

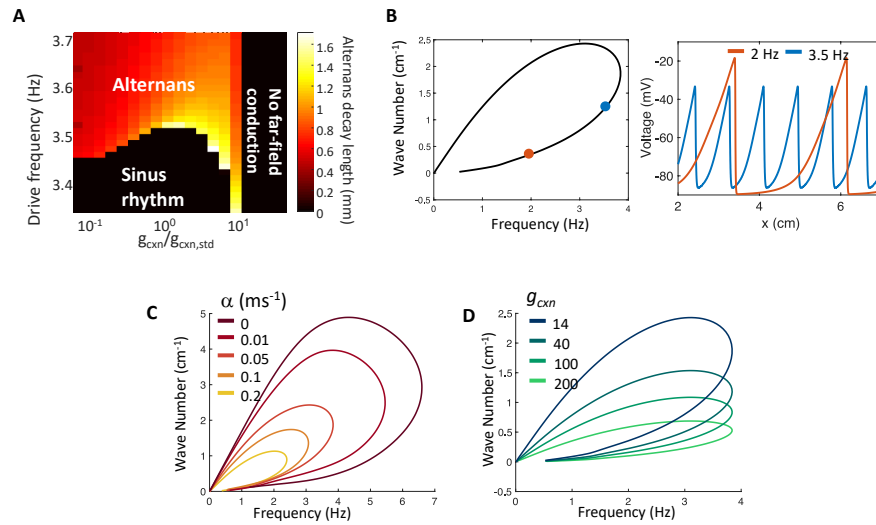


**Figure 3.9: Scaling properties of instabilities in iOS-HEK cells.** A) Frequency of near-field alternans onset as a function of gap junction coupling strength. The onset frequency varies by  $< 2\%$  over a 100-fold variation in  $g_{cxn}$ . Pseudocolor shows the spatial extent of alternans, measured as the distance over which alternans beats decay to half of their value in the stimulus region. B-D) Nonlinear dispersion relations show which frequencies are stable in far-field and the corresponding wave numbers (inverse of peak-to-peak wavelength) selected by each frequency. In panels B-D, bottom branches of nonlinear dispersion relations are stable and the top branches are unstable. B) Left: nonlinear dispersion relation under conditions corresponding to experimental data. Right: spatial structure of voltage waves in the far-field with frequencies 2 and 3.5 Hz. Position on nonlinear dispersion relation indicated by correspondingly colored dots. C) Effect of varying the isradipine binding rate,  $\alpha$ , on the nonlinear dispersion relation. Increasing  $\alpha$  decreases the maximum frequency that propagates to the far field. D) Changes in the connexin strength,  $g_{cxn}$ , affect the wavelength but have little effect on the maximum stably propagating frequency. Thus the maximum frequency prior to alternans onset is a parameter that is largely independent of gap junction strength, and by extension, tissue geometry.

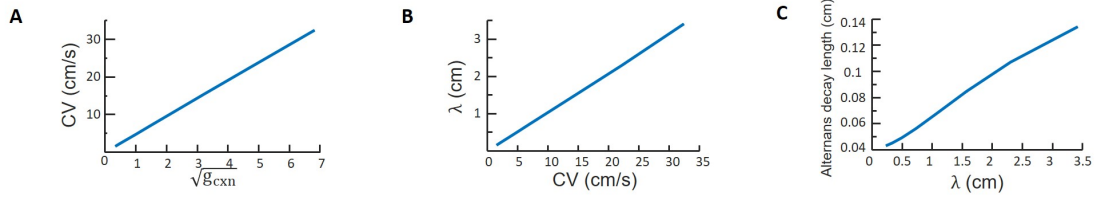


**Figure 3.10: Effect of gap junction coupling on dynamics in Hodgkin-Huxley simulations of iOS-HEK cells.** A) Linear scaling of conduction velocity with  $\sqrt{g_{cxn}}$ . B) Linear scaling of depolarized pulse length,  $\lambda$ , with conduction velocity. C) Relation of the alternans decay length to propagating pulse wavelength at a pacing frequency of 5 Hz, far above the onset of alternans.

3.9a). As anticipated from dimensional analysis, the far-field conduction velocity scaled as (Fig. S3.10a). The action potential duration (APD) was largely insensitive to  $g_{cxn}$ , so the action potential length  $\lambda$  scaled as (Fig. 3.10b). Together these results imply that scaling the size of a system by some factor  $k$  and the gap junction strength by  $\sqrt{d}$  will preserve the overall dynamics.

The propagation of spikes in the far-field is governed by the nonlinear dispersion relation, which defines the relationship between wavenumber and frequency (Fig. 3.9). The numerically simulated dispersion relation indicated that the far-field dynamics only supported frequencies up to  $f_{max} = 3.85$  Hz. Waves of greater frequency could not propagate into the far field.

The transition frequency for alternans,  $f^*$ , was largely insensitive to  $g_{cxn}$ , varying by  $< 2\%$  over a 100-fold change in  $g_{cxn}$  (Fig. 3.9a), but  $f^*$  depended sensitively on the dynamics of the slow recovery variable (Fig. 3.9c). This effect can be understood from the dispersion relation of the iOS-HEK system (Fig. 3.9b). Without isradipine ( $\alpha = 0$ ), the far field can support drive frequencies of up to  $f^* = 6.5$  Hz (set by the action potential width). As the slow recovery variable  $j$  is turned on ( $\alpha > 0$ ), the transition frequency  $f^*$  is reduced dramatically. Thus, the maximum stable frequency is a parameter that should be largely independent of gap junction strength, and by extension, tissue geometry—provided that the cells are paced via gap junction-mediated conduction rather than by direct pacing.

Can one extrapolate from *in vitro* measurements of small samples with relatively weak gap junc-

tion coupling to larger tissues with stronger gap junctional coupling? In iOS-HEK simulations, the alternans decay length,  $d$ , scaled almost linearly with  $\lambda$  (Fig. 3.10c). These simulations suggest that the action potential length,  $\lambda$ , sets a natural length scale for a bioelectric tissue. Moreover, using  $\lambda$  as a scaling parameter is advantageous since this parameter can be experimentally measured without knowledge of gap junction conductance or other system parameters.

The conduction velocity in the atria and ventricles of the human heart *in vivo* is approximately 50 cm/s<sup>75,123</sup>, and action potential durations are typically 350 ms, implying an action potential length of  $\lambda = 18$  cm. An adult human heart is approximately  $L = 12$  cm long, so  $L \approx 0.7\lambda$ . Pacemaker-triggered action potentials *in vivo* are thus primarily in the near-field and close far-field regimes. Remarkably, the near-field is the only regime in which we observed arrhythmias in either the iOS-HEK cells or in the hiPSC-CMs, either in experiment or in simulation.

In the cultured hiPSC-CM the action potential length was  $\lambda = 2.6$  cm, so to best match the geometrical regime of the heart, the culture should have size  $L \approx 0.7\lambda$ , or  $\sim 1.7$  cm. Others have reported conduction velocities *in vitro* ranging from 3.5 to 20 cm/s,<sup>272,71,292</sup> corresponding to  $\lambda = 1.2$  to 7 cm (assuming a 350 ms AP width). While cultures of size  $L \approx 0.7\lambda$  are easily accessible on the smaller end of the  $\lambda$  range, 5 cm-wide hiPSC-CM cultures are impractical. This challenge can be addressed either by cell patterning to produce serpentine tracks, or by adding gap junction blockers such as 2-APB to diminish the strength of the gap junction coupling and thereby to slow the conduction velocity.

*In vivo*, the heart is paced by autonomous cells in the sinoatrial node, which initiate waves that propagate across the myocardium. To best mimic wave conduction in the heart, cultures of hiPSC-CM should be stimulated locally to launch propagating waves. Whole-field stimuli, e.g. as delivered by field stimulation electrodes or wide-area optogenetic stimulation, will induce synchronous depolarization of all cells, mimicking the oD case and missing possibly important gap junction-mediated dynamical instabilities. One should ideally perform spatially-resolved voltage measurements to re-

veal the distinct dynamics in the near- and far-field regimes. While it is not possible to recapitulate the full spatial structure of connectivity of the adult myocardium *in vitro*, one can use the *in vitro* measurements to benchmark dynamical regimes according to biophysical parameters (e.g.  $\lambda$  and  $L$ ) which can be measured *in vivo*. We expect that these considerations will be important for ongoing efforts to develop *in vitro* models of cardiac dynamics.

### 3.9 CONCLUSIONS

Gap junction-mediated currents convey the effects of boundaries to all cells in the tissue. In the highly simplified iOS-HEK ‘toy’ model, the qualitative spiking dynamics depended in a sensitive way on the overall geometry. Islands of composed of identical cells and differing only in geometry showed vastly different dynamics under identical pacing frequencies, including regular spiking, complex but repeating multi-spike patterns, and irregular spiking. This work further highlighted the importance of a slowly recovering conductance (in our case state-dependent isradipine block) to support transitions to alternans and arrhythmia.

Our experimental and theoretical approach was guided by the aim to make the simplest possible models that captured key aspects of excitable dynamics. The iOS-HEK system was simple enough to model with biophysically realistic numerical simulations, which confirmed that the observations could be explained by geometry alone. The iOS-HEK cells bore little resemblance to cardiomyocytes from a molecular perspective, lacking, for instance, voltage-gated  $\text{Ca}^{2+}$  channels, calcium-induced calcium release, delayed rectifier potassium channels, and mechano-electrical feedbacks. The observation of similar geometry-dependent bifurcations in hiPSC-CM cultures suggests that similar principles apply to physiological tissues, despite the myriad differences in channel expression and electrophysiological details between the iOS-HEK cells and cardiomyocytes. Indeed, several distinct numerical models of excitable dynamics all showed geometry dependent bifurcations and transi-

tions to irregular dynamics (Fig. 3.8). Based on these observations, we propose that long-range electrical signaling may be a generic mechanism for conveying information on tissue geometry to cells interior to a tissue.<sup>220</sup>

A cardiomyocyte in isolation would behave very differently from one embedded in a two-dimensional culture or one embedded in a real heart—even if the ion channels were identical in all three cases. This fact suggests caution regarding the CiPA initiative to extrapolate from *in vitro* measurements of arrhythmia to *in vivo* predictions. One should not naively infer that a pro-arrhythmic compound *in vitro* will be pro-arrhythmic *in vivo*. Indeed, different cell culture geometries and different mechanisms of pacing can produce dramatically different results *in vitro*. By analyzing the scaling properties of waves in excitable tissues, we propose that to best mimic conditions *in vivo*, hiPSC-CM should (a) be stimulated via gap junction-mediated conduction, and not by direct electrical or optogenetic stimulation, and (b) that the ratio of culture size to action potential length should approximately mimic the corresponding ratio *in vivo*.

### 3.10 METHODOLOGY

#### 3.10.1 IOS-HEK CELL LINE GENERATION AND CULTURE

All HEK cells were maintained in Dulbecco's modified Eagle medium with 10% fetal bovine serum (DMEM-10), penicillin (100 U/mL), and streptomycin (100 µg/mL). OS-HEK cells were generated as described previously.<sup>186</sup> Briefly, a  $\text{Na}_v1.5$  plasmid (Johns Hopkins University ChemCORE) containing a puromycin selection marker was transfected into HEK cells using TransIT-293 transfection reagent (Mirus Bio). 48 hours after transfection, 2 µg/mL puromycin was introduced into the culture medium for 14 days to select for stably expressing  $\text{Na}_v1.5$  cells. Following this selection, an Optopatch construct containing coding sequences of CheRiff-eGFP and QuasAr2-mOrange (separated by a self-cleaving P2A peptide sequence) was introduced using a lentiviral construct.<sup>120</sup> GFP-

expressing cells were enriched 10 days after infection via fluorescence-activated cell sorting (FACS). Finally, a  $K_{ir2.1}$  lentiviral construct containing a blasticidin selection marker was introduced. After 2 days, cell culture media was supplemented with 5  $\mu\text{g}/\text{mL}$  blasticidin (to select for  $K_{ir2.1}$ -expressing cells) and 2  $\mu\text{g}/\text{mL}$  puromycin (to ensure continued  $\text{Nav}1.5$  expression). After 14 days, cells were dispersed as single cells into a 48 well plate, and clonal populations were selected on their ability to spike robustly in response to a blue light stimulus.

Clonal cell lines were maintained in DMEM-10 supplemented with 5  $\mu\text{g}/\text{mL}$  blasticidin and 2  $\mu\text{g}/\text{mL}$  puromycin in 10 cm tissue culture dishes up until 80% confluence, after which they were trypsinized and cryopreserved at 500,000 cells/vial in 90% DMEM-10, 10% dimethylsulfoxide (DMSO). Cryopreserved vials were then thawed and subcultured in antibiotic-supplemented DMEM-10 in 10 cm tissue culture dishes, and were passaged via trypsinization at 80% confluence at a 1:3 ratio. A given subculture typically maintained robust blue-light induced spiking for approximately seven passages, or 2 weeks, after which cells become less excitable (presumably due to decreased  $K_{ir2.1}$  expression over time).

To prepare OS-HEK cells as iOS-HEK cells for functional experiments, cells were incubated in Tyrode's solution (containing 125 mM NaCl, 2 mM KCl, 2 mM  $\text{CaCl}_2$ , 1 mM  $\text{MgCl}_2$ , 10 mM HEPES, 30 mM glucose; pH 7.3, osmolality 305-310 mOsm) further supplemented with 10  $\mu\text{M}$  isradipine and 1  $\mu\text{M}$  BeRST1 voltage-sensitive dye for 30 minutes in a mammalian tissue-culture incubator prior to imaging.

### 3.10.2 hiPSC-CM CELL CULTURE

Cultures of hiPSC-CM cells were procured from Cellular Dynamics International (iCell Cardiomyocytes) and maintained according to vendor protocols. Briefly, iCell Cardiomyocytes were thawed from frozen stocks and plated on gelatin coated plastic tissue culture tissues in plating medium for 48 hours. While in plating medium, hiPSC-CMs were incubated with lentivirus containing a coding

sequence for CheRiff-CFP. Cardiomyocytes were then passaged and re-plated onto fibronectin-patterned dishes in maintenance medium at sufficiently high density as to completely cover dish patterns. hiPSC-CM cultures were imaged between 24 and 72 hours after re-plating in Tyrode's solution with  $1 \mu\text{M}$  BeRST1, and without including isradipine.

### 3.10.3 CELL PATTERNING

Patterned cell growth was achieved using previously described methods.<sup>227,186</sup> Cytophilic fibronectin patterns were defined on a functionalized cytophobic polyacrylamide gel using microcontact printing with patterned PDMS stamps. Patterns were first designed in silico (Inkscape) and printed onto a Mylar transparency mask (CAD Art Services). Pattern negatives were then transferred onto silicon wafers coated in SU-8 3025 via contact photolithography and subsequent development of unexposed photoresist. PDMS stamps were then cast from the silicon wafer template.

Functionalized polyacrylamide dishes were prepared from MatTek 35 mm-glass bottom dishes. Glass coverslips were chemically activated by plasma cleaning and then incubated for 30 min in a nitrogen-purged glovebox with silane solution (v/v: 0.5% 3-methacryloxypropyltrimethoxysilane, 2% acetic acid, 97.5% anhydrous EtOH). A 40:1 acrylamide:bisacrylamide gel doped with 4.2 mg/mL acryl-NHS (to allow for covalent bonding of fibronectin matrix) was then gelled for 2-3 minutes in ambient air under siliconized coverslips (to ensure smooth gel surfaces). Functionalized acryl-NHS dishes were then sealed in nitrogen and drierite and transferred to -80 C for long-term storage.

To complete dish preparation, patterned PDMS stamps were first coated in fibronectin protein (Yo Proteins no. 663) dissolved in PBS (0.05 mg/mL fibronectin final concentration) in a sterile tissue culture hood. Coating was allowed to settle for 30 minutes, after which excess fibronectin-PBS solution was carefully removed via aspiration. Stamps were further air-dried for 10 minutes to remove excess moisture that could blur pattern transfer. Functionalized dishes were then printed with fibronectin-coated stamps for 1 hour in a tissue-culture incubator, after which stamps were gently re-

moved and dishes re-sterilized for 10 minutes with UV illumination. Cells were deposited by gently pipetting 500  $\mu$ L DMEM-10 droplet containing the desired cell density (typically between 500,000 and 1M cells/mL). Cells were allowed to adhere for 30 minutes in a tissue culture laminar hood before an additional 2 mL of DMEM-10 was added and cells were transferred to an incubator.

#### 3.10.4 WIDE-FIELD ALL-OPTICAL ELECTROPHYSIOLOGY

All-optical electrophysiology of iOS-HEK and hiPSC-CM cells was performed using an adapted ‘Firefly’ ultrawidefield inverted microscope.<sup>271</sup> Spatially patterned blue excitation for optogenetic stimulation was achieved using digital micromirror device (DMD) module with an onboard 460 nm LED (Wintech DLP Lightcrafter 4500). Pixels of linear dimension 7.637  $\mu$ m were demagnified 2x for optical pattern resolution of approximately 3.8  $\mu$ m. Action potentials in iOS-HEK cells were triggered with 10 ms pulses at 100 mW/cm<sup>2</sup>; action potentials in hiPSC cardiomyocytes were triggered with 50 ms stimuli. Patterns were defined using custom software (MATLAB). DMD pixels were mapped to sample pixels by calibrating a linear transformation to a test pattern on a fluorescent target.

Near-infrared voltage sensors were excited using widefield 635 nm illumination (DILAS 8 W diode laser, M1B-638.3-8C-SS4.3-T3) configured in a near-TIRF configuration (to reduce background autofluorescence). Robust signals from BeRST1 were obtained at an illumination intensity of 2 W/cm<sup>2</sup>. Near-infrared fluorescence emission was filtered using emission filters (Chroma ET665lp and Semrock quadband 336/510/581/703) and reimaged onto a sCMOS camera (Hamamatsu Orca Flash 4.2). Movies were acquired at 100 Hz over a 5 mm x 5 mm field of view.

Custom LabView software allowed for synchronization of time-modulated signals controlling blue and red light excitation, DMD patterns, and camera acquisitions over experimental runs. All data were processed and analyzed using custom software (Quantification and Statistical Analysis). To investigate geometry-dependent dynamical regimes, spatial regions of interest (ROIs) were de-

fined and averaged across pixels to give fluorescence time-traces. A single set of ROIs was defined for a given sample dish and was applied uniformly across movies at different drive frequencies to systematically investigate dynamical responses (Figs. 3.5b and 3.7c). Using these spatially resolved measurements, we extract information from multiple replicates of oD, iD near-field, and iD far-field responses all in a single dish.

### 3.10.5 IMAGE PROCESSING AND EXPERIMENTAL DATA ANALYSIS

All data were processed and analyzed using custom software (MATLAB). For each pixel, a baseline fluorescence,  $F$ , was calculated from the first percentile of the values in the recorded time-trace. The movie was then converted into units of  $\Delta F/F$ . Pixels that did not contain cells were set to zero (using a criterion that the 99th percentile of a time trace must be over a user-specified threshold). A spatial median filter (5x5 pixel filter) was further applied to account for measurement noise. At the illumination intensities used, BeRSTi photobleaching was negligible.

To investigate geometry-dependent dynamical regimes, spatial regions of interest (ROIs) were defined and averaged across pixels to give fluorescence time-traces. A single set of ROIs was defined for a given sample dish and was applied uniformly across movies at different drive frequencies to systematically investigate dynamical responses (Figs. 3.5b and 3.7c). Using these spatially resolved measurements, we extract information from multiple replicates of oD, iD near-field, and iD far-field responses all in a single dish.

We extracted action potential amplitudes for each spike detected in each feature across movies taken at different pacing frequencies. Spike upstrokes were detected via a threshold on the time derivative. Spike amplitudes (in units  $\Delta F/F$ ) were defined as the difference between the maximum value after a given upstroke and the minimum value preceding the upstroke. Between 10 and 300 spikes per feature were collected in a given movie, depending on drive frequency and acquisition time. Beeswarm plots of spike amplitudes at each pacing frequency were used to visualize the dy-

namical patterns of activity (Figs. 3.5b and 3.7c). Only spikes taken from the second half of movies are visualized to avoid early transients which decay as patterns converges to a stable cycle. The drive frequency in oD and iD near field measurements was set by the frequency of the blue light-gated CheRiff activation; in iD far-field measurements, the pacing frequency is defined as the local frequency (i.e., the reciprocal of the interval between successive spikes).

The transition between the near-field and far-field region was mapped using kymographs (Figures 3.5 and 3.6). Kymographs were generated by spatially averaging  $\Delta F/F$  movies across the short dimension of a linear track. For serpentine tracks (Figure 5), tracks segments were first computationally aligned into a single long track, and then spatially averaged along the short dimension. Alternans transitions were spatially mapped by performing spike detection (as described above) across linear windows of 8 pixels (Fig. 3.5c).

### 3.10.6 NUMERICAL MODELING OF IOS-HEK CELLS

In the conductance-based model, the voltage dynamics are governed by the equation:

$$C_m \frac{\partial V}{\partial t} = G_{cxn} \nabla^2 V - (I_{NaV} + I_{Kir} + I_{ChR}) \quad (3.3)$$

where  $V$  is the voltage in mV. Recall  $G_{cxn} = g_{cxn} \times l$ , where  $g_{cxn}$  is the gap junction conductance between cells, and  $l$  is the linear dimension of a cell. The ionic currents drive local dynamics, while the diffusion term couples neighboring regions. Units of space are  $10^{-5}$  m (corresponding to linear size of one cell), and time is in ms. Conductances are measured in nS/pF and ionic currents in pA/pF. The currents are:

$$I_{NaV} = g_{NaV} m_{\infty}^3(V) h(1-j)(V - E_{Na}) \quad (3.4)$$

$$I_{Kir} = g_{Kir}(V)(V - E_k) \quad (3.5)$$

$$I_{ChR} = g_{ChR}(x, t)(V - E_{ChR}) \quad (3.6)$$

The gating variables for the sodium activation and inactivation gates,  $m$  and  $h$  respectively, and for the effect of isradipine,  $j$ , are dimensionless variables which take values between 0 and 1. The inactivation gate evolves following:

$$\frac{\partial h}{\partial t} = \frac{1}{\tau_h(V)} (h_{\infty}(V) - h) \quad (3.7)$$

To capture the use-dependent sodium block by isradipine, we introduced a slowly activating and recovering gate,  $j$ , with behavior governed by:

$$\frac{\partial j}{\partial t} = \alpha m_{\infty}(V)(1-j) - \mu j \quad (3.8)$$

That is, the drug binds sodium channels in its open state with rate  $\alpha$ , and unbinds with rate  $\mu$ . These kinetic parameters were chosen to fit the experimentally observed dynamical transitions.

Since the time constant of the sodium activation gate,  $m$ , is orders of magnitude faster than the other gates, the gate was replaced with the asymptotic limit,  $m_{\infty}$ . This standard approximation allowed for more efficient computations without impacting the simulation results.

The gating variables approach steady-state asymptotic values, which are functions of the voltage:

$$h_{\infty}(V) = \left( 1 + \exp\left(\frac{V + 71.55}{7.43}\right) \right)^{-2} \quad (3.9)$$

$$j_{\infty}(V) = \frac{\alpha m_{\infty}(V)}{\alpha m_{\infty}(V) + \mu} \quad (3.10)$$

$$m_{\infty}(V) = \left(1 + \exp\left(\frac{-56.86 - V}{9.03}\right)\right)^{-2} \quad (3.11)$$

Time constants for each gate tell how quickly the behaviors approach the asymptotic values, and are given by:

$$\tau_h = \frac{1}{2} \left(1 - \tanh\left(\frac{V + 40}{10}\right)\right) \tau_{h1}(V) + \frac{1}{2} \left(1 + \tanh\left(\frac{V + 40}{10}\right)\right) \tau_{h2}(V) \quad (3.12)$$

$$\tau_{h1} = \left(0.057 \exp\left(\frac{-V - 80}{6.8}\right) + 2.7 \exp(0.079V) + (3.1 \times 10^5) \exp(0.3485V)\right)^{-1} \quad (3.13)$$

$$\tau_{h2} = \frac{0.13 \left(1 + \exp\left(\frac{-V - 10.66}{11.1}\right)\right)}{0.77} \quad (3.14)$$

$$\tau_j(V) = (\alpha m_{\infty}(V) + \mu)^{-1} \quad (3.15)$$

The equations governing the sodium channel activation, m, and inactivation, h, gates were set following literature values.<sup>252,253</sup> Minor modifications were made to the h time constant, to smooth the discontinuous function. The channelrhodopsin was modeled as a linear conductance, modulated in space, x, and time, by the blue light illumination. The repolarization conductance g<sub>Kir</sub> was modeled as an instantaneous function of voltage derived from a smoothing spline fit to the action potential waveform at low drive frequency (f = 2 Hz).

Numerical simulations were run on single-cells for the oD case, and 2 cm 1D tracks with Neumann (no-flux) boundary conditions at each end. The 1D tracks were discretized with a spatial step size,  $dx$ , equal to  $10 \mu\text{m}$ , the length of one OS-HEK cell. With this discretization size, each grid point represented one cell, allowing the simulations to have similar spatial resolution as the experiments.

The Laplacian was modelled with a fourth-order centered finite difference scheme. Boundary conditions were implemented using the standard ghost-point method. A combination IMEX scheme was used for the time evolution, with implicit Crank-Nicholson applied to the diffusion terms and explicit Adams-Bashforth applied to the remaining nonlinear terms (ion currents and gating dynamics). A time step of  $0.1 dx \text{ ms}$  ( $10^{-6} \text{ ms}$  in the case of  $10 \mu\text{m}$  spatial step) was used, which is well within the accuracies of the numerical scheme and is significantly smaller than any time scales in the model. Single cell, oD dynamics were modelled by setting to zero, and time evolution was performed with the same Adams-Bashforth scheme. All computations were performed using MATLAB.

Initial model parameters were experimentally constrained and fit using a combination of patch clamp measurements and fluorescent voltage recordings. Reversal potentials of  $E_{Na} = 75 \text{ mV}$ ,  $E_K = -107 \text{ mV}$ , and  $E_{ChR} = 0 \text{ mV}$  were determined according to Nernst equation for the corresponding intracellular and extracellular ionic concentrations. All conductances were expressed as specific conductances per unit capacitance, allowing us to set  $C_m = 1$ . The sodium conductance  $g_{NaV}$  was set to  $1.5 \text{ nS/pF}$ , corresponding to a maximum transient current of  $3 \text{ nA}$  at  $-25 \text{ mV}$  (measured in a  $20 \text{ pF}$  patch clamp recording). The channelrhodopsin conductance was determined to be  $15 \text{ pS/pF}$  following similar methodology. The inward rectifying potassium current  $g_{Kir}$  was represented as an instantaneous function of voltage, determined by fitting to the experimentally observed fluorescence repolarization waveform at low drive frequency ( $2 \text{ Hz}$ ). Because fluorescence traces do not report absolute voltage, we assumed a resting potential of  $-90 \text{ mV}$  and peak voltage of  $+30 \text{ mV}$ , in accordance with patch clamp recordings. The diffusion coefficient  $G_{cxn}$  is given by  $G_{cxn} = g_{CxN} \times l^2$ ,

where  $l = 1$  cell. The connexin conductance  $g_{cxn}$  was estimated according to measurements of the static electronic coupling length<sup>186</sup> as 40 nS/pF.

The parameters  $\alpha$  and  $\mu$  were chosen to match experimentally determined dynamical regimes. Setting  $\alpha = 0.5$  ms<sup>-1</sup> and  $\mu = 0.015$  ms<sup>-1</sup> gave close agreement with the complex landscape of dynamical transitions observed experimentally (Fig. 3.4c) as well as simulated voltage traces which closely resembled experimental observations (Fig. 3.4b). Sensitivity analysis was performed to validate these parameter choices.

Model dynamics were characterized using analogous parameters as for experimental results. Simulations were conducted for both an isolated cell which was directly paced ('oD') as well as for linear tracks of 2000 cells (i.e.  $L = 2$  cm) in which 40 cells were paced on one end. Simulations were run across a range of stimulus intervals between 500 ms (2 Hz) and 100 ms (10 Hz), sampled at 10 ms intervals. For each numerical experiment, we detected spike upstrokes as upward deflections of the derivative of the simulated voltage trace.

### 3.10.7 SENSITIVITY ANALYSIS

Parameter values for were selected to match as closely as possible the experimental results in both the oD and iD settings. The model was simulated for 1,500 ms with a given set of parameters under 2 Hz stimuli, and the resulting voltage at times  $t_k$ ,  $V(x, t_k)$ , was compared to analogous experimental results,  $W(x, t_k)$ , using the ordinary least squares (OLS) objective function

$$OLS_{obj} = \sum_k |W(x, t_k) - V(x, t_k)|^2 \quad (3.16)$$

Simulated and experimental voltage values were scaled to be between 0 and 1 to allow for direct comparison. An optimal set of parameters minimizes the objective function; minimization was performed with the MATLAB constrained optimization function `fmincon`. Realistic parameter

constraints were chosen from the patch clamp data.

Sensitivity of model parameters was tested using Latin Hypercube Sampling (LHS).<sup>178</sup> The LHS results identified  $\alpha$ ,  $\mu$ , and  $g_{NAV}$  as the most sensitive parameters, with  $g_{cxn}$  as the least. That is, small changes in the connexin strength, had negligible impact on the simulated voltages. Regardless, changing any model parameters over a modest regime maintained the main geometry-dependent differences in stability, giving confidence in the appropriateness of the model. Nonlinear dispersion analysis of far-field dynamics

### 3.10.8 NONLINEAR DISPERSION ANALYSIS OF FAR-FIELD DYNAMICS

In the far-field, the waves become spatially periodic structures of constant shape and velocity, both of which are uniquely determined by the frequency. The nonlinear dispersion relation of the far-field equation indicates which wave number (inverse of peak-to-peak wavelength) is selected by each frequency (Fig. 3.9b). The nonlinear dispersion relation is computed by considering the far-field traveling waves as periodic stationary solutions in a moving frame, which allows for the traveling wave and wave number to be solved for as a function of frequency. The full dispersion relation curve is traced out with pseudo-arclength numerical continuation implemented in MATLAB, and using the spatial discretization scheme as in the numerical simulations.

Each frequency has two associated wave numbers, with the bottom branch stable and top branch unstable. Two examples of the spatial structure of the far-field waves are given, and their positions along the dispersion relation marked. The curve does not extend past 3.85 Hz, indicating the far-field equation does not support waves of higher frequencies. Therefore, for drive frequencies above 3.85 Hz, each stimulus will not propagate into the far-field, leading to the appearance of near-field alternans, and aligning with the experimentally and numerically observed behavior.

Changing the drug binding rate,  $\alpha$ , and connexin strength,  $g_{cxn}$ , have different impacts on the nonlinear dispersion relation (Fig. 3.9c and 3.9d). Small changes in  $\alpha$  lead to large shifts in the tran-

sition frequency, indicating that faster binding rates will induce near-field alternans at lower drive frequencies. However, large changes to the coupling strength change properties of the traveling waves, such as wave number, wave length, and speed, but do not appreciably change the range of allowed frequencies or transition frequency. Changes to model parameters  $\mu$  (drug unbinding rate) and  $g_{Na}$  (sodium conductance) are not shown, but have a similar effect as changing  $\alpha$ .

The 2:1 conduction block observed from local changes in the connexin strength (Fig. 3.6) is also explained from the nonlinear dispersion relation. As the spike propagates through the small region of lower connexin strength, the wavenumber and frequency are adjusted to values that are no longer stable when the wave reenters the region of higher connexin strength (observe the differences in the curves with  $g_{cxn}$  values of 40 and 14 in Fig. 3.9d). The modification of wavenumber and frequency upon the reentry results in the observed 2:1 conduction block.

### 3.11 PUBLICATION INFORMATION

A version of this chapter appeared previously as: McNamara, H.M., Dodson, S., Huang, Y.L., Miller, E.W., Sandstede, B. and Cohen, A.E., 2018. Geometry-dependent arrhythmias in electrically excitable tissues. *Cell Systems*, 7(4), pp.359-370.<sup>184</sup>

### 3.12 CONTRIBUTIONS

Adam Cohen and I designed the study. I conducted and analyzed experiments. Stephanie Dodson and I developed and simulated the iOS-HEK numerical models. Stephanie Dodson and Björn Sandstede conducted dispersion analysis and Noble model simulations. Yi-Lin Huang and Evan Miller provided BeRST1 dye reagent. Adam Cohen and I wrote the manuscript, with input from Stephanie Dodson and Björn Sandstede. Adam Cohen and Björn Sandstede oversaw the research.

We thank Christopher Werley and Miao-Ping Chien for the hiPSC-CM image in Fig. 3.7a. This

work was supported by the Howard Hughes Medical Institute. I was supported by the Department of Defense (DoD) through the National Defense Science and Engineering Graduate Fellowship (NDSEG) program. Stephanie Dodson was supported by the NSF Graduate Research Fellowship Program under Grant No 1644760. Yi-Lin Huang and Evan Miller were supported by NIH grant R35GM119855.

# 4

## Bioelectric domains, phase transitions, and signaling via domain wall migration

ELECTRICAL SIGNALING IN BIOLOGY is typically associated with action potentials, transient spikes in membrane voltage that return to baseline. The Hodgkin-Huxley equations of electrophysiology belong to a more general class of reaction-diffusion equations which could, in principle, support

patterns of membrane voltage which are stable in time but structured in space. Here we show theoretically and experimentally that homogeneous or nearly homogeneous tissues can undergo spontaneous spatial symmetry breaking into domains with different resting potentials, separated by stable bioelectrical domain walls. Transitions from one resting potential to another can occur through long-range migration of these domain walls. We map bioelectrical domain wall motion using all-optical electrophysiology in an engineered cell line and in human iPSC-derived myoblasts. Bioelectrical domain wall migration may occur during embryonic development and during physiological signaling processes in polarized tissues. These results demonstrate a novel form of bioelectrical pattern formation and long-range signaling.

#### 4.1 MOTIVATION

In 1952, Hodgkin and Huxley introduced a mathematical model of action potential propagation in the squid giant axon, based on nonlinear dynamics of electrically coupled ion channels.<sup>121</sup> In the same year, Alan Turing proposed a model for biological pattern formation, based on diffusion and nonlinear reaction dynamics of chemical morphogens.<sup>260</sup> These two seemingly unrelated models have an underlying mathematical kinship: both are nonlinear reaction-diffusion equations, first order in time and second order in space. Thus, from a mathematical perspective, one expects parallel classes of solutions. These solutions can be organized by whether they are uniform or patterned in space, and stable or varying in time (Fig. 4.1). All four combinations of spatial and temporal structure have been observed in chemical reaction-diffusion systems<sup>156</sup>, but only three of the four have been reported in systems governed by the Hodgkin-Huxley equations. We thus sought to observe the fourth class of electrophysiological dynamics: spontaneous spatial symmetry breaking in a nominally homogeneous tissue to create patterns of membrane voltage that are static in time but that vary in space.

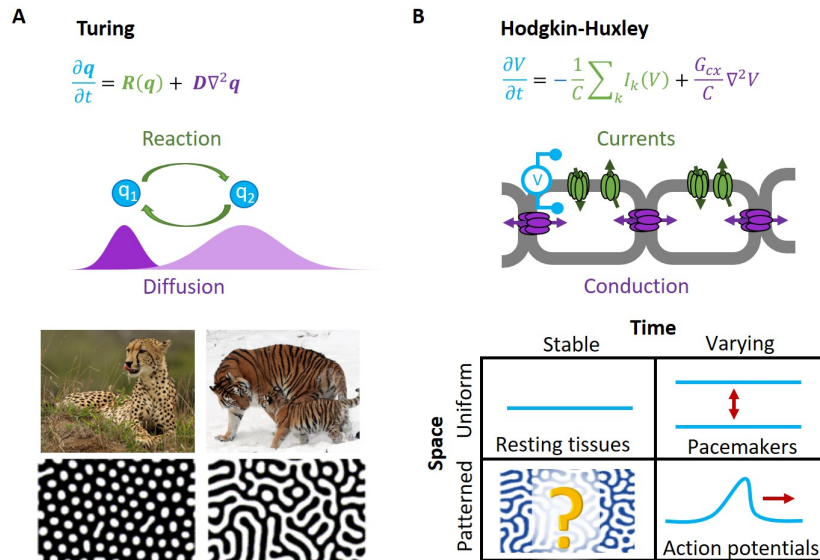


**Figure 4.1: Biochemical and bioelectrical pattern formation.** A) In chemical Turing patterns, a nonlinear chemical reaction coupled to diffusion leads to spontaneous formation of stable concentration patterns like ones seen in Nature. Here  $q = (q_1, q_2)$  is the vector of reagent concentrations,  $R(q)$  is the nonlinear relation between concentration and reaction rate, and  $D$  is the vector of diffusion coefficients. B) The Hodgkin-Huxley equation has the same structure as the Turing equation. Here  $V$  is the membrane voltage,  $C$  is the membrane capacitance,  $I_k$  is the current through the  $k$ th ion channel, and  $G_{cx}$  is the connexin conductivity. The chart shows possible solutions to the Hodgkin-Huxley equation, classified by variation in space and time. Spatially varying but temporally constant patterns are a little-explored possibility in electrophysiology. Images of natural and simulated patterns adapted from Wikipedia and Kondo et al.<sup>156</sup>

Spatial symmetry breaking might emerge during slow transitions in membrane potential, such as occur during embryonic development and in signaling processes in peripheral organs. While pattern-forming processes in electrophysiology have been contemplated,<sup>26,41,220</sup> unambiguous observations with clear mechanistic interpretations have been lacking. Part of the experimental challenge comes from the difficulty of spatially mapping membrane voltage. Patch clamp measurements of membrane potential probe the voltage at only discrete points in space, and are thus ill-suited to mapping spatial structure. Recent advances in voltage imaging facilitate spatially resolved measurements<sup>2,120</sup>, and optogenetic stimulation offers the prospect to tune the electrophysiological state of a tissue and perhaps to drive it into a regime of spontaneous symmetry breaking.

Here, we explore these ideas experimentally in engineered cells expressing the inward-rectifying potassium channel  $K_{ir2.1}$  and the channelrhodopsin CheRiff (Fig. 4.2a,b). While this two-component cellular model is so simple as to appear almost trivial, we find that coupled ensembles of these cells show richly diverse transitional behaviors, including electrical bistability, bioelectrical domain walls, and noise-induced breakup into discrete electrical domains. We further show that similar dynamics occur in human induced pluripotent stem cell (iPSC)-derived myocytes during differentiation. Our results demonstrate bioelectrical pattern formation and domain wall motion as generic mechanisms by which tissues can switch from one membrane voltage to another.

## 4.2 BISTABLE MEMBRANE VOLTAGES

The lipid bilayer cell membrane behaves, electrically, as a parallel plate capacitor. Transmembrane protein channels can pass ionic currents which alter the intracellular charge, and hence the membrane voltage. In a single cell or a small isolated patch of tissue, the membrane voltage follows:

$$C_m \frac{dV}{dt} = -I \quad (4.1)$$

where  $C_m$  is the membrane capacitance and  $I$  is the current through all ion channels (outward positive). Channel gating dynamics can impose a nonlinear and history-dependent relation between  $I$  and  $V$  which causes complex dynamics in excitable cells.

Resting potential ( $\frac{dV}{dt} = 0$ ) in most polarized cells is set by an inward rectifier potassium channel,  $K_{ir}$ . The current through the  $K_{ir}$  channel is :

$$I_{K_{ir}} = g_K x_\infty(V)(V - E_K) \quad (4.2)$$

where  $g_K$  is the conductance (proportional to the number of channels in the membrane), and  $x_\infty(V)$  captures the voltage-dependent gating of the channel (shut at depolarized voltages, open at polarized voltages).<sup>252</sup> The term  $(V - E_K)$ , where  $E_K \sim -90$  mV is the potassium Nernst potential, accounts for the electrochemical driving force for ions to cross the membrane. The function  $I_{K_{ir}}(V)$  crosses the x-axis at the potassium reversal potential. Inward rectification implies a drop in  $K_{ir}$  current at more positive potentials. Together these attributes give  $K_{ir}$  channels a non-monotonic  $I$ - $V$  relationship (Fig. 4.2c).<sup>117,165</sup> To a good approximation, the  $K_{ir}$  conductance depends on present voltage only, not on history.

Cells typically have one or more leak conductances. We consider the simplest case: an Ohmic leak with reversal potential 0 mV and conductance  $g_l$ , leading to a straight line  $I$ - $V$  relation,

$$I_{leak} = g_l V \quad (4.3)$$

Leak conductances can be gated by external variables, e.g. by chemical ligands or mechanical forces. Below we use a non-selective cation-conducting channelrhodopsin, CheRiff, as a leak conductance where the value of  $g_l$  is readily tunable via blue light.<sup>120</sup>

The total current is the sum of the  $K_{ir}$  and leak currents (Fig. 4.2c). When  $g_l$  dominates, one has a single depolarized fixed point ( $I = 0$ ) near 0 mV ( $P_D$ ). When  $g_K$  dominates, one has a single

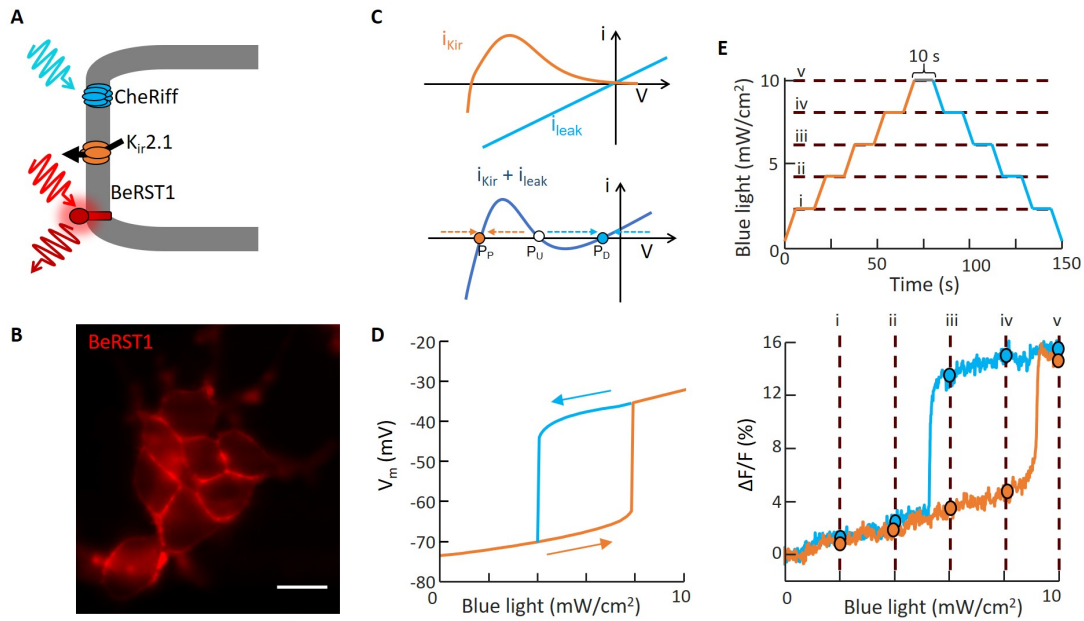


**Figure 4.2: Electrophysiological bistability in an engineered cell line.** A) Bi-HEK cells expressed an inward-rectifier potassium channel,  $K_{ir}2.1$ , and a light-gated ion channel, CheRiff. A far-red voltage-sensitive dye, BeRST1, reported membrane potential. B) Fluorescence image of bi-HEK cells labeled with BeRST1. Scale bar 20  $\mu\text{m}$ . C) Expression of an inward rectifier potassium channel (e.g.  $K_{ir}2.1$ ) and a non-selective leak conductance (e.g. channelrhodopsin) are sufficient, together, to produce electrical bistability. D) Numerical simulations showing hysteresis of steady-state membrane potential under ramped optogenetic stimulation. Simulations were based on measured  $I-V$  curves of bi-HEK cells. E) Top: optogenetic stimulus waveform. Epochs of constant illumination intensity have been indicated with Roman numerals. Bottom: Optical measurements of membrane voltage in a small cluster of bi-HEKs, exposed to the stimulus waveform above. Circles denote points where the optogenetic stimulus strength was held constant for 10 seconds.

polarized fixed point near  $-90\text{ mV}$  ( $P_P$ ). When  $g_I$  and  $g_K$  are approximately balanced, one has an N-shaped  $I-V$  curve which crosses the x-axis three times. This situation implies coexistence of stable fixed points  $P_D$  and  $P_P$  with an unstable fixed point ( $P_U$ ) in between, leading to overall bistability.<sup>40,98</sup> From a dynamical systems perspective, this situation is analogous to the bistability observed in the famous *E. coli* Lac operon system.<sup>208,214</sup>

We genetically engineered a HEK293 cell line that stably expressed  $K_{ir}2.1$  and CheRiff.<sup>186,184</sup> We call these bistable-HEK cells (bi-HEKs). Patch clamp measurements on small clusters ( $\sim 50\ \mu\text{m}$

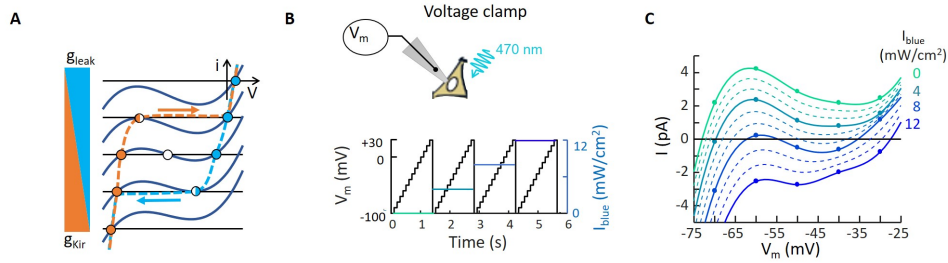


**Figure 4.3: Electrophysiological characterization of bi-HEK cells.** A) Cartoon showing origin of bistability in cells expressing a  $K_{ir}$  channel and a leak conductance. Changes in the ratio of leak to  $K_{ir}$  conductance drive the  $I$ - $V$  curve through two saddle-node bifurcations. B) Protocol for measuring the  $I$ - $V$  curve under different levels of optogenetic drive. Measurements were performed in voltage clamp mode. C) Patch clamp measurements of the  $I$ - $V$  curve of a small island of bi-HEKs under varying blue light illumination. Points represent measurements. Dotted lines are interpolations.

diameter) of bi-HEKs revealed a non-monotonic  $I$ - $V$  curve, which could be driven through two saddle-node bifurcations by light (Fig. 4.3). We performed numerical simulations of a cell governed by Eq. 4.1, using the measured  $I$ - $V$  curve. Under continuous variation in blue light the simulated membrane potential underwent sudden jumps at saddle node bifurcations where  $P_U$  annihilated either  $P_P$  or  $P_D$ . The jumps occurred at different values of blue light in the polarizing and depolarizing directions, leading to hysteresis (Fig. 4.2d); i.e. within the hysteretic region, the membrane voltage was bistable.

We used a far-red voltage-sensitive dye, BeRST1<sup>125</sup>, to report the membrane voltage in small clusters of bi-HEKs. Homogeneous blue illumination was slowly increased (0 to 10 mW/cm<sup>2</sup> over 75 s) and then decreased using a piecewise-continuous waveform comprising linear ramps alternating with 10 s intervals of constant intensity (Fig. 4.2e, top). The 10 s periods of constant intensity were  $\sim 10^3$ -fold longer than the membrane electrical time constant ( $\sim 10$  ms), sufficient to ensure that the

membrane voltage reached steady state. The optically recorded membrane voltage showed abrupt transitions and hysteresis, in close agreement with the numerical simulations (Fig. 4.2e, bottom). Furthermore, we did not detect drift in the membrane voltage during the periods of constant optogenetic drive, confirming that the dynamics were quasi-static. Thus, cells expressing  $K_{ir} + \text{leak}$  exhibited a form of non-genetic electrophysiological memory: the steady-state membrane voltage was not uniquely specified by the ion channels alone. Rather, in the hysteretic regime the steady-state voltage depended on the history of ionic currents, which could in turn depend on the history of stimuli to the cell or, in principle, on the history of gene expression (e.g. whether the leak or the  $K_{ir}$  channel was expressed first).<sup>165</sup>

### 4.3 BIOELECTRICAL DOMAINS IN EXTENDED TISSUES

In an extended tissue, neighboring cells can be coupled by gap junctions. When the voltage on a cell deviates from the mean of its neighbors, ionic currents flow through the gap junctions to minimize this deviation. The dynamics then become:

$$C_m \frac{\partial V}{\partial t} = -I + G_{cxn} + \nabla^2 V \quad (4.4)$$

where  $G_{cxn}$  is the sheet conductance due to gap junction channels. When the membrane potential is bistable (i.e. the ratio  $g_l/g_K$  is in the hysteretic portion of Fig. 4.2e), different regions of the tissue may sit at different resting potentials,  $P_U$  and  $P_D$ .<sup>42</sup> A domain wall then emerges at the interface between these regions (Fig. 4.4a). In a homogeneous tissue, the domain wall is stationary only when the  $K_{ir}$  and leak conductances are perfectly balanced, i.e. when the areas of the positive and negative portions of the  $I-V$  curve between  $P_U$  and  $P_D$  are equal.<sup>20</sup> Otherwise the domain wall migrates to expand the territory of the stronger conductance (Fig. 4.5a-c).

To aid intuition, we introduce a simple analytical model of a bioelectrical domain wall. We ap-

proximate the  $I$ - $V$  relation by a sinusoidal function,

$$I(V) = A \sin\left(\frac{2\pi}{|E_k|}\right) \quad (4.5)$$

While the sinusoidal approximation does not replicate the detailed shape of the  $I$ - $V$  curve, it correctly captures the three zero-crossings between  $E_k$  and 0 mV (Fig. 4.4A). In one dimension, the steady-state domain wall profile ( $\frac{\partial V}{\partial t} = 0$ ) obeys:

$$G_{cxn} \frac{d^2 V}{dx^2} = A \sin\left(\frac{2\pi}{|E_k|}\right) \quad (4.6)$$

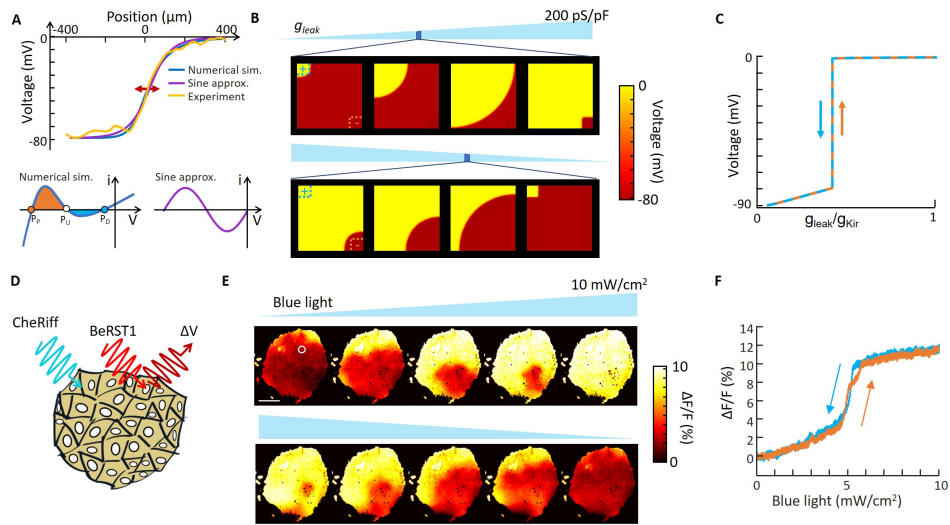
Differential equations of this form appear in many contexts, perhaps most famously to describe the dynamics of a physical pendulum (with time replacing position as the independent variable).<sup>54</sup> The domain wall profile is described by the separatrix solution which delineates the oscillatory from the rotatory solutions:

$$V(x) = \frac{2E_k}{\pi} \tan^{-1} \left[ \exp\left(\sqrt{\frac{2\pi A}{G_{cxn} E_k}} x\right) \right] \quad (4.7)$$

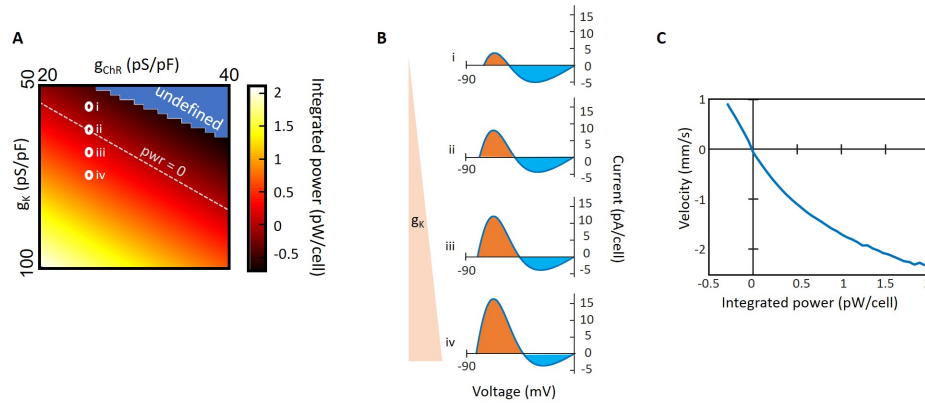
The domain wall width scales as  $\lambda \sim \sqrt{\frac{G_{cxn} E_k}{2A}}$ . The parameter  $A$  is a measure of the strength of the (non-gap junction) ionic currents, i.e.  $g_k$  and  $g_l$  in the more detailed biophysical model.

Fig. 4.4a compares the analytical approximation (Eq. 4.7) with numerical simulation using the complete expression for the  $K_{ir2.1}$  + leak I-V relation. The numerical and analytical domain wall profiles differ by at most 3.5 mV for a domain wall of height 77.5 mV.

Dual patch clamp measurements have shown that  $G_{cxn}$  is maximal at zero voltage difference between adjoining cells and decreases when the intercellular voltage exceeds approximately  $\pm 40$  mV.<sup>195</sup> Our simulations showed that in the domain walls the maximal nearest-neighbor voltage difference was  $< 1$  mV, implying that the voltage dependence of  $G_{cxn}$  could safely be neglected. This



**Figure 4.4: Bioelectric domain walls in an engineered cell line.** A) Top: Profile of a bioelectrical domain wall in one dimension, comparing numerical simulations based on a balanced  $K_{ir}$  and leak current, an analytical approximation based on a sinusoidal  $I$ - $V$  relation, and experimental data. Bottom:  $I$ - $V$  curves based on a detailed biophysical model of  $K_{ir}$  + leak (left) or a sinusoidal approximation (right). In a homogeneous tissue, the domain wall migrates in a direction set by the relative areas of the orange and blue shaded regions of the  $I$ - $V$  curve, favoring the fixed point with the larger shaded region. B) Simulation of domain wall growth in a homogeneous tissue with two discrete defects to nucleate transitions (clamped at  $V = 0$  on the top left, clamped at  $V = -90$  mV on the bottom right). The transitions in the bulk tissue occurred over a narrow range of  $g_{leak}$ . C) Simulation of membrane voltage in the tissue in (B) as a function of leak conductance. D) Confluent islands of bi-HEK cells were illuminated with uniform blue light to stimulate CheRiff, and with red light to elicit voltage-dependent fluorescence of BeRST1. E) Fluorescence images of an island of bi-HEKs under gradually increasing optogenetic stimulation. Scale bar 1 mm. White circle denotes region with voltage plotted in (F). F) Fluorescence as a function of optogenetic stimulus strength from the region circled in white in (E). Domain wall migration in the large island led to a step-like change in membrane potential without hysteresis.



**Figure 4.5: Balance of ionic currents determines velocity of domain wall motion in homogeneous tissues.** The balance of currents is set by the integral of the  $I$ - $V$  curve between the two stable fixed points, or equivalently the relative areas of the orange and blue shaded regions in panel (B). The area under the curve ( $\int IdV$ ) has units of power. A) Area under the  $I$ - $V$  curve as a function of the  $K_{ir2.1}$  and channelrhodopsin conductance levels. The white dotted line corresponds to a stationary domain boundary. In the blue region there is only one stable fixed point (near  $V = 0$ ), so the area under the curve is undefined. B) Example  $I$ - $V$  curves from the corresponding circled regions in (A). C) Domain wall velocity as a function of the area under the  $I$ - $V$  curve. Positive velocities indicate growth of the depolarized domain.

effect may be necessary to include when the width of the domain wall approaches the size of a cell.

In two dimensions, simulations predicted that bioelectrical domains nucleated at defects (e.g. cells that expressed only leak or only  $K_{ir}$ ) and spread through the tissue (Fig. 4.4b). In a tissue that was homogeneous but for an arbitrarily low density of nucleation points, the hysteresis vanished and the transition between depolarized and polarized states was abrupt (Fig. 4.4c). Thus the collective nature of the transition in an extended tissue was predicted to convert a gradual change in ionic currents into a highly sensitive phase change-like switch in membrane potential.

HEK cells endogenously express connexins 43 and 45 which mediate nearest-neighbor electrical coupling,<sup>33,164</sup> so we reasoned that confluent monolayers of bi-HEK cells might support bioelectrical domain walls. We performed optogenetic stimulation and voltage imaging experiments in confluent

islands of bi-HEKs with dimensions  $\sim 2 \times 2$  mm, corresponding to  $\sim 4 \times 10^4$  cells (Fig. 4.4d). Initially (in the absence of optogenetic stimulation) the tissue was homogeneously polarized. Illumination with dim blue light led to nucleation of depolarized domains near the tissue boundaries. We extracted the mean fluorescence intensity profile across the domain wall. When scaled to match the voltage axis, the profile agreed closely with the predictions of both the numerical simulation and the analytical approximation (Fig. 4.4a).

As the blue light further increased, the domain walls migrated across the tissue, until the whole tissue was depolarized (Fig. 4.4e). The fluorescence intensity of most regions in the island showed step-like depolarization with little hysteresis, consistent with the theoretical predictions. Domain wall formation and migration were observed in 8 of 8 independently prepared and measured islands (Fig 4.6), though in some cases defects prevented depolarization of the entire island.

To test the stability of the domain walls, we applied a piecewise-continuous blue light waveform comprising linear ramps alternating with 10 s intervals of constant intensity, as in Fig. 4.2e. During each period of constant illumination the domain walls remained stationary. During each period of increasing or decreasing illumination, the domain walls advanced or retreated, respectively (Fig. 4.7). The 10 s periods of domain wall stability were  $\sim 10^3$ -fold longer than the membrane relaxation time constant of  $\sim 10$  ms, demonstrating the quasi-static nature of the electrical patterns. These experiments confirmed the existence of stable domain walls in a nominally homogeneous tissue, a hallmark of spontaneous spatial symmetry breaking.

We confirmed the role of gap junctions in domain wall migration by adding a gap junction blocker 2-aminoethyl diphenylborinate (2-APB, 50  $\mu$ M) to island cultures of bi-HEKs. Before adding the gap junction blocker, a ramp of blue light caused the island to depolarize over a narrow range of blue light levels via domain wall migration, and the membrane potential showed little hysteresis. After adding the blocker, individual cells showed discrete hysteretic switching, each with its own transition points set by the cell-specific expression levels of  $K_{ir2.1}$  and CheRiff (Fig. 4.8). Thus gap

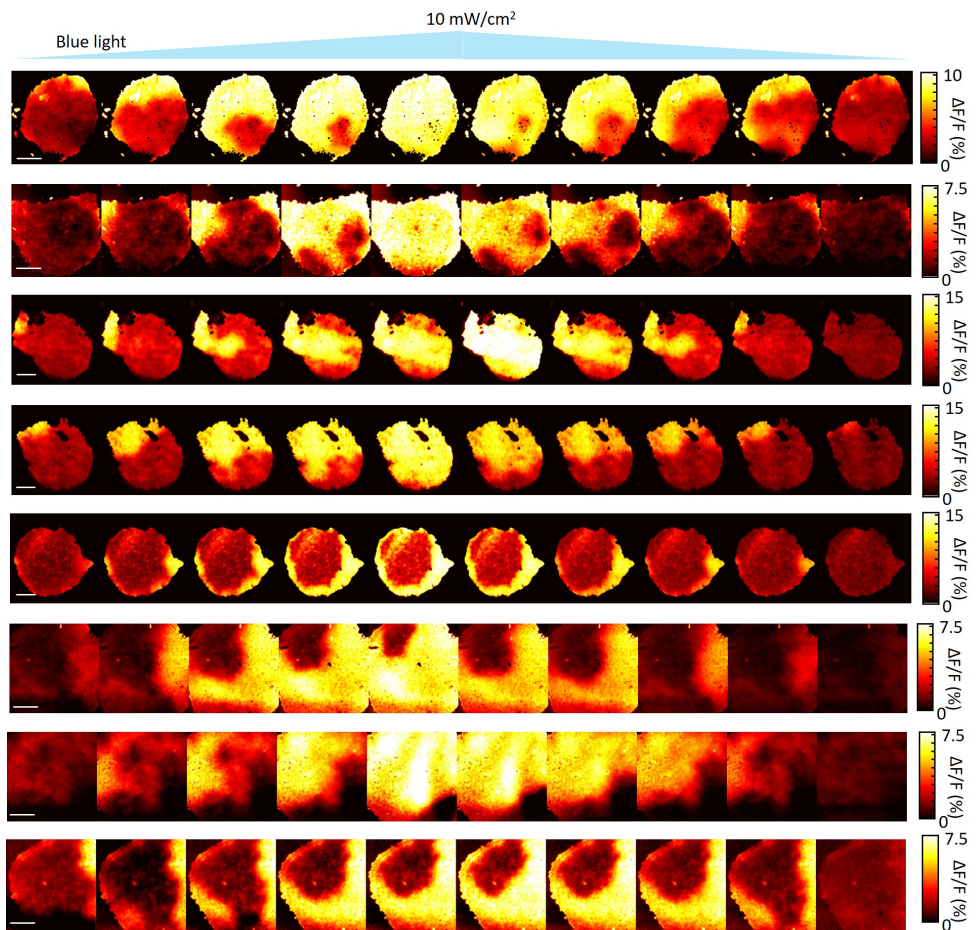


**Figure 4.6: Bioelectrical domain wall formation in eight distinct islands.** Each island showed a unique pattern of domain wall nucleation and growth. In some islands the optogenetic drive was not sufficiently powerful to depolarize the entire island. Scale bars 1 mm.

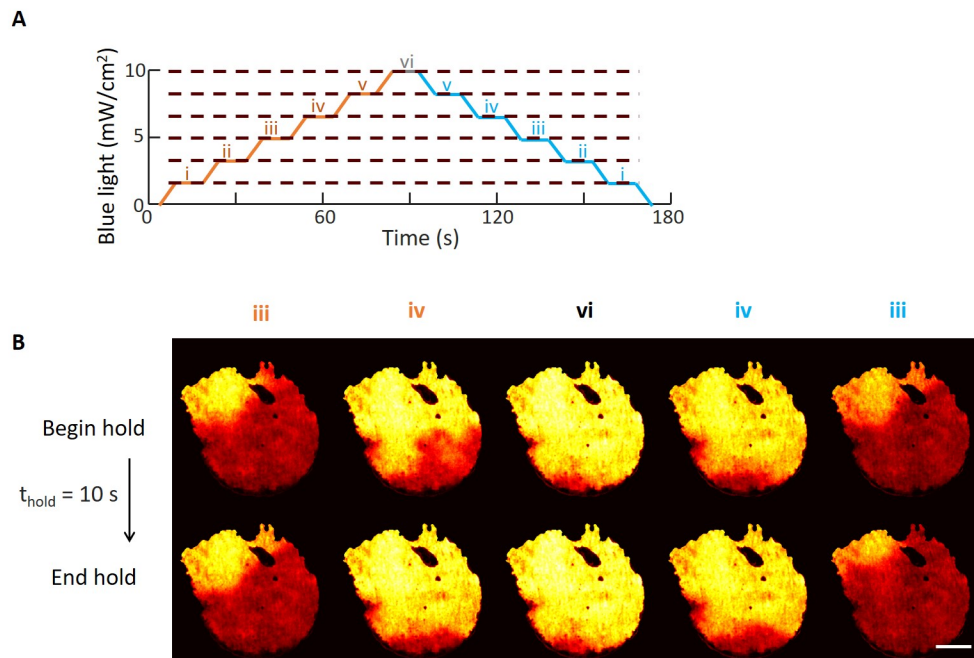


**Figure 4.7: Stability of bioelectrical domain walls.** A) Optogenetic stimulation comprised alternating ramps and 10 s pauses. B) During each pause the domain wall profile remained stable. Slight drifts in domain wall position occurred at the beginning of some hold periods due to slow switching of domains nearly balanced between depolarized and polarized states. Scale bar 1 mm.

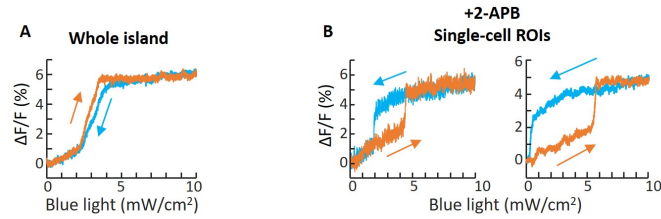


**Figure 4.8: Gap junction blockers convert 2-D behavior in an island to an ensemble of independent 0-D systems.** A) Fluorescence as a function of optogenetic stimulation strength in a confluent island of bi-HEK cells. B) Two single-cell regions from the island after addition of gap junction blocker 2-APB (50  $\mu$ M). Each cell developed a hysteresis loop with transitions set by the local  $K_{ir}2.1$  and CheRiff expression levels.

junctional coupling was necessary for the transition from zero-dimensional to two-dimensional behavior.

#### 4.4 NOISE-INDUCED BREAKUP OF DISCRETE BIOELECTRIC DOMAINS IN A CONTINUOUS TISSUE

No tissue is perfectly uniform, so we explored via simulation tissues with cell-to-cell variations in expression of  $K_{ir}$  or leak. Noisy ion channel expression introduced an effective friction for domain wall motion, stabilizing droplet-like domains of high or low voltage and broadening the transition in tissue-average voltage under a ramp in  $g_I$  (Fig. 4.9). Sufficiently strong heterogeneity led to stick/slip saltatory domain wall motion. The tissue-average voltage then showed Barkhausen-like fine-structure noise (Fig. 4.10). Tissue heterogeneity also restored some degree of hysteresis in the tissue-average voltage, and, when strong enough, broke the tissue into discrete domains that switched independently. The predicted voltage dynamics of coupled cells expressing leak +  $K_{ir}$  thus exhibited many of the features found in magnetization of a disordered soft ferromagnet.<sup>16</sup>

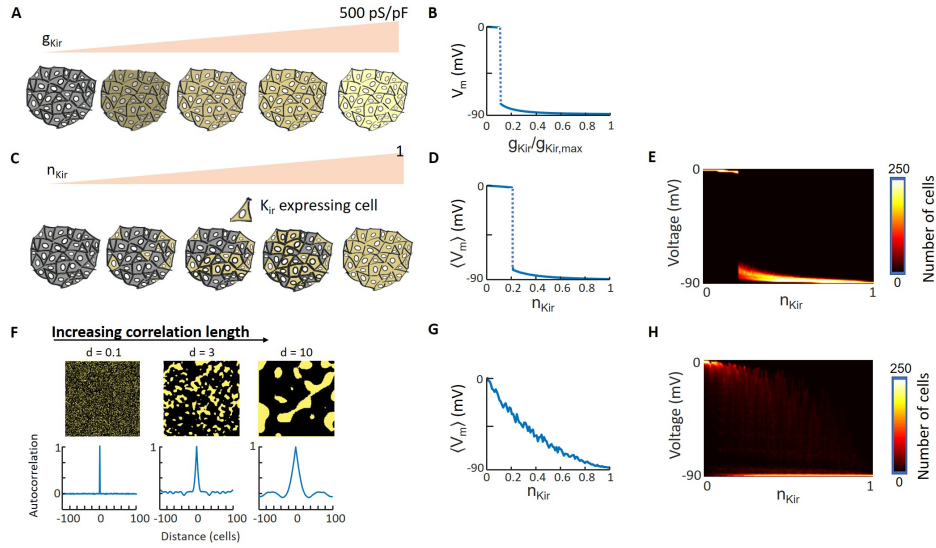


**Figure 4.9: Effect of noisy gene expression on domain wall properties.** A) Cartoon showing a homogeneous tissue with constant leak conductance and gradually increasing  $K_{ir2.1}$  conductance. B) Membrane voltage ( $V_m$ ) as a function of  $g_{K_{ir}}$ . Abrupt polarizing transition arises when  $g_{K_{ir}}$  is sufficient to drive polarized domain wall growth. C) Cartoon showing a heterogeneous tissue where the fraction of cells that express  $K_{ir2.1}$  gradually increases. In this cartoon the probability of expression is independent in each cell. D) As in the homogeneous tissue, at a critical expression density the tissue-average voltage polarizes in a step-wise manner due to domain wall migration. E) Probability distribution of single-cell voltage values as a function of  $n_{K_{ir}}$ . In the heterogeneous tissue, the voltage can vary between cells, though when the size of each cell is much smaller than the domain wall width,  $\lambda \sim \sqrt{(G_{cxn}/g_K)}$ , then the distribution of single-cell voltages is narrowly centered around the mean. F) Introduction of spatially correlated gene expression in models of bi-HEK cells. Top: example images of  $K_{ir2.1}$  expression with different degrees of spatial correlation. Bottom: radially averaged autocorrelation functions of the simulated tissues shown above. G) Tissue-average membrane potential as a function of  $n_{K_{ir}}$  in the case of correlated disorder ( $d = 10$  cells). The step-wise transition to polarization is replaced by a patchwork of polarized and depolarized domains. Changes in  $n_{K_{ir}}$  change the relative populations of these two domains. H) Probability distribution of single-cell voltage values as a function of  $n_{K_{ir}}$  in the tissue simulated in (G).

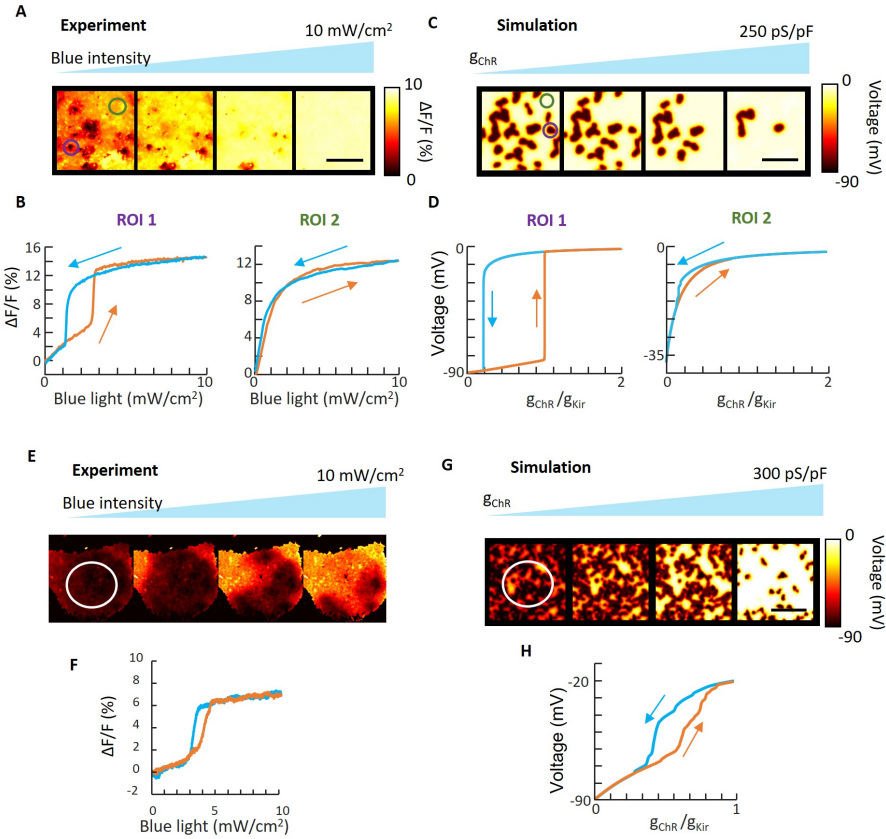


**Figure 4.10: Spatially correlated variability in  $K_{ir}2.1$  expression drives breakup of tissues into discrete domains.** A monoclonal cell line expressing CheRiff only was transfected with plasmid for  $K_{ir}2.1$  and then allowed to grow for 3 days to reach confluence, leading to clusters of correlated expression  $\sim 3$  cells wide. A) Images of fluorescence increase ( $\Delta F/F$ ) in a heterogeneous culture under ramped optogenetic stimulation. Scale bar 1 mm. B) Plots of fluorescence from the two indicated regions of interest (ROIs) in (A). Some ROIs showed hysteresis while others showed smooth and reversible depolarization. C) Frames from a simulation with noisy  $K_{ir}2.1$  expression and ramped optogenetic drive. Scale bar 0.5 mm. D) Regions of the simulation showed ROIs with hysteresis and others without. E) Island of bi-HEK cells driven with a triangle wave of blue light showing depolarization via domain wall migration. F) Fluorescence averaged over the circled region in (E), showing partial hysteresis and Barkhausen-like noise in a disordered sample. G) Simulation of depolarization of a noisy tissue under ramped optogenetic stimulation. H) Mean voltage in the circled region in (G) showing partial hysteresis and Barkhausen-like noise in a disordered sample.

#### 4.5 ELECTRICAL BISTABILITY AND HYSTERESIS DURING MYOGENESIS

Early embryonic tissue has a membrane voltage,  $V_m \sim 0$  mV.<sup>62</sup> During myogenesis, myoblast precursors polarize electrically, exit the cell cycle, and fuse into myocytes whose resting potential is  $\sim -85$  mV.<sup>170</sup> Expression of  $K_{ir2.1}$  initiates this hyperpolarization.<sup>157</sup> In mammals, myoblast precursors couple transiently via gap junctions during differentiation and prior to fusion.<sup>140</sup> We thus hypothesized that bistability and bioelectric domain wall motion might occur during myogenesis.

We performed all-optical electrophysiology experiments in human induced pluripotent stem cell (hiPSC) derived myoblasts as they differentiated into myocyte fibers in vitro (Fig. 4.11a). HiPSC myoblasts were seeded at low density, lentivirally transduced to express CheRiff, and then allowed to proliferate to form a confluent monolayer (Fig. 4.11). The cells were then differentiated into myocytes. After one week of differentiation, cells stained positive for myogenin, PAX7, and myosin heavy chain, and adopted an elongated fiber-like morphology, indicative of differentiation toward mature myocytes (Fig. 4.11b). RNAseq measurements on matched samples showed a significant increase in  $K_{ir2.1}$  expression during the differentiation process (5.6-fold,  $p < 0.001$ ) and high expression of gap junction proteins Cx43 and Cx45 throughout. We performed voltage imaging under ramped wide-field optogenetic stimulation at two time-points during differentiation to test for signatures of electrical bistability in isolated cells and domain wall motion in confluent cultures.

In myoblast precursors that had not yet reached confluence (day 3), we observed heterogeneous responses to ramped optogenetic stimulation: Cells showed either a smooth response with saturation-like behavior and little hysteresis (67%, 34 of 51, Fig. 4.11c left) or a step-wise depolarization, which did not reverse upon cessation of the optogenetic stimulus (33%, 17 of 51, Fig. 4.11c middle). In immature myocytes mechanically dissociated from a confluent culture (day 6, 3 days after start of differentiation), we observed sub-populations with behavior similar to day 3 (smooth depolarization with no hysteresis: 47%, 42 of 89; step-wise, irreversible depolarization: 29%, 26 of 89). We also

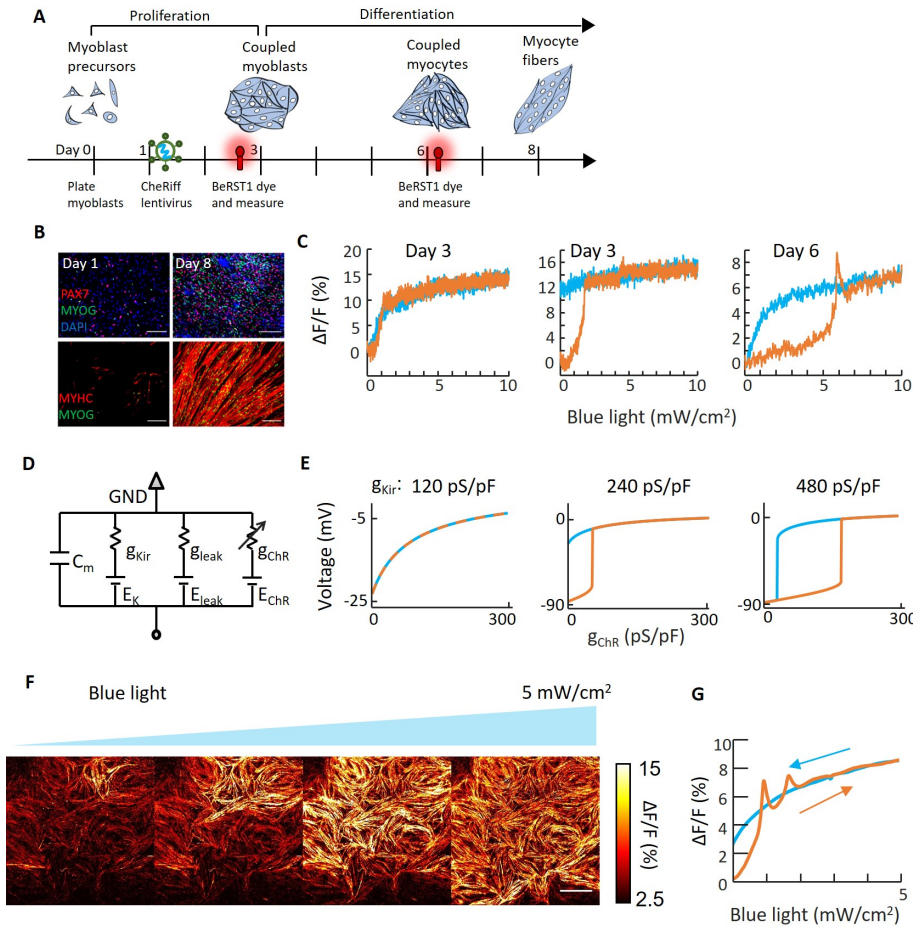


**Figure 4.11: Bioelectric domain wall propagation in stem cell-derived myocytes.** A) Timeline for differentiation, viral transduction, and measurement. B) Immunocytochemistry staining of myocyte cultures during differentiation. Stains show PAX7, myogenin (MYOG), and myosin heavy chain (MYHC). Scale bars 200  $\mu\text{m}$ . C) Optical measurements of membrane potential in individual isolated myoblasts at different times after differentiation. D) Simple electrical circuit model for myoblasts. The  $K_{ir}$  channel was modeled as a nonlinear conductance, the leak was treated as Ohmic with  $E_{leak} = -20$  mV, and the channelrhodopsin was treated as Ohmic with  $E_{ChR} = 0$  mV. E) Simulations of optogenetically induced changes in membrane voltage at different values of  $g_{K_{ir}}$ . All other parameters of the simulation were kept constant between the three panels. F) Bioelectrical domain wall migration in a monolayer of electrically coupled myocytes (measured 3 days after start of differentiation). Scale bar 1 mm. G) Optical measurements of membrane voltage as a function of optogenetic stimulus strength in the confluent culture. Depolarization-activated inward currents led to spikes atop the optogenetically induced depolarizations.

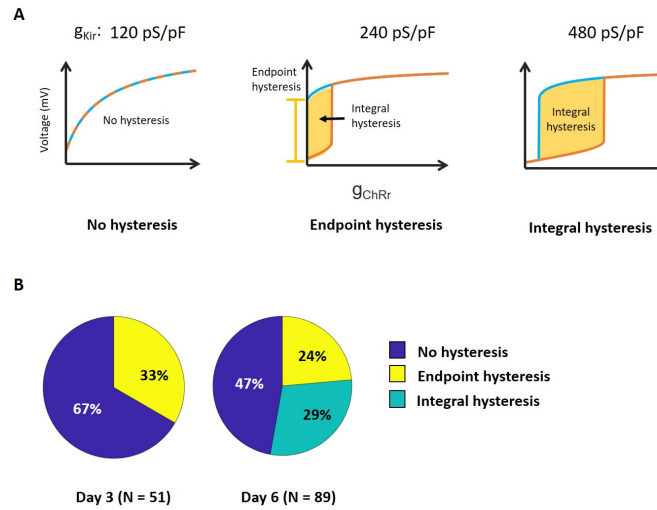


**Figure 4.12: Electrophysiological phenotypes in immature isolated myocytes.** A) Definition of electrophysiological classes showing “No hysteresis”, “Endpoint hysteresis” and “Integral hysteresis.” The plots show numerical simulations of the  $K_{ir}$  + leak + ChR model with increasing levels of  $K_{ir}$  and all other parameters held constant. B) Distribution of phenotypes by day of measurement.

observed a new sub-population comprising cells with closed hysteresis loops that resembled the bi-HEKs (24%, 21 of 89, Fig. 4.11C right, Fig. 4.12).

These three seemingly disparate behaviors could all be explained by a simple model containing a leak, a channelrhodopsin, and  $K_{ir}$  expression which increased on average between day 3 and 6 (Fig. 4.11D, Fig. 4.12). At the lowest  $K_{ir}$  level, the  $I-V$  curve was monotonically increasing, so channelrhodopsin activation shifted a single stable voltage fixed point along the  $I = 0$  axis. This led to a continuous and reversible change in voltage (Fig. 4.11E). At intermediate  $K_{ir}$  level, the  $I-V$  curve was N-shaped and crossed the  $I=0$  axis three times in the absence of channelrhodopsin activation. Blue light drove step-wise depolarization via a saddle node bifurcation. The depolarized state remained stable in the absence of optogenetic drive, leading to non-recovering depolarization. At the highest  $K_{ir}$  level, the hysteresis curve shifted to the right and the cells repolarized in the absence of

optogenetic drive. Thus, a simple model with one tuning parameter captured the three qualitatively distinct single-cell responses to channelrhodopsin activation.

In confluent monolayers at day 6, we used patterned optogenetic stimulation to excite a portion of the tissue. The evoked action potentials propagated beyond the stimulated region, confirming the presence of gap junctional electrical coupling (Fig. 4.13). Under spatially homogeneous ramped optogenetic stimulation, we observed optogenetically induced domain wall propagation (Fig. 4.11f). The presence of domain wall propagation was surprising, considering that only a minority (24%) of the isolated cells were bistable. Simulations showed that due to strong electrotonic coupling, the global behavior of a tissue could be dominated by a minority of cells expressing  $K_{ir2.1}$  (Fig. 4.9). As in the bi-HEKs, the whole-tissue average voltage showed little hysteresis as a function of optogenetic drive (Fig. 4.11g), consistent with depolarization via domain wall migration. These observations show that differentiating myoblasts exhibit electrical bistability when isolated and collective domain wall migration during an essential step of myogenesis.

In contrast to the bi-HEK cells, the myoblasts also supported propagation of regenerative action potential waves. These waves manifested as spikes in the whole-tissue fluorescence during a gradual optogenetic depolarization (Fig. 4.11g). The additional depolarizing drive associated with these spikes caused the waves to propagate rapidly across the tissue, without disruption from the defects which could pin the motion of domain walls.

## 4.6 CONCLUSIONS

In vitro, muscle cells must be aggregated to differentiate, a phenomenon called the “community effect.”<sup>113</sup> Our results show that electrical coupling can mediate community effects, i.e. that the collective electrical dynamics of coupled cells can be strikingly different from the individuals, even if all cells are identical. Domain wall migration mediates polarization in extended tissues, whereas iso-

Blue intensity

10 mW/cm<sup>2</sup>

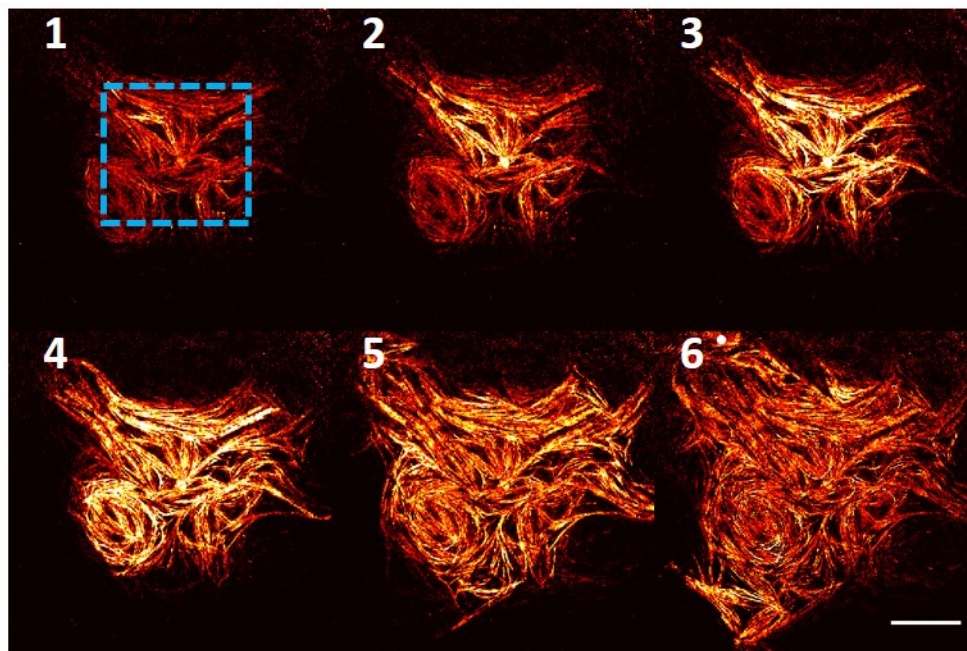


**Figure 4.13: Gap junction coupling in confluent cultures of immature myocytes.** A) Image of the myocyte culture showing region of cells stimulated with blue light. B) Fluorescence of BeRST1 indicating electrical depolarization as a function of optogenetic stimulus strength. Propagation of the depolarization to cells outside the stimulated region establishes the presence of gap junction-mediated electrical coupling in the culture. Scale bars 1 mm.

lated cells or small clumps must polarize all at once. Consequently, under ramped  $K_{ir2.1}$  expression, an electrically coupled, extended tissue will polarize before an isolated cell or small patch, even if all other conditions are identical.  $K_{ir2.1}$  expression is required for the expression of the myogenic transcription factors Myogenin (MyoG) and Myocyte Enhancer Factor-2 (MEF2).<sup>157</sup> Disruption of gap junction coupling is sufficient to disrupt myogenesis.<sup>224</sup> Together, these observations suggest that bioelectric domain walls might play a functionally important role in myogenesis. This prediction merits further mechanistic tests in cultured myocytes and *in vivo*. It will be interesting to relate the bioelectrical response properties of developing muscle to the shifts that occur as myocytes fuse and gap junctional coupling diminishes during maturation.

Many combinations of ion channels can produce N-shaped  $I-V$  curves and thereby mediate electrical bistability. For instance, the combination of a  $K^+$ -selective leak current and the steady-state window current of T-type  $CaV$  channels mediates plateau potentials in thalamocortical neurons.<sup>63,126</sup> In this case, one would expect electrical bistability to be accompanied by bistability in intracellular  $Ca^{2+}$  concentration, which might then couple to downstream biochemical or genetic signaling pathways.

The combination of a persistent voltage-gated sodium current and a  $K^+$ -selective leak current can also drive bistability. Persistent  $NaV$  currents have been observed in striated cardiac and skeletal muscle and in many types of mammalian neurons.<sup>60</sup> Persistent sodium and persistent L-type calcium currents contribute to sustained activation in a spinal cord injury model.<sup>167</sup> Finally, persistent sodium currents are thought to play a role in propagating and amplifying the influence of distal synaptic inputs during dendritic integration.<sup>238</sup> In principle, any of these bistable scenarios could produce bioelectrical domain walls in electrotonically extended systems, though we are not aware of any such direct observations.

Gap junctions are necessary for proper formation of many tissues during development, including in heart, liver, skin, hair, cartilage, bone, and kidney,<sup>56,166</sup> though the physiological roles of these gap

junctions remain unclear. Our work suggests that gap junction-mediated bioelectrical domain wall motion may be an important feature in some of these systems. For instance, chondrocytes express  $K_{ir}$  channels<sup>190</sup>, gap junctions<sup>17</sup>, and the ionotropic serotonin receptor 5-HT<sub>3A</sub><sup>251</sup> which is a nonselective cation channel electrically similar to channelrhodopsin. These conditions suggest that the ingredients are present for regulation of membrane potential via domain wall migration. Wounding in endothelial monolayers has been shown to induce slowly migrating zones of depolarization<sup>50</sup>, suggesting that these cells might also support bioelectrical domain walls. The presence of long-lived electrical bistability in tissues could provide a means to couple bioelectric patterns to biochemical and genetic signaling networks.<sup>41,165,220</sup> The shape of the I-V curve in our experiments is qualitatively captured by a cubic (Fitzhugh Nagumo-type) nonlinearity.<sup>94,200</sup> Models of this sort have been applied to describe similar dynamics (zero-dimensional hysteresis, domain nucleation, growth and disorder-driven breakup) in magnetic domain reversals in ferromagnets,<sup>212</sup> in the spread of forest fires,<sup>284</sup> in phase transitions,<sup>20</sup> and in expanding species ranges with a strong Allee effect.<sup>5</sup> Spontaneous spatial symmetry breaking and pattern formation are well established in neural field theories<sup>57</sup> and in models of cardiac arrhythmias.<sup>80,241</sup> In these systems, however, the membrane voltage varies with time, i.e. the systems are described by the lower right quadrant of Fig. 4.1b. Our work shows that the reaction-diffusion formalism can be applied to purely spatial symmetry breaking in electrophysiology.

In the Turing model, formation of quasi-periodic patterns requires interaction of two or more morphogens, often described as an activator and an inhibitor. The Hodgkin-Huxley equations describe the dynamics of voltage, a scalar quantity. The spatial symmetry breaking studied in this report does not constitute a classical Turing pattern, in that voltage is only a one-dimensional state variable. As a result, the patterns of membrane voltage did not have a characteristic finite spatial frequency. To achieve a classical Turing-like pattern would require coupling of voltage to another diffusible species, e.g.  $Ca^{2+}$ . It is not known whether classical Turing-like patterns of membrane

voltage can be created.

## 4.7 METHODOLOGY

### 4.7.1 EXPERIMENTAL DESIGN

The goal of this study was to discover and characterize bioelectrical domain walls: electrophysiological entities through which tissues can mediate long-range electrical signaling without using action potentials. We modeled electrically bistable cells as a one-component reaction-diffusion system with a bistable electrical nonlinearity. The nonlinear I-V curve was composed of an inward-rectifying potassium conductance ( $K_{ir2.1}$ ) and an Ohmic leak conductance with reversal potential near 0 mV.

To explore bioelectrical domain walls experimentally, we generated an engineered electrically bistable HEK cell line (bi-HEKs) which expressed  $K_{ir2.1}$  and light-gated channelrhodopsin leak conductance. To probe for domain wall formation in a physiological system we studied the electrophysiology of myocytes during differentiation. We chose this system because myoblast precursors gradually express an inward rectifying potassium conductance during differentiation, and myocyte differentiation requires spatial coupling between myoblast precursors. Myogenesis therefore offered a plausible physiological system in which to observe bioelectrical domain wall formation.

### 4.7.2 NUMERICAL MODELING OF ELECTRICALLY BISTABLE CELLS AND TISSUES

In the conductance-based model, the voltage dynamics are governed by the equation:

$$C_m \frac{\partial V}{\partial t} = G_{cxn} \nabla^2 V - (I_{K_{ir}} + I_{leak} + I_{ChR}) \quad (4.8)$$

The gap junction sheet conductance is defined as  $G_{cxn} = g_{cxn} \times l$ , where  $g_{cxn}$  is the gap junction conductance between adjacent cells, and  $l$  is the linear dimension of a cell. If  $g_{cxn}$  is measured as an

areal conductance ( $S/m^2$ ), then the units of  $G_{cxn}$  are S (i.e. sheet conductance, which has no spatial dimension). If  $C_m$  is measured as an areal capacitance ( $F/m^2$ ), then the ratio  $G_{cxn}/C_m$  has units of a diffusion coefficient ( $m^2/s$ ), making explicit the connection between the Hodgkin-Huxley equations and the reaction-diffusion equation.

For convenience in simulations, units of space were  $10 \mu m$  (corresponding to linear size of one cell), units of time were ms, and units of voltage were mV. We assumed the capacitance of a cell was 10 pF. Conductances were measured in nS/pF, ionic currents in pA/pF, and voltage in mV. Parameters used in all simulations are given in the tables following this section.

Simulations were run in Matlab using custom software. Single-cell voltages in oD were determined by finding fixed points of cell-autonomous current-voltage curves. Extended tissues were numerically simulated as two-dimensional grids of  $100 \times 100$  cells with periodic boundary conditions and one grid-point per cell. Simulations and experiments thus had similar spatial scales. For simulations of nucleation events in homogenous tissues (Fig. 4.4b),  $300 \times 300$  cell grids with no-flux boundary conditions were implemented to match experimental conditions. The discrete Laplacian was implemented using the MATLAB `delz` function (with default spacing) and solutions were time-integrated using Euler's method with 10 kHz sampling.

The inward rectifying potassium current from  $K_{ir2.1}$  was based on a model from ten Tusscher et al.<sup>252</sup> as:

$$I_K = g_K x_{K\infty}(V)(V - E_k) \quad (4.9)$$

with reversal potential at  $E_K = -90$  mV. The parameter  $x_{K\infty}(V)$  is a time-independent rectification factor that depends on voltage, with the following form:

$$x_{K\infty} = x_0 \frac{\alpha_K}{\alpha_K + \beta_K} \quad (4.10)$$

$$\alpha_K = \frac{0.1}{1 + e^{0.06(V-E_K-200)}} \quad (4.11)$$

$$\beta_K = \frac{3e^{0.0002(V-E_K+100)} + e^{0.1(V-E_K-10)}}{1 + e^{-0.5(V-E_K)}} \quad (4.12)$$

The scaling factor  $x_0 = 100$  was introduced to make  $x_{K_\infty}$  of order unity between -90 and -60 mV. In our simulations the conductance magnitude  $g_K$  was the only parameter varied to mimic changes in expression of  $K_{ir2.1}$ . The variable leak was modeled as an Ohmic conductance with reversal potential 0 mV. For homogeneous tissues all cells had identical  $K_{ir2.1}$  and leak conductances.

To introduce disorder into the tissue, a fraction  $n_K$  of the cells were randomly assigned to express  $K_{ir2.1}$  (all with conductance  $g_K$ ) while the remaining cells had no  $K_{ir2.1}$  expression (Figure 4.9, 4.10). Spatial correlations in  $K_{ir2.1}$  expression were introduced by assigning a random number to each cell, independently sampled from a uniform distribution on  $[0, 1]$ . The values were then smoothed with a two-dimensional Gaussian kernel of width  $d$ . A threshold was selected so that a fraction  $n_K$  of the cells were above threshold. These cells were assigned to express  $K_{ir2.1}$  with conductance  $g_K$  and cells below threshold did not express. The extent of the spatial correlations was tuned by varying  $d$ . In the simulation for Fig. 4.10h,  $K_{ir2.1}$  and CheRiff expression were heterogeneous, and independent of each other. The distribution of CheRiff expression was calculated following the same procedure as for  $K_{ir2.1}$ , using the same smoothing parameter,  $d$ , but different thresholds  $n_K$ , and  $n_{ChR}$ .

Cells in simulated tissues were first initialized to their cell-autonomous resting potential, i.e. the resting potential in the absence of influences from the neighbors. Bistable cells were initialized to the fixed point which had the greater area under the curve between it and the unstable fixed point. Tissues were then time-evolved to generate an initial steady state voltage profile. To simulate bioelectrical dynamics under changes in parameters, conductances were gradually changed over timescales

Parameter	Explanation
$C_m = 10 \text{ pF}$	Single cell capacitance
$l = 10 \text{ } \mu\text{m}$	Size of an individual cell; discretization size of simulated tissues
$E_K = -90 \text{ mV}$	Potassium reversal potential
$E_{ChR} = 0 \text{ mV}$	Channelrhodopsin reversal potential
$E_{leak} = -20 \text{ mV}$	Additional leakage reversal potential. Used for myocyte models (Fig. 4.11) and for domain model (Fig. 4.10).
$G_{cxn} = 2 \text{ nS/pF} \times l^2$ $= 200 \text{ (nS/pF)} \times \mu\text{m}^2$	Strength of gap junction coupling between bi-HEK cells
$n_{K_{ir}} = 0 \text{ to } 1$	Proportion of cells initialized to express $K_{ir2.1}$ .
$n_{ChR} = 0.75 \text{ to } 1$	Proportion of cells initialized to express CheRiff. Expression is uniform ( $n_{ChR} = 1$ ) in all panels except for Fig. 4.10h (in which $n_{ChR} = 0.75$ ).
$d = 0.001 \text{ to } 10 \text{ cells}$	Width of gaussian smoothing kernel used to introduce spatial correlations in $K_{ir2.1}$ expression
$g_K = 0 \text{ to } 500 \text{ pS/pF}$	$K_{ir2.1}$ conductance. This conductance is multiplied by the inward rectifying function $x_{K_{\infty}}$ .
$x_o = 100$	Scaling factor to set $x_{K_{\infty}}$ to order unity between $E_K$ and the point of maximum outward current ( $V_{max} \sim -69 \text{ mV}$ ).
$g_{ChR} = 0 \text{ to } 100 \text{ pS/pF}$	Conductance of the channelrhodopsin CheRiff. Varied continuously in simulations of blue light intensity ramps.
$g_{leak} = 5 \text{ pS/pF}$	Additional leak conductance added to myocyte model.

**Table 4.1:** Default model parameters and definitions

slower than any of the internal relaxation dynamics. For simulations of domain boundary velocities in homogeneous tissues with bistable I-V curves (Fig. 4.5), the left half of the tissue was initialized in a depolarized state and the right half in a hyperpolarized state.

#### 4.7.3 BI-HEK CELL GENERATION AND CULTURE

Genetic constructs encoding the inward rectifying potassium channel  $K_{ir2.1}$  and the blue-shifted channelrhodopsin CheRiff were separately cloned into lentiviral expression backbones (FCK-CMV) and then co-expressed in HEK 293T cells along with the lentiviral packaging plasmid PsPAX2 (Ad-

Figure panel	Parameters
4.2c	$g_{ChR} = 50 \text{ pS/pF}, g_K = 200 \text{ pS/pF}$
4.4a	$g_{ChR} = 50 \text{ pS/pF}, g_K = 200 \text{ pS/pF}, n_{K_{ir}} = 1$
4.4b, top	$g_{ChR} = 70 \text{ pS/pF}, g_K = 200 \text{ pS/pF}, n_{K_{ir}} = 1$
4.4b, bot	$g_{ChR} = 60 \text{ pS/pF}, g_K = 200 \text{ pS/pF}, n_{K_{ir}} = 1$
4.4c	$g_{ChR} = 1 \text{ to } 200 \text{ pS/pF}, g_K = 200 \text{ pS/pF}, n_{K_{ir}} = 1$
4.11e	$g_{leak} = 100 \text{ pS/pF}, g_{ChR} = 0.1 \text{ to } 300 \text{ pS/pF}$ (ramped) $g_K = 120, 240, 480 \text{ pS/pF}$ (left, middle, and right panels)
4.5b	$g_{ChR} = 24.5 \text{ pS/pF}, g_K = 60, 72.5, 85, 97.5 \text{ pS/pF}$ (top to bottom)
4.5c	$g_{ChR} = 22 \text{ pS/pF}, n_{K_{ir}} = 1$
4.9b	$g_{ChR} = 20 \text{ pS/pF}, g_K = 1 \text{ to } 500 \text{ pS/pF}, n_{K_{ir}} = 1$
4.9d,e	$g_{ChR} = 20 \text{ pS/pF}, g_K = 1 \text{ to } 500 \text{ pS/pF},$ $n_{K_{ir}} = 0 \text{ to } 1, d = 0.001$
4.9g,h	$g_{ChR} = 20 \text{ pS/pF}, g_K = 1 \text{ to } 500 \text{ pS/pF},$ $n_{K_{ir}} = 0 \text{ to } 1, d = 10$
4.10c,d	$g_{ChR} = 0 \text{ to } 250 \text{ pS/pF}, g_K = 50 \text{ pS/pF}, g_{leak} = 20 \text{ pS/pF}, E_{leak} = -20 \text{ mV}$ $n_{K_{ir}} = 0.5, d = 3$
4.10g,h	$g_{ChR} = 1 \text{ to } 300 \text{ pS/pF}, g_K = 600 \text{ pS/pF},$ $n_{K_{ir}} = 0.5, n_{ChR} = 0.75, d = 1.5$
4.12a	$g_{leak} = 100 \text{ pS/pF}, g_{ChR} = 0.1 \text{ to } 300 \text{ pS/pF}$ (ramped) $g_K = 120, 240, 480 \text{ pS/pF}$ (left, middle, and right panels)

**Table 4.2:** Model parameters associated with specific figure panels

dgene) and the envelope plasmid VsVg (Addgene) via polyethylenimine transfection (Sigma). Lentiviral particles were harvested at 36 and 72 hours post-transfection, and then concentrated 20-fold using the Lenti-X concentrator system (Takara).

For experiments where nominally homogeneous expression was the goal (Figs. 4.2,4.4), HEK cells were incubated with both Kir2.1 and CheRiff lentiviral vectors for 48 hours prior to measurement, and then passaged and replated onto poly-D-lysine coated glass-bottom tissue culture dishes (MatTek). For patch clamp measurements (Fig. 4.3), bi-HEKs were plated sparsely onto Matrigel coated dishes. For wide-field measurements (Fig. 4.4), adhesive islands were prepared by manually spotting poly-d-lysine onto MatTek plates. Bi-HEKs were plated onto these plates to create confluent patches of cells approximately 2 mm in diameter.

For experiments where disordered expression was the goal (Fig. 4.10), Kir2.1 and CheRiff constructs were transiently expressed (using Mirus 293T) in HEK cells which were then grown to confluence for an additional 72 hours prior to measurement. High-disorder samples were not replated prior to measurement.

#### 4.7.4 HiPSC MYOBLAST AND MYOCYTE DIFFERENTIATION

HiPSC-derived myoblasts were differentiated into myocyte fibers according to an established serum-free differentiation protocol.<sup>43</sup> Briefly, 3-4 weeks old primary myogenic cultures generated from wild-type hiPSCs were dissociated as described and myogenic progenitors (myoblasts) were replated at low density (35-40k/cm<sup>2</sup>) onto Matrigel (Corning, Cat#354277)-coated dishes in skeletal muscle growth media (SKGM-2, Lonza CC-3245) with 10  $\mu$ M ROCK inhibitor.<sup>43</sup> After 24 hours, medium was changed to SKGM-2 media without ROCK inhibitor and incubated with low-titer lentivirus encoding CheRiff-CFP. Myoblast cultures were proliferated for up to 72 hours, at which point cultures reached  $\sim$  90% confluence. Cultures were then induced for myogenic differentiation with DMEM/F12 supplemented with 2% knock-out serum replacement (Invitrogen, Cat. # 10828028), 10

$\mu$ M of the TGF $\beta$  inhibitor SB431542 (Tocris, Cat. # 1614), 1  $\mu$ M Chiron (Tocris, Cat. # 4423), 0.2% Pen/Strep (Life Technologies, Cat. # 15140122) and 1x ITS (Life Technologies, Cat. # 41400045).<sup>43</sup> Following induction, medium was changed on days 1 and 2 and then was refreshed every other day for up to 10 days post-differentiation to generate mature and fused myocyte fibers. Samples were measured between 0 and 3 days after start of differentiation (i.e., after 3 and 6 days in culture).

#### 4.7.5 IMMUNOSTAINING AND IMAGING

Human iPSC-derived myocyte cultures were fixed for 20 minutes in 4% formaldehyde. Cultures were rinsed three times in phosphate-buffered saline (PBS), followed by blocking buffer composed of PBS supplemented with 10% fetal bovine serum (FBS) and 0.1% Triton X-100. Primary antibodies were then diluted in blocking buffer and incubated overnight at 4 °C. Cultures were then washed three times with PBST (PBS supplemented with 0.5% Tween-20) and incubated with secondary antibodies conjugated with an AlexaFluor dye (Molecular probes) and DAPI (5  $\mu$ g/mL) in blocking buffer for 2 h at room temperature. Cultures were washed with PBST followed by PBS, followed by imaging. Antibodies were: anti-PAX7 (Developmental Studies Hybridoma Bank, DSHB), anti-Myogenin (Santa Cruz, SC-576X) and embryonic anti-MyHC (DSHB, F1.652).

#### TRANSCRIPTOMIC PROFILING: LIBRARY PREPARATION AND SEQUENCING

RNA was extracted from cells using Trizol (Invitrogen) or with the RNeasy Mini Kit (Qiagen). Libraries were prepared using Roche Kapa mRNA HyperPrep sample preparation kits from 100 ng of purified total RNA according to the manufacturer's protocol. The finished dsDNA libraries were quantified by Qubit fluorometer, Agilent TapeStation 2200, and RT-qPCR using the Kapa Biosystems library quantification kit according to manufacturer's protocols. Uniquely indexed libraries were pooled in equimolar ratios and sequenced on two Illumina NextSeq500 runs with single-end

75bp reads by the Dana-Farber Cancer Institute Molecular Biology Core Facilities.

#### 4.7.6 TRANSCRIPTOMIC PROFILING: RNASEQ ANALYSIS

Sequenced reads were aligned to the UCSC hg19 reference genome assembly and gene counts were quantified using STAR (v2.5.1b).<sup>73</sup> Differential gene expression testing was performed by DESeq2 (v1.10.1)<sup>173</sup> and normalized read counts (FPKM) were calculated using cufflinks (v2.2.1).<sup>259</sup> RNAseq analysis was performed using the VIPER snakemake pipeline.<sup>58</sup>

#### 4.7.7 PATCH CLAMP AND ALL-OPTICAL ELECTROPHYSIOLOGY

All electrophysiological measurements were performed in Tyrode's solution, containing (in mM) 125 NaCl, 2 KCl, 2 CaCl<sub>2</sub>, 1 MgCl<sub>2</sub>, 10 HEPES, 30 glucose. The pH was adjusted to 7.3 with NaOH and the osmolality was adjusted to 305–310 mOsm with sucrose. Prior to measurements, 35-mm dishes were washed twice with 1 mL phosphate-buffered saline (PBS) to remove residual culture media, then filled with 2 mL Tyrode's solution.

For patch clamp measurements, filamented glass micropipettes (WPI) were pulled to a resistance of 5–10 M $\Omega$  and filled with internal solution containing (in mM) 140 KCl, 1 MgCl<sub>2</sub>, 10 EGTA, 10 HEPES, 3 Mg-ATP, pH adjusted to 7.3 with KOH. The patch electrode was controlled via a low-noise patch clamp amplifier (A-M Systems, model 2400). Voltage traces were collected under  $I = 0$  current clamp mode, and current traces were collected in voltage clamp mode. Blue light for optical stimulation (Coherent Obis 488 nm) was modulated using an acousto-optic tunable filter (Gooch and Housego GH18A series). Patch clamp measurements were performed on small clusters of cells (approximately 6 cells).

Spatially resolved optical electrophysiology measurements were performed using a home-built upright ultra-widefield microscope<sup>271</sup> with a large field of view (4.6x4.6 mm<sup>2</sup>, with 2.25x2.25  $\mu$ m<sup>2</sup>

pixel size) and high numerical aperture objective lens (Olympus MVPLAPO 2XC, NA 0.5). Fluorescence of BeRST<sub>1</sub> was excited with a 639 nm laser (OptoEngine MLL-FN-639) at 100 mW/cm<sup>2</sup>, illuminating the sample from below at an oblique angle to minimize background autofluorescence. BeRST<sub>1</sub> fluorescence was separated from scattered laser excitation via a dichroic beam splitter (Semrock Dior-R405/488/561/635-t3-60x85) and an emission filter (Semrock FFO1-708/75-60-D). Images were collected at 100 Hz frame rate on a Hamamatsu Orca Flash 4.2 scientific CMOS camera. Optogenetic stimulation was performed by exciting CheRiff with a blue LED (Thorlabs M470L3) with a maximum intensity of at 10 mW/cm<sup>2</sup>.

Prior to measurement, cells were incubated with 1  $\mu$ M BeRST<sub>1</sub> dye in phosphate buffered saline for 30 minutes in a tissue culture incubator. Samples were then washed and prepared in Tyrode's solution immediately before imaging.

#### 4.7.8 DATA ANALYSIS AND IMAGE PROCESSING

Optical recordings of voltage-sensitive BeRST<sub>1</sub> fluorescence were acquired for isolated cells, small clusters of cells (4-12 cells), and extended tissues (>2 mm linear size). Recordings were processed using custom MATLAB software. Briefly, to minimize uncorrelated shot-noise, movies were subjected to 4x4 binning, followed by pixel-by-pixel median filtering in the time domain (9 frame kernel). A background signal was calculated from a cell-free region of the field of view and subtracted from the region containing the cells. Mean sample images were generated by measuring the average fluorescence of the tissue prior to optogenetic stimulation. Functional recordings were divided pixel-wise by this baseline to generate movies of  $\Delta F/F$ . Plots of voltage-dependent fluorescence were generated by averaging the time-lapse movies over the relevant region of interest (e.g. small clusters for oD data; localized spots within extended cell culture islands for 2D local measurements; and over entire cell culture islands for 2D mean measurements).

#### 4.7.9 STATISTICAL ANALYSIS

Statistical analysis was performed on optical electrophysiology recordings from immature myocyte precursors to assess the significance of population-level differences in electrophysiological phenotypes at different time points. Measurements were performed on populations of isolated cells taken at 3 and 6 days in culture (see hiPSC myoblast and myocyte differentiation methods above). Fluorescent recordings of voltage were acquired for 100 ms prior to illumination, during a 40 s ramp of blue light (increasing from 0 to 10 mW/cm<sup>2</sup> for 20 s, then decreasing for 20 s), and then for 5 s after the blue light was turned off. Raw acquisitions were converted to  $\Delta F/F$  for further analysis.

Electrophysiological phenotypes were parameterized by calculating the total endpoint hysteresis and the mean integral hysteresis for each identified cell (Fig. 4.12). Endpoint hysteresis was defined as the difference in  $\Delta F/F$  between the 5 s at the end of the acquisition and the 100 ms at the start of the acquisition. Integral hysteresis was defined as the difference between the mean  $\Delta F/F$  over the decreasing phase of the blue light ramp and the mean  $\Delta F/F$  during the increasing phase of the blue light ramp (each averaged over the corresponding full 20 s ramp).

In each sample, individual cells which responded to CheRiff stimulation were first manually identified via an overall mean  $\Delta F/F$  image. 51 and 89 cells were identified in the day 3 and day 6 measurements, respectively. Endpoint hysteresis and mean hysteresis were then calculated for each identified cell, and a cell was sorted as hysteresis-positive if it demonstrated a value greater than 0.3 for either measure (Figure S4). Cells which showed endpoint hysteresis  $> 0.3$  were sorted into the endpoint hysteresis cluster, regardless of their integral hysteresis value. Cells with integral hysteresis  $> 0.3$  and endpoint hysteresis  $< 0.3$  were sorted into the integral hysteresis cluster. Statistical errors were estimated as the standard deviation from a binomial distribution; i.e.,

$$\sigma = \sqrt{Np(1-p)} \quad (4.13)$$

The significance of population level phenotypes was assessed via paired two-sample t-tests using standard MATLAB functions (`ttest2`). Smooth depolarizations without hysteresis were observed on day 3 in 34 of 51 cells and on day 6 in 42 of 89 cells, a significant decrease ( $p = 0.026$ ). Endpoint hysteresis was observed on day 3 in 17 of 51 cells and on day 6 in 26 of 89, not a significant difference ( $p = 0.61$ ). Integral hysteresis was observed on day 3 in 0 of 51 cells and on day 6 in 21 of 89 cells ( $p < 0.001$ ).

#### 4.8 PUBLICATION INFORMATION

A version of this chapter appeared previously as: McNamara, H.M., Salegame, R., Al Tanoury, Z., Xu, H., Begum, S., Ortiz, G., Pourquie, O. and Cohen, A.E., 2019. Bioelectrical signaling via domain wall migration. *bioRxiv*, p.570440. <sup>185</sup>

#### 4.9 CONTRIBUTIONS

Adam Cohena and I conceived and designed the study. I conducted experiments and analyzed results, with assistance from Rajath Salegame, Haitan Xu, and Shahinoor Begum. I designed and simulated numerical models of electrically bistable cells. Ziad Al-Tanoury and Olivier Pourquie provided hiPSC-derived myoblasts for myocyte differentiation and characterized these cells via immunocytochemistry and RNAseq. Gloria Ortiz provided BeRSTi dye reagent. Adam Cohen and I wrote the manuscript, with input from Ziad Al-Tanoury and Olivier Pourquie. Adam Cohen and Olivier Pourquie oversaw the research.

We thank Urs Boehm, Amanda Klaeger, Juanita Mathews, and Michael Levin for helpful discussions. We thank Evan Miller for help providing the BeRSTi dye. This work was supported by the Allen Discovery Center at Tufts University, the Vannevar Bush Fellowship Foundation, and the Howard Hughes Medical Institute. I was supported by the Department of Defense (DoD) through

the National Defense Science and Engineering Graduate Fellowship (NDSEG) Program. Gloria Ortiz was supported by the Howard Hughes Medical Institute Gilliam Fellowship.

# 5

## Spatiotemporal control of embryonic development using Opto-Nodal

In the embryo, patterns of ‘morphogen’ signals communicate long-range instructions which organize collective developmental programs and decisions. While the molecular mechanisms of these signaling pathways are increasingly well understood, the dynamical principles through which they coordinate development and morphogenesis remain largely mysterious. While one can posit mod-

els which are consistent with observed developmental trajectories, demonstrating that these models capture fundamental and generalizable principles demands sophisticated tools for manipulating the structure of morphogen signals with spatiotemporal precision.

This chapter describes progress towards developing an optogenetic platform for patterning Nodal signaling within dozens of zebrafish embryos in parallel, and its application to the study of germ layer differentiation and gastrulation. The Nodal/Activin pathway is a canonical morphogen pathway within the TGF $\beta$  superfamily. A combination of genetic knockout, transplant, and over-expression studies have previously established that Nodal is necessary to organize zebrafish gastrulation and axis formation. Less well established are the design principles that the Nodal signal satisfies – does the Nodal gradient specify positional information via the local concentration of Nodal ligands? Are alternative cell fate decisions influenced by the arrival time of Nodal ligand at a given embryonic coordinate? To what extent can positive and negative feedbacks within the Nodal pathway self-organize gastrulation in the presence of a non-graded signal? The optogenetic platform we describe herein can test these hypotheses with a precision that is not achievable with previously available techniques.

All of the work described in this chapter was performed in close collaboration with Nathan Lord and Alexander Schier.

## 5.1 MOTIVATION

### 5.1.1 NODAL SIGNALING ORGANIZES EARLY EMBRYONIC DEVELOPMENT

Cells of the embryo send and receive signals via diffusible Nodal ligands (Fig. 5.1). In zebrafish, there are three genes encoding Nodal ligands: *cyclops* (*cyc*), *squint* (*sqt*), and *southpaw* (*spaw*). *cyc* and *sqt* are involved in germ layer commitment during gastrulation,<sup>93</sup> and *spaw* is expressed during left-right symmetry breaking.<sup>172</sup> The biochemically active forms of Nodal are in fact heterodimers of *vgr* with

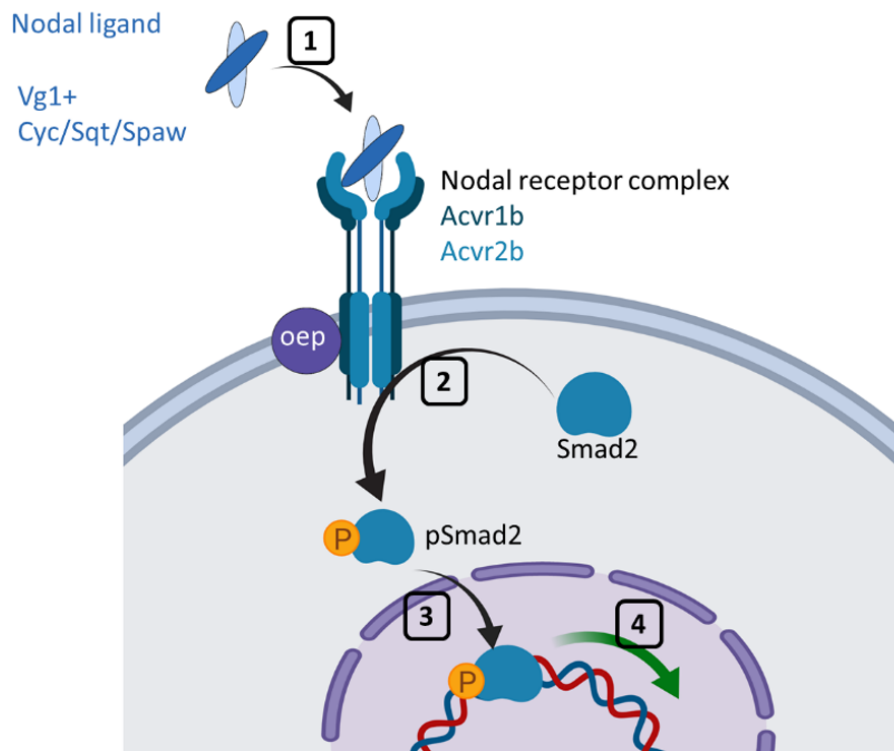


**Figure 5.1: Overview of Nodal signaling pathway.** 1) Nodal ligands (heterodimers of *vg1* and *cyc/sqt/spaw*) bind the extracellular domain of type 1 and type 2 receptors (*acvr1b* and *acvr2b*). 2) In concert with the coreceptor *oep*, the bound receptors phosphorylate the transcription factor Smad2. 3) pSmad2 translocates to the nucleus and 4) induces transcription of target genes.

one of *cyc / sqt / spaw*.<sup>193</sup> Nodal ligands in the extracellular space bind the TGF $\beta$  receptors *acvr1* and *acvr2*, which complex together with their obligate coreceptor one-eyed pinhead (*oep*)<sup>290</sup> and phosphorylate the transcription factor Smad2. The phosphorylated Smad2 (pSmad2) can then translocate to the nucleus and initiate the transcription of target genes. The ability for cells to communicate over long distances via diffusible Nodal ligands constitutes a classical example of a morphogen system.

Nodal plays several crucial roles in the zebrafish embryo. Very early in development, Nodal signaling participates in the function of the dorsal organizer.<sup>108</sup> The activity of cells in the dorsal organizer is essential to establishing an anterior-posterior (AP) body axis. Transplantation of cells

from the dorsal region of a donor gastrula (i.e. the location corresponding to the embryonic shield) into the ventral margin of a host gastrula can result in an axis duplication, demonstrating the sufficiency of this structure to organize a range of anatomical landmarks.<sup>91</sup> Nodal signaling is known to be involved in these specifications.<sup>108</sup> The Nodal target gene goosecoid (*gsc*) is expressed in the prechordal plate progenitors associated with the dorsal organizer, and the Nodal target floating head (*fl*) is expressed in notochord progenitors near the organizer but further from the margin. *gsc* and *fl* represent high-threshold and intermediate-threshold Nodal target genes respectively,<sup>240</sup> so this expression pattern is consistent with a gradient of Nodal signaling activity originating from the organizer. Paired injection of Nodal and BMP ligand is also sufficient to induce an axis duplication in the zebrafish embryo without transplantation.<sup>278</sup> Opposing gradients of Nodal and Wnt signaling have also been found to reconstitute an organizer in human embryonic stem cell cultures.<sup>180</sup>

Nodal signaling also specifies mesendodermal tissues during gastrulation.<sup>93,92</sup> During vertebrate gastrulation, cells which are specified for a mesodermal or endodermal fate will internalize towards the center of the embryo, generating the layered structure ('germ layers') that will ultimately give rise to the organs of the body.<sup>244</sup> In zebrafish, this is initiated by a ring of Nodal signaling around the margin that initiates from the yolk syncytial layer (YSL).<sup>93</sup> Imaging the nuclear localization of pSmad2 near the margin at this stage reveals a gradient of nodal activation.<sup>115</sup> An initially mixed mesendodermal population will then bifurcate into endodermal and mesendodermal lineages.<sup>92,268</sup> Within the first few cell tiers abutting the YSL, several cells adopt an endodermal lineage and internalize first. Further from the YSL, the majority of cells adopt a mesodermal fate.<sup>261</sup> This pattern can be recapitulated with ectopic Nodal sources, with endodermal progenitors appearing close to the Nodal source and mesodermal progenitors appearing further away.<sup>78</sup> These observations have been postulated to suggest a role for the Nodal gradient in encoding positional information: i.e., cells measure different local concentrations of Nodal as a function of their distance from the YSL, and adopt correspondingly different germ layer fates.<sup>14</sup>

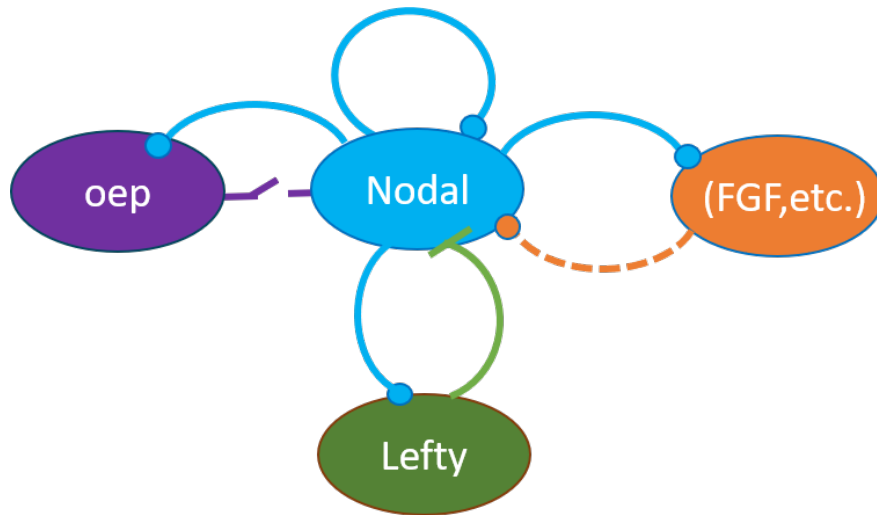


**Figure 5.2: Feedbacks in nodal signaling.** Activation of the Nodal signaling pathway includes positive feedback (via the induction of Nodal ligand expression, as well as expression of the Nodal co-receptor *oep*), negative feedback (via induction of the inhibitors Lefty1/2), as well as interactions with other signaling pathways (e.g. FGF) which may in turn regulate Nodal signaling through complex interactions.

### 5.1.2 FEEDBACKS AND PATTERN FORMATION IN NODAL SIGNALING

Nodal signaling in the zebrafish embryo is decorated with several feedback mechanisms. Firstly, Nodal has positive feedback: Nodal ligands (e.g. *cyc*, *sqt*) are themselves Nodal targets.<sup>273</sup> Nodal signaling also induces production of the Nodal inhibitor Lefty (which comes in two flavors, *lefty1* and *lefty2*)<sup>47</sup>. Lefty proteins also are secreted to diffuse throughout the extracellular space, creating a feedback inhibition mechanism through which cells can regulate Nodal signaling during development. In Lefty loss-of-function mutants, the range of Nodal signaling (and subsequent mesendodermal cell fate specification) is expanded<sup>233</sup>; overexpression of Lefty has the opposite effect and recapitulates phenotypes of Nodal loss-of-function mutants.<sup>24</sup> Notably, measurements of diffusion coefficients in Nodal-GFP ligands and Lefty-GFP ligands show that Nodal diffusion is more restricted than that of Lefty.<sup>197</sup> The simultaneous presence of short-range positive feedback and long-range feedback inhibition in Nodal-Lefty signaling is consistent with the description of a classical Turing

patterning system.<sup>197</sup> Collectively, these features suggest Nodal as a classical morphogen system: a gradient of diffusible morphogen which encodes positional information in its concentration profile, and which is tightly regulated towards this target profile via reaction-diffusion feedbacks.

However, this picture is complicated by several open questions about Nodal signaling. For example, *Lefty* mutants can be rescued by uniform application of a small-molecule Nodal inhibitor.<sup>232</sup> This open-loop patterning scheme is more sensitive to embryonic challenges than the intact closed-loop system, but its suitability suggests that complex reaction-diffusion patterning may be dispensable in the Nodal pathway. There is also evidence that classical threshold models are insufficient to predict the response of Nodal target genes without accounting for the temporal profile of Nodal signaling.<sup>78</sup> Timing of Nodal activation has also been proposed to play a role in separating the endodermal from mesodermal lineages via the feedforward inhibition of FGF signaling (FGF is itself a Nodal target which inhibits endodermal specification).<sup>261</sup> However, it remains challenging to disambiguate the degree to which Nodal concentration and Nodal arrival time determine cell fate *in vivo* using classical methods: any ectopic source of diffusible ligand will generate a gradient in both space and in time.

What is the role of signaling feedbacks in Nodal-organized morphogenic signaling? What design criteria does this system satisfy, and how is the spatiotemporal pattern of Nodal signaling regulated in order to robustly organize gastrulation and mesendodermal specification in the presence of environmental fluctuations? The ability to experimentally manipulate Nodal signaling patterns with arbitrary spatiotemporal content would provide a new platform to disambiguate essential and dispensable features of the Nodal pattern.

## 5.2 OPTONODAL: CONTROLLING A MORPHOGEN PATHWAY WITH LIGHT

In order to manipulate Nodal signaling with light, we first require reagents which can recapitulate Nodal signaling in the presence of photons, but in the absence of Nodal ligands. Photoassociating domains (PADs) offer the means to induce the dimerization of type 1 and type 2 Nodal receptors in this way. By removing the extracellular ligand-binding domain from the N-terminus of a receptor kinase and introducing a photoassociating domain on the intracellular C-terminus, photons can functionally masquerade as receptor ligands, directly recapitulating the downstream signaling pathways that drive expression of target genes.

This strategy was first applied to the Nodal pathway by Carl-Philipp Heisenberg and colleagues.<sup>235</sup> By removing the ligand binding domains of *acvr1b* and *acvr2b*, and fusing the LOV domain of the Aureochrome protein to the intracellular portion of each receptor, these Opto-Acvr receptors could be induced to complex via blue-light sensitive homodimerization of AuLOV. These reagents could recapitulate phosphorylation of Smad2 to pSmad2 without complexing of the coreceptor *oep* (Fig 1). Heisenberg and colleagues used mRNA injections of OptoAcvrs to test how temporal aspects of Nodal activation determine the expression of target genes.<sup>235</sup>

The AuLOV-based reagents demonstrated proof-of-principle for optogenetic control of Nodal signaling. However, these reagents carry several important restrictions which limit their utility. Most crucially, we found their dynamic range to be insufficient to span the range of Nodal responses observed in the zebrafish embryo *in vivo*. Split optogenetic constructs have some finite affinity ( $K_d$ ) in the dark, and this affinity increases and ultimately saturates as a function of blue illumination intensity. Optogenetic control of signaling pathways requires titrating doses of both receptors and photons in order to suppress activity in the dark, and maximize activity in the light. We found that when *acvr*-AuLOV reagents were expressed to the maximum dose which showed no aberrant dark phenotypes at 24 hpf, blue light illumination (10 uW/mm<sup>2</sup> 470 nm illumination) was insufficient to

drive high-threshold nodal targets (e.g. the endodermal marker *Sox32*). High-threshold targets could be activated under blue illumination with larger doses of mRNA injection (40 pg/receptor), but this same injection showed Nodal gain of function phenotypes in unilluminated embryos, suggested dark activity of the AuLOVs at this dose. In addition to dynamic range limitations, the temporal resolution of these reagents is limited by the slow kinetics of the AuLOV photocycles (>10 minutes half-life for recovery of the photoexcited state<sup>116</sup>).

In order to impose physiological relevant patterns of Nodal signaling with light, we required more powerful molecular reagents. We hypothesized that two changes to the construct design may improve the dynamic range and overall performance of OptoAcvr constructs: 1) exchanging the AuLOV domains for alternative PADs with higher dynamic range and/or faster kinetics, and 2) targeting one or both receptors to the cytosol (rather than the membrane) in order to decrease dark interactions. We tested 4 sets of PAD domain constructs (the original AuLOV domain, the alternative Cry2/CIB1, and the engineered LOV variants iLIDs<sup>113</sup> and nMag/pMag<sup>146</sup>), and tested each PAD set in all 4 possible targeting configurations (both membrane bound, both cytoplasmic, and either combination of one cytosolic and one membrane localized).

Constructs based on the iLID and Magnet reagents showed no Nodal signaling activity, even at high doses of receptor and blue light intensity. This may be related to the association topology of the particular receptors, or due to a reduction of homo-oligomerization in receptors designed to form obligate heterodimers. In both AuLOV and CRY2/CIB1 based designs, the greatest dynamic range was achieved by localizing the type 1 receptor *acvr1b* to the membrane, and the type 2 *acvr2b* to the cytosol. Interestingly, the converse design (*acvr1b* in cytosol, *acvr2b* in the membrane) showed no signaling activity. The CRY2/CIB1 based constructs showed improved overall maximum signaling intensity at a given dose relative to the corresponding AuLOV design. Ultimately, the screen identified a next generation Opto-Nodal reagent design comprising Myr-Acvr1b-CRY2 and Acvr2b-CIB1. These were capable of spanning the full range of physiological Nodal signaling levels at a single

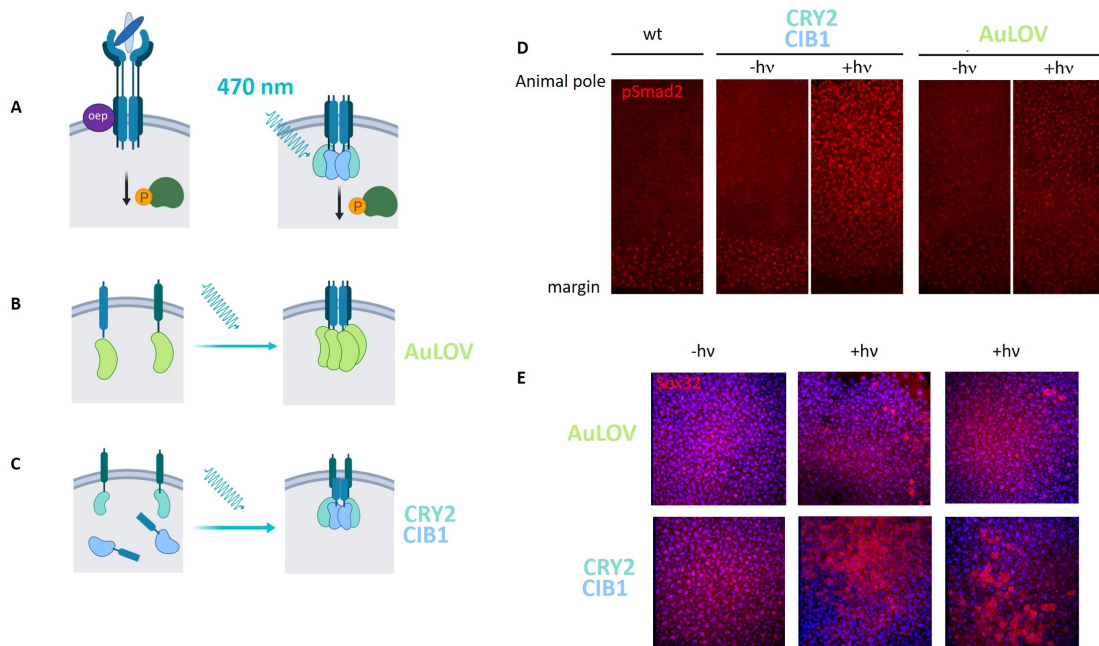


**Figure 5.3: Controlling Nodal signaling with light.** A) Left: The endogenous signaling process is initially through the phosphorylation of Smad2 by a complex of nodal ligand, type 1 and type 2 receptor, and oep coreceptor. Right: by fusing the type 1 and type 2 receptors to photoassociating domains, Smad2 phosphorylation can be initiated by blue light in the absence of oep and nodal ligand. B-C) Comparison of previously reported Opto-Nodal constructs (OptoNodal1)<sup>235</sup> (B), and updated constructs we developed (OptoNodal2). D-E) Embryos were injected with the maximum mRNA dose of each construct which did not show dark phenotypes at 24 hpf (40 pg/receptor for AuLOV; 20 pg/receptor for CRY2/CIB1). D) Staining for nuclear localization of phosphorylated Smad2 shows improved dynamic range of new constructs when compared to first-generation constructs. E) Staining for a high-threshold Nodal target (Sox32) further demonstrates improved dynamic range of response with OptoNodal2. Nuclei are labeled in blue with a DAPI costain.

receptor dose of 20 pg/receptor(Fig. 5.3).

### 5.3 A PLATFORM FOR PERTURBING AND IMAGING DOZENS OF EMBRYOS IN PARALLEL

Embryos are dynamic samples which change shape and exert forces as they develop. In order to interpret complex and potentially stochastic developmental responses of embryos to OptoNodal stimulation, we required a means to project patterns of illumination onto many embryos in a single parallelized experiment, and for maintaining the orientation of these samples over several hours of morphological changes in the embryo (e.g. throughout gastrulation). We combined optics, rapid prototyping / digital fabrication, and control software in order to develop a new sample preparation which could address these criteria.

First, we developed an agarose based ‘egg crate’ mount which can orient an array of dozens to hundreds of zebrafish embryos such that their animal-vegetal axis is aligned with the optical axis of a microscope(Fig. 5.4). We used a stereolithography based 3D printer (Form2 from Formlabs) to print an array of ‘post’ features of variable shapes (e.g. cylinders, cones, rectangles), sizes, and spacings. These stamps can be used to imprint an array of slots into an agarose mold, which can then be loaded with zebrafish embryos. We tested a variety of crate designs in order to identify one which constrains the embryo with appropriate stiffness: i.e., that will preserve the orientation of embryos along the optical axis of the microscope, but which are sufficiently fluid to allow for the retrieval of embryos after experimental treatment so that samples can be grown to 24 hours post fertilization (hpf) timepoints and beyond. Ultimately, we found that setting a 1 mm x 1 mm spaced array of cylinders with diameter of 550 microns in a 0.3% agarose gel, loading embryos, and then overlaying a 0.15% low-melt agarose solution on top of loaded embryos allows for the maintenance of sample orientation during illumination while still permitting injury-free retrieval post-treatment.

In order to pattern light, we utilized a digital micromirror device (DMD). In particular, we used

a Vialux V-7001 module which comprises an array of 1024 x 768 individually addressable micromirrors (13.7  $\mu\text{m}$  pitch) which can be flickered between two positions at framerates of over 20 kHz (up to 290 Hz for 8-bit grayscale images). When placed in the illumination path of an optical microscope and de-magnified 2x on the sample, the DMD acts as an amplitude mask with contrast of up to 1000:1 between illuminated and unilluminated pixels. Because the DMD pixels can be modulated on timescales much faster than the photocycle relaxation of OptoNodal proteins, duty cycle modulation can be used as a means of projecting analog signals onto samples. In order to accomplish this quantitatively, one must first calibrate the illumination intensity at each pixel under 100% duty cycle by comparing the fluorescence profile of a calibration target to the total integrated power measured with a silicon photodiode (Thorlabs S170C). This calibration pattern can then be used to back out the pixel duty cycle required to illuminate a sample with a target power. Additionally, placing an iris within the illumination path allows for the regulation of the angular content of patterned illumination; by illuminating with low numerical aperture (i.e. collimated) light, patterns could be made robust in the presence of height variations between embryos within the agarose mount.

Achieving optical patterning of Nodal signals further demands that the OptoNodal receptors are expressed homogeneously throughout the embryo; otherwise, Nodal activation patterns will be unpredictable convolutions of optical patterns and expression patterns. In principle, this could be addressed by developing a transgenic zebrafish line which expresses OptoNodal constructs throughout its progeny embryos; however, it would be challenging to titrate the overall expression level using this method. Conventional injections of purified mRNA at the one cell stage failed to yield satisfactory results as well due to stochastic and highly asymmetric partitioning of the slowly-diffusing mRNAs during early cell divisions, resulting in highly spatially structured patterns of OptoNodal. Ultimately, the criterion of uniform expression was addressed by applying quadruple injections: one injection into each cell at the 4 cell stage. These scheme required a manageable scale of injections, and involved diffusion volumes small enough for mRNA to mix well prior to the subsequent cleav-

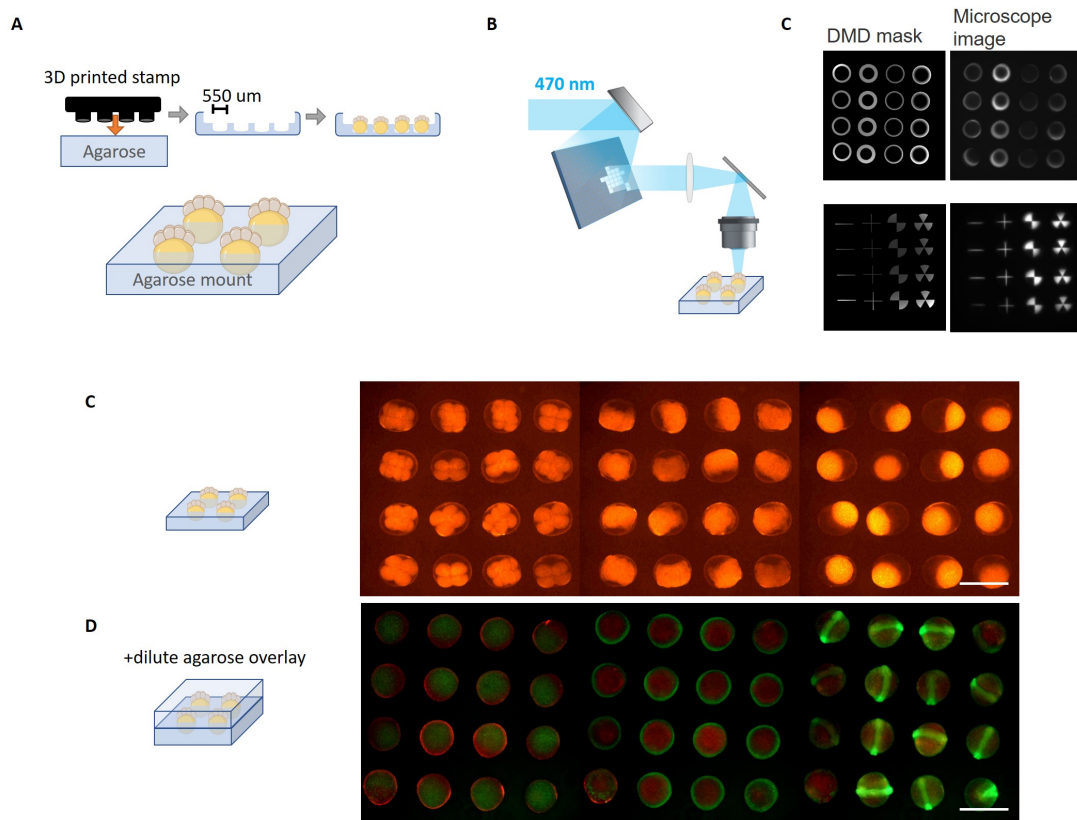


**Figure 5.4: A platform for high-throughput optical patterning of embryos.** A) Cartoon schematic of mounting scheme. A negative of the target was fabricated using a 3D printer (FormLabs Form2), and then used to stamp and cast an agarose mount. Embryos can then be loaded into the mount with the animal-vegetal axis aligned along the length of the cylindrical wells. B) By using a digital micromirror device, we can pattern light onto the sample plane. C) Example image showing DMD masks and corresponding embryo patterns observed in the imaging path of the microscope (not diagrammed). C-D) Patterning experiments required that embryos be sufficiently constrained such that they maintain their orientation throughout the course of the experiment, but not so constrained that their morphogenic movements are interrupted. C) Without a dilute agarose overlay, embryos 'tumble' and change orientation as they undergo gastrulation. D) With a dilute agarose overlay, embryos maintain their orientation through gastrulation and axis elongation. This scheme also allows for retrieval of the embryos from the mounts for continued mount-free development.

age to 8-cell stage.

Finally, temperature and moisture control had to be maintained in order to ensure consistent staging of embryos to canonical developmental timelines. A heated stage was used in an open-loop format, and calibrated such that the temperature in the center of a 35 mm dish filled with water was constant at 29 C over several hours. The evaporation rate of water at this temperature was quantified, and a syringe pump was calibrated to return water to the sample dish at a rate exactly offsetting evaporation.

### 5.3.1 ANALYSIS AND CHARACTERIZATION

Zebrafish samples which were patterned with OptoNodal stimulation were subjected to two basic types of analysis. In the first experimental category, embryos were injected with OptoNodal reagents, mounted in the aforementioned apparatus and treated with light during an interval between 3 and 6 hours post-fertilization. At 6 hours post fertilization, the embryos were removed from the agarose mount and returned to a multiwell plate which was kept isolated from any light which would further activate OptoNodal signaling. Embryological morphologies were then observed at timepoints between 24 and 48 hpf, and compared to classical developmental phenotypes associated with Nodal gain- and loss-of function mutations.

The second category of analysis involved direct visualization of target gene expression. After cessation of optical treatment at 6 hpf, embryos were removed from mounts and immediately fixed overnight and stained using a single molecule fluorescence *in situ* hybridization (smFISH) labeling protocol.<sup>210</sup> This was frequently performed in concert with Kaede-mediated photoconversion. Kaede is a fluorescent protein which undergoes an irreversible red-shift in both its absorption and emission spectra after exposure to near-UV light (e.g. 405 nm). By co-injecting Kaede mRNA with the mRNA encoding OptoNodal receptors, Kaede photoconversion was found to remain detectable after the aforementioned smFISH fixation, and could be used to ‘watermark’ the optically

treated region of the embryo.

#### 5.4 OPTICAL INDUCTION OF GERM LAYER FATE WITHIN THE VERTEBRATE EMBRYO

<https://www.overleaf.com/project/5d44dda45eabb619a71d3545>

We first deployed this system to explore how Nodal signaling specifies germ layer cell fates in the embryo. In wild type embryos injected with OptoNodal receptors, patterns of blue light were applied at the animal pole between 3 and 6 hpf. In normal development, these cells do not see Nodal and therefore adopt ectodermal lineages. In the presence of patterns of blue light, staining the endodermal marker *Sox32* (understood to be a high-threshold Nodal target) revealed ectopic patterns of cell fate decision which mimicked the optical stimulus. For embryos in which Kaede watermarking was performed, expression of *Sox32* target genes had a clear but indirect correspondence to the watermarked cells (Fig. 5.5)

This observation has potential implications for now Nodal-exposed cells break symmetry and bifurcate into mesodermal and endodermal lineages. *In vivo*, while endodermal cells only appear within the first cell tiers abutting the YSL, not every cell within these tiers becomes endodermal. It is not clear whether this stochastic pattern reflects variation in upstream signaling, or some self-organizing symmetry breaking amongst Nodal-exposed cells. We used light to apply a uniform optogenetic Nodal stimulus across a large segment of the animal pole, and measured responses. Stains for *Sox32* transcripts show a ‘salt-and-pepper’ pattern within the targeted region. A costain for *Lefty1* transcripts shows uniform expression, indicating that the pattern of Nodal activation was indeed uniform. *Sox32* positive cells appeared to further segregate into domains of coexpressing cells, suggesting some form of patterning process (either before induction or in response to induction). The overall expression pattern *Sox32* expression in these cells further suggests that this choice is all-or-none, in which cells bifurcate into a bimodal distribution of endodermal and mesodermal precu-

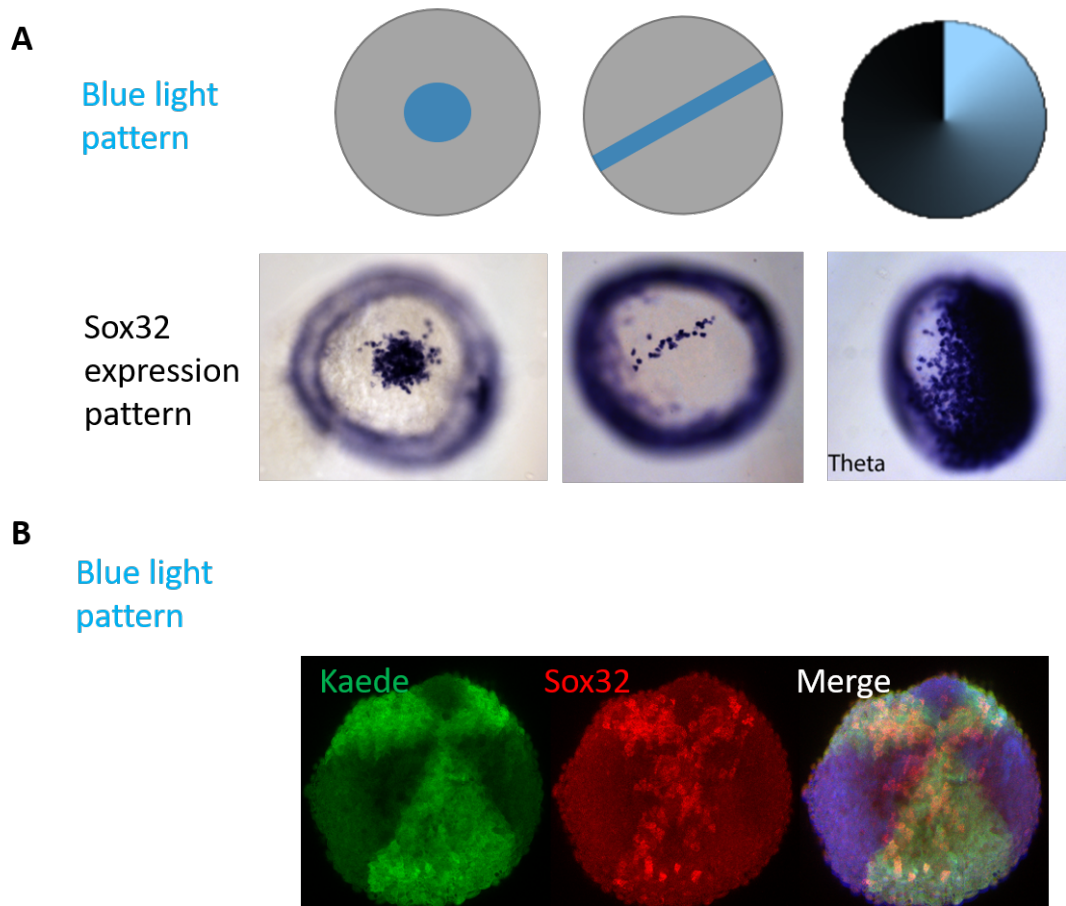


**Figure 5.5: Painting cell fate in the vertebrate embryo.** A) Patterns of OptoNodal stimulation can induce (nearly) arbitrary structures of endodermal germ layer decisions as indicated by Sox32 staining. B) When the photoconvertible protein Kaede is co-expressed with OptoNodal, 405 nm light can be used to watermark the treated area.

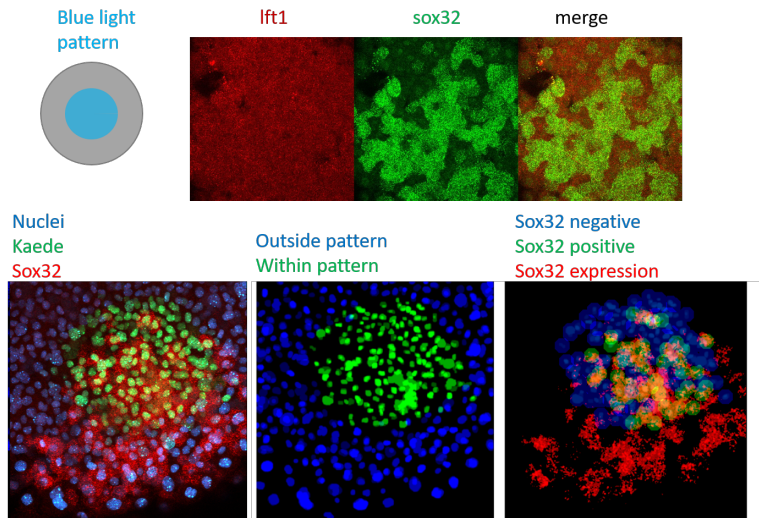


**Figure 5.6: Stochastic aspects of the endodermal decision** . Top: Application of a uniform disc of OptoNodal stimulation at the animal pole, where there is no endogenous Nodal signaling. Co-stains of the direct Nodal target *lft1* and of the endodermal marker *sox32*. Bottom: segmentation of illuminated cells, as well as *sox32* negative and *sox32* positive cells. Comparison of these populations suggest that endodermal decision is a stochastic and binary decision, even in the presence of a (nearly) uniform stimulus.

sors.

## 5.5 OPTICAL RESCUE OF EMBRYONIC DEVELOPMENT

We then deployed the OptoNodal<sub>2</sub> platform to test which aspects of the endogenous Nodal signal are sufficient to organize more complex morphogenic processes: gastrulation, and the subsequent specification of tissues that comprise overall body plan of the organism. In *MZoepe* mutant embryos, a lack of functional Nodal signaling results in severe morphological defects: no endodermal tissue forms; no appreciable trunk or axial mesoderm forms (e.g. no notochord); the specification of fore-brain, hindbrain, and midbrain boundaries is disrupted; and the eye fields fail to separate. We asked how much of this developmental phenotype could be rescued by systematically varying spatial aspects of the Nodal signal. Which parts of the signal are necessary and/or sufficient, and which are

dispensable?

First, we illuminated OptoNodal-sensitized *MZoep* embryos with marginal ‘stripes’ of a given size and uniform intensity (i.e. a radial step-function)(Fig. 5.7). Images of the embryo samples were acquired and segmented in order to define embryo centroid coordinates; patterns were set to the target intensity within a distance between an outer radius (the outer radius of the embryo) and an inner radius (which sets pattern width). Patterns were set to zero elsewhere. First, we kept the stripe width constant at 50 microns, but varied the illumination intensity from 0.5 to 2  $\mu\text{W}/\text{mm}^2$  time-averaged. For low intensities, some incomplete degree of rescue in axial mesoderm was observed (Fig. 5.7). At high intensities, embryos appeared dorsalized, indicating a Nodal gain of function phenotype. At intermediate intensities, significant rescue of trunk and axial mesoderm could be achieved. However, head tissues failed to organize, and in some cases appeared inhibited even relative to the *oep* background. This suggested that, at this particular stripe width during this particular exposure window, no single analog value could rescue organization of the entire embryo.

We next fixed the pattern intensity at the optimal value from the prior experiment (1  $\mu\text{W}/\text{mm}^2$ ), and iterated the pattern width from 30 to 60  $\mu\text{m}$  (with 10  $\mu\text{m}$  intervals)(Fig. 5.8). The equivalent conditions from the prior experiment again produced phenotypes with enlarged trunk somites relative to wildtypes, and less head tissue. Thicker stripe widths resulting in highly dorsalized embryos (resembling *Lefty* mutant phenotypes<sup>233</sup>). For the thinnest stripe width, we observed moderate rescue of axial mesoderm (mimicking the low-intensity conditions from Fig. 5.7). However, for a stripe width of 40  $\mu\text{m}$ , we observed considerably improved rescue of the overall body plan, including some samples which axial and trunk mesoendodermal rescue occurred simultaneously with improved brain region separation and specification.

Collectively, these results demonstrated that patterned OptoNodalz can recapitulate key developmental landmarks, including the formation of trunk somites, formation of a spinal cord, formation of a beating heart and a hatching gland (both requiring endodermal specification), and the separa-

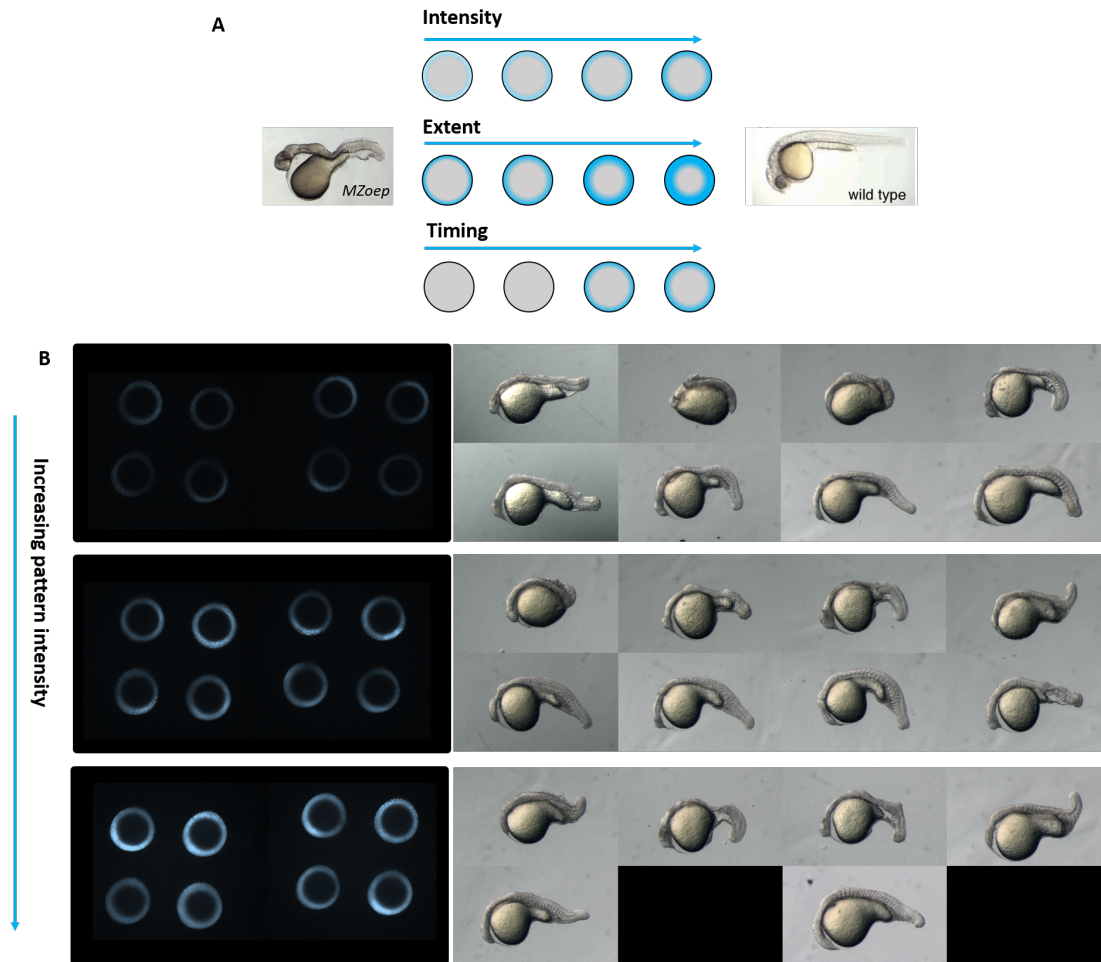


**Figure 5.7: Testing the spatiotemporal demands of Nodal patterning with optogenetics 1: signal magnitude.** A) By systematically changing quantitative aspects of the Nodal signal (e.g. signal magnitude, extent of the signaling region, timing of exposure) we can test what demands Nodal signaling must satisfy in order to organize embryonic development. B) For a uniform pattern extent (50  $\mu\text{m}$ ) and exposure time (4-6 hpf), the intensity of OptoNodal exposure was increased from 0.5 to 2  $\mu\text{W}/\text{mm}^2$ . At low intensities (top two rows), some rescue of axial and mesoderm was achieved. At intermediate intensity (middle two rows), robust achievement of axial and trunk mesoderm was achieved, including improved yolk extension. At high intensity (toom two rows), tail mesoderm becomes malformed and head tissues disappear, resembling nodal gain-of-function phenotypes.

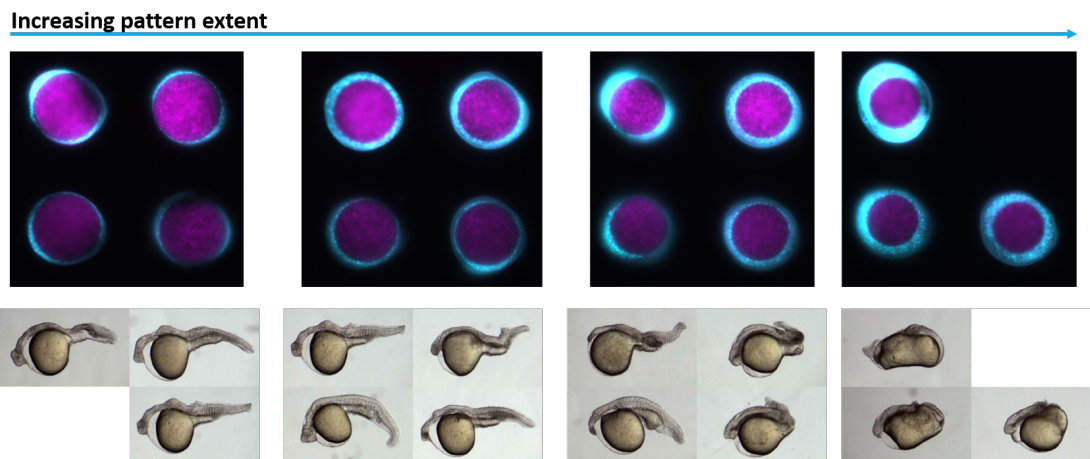


**Figure 5.8: Testing the spatiotemporal demands of Nodal patterning with optogenetics 2: signal extent.** We systematically varied the extent of the ring of illuminated cells from 30 to 60  $\mu\text{m}$ . Top: images of embryos (visualized by TMR fluorescence, magenda) and illuminated area (cyan, visualized by GFP fluorescence). Bottom: 24 hpf phenotypes observed in each embryo. At low pattern extent, rescue of some axial mesoderm was observed (left). At large pattern extent, embryos were severely dorsalized or had enlarged trunks. For 40 micron pattern extent (second condition from the left), significant rescue of trunk and axial mesoderm was observed, and some rescue of brain region specification was observed.

tion of the eye fields (Fig. 5.9).

## 5.6 OUTLOOK

The combination of next-generation OptoNodal reagents, patterned illumination using digital micromirror devices, and rapid-prototyping based sample preparation enables the simultaneous manipulation of Nodal signaling in dozens of embryos in parallel with spatiotemporal precision. Application of this method is ongoing, but several provocative results have already been observed.

The first observation regards the role of pattern formation and symmetry breaking in the endodermal cell fate specification. The salt-and-pepper appearance of endodermal cells within the mesendodermal domain is a suggestive observation that appears at odds with classical threshold-based positional information models. With a diffusible Nodal ligand (either from the YSL, from



**Figure 5.9: Rescue of overall body plan with OptoNodal2.** Example of an optically stimulated *MZoeP* zebrafish at 48 hpf. The morphology of the fish demonstrates successful rescue of trunk and axial mesoderm, a beating heart (orange arrow), a hatching gland (blue arrow), and separation of the eye fields (green arrow).

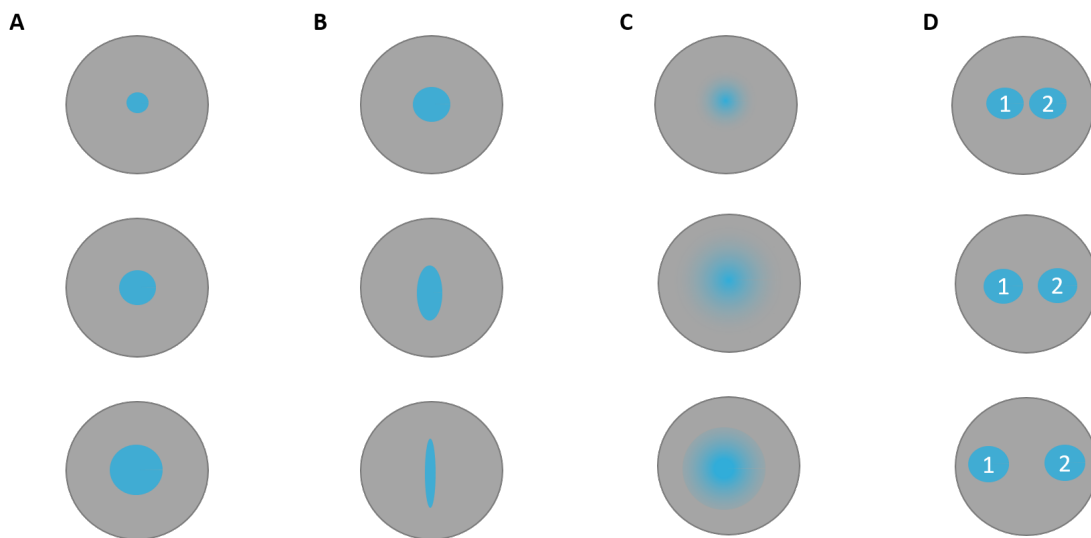


**Figure 5.10: Testing for nonlinearities in the mesendoderm decision.** By systematically varying features of the target pattern, we can test the *Sox32* response as a black box. A) Testing for a community effect. I.e., does the likelihood with which cells commit to endoderm depend on the number of stimulated cells? B) Testing for boundary effects. For a fixed illuminated area, does changing the curvature (and therefore the relative average distance between stimulated cells and the boundary) affect response statistics? C) Testing whether a gradient affects response statistics. D) Testing for long range signaling. Do the responses of two illuminated spots depend on their relative separation?

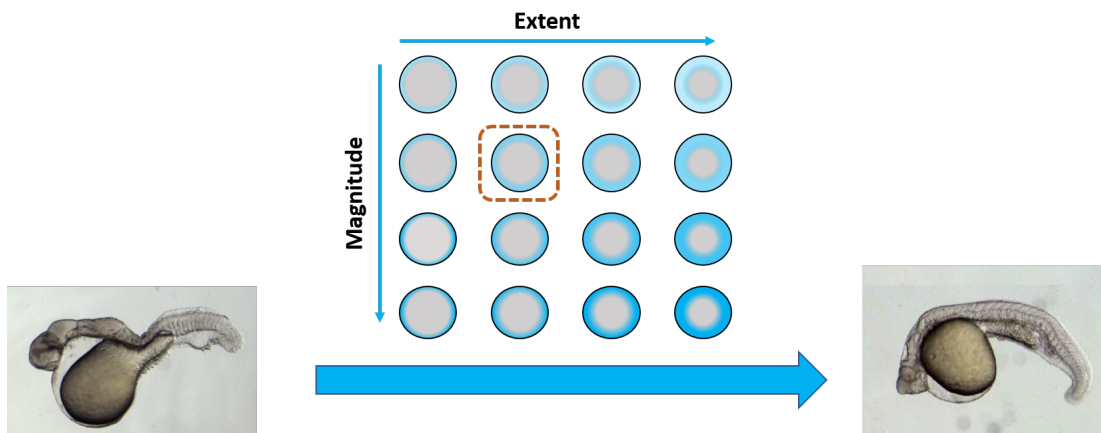


**Figure 5.11: Design criteria of the Nodal signal.** By systematically varying the extent and intensity of the Nodal signal, we have mapped a ‘sweet spot’ of signal which rescues the most complete portion of developmental landmarks. By continuing to perturb aspects of the signal (e.g. time of exposure, presence of a gradient) we may improve the degree of rescue achieved.

an injection, or from a Nodal source transplant cell) there will always be a gradient in which some cells are exposed to a higher value of Nodal than their neighbors, and in the presence of cell migration it is challenging to rule out positional information hypotheses. However, here we observed a striking salt and pepper pattern even in the presence of uniform stimulus. Does this reflect some underlying reaction-diffusion pattern forming process? This design might be advantageous if the embryo needs to regulate a certain target number of endodermal cells in the presence of environmental fluctuations. Our next steps will involve pressure-testing this hypothesis in new experimental designs (Fig. 5.10). Does the likelihood of a cell becoming Sox32 positive depend on the number of neighbors which have seen Nodal (i.e. a “community effect”)? Does the response likelihood depend on the presence of gradients or boundaries in the Nodal pattern? Testing these hypotheses in both wild type and mutant embryo lines can dissect the role of feedbacks in regulating this crucial lineage bifurcation.

Second, we have seen that even comparatively simple spatial patterns (e.g. a radial step function over a discrete interval) can rescue a significant amount of embryonic development in *MZoep* em-

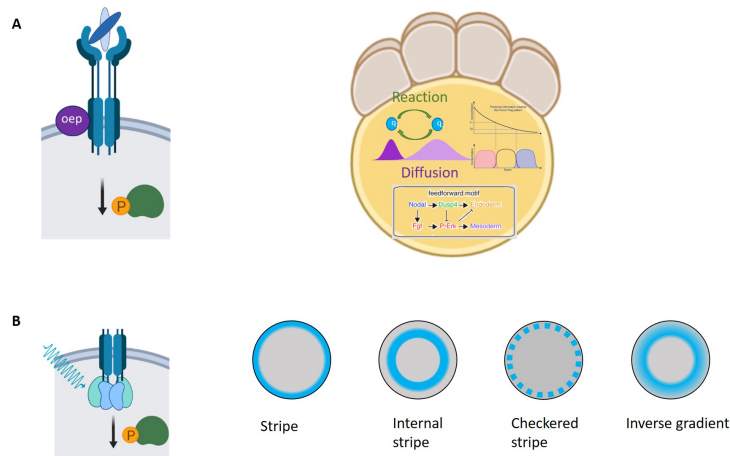


**Figure 5.12: Playing arbitrary developmental programs with light.** Any complete model of Nodal's role in morphogenesis must not only be consistent with *in vitro* developmental trajectories, but must also explain how the embryo responds to arbitrary developmental programs.

bryos which lack functional Nodal signaling. By systematically varying quantitative aspects of the Nodal pattern (e.g. magnitude, extent, and timing of signal) we can map the tolerances of embryonic development to specific features of a morphogen signal (Fig. 5.11). Optical methods are uniquely suited to test the necessity and sufficiency of different pattern parameters in order to probe the design criteria of this morphogen signal. Is the gradient truly necessary to organize embryonic development, or is it merely the consequence of signaling with a diffusible source? An intermediate answer could be that while a gradient of concentrations is not itself necessary to encode positional information, but does act to break symmetry and specify directional axes for other self-organizing downstream signaling pathways. By continuing to perturb aspects of the OptoNodal signal (e.g. timing? Dorsal-ventral gradients and asymmetries?) we anticipate that this method can shed new light on the role of the Nodal gradient in organizing gastrulation. Ultimately, any complete model of Nodal's role in morphogenesis should generalize to predict how the embryo responds to arbitrary, non-physiological signaling patterns (Fig. 5.12).

Finally, there are many opportunities to extend this approach to other developmental processes

which involve spatially organized signals. For example, the recent identification of the *buluwa* mutant line<sup>280</sup> could enable the use of OptoNodal to study its role in the dorsal organizer. Development of spectrally orthogonal tools for manipulating other signaling pathways (e.g BMP) will enable the study of complex and nonlinear interactions between distinct morphogen signals. Combining these methods with emerging techniques for mapping gene expression (e.g. MERFISH<sup>45</sup>) will also provide a deeper picture of how embryonic development responds to complex signals. By continuing to develop and apply optical tools in developmental biology, we can begin to unravel embryo as a dynamical system, and ultimately understand the design principles through which it builds itself.

## 5.7 CONTRIBUTIONS

Nathan Lord and I conceived and designed this project, and conducted the experiments described herein. Vicente Parot and Samouil Farhi helped design and build the ultrawidefield, upright patterned illumination microscope, based on an original design by Christopher Werley. Adam Carte, Jeffery Farrell, James Gagnon, and Deniz Aksel provided helpful feedback. Adam Cohen and Alexander Schier oversaw the research.

# 6

## Spatially-resolved single cell transcriptomics through photochemical barcoding

Understanding genetic pattern formation requires tools for mapping the genetic structure of biological samples. This is a daunting challenge given the high-dimensionality of genetic space: the human transcriptome contains  $10^4$  genes, and mapping expression levels of each of these genes within an extended sample is not feasible with conventional fluorescence-microscopy based techniques.

The recent development of single-cell RNA sequencing methods (scRNAseq) has created a powerful alternative. By using droplet microfluidics to separate and encapsulate individual cells with barcoded beads, a single measurement can characterize expression levels across  $10^4$  genes in over  $10^4$  cells in parallel, all while retaining the correlations in gene expression at the single cell level. This approach has revolutionized cell biology and achieved widespread adoption, and it promises to describe the complexity of biological systems with unprecedented precision. However, for what scRNAseq methods gain in transcriptomic depth, they sacrifice all spatial information about a given sample. While alternative methods for spatially resolved deep transcriptomics have been described, all have considerable drawbacks relative to droplet sequencing methods.

In this chapter, we describe progress towards a new platform for spatially-resolved scRNAseq using photochemical barcoding. By utilizing photochemistry to tag cells with spatial ‘zipcodes’ as a form of feature barcoding, we can layer spatial information onto existing droplet sequencing pipelines without sacrificing the considerable power of the original method. We will describe overall proof-of-principle experiments and outline a roadmap toward a full demonstration of the concept in a practical application.

## 6.1 MOTIVATION

Single-cell RNA sequencing technologies enable the assignment of individual cDNA molecules to their corresponding cells of origin in extremely high throughput (i.e., in tens of thousands of cells in a single measurement).<sup>153,175</sup> scRNAseq achieves this through the use of barcoded beads which are decorated with ssDNA primers that contain a shared sequence for each cell on a given bead (the ‘bead barcode’), a separate randomized sequence which is different for each primer (the ‘unique molecular identifier’, or UMI), and a poly-T tail for mRNA capture. Using a microfluidic chamber, a water-in-oil emulsion is prepared in which flow rates are titrated to encapsulate one cell and one

barcoded bead in a given droplet. By subsequently lysing cells and running a reverse-transcriptase (RT) reaction within this emulsion, the mRNAs from each individual cell are ligated and captured by primers originating from their correspondingly distinct barcoded bead. Because all of the primers on a given bead carry a single shared bead barcode, next-generation sequencing of this cDNA library can leverage these barcodes to associate all cDNAs with their cell of origin.

These methods have opened new avenues in cell biology, enabling the identification of rare cell types that are undetectable in bulk assays<sup>128</sup> and the tracing of developmental lineages in the embryo.<sup>88,182</sup> However, the preparation of this emulsion requires dissociating the target tissue of interest, thereby scrambling the cells in suspension and discarding all spatial information about identified cells. Alternative methods have been proposed to achieve deep single-cell transcriptional profiling while retaining spatial information. Several involve some form of *in situ* hybridization of the target mRNAs. For example, super-resolution microscopy (e.g. STORM) can localize fluorescence *in situ* hybridization (FISH) probes with exceptional precision. By designing probe libraries using error-robust encoding strategies, this technique can be pushed to measure the full transcriptome with super-resolution.<sup>45</sup> This approach of Multiplexed Error-Robust FISH (MERFISH) has been demonstrated in tissue samples; however, the imaging bandwidth required to accomplish this in extended samples (i.e. of order mm x mm) requires restricting transcriptional coverage to around 100 genes.<sup>192</sup> This depth may be suitable for comparing samples to independently measured droplet sequencing reference databases;<sup>191</sup> however, it leaves 99% of the transcriptome unprofiled in any given sample.

An alternative demonstration involved stamping a fixed tissue with a 'puck' of barcoded beads whose molecular indices are imaged beforehand in order to create a reference map.<sup>230</sup> When stamped onto a tissue sample, the barcoded beads hybridize target mRNAs *in situ*. The resultant cDNA library can then be sequenced using NGS and barcodes can be compared to a reference atlas in order to localize transcripts within the tissue. This method has been demonstrated using beads which

are of the same size scale as individual cells (10  $\mu\text{m}$ ), so it conceivably realizes cellular resolution. However, by fixing and ligating mRNAs *in situ*, this technique does not maintain the single-cell discretization of droplet-based methods. Depending on precise registration, barcoded beads will mix transcripts from neighboring or overlapping cells, especially in complex tissues like the brain.

Existing experimental methods for spatially resolved transcriptomics therefore require sacrificing either the majority of transcriptomic information in a given sample, or the single-cell discretization of gene expression profiling which has made scRNAseq so powerful. Ideally, one could directly layer spatial information onto existing scRNAseq pipelines in order to strictly improve this technique without introducing new drawbacks. This ‘feature barcoding’ approach of tagging features beyond gene expression with DNA barcodes has been demonstrated in other contexts. For example, DNA barcode-tagged antibodies can be used to layer proteomic information onto scRNAseq measurements,<sup>246</sup> or barcoded CRISPR libraries can be used to associated scRNAseq reads with deleted targets in high-throughput CRISPR screens.<sup>68,72,133</sup> By designing barcode families with a shared primer adaptor, library preparation protocols can be adopted to amplify the relative fraction of this signal in a given sequencing run, enabling sensitive measurement of non-transcriptional features of a sample.

We hypothesized that tagging a cell’s location as a barcoded feature may represent a route to layer spatial resolution onto existing scRNAseq pipelines. In order to accomplish this, we turned to photochemical strategies that could be paired with patterned illumination in order to paint patterns of ‘zipcodes’ onto target cells.

## 6.2 PHOTOCHEMICAL PATTERNING OF DNA ZIPCODES

The overall design of the spatial barcoding scheme is outlined in Fig. 6.1. In proteomic feature barcoding, samples are labeled with antibodies decorated with DNA oligonucleotide barcodes that

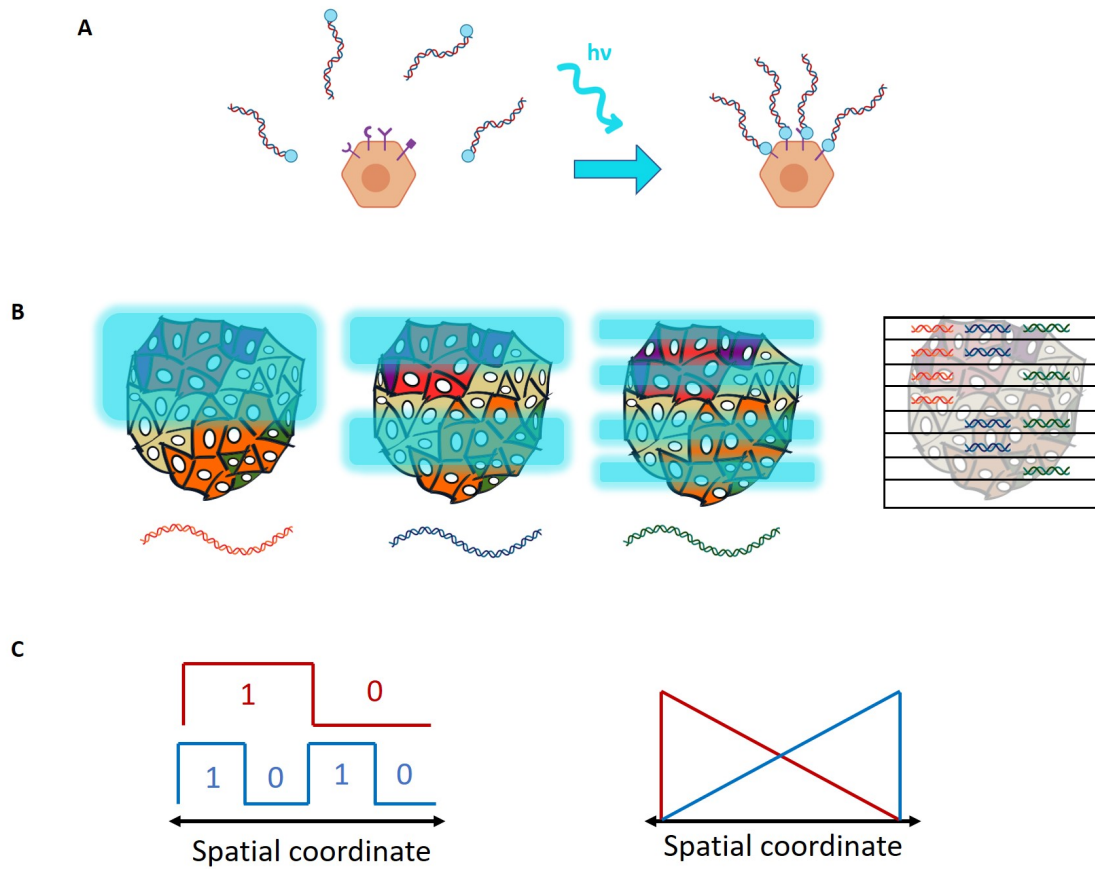


**Figure 6.1: Photochemical barcoding design and strategy.** A) By functionalizing DNA oligonucleotide barcodes with optically-controlled attachment chemistry, one can use patterns of light to decorate cells with spatially targeted feature barcodes. B) Sequentially layering patterns of barcodes can build up 'zipcodes' which reflect a cell's spatial location. C-D) Potential encoding schemes of photochemical barcodes. Barcode detection may be digital (C) (in which each barcode in each cell is only classified as detected or undetected) or analog (in which precise barcode counts are quantified and normalized relative to an opposing gradient to control for cell-specific labeling affinity).

masquerade as mRNAs during sequencing. We adopted this general strategy, but instead of relying on antibody-antigen affinity interactions we functionalized DNA oligos to have their attachment chemistry under optical control (Fig. 6.1a). Serial application of photochemical DNA barcodes under different patterns of illumination can build up ‘zipcodes’ which uniquely identify particular sample locations via the combination of photochemical barcodes present in a cell (for clarity, we henceforth refer to photochemical barcodes as zipcodes) (Fig. 6.1b). Multiple encoding schemes are conceivable. In a digital encoding scheme, series of overlapping patterns are applied. For a given cell, binary classifications are made on whether each individual zipcode digit is present, and the overall combination of detected zipcodes enables assignment of the cell’s location into a discrete bin (Fig. 6.1b-c). Alternatively, if a gradient of light is applied, the total number of counts in a given zipcode channel can encode analog spatial information. (Fig. 6.1d) This strategy may be more robust to sample noise (caused by e.g. variations in cell size or total available surface area; optical illumination profile) if a normalization scheme is applied (for example, by taking the ratio of two opposing gradients).

We realized photochemical control of DNA oligo labeling using a combination of phenyl azide photoactivation and click chemistry conjugation (Fig. 6.2). Phenyl azide moieties undergo promiscuous cross-linking when excited by near-ultraviolet light, with a preference for primary amine target sites. Nitrophenyl azide (NPA) moieties are particularly attractive for their red-shifted absorption spectra. Chen and collaborators demonstrated that patterned illumination of the NPA reagent SANPAH can achieve surface labeling of biological samples with high spatial resolution, presumably through the labeling of amine residues within surface proteins.<sup>49</sup>

We investigated the feasibility of using NPA-functionalized DNA molecules to directly label cell culture samples in a single step; however, we were unable to achieve patterned labeling with NPA-DNA. Multiple considerations could explain the lack of NPA conjugation when directly attached to DNA. For one, DNA cargo contains myriad primary amine moieties itself for photoactivated NPAs

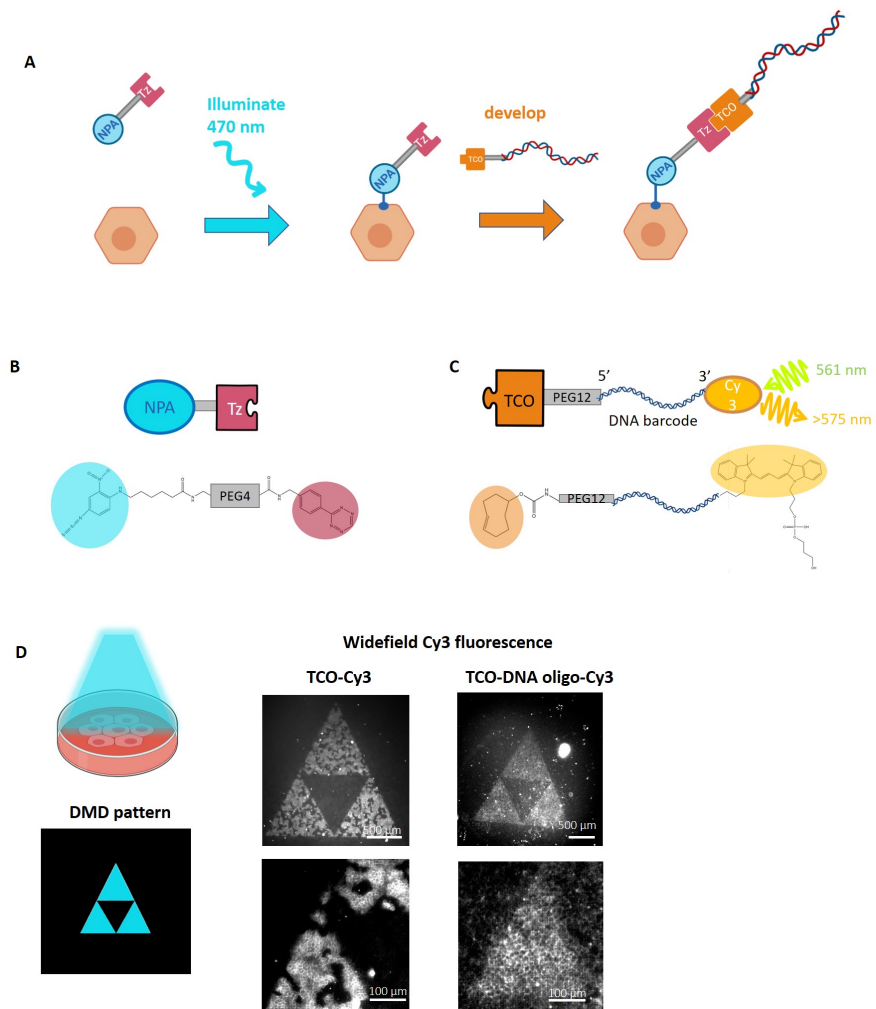


**Figure 6.2: Patterning DNA barcodes using sequential photo-click chemistries.** A) Outline of the attachment protocol. First, a nitrophenyl azide - tetrazine reagent (TzNPA) is photochemically tagged to the cell surface via NPA photocrosslinking. After a washout, the pattern of Tz aptamers is developed using TCO-functionalized DNA oligonucleotides. B) Construction of the TzNPA reagent. Sulfo-SANPAH is conjugated to amine-functionalized Tz-PEG4 via an NHS ester moiety in Sulfo-SANPH. The resultant reagent contains both photocrosslinking (NPA) and click (Tz) groups. C) Construction of functionalized oligonucleotides. A TCO-PEG12-NHS reagent is conjugated to amine-functionalized DNA oligonucleotide. D) Demonstration of pattern attachment chemistry. Two-step photopatterning and development yielded crisp patterns using both small molecule TCO-Cy3 (left column) and DNA oligonucleotide (right column) cargos.

to conjugate. Competition with this self-labeling reaction, or labeling between separate NPA-DNA molecules, may overwhelm the target labeling of cell surface proteins. Even without self-labeling, steric hinderance from the DNA oligo cargo may severely limit the kinetics of the target reaction.

In order to address these limitations, we formulated a two-step labeling scheme using a bio-orthogonal ‘click’ reaction(Fig. 6.2). Click chemistries include several classes of reaction pairs which are highly specific and biocompatible<sup>196</sup>; we adopted the tetrazine-TCO reaction in particular for its fast kinetics, with rate constants in excess of  $1000 \text{ M}^{-1}\text{s}^{-1}$  in phosphate-buffered saline solution.<sup>174</sup> Rather than directly conjugating DNA oligos with the NPA moiety, we instead decorated NPA moieties with a tetrazine (Tz) handle. By functionalizing the DNA oligo with the corresponding click partner trans-cyclooctene (TCO), the target cargo could be delivered to photopatterned Tz aptamers in a second development step (Fig. 6.2a). By separating NPA photopatterning and DNA conjugation into separate reactions, we observed a substantial kinetic improvement and sharp patterning of dye-labeled DNA oligo reactions(Fig. 6.2). TzNPA was synthesized via an NHS-Ester conjugation of Sulfo-SANPH (ThermoFisher) and Tetrazine-mPEG-amine (Kerafast). TCO-functionalized oligos were prepared by a seaparate NHS-Ester conjugation of TCO-PEG<sub>12</sub>-NHS (Kerafast) and C<sub>12</sub> aminolink-functionalized DNA oligonucleotides (IDT).

Optimizing illumination and development conditions demonstrated that these steps could be achieved in relative short time intervals (5 min Tz-NPA illumination at  $5 \mu\text{M}$ , followed by 1 min TCO-DNA development at  $1 \mu\text{M}$ ) making it feasible in principle to multiplex many barcode channels through serial patterning (Fig. 6.3 We also found that 470 nm illumination was suitable for achieving crisp and high-density labeling, despite previous reports utilizing shorter wavelength illumination).<sup>49</sup> We also noted that including divalent cations in the development buffer with DNA oligonucleotides ( $3 \mu\text{M Ca}^{++}$ ,  $1 \mu\text{M Mg}^{++}$ ) helped improve labeling density with DNA conjugated reagents, perhaps due to charge screening effects. Application of dye-based TCO reagents in brain slice cultures demonstrated that this chemistry is viable in tissue as well(Fig. 6.4). High-

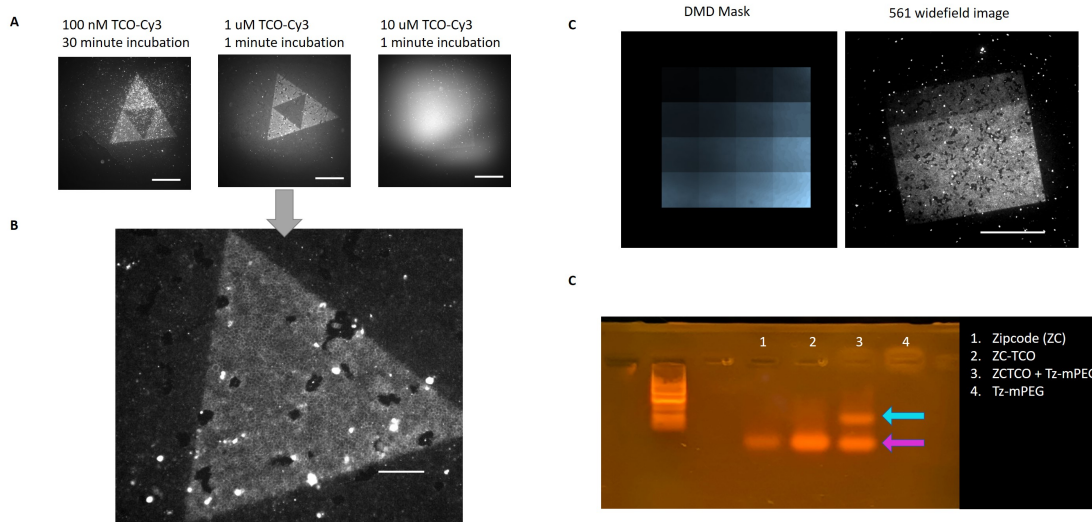


**Figure 6.3: Protocol optimization for photochemical barcoding.** A) Testing reagent concentration and incubation time for the TCO development step. 1 minute at 1  $\mu$ M TCO reagent is sufficient to ensure crisp saturation of tetrazine photopatterns. Lower concentrations require extended incubation times, and higher concentrations increase nonspecific background without improving labeling contrast. Scale bars 1 mm. B) Zoom of the central image showing clear labeling with cellular scale resolution in pattern boundaries. Scale bar 100  $\mu$ m. C) Calibrating exposure time during TzNPA photopatterning. At strong blue light intensities, 5 minutes of blue light patterning saturates cell surface labeling. D) A gel electrophoresis assay for assessing TCO functionalization of oligonucleotides. Incubation with PE-Glylated tetrazine causes a molecular weight increase in functionalized oligonucleotides, leading to splitting of bands between functionalized (cyan arrow) and unfunctionalized (magenta arrow) fractions of the oligo pool. This assay can be used to assess success of TCO functionalization and maintenance of reactivity in DNA zipcode reagents.

density DNA conjugation in tissue may require fixed-sample sequencing strategies<sup>114</sup> due to the extra time required for diffusion of DNA cargo in tissue.

### 6.3 SEQUENCING ZIPCODES

After successfully demonstrating that DNA barcodes could be spatially patterned onto a biological sample, we next sought to demonstrate that these barcodes could be retrieved for sequencing. Our overall sequencing strategy is analogous to other feature barcoding strategies (Fig. 6.5a). After photochemical patterning, DNA zipcodes remain covalently bound to the cell surface while the tissue is digested and prepared as a suspension. Microfluidic encapsulation of cells and barcoded beads

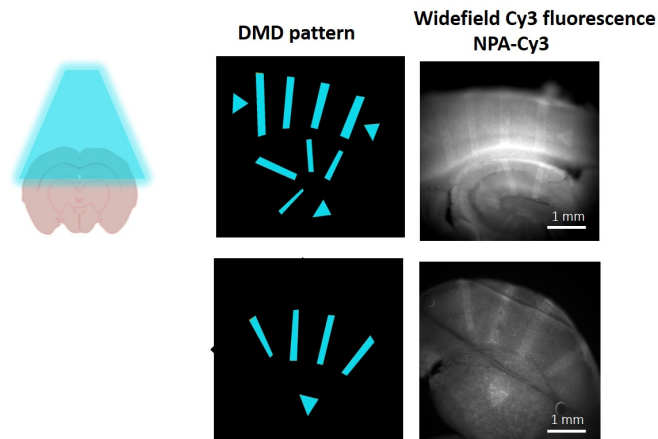


**Figure 6.4: Demonstration of photochemical labeling in brain tissue.** Application of patterned 470 nm light in the presence of TzNPA and subsequent development with TCO-Cy3 enables photochemical labeling within brain slice samples..

within droplets allows for the ligation of zipcodes from a given cell with their corresponding bead barcodes during reverse-transcriptase mediated cDNA generation. The resultant cDNA library can then be prepared and submitted for next-generation sequencing (NGS) according to standard protocols.<sup>246</sup>

The specifics of barcode ligation scheme are outlined in Figure 6.5b. Spatial zipcodes are designed to have a common 5' adapter, a 3' polyA tail, and a unique barcode associated with its corresponding pattern. Bead-associated DNA oligos in turn have a polyT tail (for mRNA capture), a bead barcode which can be used to identify an individual cell, a UMI which can be used to detect an individual ligated transcript post-amplification, as well as a shared 5' adapter. The polyA tail of the zipcodes allows these molecules to masquerade as mRNAs and ligate to bead barcodes via reverse transcriptase activity. The corresponding dsDNA molecule contains co-occurring zipcodes, bead barcodes, and UMIs on a single molecule, allowing for the quantitative assignment of zipcode counts for single cells.

We performed a pilot experiment using the 10x Genomics Chromium platform. Two samples

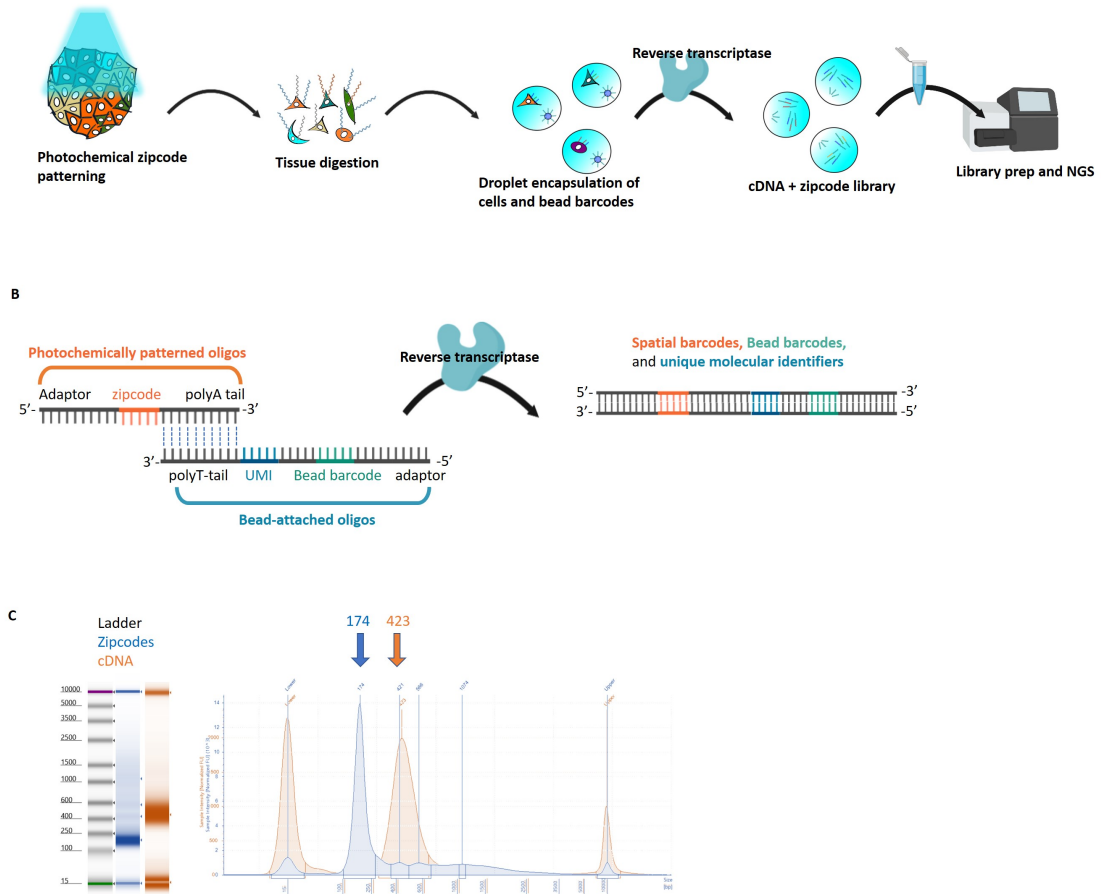


**Figure 6.5: Sequencing zipcodes.** A) Strategy for entirely sequencing pipeline. After photochemical patterning of barcode patterns, cells retain surface-labeled DNA through droplet encapsulation and cDNA generation. During library preparation, a size separation step can be used to enrich the relative proportion of the library containing zipcodes. B) Molecular biology of zipcode assignment. A polyA tail on the 3' end of the zipcode allows it to masquerade as an mRNA and capture bead primer sequences. Reverse transcription ligates zipcode sequences to bead barcodes and UMIs, allowing for association and quantification of features with their corresponding cells. C) TapeStation profile of sequencing libraries after photopatterning and encapsulation with a 10x Genomics Chromium system. The zipcode library shows a peak at 174 basepairs, indicative of successful ligation and retrieval of zipcode-bead barcode constructs.

were prepared: one each using a binary encoding scheme, and another using an analog encoding scheme. Each sample was encoded with two zipcodes in 20 minute illuminations ( $5\ \mu\text{M}$  TzNPA) followed by 2 minutes of development with  $2\ \mu\text{M}$  zipcode oligo). After labeling, cells were dispersed from the sample and washed three times in PBS prior to resuspension in 10x Genomics buffer (PBS with 0.4 % BSA). Separate zipcode sets were used for the two photopatterned samples (for a total of four separate barcode sequences), and cells were pooled prior to preparation of the Gel bead-in Emulsion (GEM). This created an internal control so that cell-attached reads (which should separate between cells in the two conditions) could be disambiguated from background oligos (which will be distributed evenly across all cells due to pooling).

Over 200k cells were recovered from the pooled samples. Prior to running the 10x Chromium system, cells were diluted to a working concentration of 900 cells/ $\mu\text{L}$ . Optical measurements indicated 95% cell viability after photopatterning and re-suspension, comfortably above the recommended cutoff and suggesting that the photochemical barcoding scheme is not coarsely injurious to the target sample. We loaded 8.9  $\mu\text{L}$  of cell suspension (at 900 cells/ $\mu\text{L}$ ) and 37.7  $\mu\text{L}$  of nuclease-free water into a Chromium chip in order to target a recovery density of 5000 cells. After GEM formation and cDNA amplification, we split the resultant DNA pool into a high-molecular weight fraction (containing the cDNAs) and a low-molecular weight fraction (containing our zipcode-bead barcode ligations) prior to further processing using a magnetic-bead based size selection.<sup>246</sup> The cDNA library was then fragmented to a target size distribution of  $\sim 400$  bp, in line with Illumina flow cell requirements. In parallel, the low-molecular fraction was amplified using the shared zipcode and bead barcode adapter primers in order to enrich the pool of target molecules.<sup>246</sup> After two successive amplifications (first 8x, then 12x thermocycles) we measured the size distribution of both zipcode and cDNA fragment libraries on an Agilent 4200 TapeStation (High Sensitivity D5000 Screen type) (Fig. 6.5). The observed distributions suggested successful retrieval of both zipcode libraries (expected length = 180 bp) and cDNA fragments (expected length  $\sim 400$  bp).

At the time of writing, next-generation sequencing of these libraries is still pending. These results will conclusively assess the viability of labeling photopatterned zipcodes onto existing commercially available scRNAseq pipelines; whether multiple zipcodes can be multiplexed in serial; and whether graded patterns of light can be used to encode analog information.

#### 6.4 OUTLOOK

A means of photochemically mapping cells which are profiled through droplet-based scRNAseq would unlock transformative applications in systems biology. Crucially, this method could resolve spatial location and single cell gene expression profiles on the same sample, and in many thousands of single cells in parallel. Alternative methods for mapping deep transcriptomic data all rely on some form of referencing to independently measured atlases. For example, MERFISH and SlideSeq require cross-referencing with independent scRNAseq datasets in order to combine spatial resolution with full-depth transcriptional profiling in single cells.<sup>191,230</sup> Computational methods of spatial inference similarly rely on databases of serially acquired *in situ* hybridizations of ‘sentinel’ genes.<sup>237</sup> For the study of systems where patterns of gene expression are reliably consistent and well-understood between measured replicates (e.g. in a classical model organism), the use of a reference atlas may be straightforward and appropriate. However, this reliance imposes a fundamental constraint on the application of these techniques to systems where genetic patterns may deviate considerably from any known other sample.

One promising application of photochemical barcoding may be in the study of *in vitro* stem cell based models of embryonic development (Fig. 6.6a).<sup>266</sup> While these systems recapitulate essential features of embryonic patterning, they execute this self-organization in a different biophysical context and may not exactly recapitulate patterns observed in a reference embryo. By generating spatial maps of scRNAseq data in a single sample, one can generate assumption-free maps of stem cell self-

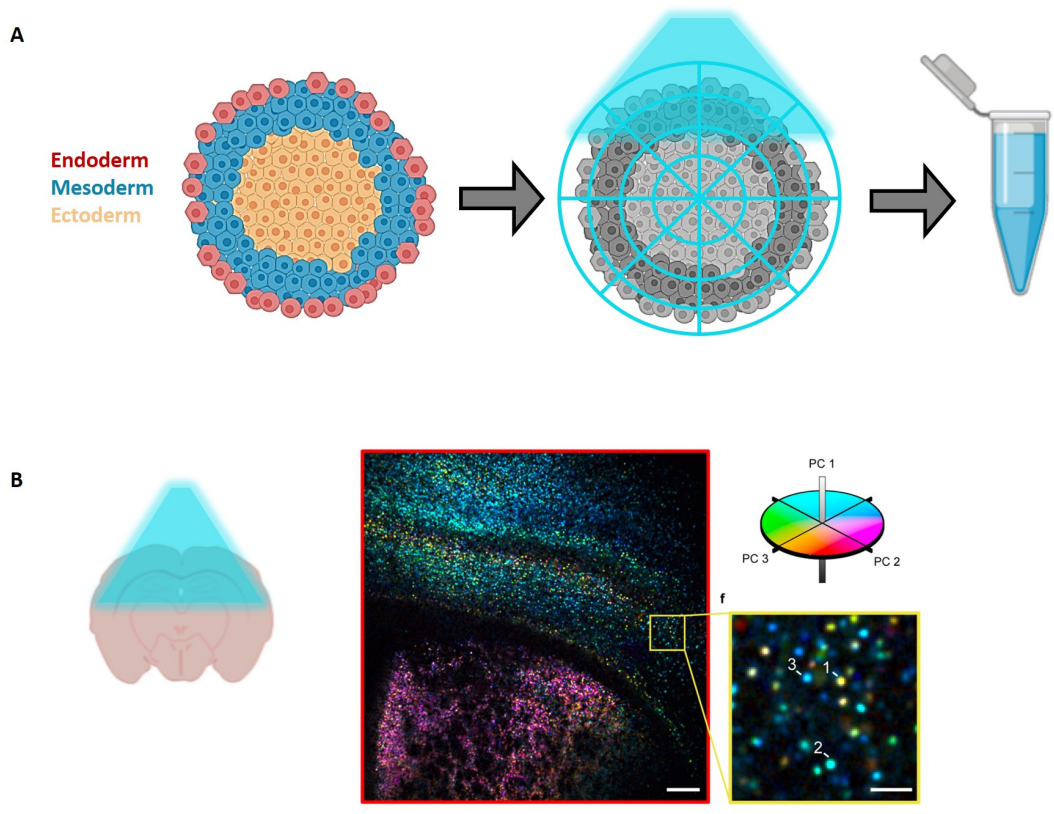


**Figure 6.6: Applications of photochemical zipcoding.** A) By using zipcode photopatterning to apply spatial coordinates to a colony of embryonic stem cells, the spatial structure of the full-transcriptome response can be mapped to study fundamental principles of biological self-organization. Because the coordinates are optically defined, they can be flexibly configured depending on the question of interest (e.g. analog of binary encoding? Cartesian or polar coordinates?). B) Panel excerpted from Farhi, Parot et al<sup>87</sup> depicting widefield characterization of electrophysiological phenotypes of thousands of cells in parallel. Combining functional neurophysiological measurements with maps of full-depth gene expression in single cells can reveal to what extent the transcriptional profile of a cell determines its physiological function.

organization. Correlations in these patterns within samples, or deviations across samples grown under different growth conditions, may yield insight into the fundamental principles through which stem cells self-organize.

Another application may lie in the mapping of pathologies of self-organization. In the context of normal development, patterns of cell types may be reproducible and amenable to atlas referencing, but in the setting of disease, each pathology may manifest in its own way. For example: mapping gene expression in tumor sections could be a powerful way to understand pattern-forming principles underlying cancer metastasis. Because our photochemical method does not require the expression of any transgenic constructs, it could in principle be applied to clinical samples resected from human patients. If this technique were to mature to scale of clinical application, the requirement to measure spatial location and gene expression in the same sample would become particularly urgent. Each patient's cancer is unique and cannot be strictly compared to any canonical reference. By mapping spatial distributions of rare and cancer-associated cell types in a single sample, new insights may be gained into clinical oncology.

A final application may come in correlating transcriptomic classification with physiological dynamics (Fig. 6.6b) It is an outstanding challenge to connect the profiling of cells types via scRNAseq with their functional roles in a physiological context: for example, how the gene expression profile of a neuronal subtype predicts its electrophysiological dynamics within a circuit. By pairing new methods for optically profiling physiology<sup>87</sup> with spatially resolved scRNAseq, we can assemble a more complete picture of how transcriptional heterogeneity dictates biological function.

The potential for photochemical barcoding to realize each of these applications will depend on the spatial resolution and scale which it can achieve. In principle, photochemical patterning can achieve diffraction-limited resolution, so cellular-scale spatial resolution is achievable (as droplet sequencing methods ultimately bin spatial location at the level of individual cells). In practice, spatial resolution may be set by tissue scattering or signal bandwidth. The former can be addressed by

using tissue fixation and sectioning preparations which are compatible with nuclear scRNAseq. Ultimately, even somewhat coarse-grained spatial 'zipcoding' of scRNAseq data could address many open questions in embryology, pathology, and physiology.

## 6.5 CONTRIBUTIONS

Adam Cohen and I conceived of the overall strategy for photochemically barcoding features for scRNAseq, with input from Daniel Hochbaum. I designed the two step photochemical labeling scheme, synthesized reagents, demonstrated optical patterning of DNA barcodes, and generated the pilot library using a 10x Chromium system. Nicole El-Ali and the Harvard Bauer Core Facility team trained me on 10x Genomics instrumentation and operation, and supervised the pilot library preparation. Sunia Trager at the Harvard Bauer Core assisted in mass spectrometry validation of synthesized reagents. Tian He and Nate Lord also gave helpful feedback and commentary. Adam Cohen oversaw and supervised this project.

# 7

## Conclusion

Light is a generically powerful medium for interfacing with complex biological systems. By pairing methods from optical physics to pattern and collect photons with precise resolution with combinations of naturally-evolved and engineered photoresponsive reagents, optogenetics can be used to generate high-dimensional, spatiotemporally precise interfaces to a range of physiological processes. While the utility of optogenetics in modern systems neuroscience is now well-established, there are ample opportunities to extend these approaches to the study of complex and multiscale interactions

during embryonic development. By combining optogenetics with reduced experimental systems which capture basic principles of biological organization in a setting isolated from confounding factors, ‘synthetic physiology’ can continue to reveal fundamental mathematical principles which coordinate biological patterning.

Our work in synthetic electrophysiology demonstrates that engineering bioelectrical tissues with all-optical electrophysiological interfaces enables the study of electrical tissues as excitable media. We have shown that synthetic bioelectric tissues can be used to engineer functional modules capable of information processing<sup>186</sup>; to study biophysical determinants of stability and chaos<sup>184</sup>; and to reveal new classes of electrical patterning.<sup>185</sup> Future work could build upon these results in at least two directions. First, hypotheses generated *in vitro* could be used to hunt for physiological instantiations *in vivo*. Can an electrical phase transition be observed during myogenesis in a developing zebrafish embryo? Could electrical domains be involved in systems where Kir2.1 mutations have been found to result in developmental abnormalities?<sup>65</sup>

Another extension of synthetic electrophysiology will involve the study of mechanisms through which changes in voltage can be biochemically transduced into changes in gene expression. Electrical regulation of intracellular calcium (through e.g. window currents in voltage-gated calcium channels) is one intuitive mechanism, but the widespread coupling of calcium to myriad biochemical pathways raises the question of whether more specific transduction mechanisms are possible. For example, is the signaling activity of transmembrane morphogen receptors at all voltage dependent? In principle, any transmembrane protein could have voltage-gated activity, but characterizing these effects *in vivo* would be extremely challenging. Combining optogenetic control of membrane potential with reduced systems for measuring morphogen signaling<sup>8</sup> could allow for the explicit demonstration of voltage regulation in a specific morphogen pathway (Fig. 7.1a). In principle, voltage *gradients* could also couple to gene expression through the electrophoretic accumulation of gap-junction permeable second messengers (Ca, cAMP) near domain boundaries (Fig. 7.1b). Reduced

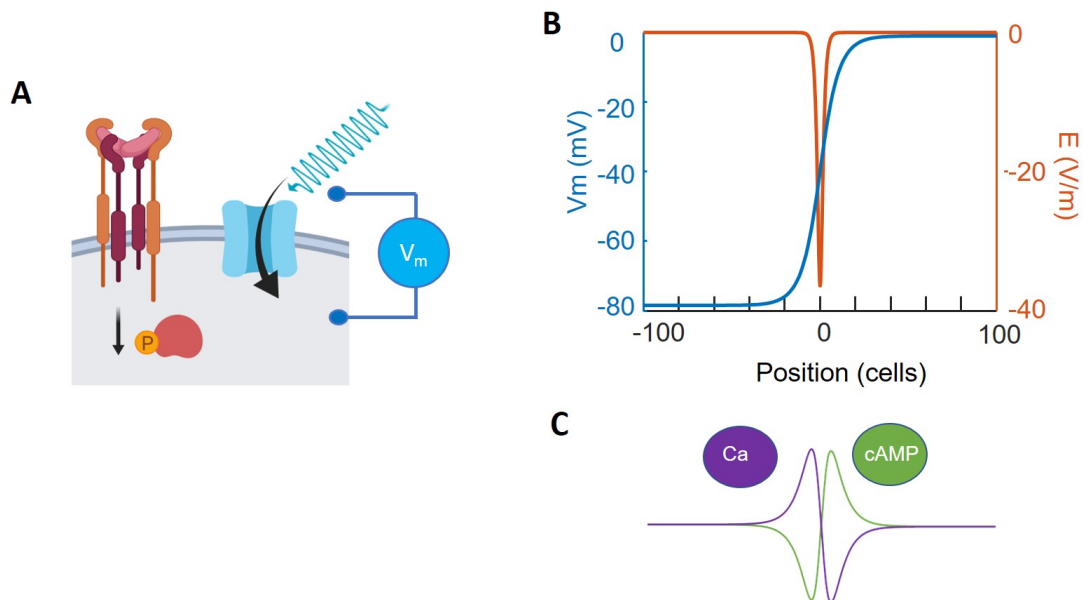


**Figure 7.1: Voltage as a morphogen.** A) By expressing depolarizing and hyperpolarizing ion channels in morphogen reporter cell lines, we can test whether physiological perturbations to voltage can modulate the signaling activity of receptor kinases. B) Analytical solution to the domain wall profile in electrical bistable cells, and the associated electric field. C) Assuming some baseline calcium and cyclic AMP maintenance, bio-electrophoresis could in principle drive depletion and accumulation zones of second messengers. The effects in B) and C) would be analogous to those found in semiconductor P-N junctions.

systems represent ideal platforms to study these effects which may be obscured *in vivo* by biological complexity.

The remainder of this thesis has focused on developing analogous optical tools for studying biochemical-genetic pattern formation with spatiotemporal precision. The application of our OptoNodal platform to the zebrafish model system can enable new pressure-tests of mutually consistent models of Nodal's role in embryonic morphogenesis. The ability to specify germ layer identity within a vertebrate embryo can also enable quantitative study of a cell fate decision as a stochastic process. Photochemical barcoding can, if successfully developed into a mature pipeline, provide a complementary optical method for reading out responses of the embryo to these (nearly) arbitrary perturbations.

Eventually, the most powerful application of these tools may come in reduced, *in vitro* models

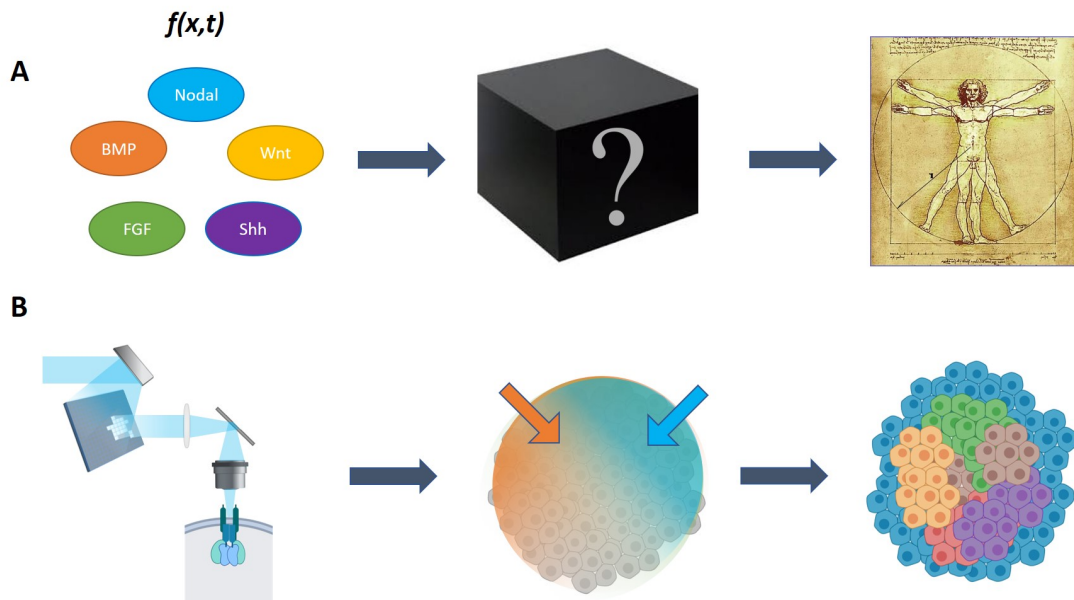


**Figure 7.2: Using light to study developmental decisions as dynamical systems.** A) Cartoon schematic of project motivation. Various spatiotemporally structured signals interact during embryonic development in order to assemble an organism, but the algorithms on which they rely on remain largely a 'black box'. B) By using patterns of light to activate optogenetic actuators (left) in reduced stem cell microcolony systems (middle) and then mapping transcriptional responses (right), we can measure how precise spatiotemporal aspects of morphogen signals determine developmental outcomes. Ideally, spectrally orthogonal control of multiple pathways could be realized.

of embryonic development (Fig. 7.2). Interpreting the response of a vertebrate embryo to complex morphogen signals is complicated by the concomitant activity of multiple background signaling pathways (e.g. BMP, FGF, etc) over which the experimenter has limited control. Deploying optical control of morphogen signaling in stem cell microcolonies could, to some extent, isolate the responses of embryonic self-organization from confounding factors. By deploying spatially resolved transcriptomic methods on these samples, one can build input-output models that characterize how embryonic cells processing morphogens as dynamical systems. The further development of spectrally orthogonal morphogen actuators (using e.g. red-light sensitive phytochromes<sup>139</sup>) will enable the study of how interactions between morphogen signals generate biological complexity.

Ultimately, the tools of synthetic physiology promise to enable more powerful studies of the mathematical and physical principles underlying biological self-organization. An improved understanding of these principles may enable more powerful *in vitro* model systems (e.g. embryoids, gastruloids, and organoids), which can in turn can enable more precise tests of biophysical models. Ideally, this approach could give rise to a virtuous cycle which yields new scientific insights as well as new strategies to fix biological self-organization in the setting of disease.

## References

- [1] Abdelfattah, A. S., Kawashima, T., Singh, A., Novak, O., Liu, H., Shuai, Y., Huang, Y.-C., Campagnola, L., Seeman, S. C., Yu, J., Zheng, J., Grimm, J. B., Patel, R., Friedrich, J., Mensh, B. D., Paninski, L., Macklin, J. J., Murphy, G. J., Podgorski, K., Lin, B.-J., Chen, T.-W., Turner, G. C., Liu, Z., Koyama, M., Svoboda, K., Ahrens, M. B., Lavis, L. D., & Schreiter, E. R. (2019). Bright and photostable chemigenetic indicators for extended in vivo voltage imaging. *Science*, (pp. eaav6416).
- [2] Adam, Y., Kim, J. J., Lou, S., Zhao, Y., Xie, M. E., Brinks, D., Wu, H., Mostajo-Radji, M. A., Kheifets, S., Parot, V., Chettih, S., Williams, K. J., Gmeiner, B., Farhi, S. L., Madisen, L., Buchanan, E. K., Kinsella, I., Zhou, D., Paninski, L., Harvey, C. D., Zeng, H., Arlotta, P., Campbell, R. E., & Cohen, A. E. (2019). Voltage imaging and optogenetics reveal behaviour-dependent changes in hippocampal dynamics. *Nature*, 569(7756), 413–417.
- [3] Adamatzky, A. (2001). *Computing in nonlinear media and automata collectives*. CRC Press.
- [4] Aliev, R. R. & Panfilov, A. V. (1996). A simple two-variable model of cardiac excitation. *Chaos, Solitons & Fractals*, 7(3), 293–301.
- [5] Allee, W. C., Park, O., Emerson, A. E., Park, T., & Schmidt, K. P. (1949). *Principles of animal ecology*.
- [6] Amin, A. S., Tan, H. L., & Wilde, A. A. (2010). Cardiac ion channels in health and disease. *Heart Rhythm*, 7(1), 117–126.
- [7] Anderson, P. W. (1972). More Is Different. *Science*, 177(4047), 393–396.
- [8] Antebi, Y. E., Linton, J. M., Klumpe, H., Bintu, B., Gong, M., Su, C., McCardell, R., & Elowitz, M. B. (2017). Combinatorial Signal Perception in the BMP Pathway. *Cell*, 170(6), 1184–1196.e24.
- [9] Antzelevitch, C. (2001). Basic mechanisms of reentrant arrhythmias. *Current Opinion in Cardiology*, 16(1), 1–7.
- [10] Aramaki, T. & Kondo, S. (2018). Method for disarranging the pigment pattern of zebrafish by optogenetics. *Developmental Biology*.

- [11] Arias, A. M. & Steventon, B. (2018). On the nature and function of organizers. *Development*, 145(5), dev159525.
- [12] Armoundas, A. A. & Cohen, R. J. (1997). Clinical utility of T-wave alternans. *Cardiac Electrophysiology Review*, 1(3), 390–394.
- [13] Ashcroft, F. M. & Rorsman, P. (1989). Electrophysiology of the pancreatic  $\beta$ -cell. *Progress in Biophysics and Molecular Biology*, 54(2), 87–143.
- [14] Ashe, H. L. & Briscoe, J. (2006). The interpretation of morphogen gradients. *Development*, 133(3), 385–394.
- [15] Banville, I. & Gray, R. A. (2002). Effect of action potential duration and conduction velocity restitution and their spatial dispersion on alternans and the stability of arrhythmias. *Journal of cardiovascular electrophysiology*, 13(11), 1141–1149.
- [16] Barkhausen, H. (1919). Zwei mit hilfe der neuen verstärker entdeckte erscheinungen. *Phys.Z*, 20, 401.
- [17] Barrett-Jolley, R., Lewis, R., Fallman, R., & Mobasher, A. (2010). The emerging chondrocyte channelome. *Frontiers in physiology*, 1, 135.
- [18] Bellono, N. W., Leitch, D. B., & Julius, D. (2017). Molecular basis of ancestral vertebrate electroreception. *Nature*, 543(7645), 391–396.
- [19] Bellono, N. W., Leitch, D. B., & Julius, D. (2018). Molecular tuning of electroreception in sharks and skates. *Nature*, 558(7708), 122.
- [20] Benguria, R. & Depassier, M. (1996). Speed of fronts of the reaction-diffusion equation. *Physical Review Letters*, 77(6), 1171.
- [21] Bennett, M. V. L., Wurzel, M., & Grundfest, H. (1961). The Electrophysiology of Electric Organs of Marine Electric Fishes. *The Journal of General Physiology*, 44(4), 757–804.
- [22] Bers, D. M. (2002). Cardiac excitation–contraction coupling. *Nature*, 415(6868), 198–205.
- [23] Birket, M. J., Ribeiro, M. C., Verkerk, A. O., Ward, D., Leitoguinho, A. R., Den Hartogh, S. C., Orlova, V. V., Devalla, H. D., Schwach, V., & Bellin, M. (2015). Expansion and patterning of cardiovascular progenitors derived from human pluripotent stem cells. *Nature biotechnology*, 33(9), 970–979.
- [24] Bisgrove, B. W., Essner, J. J., & Yost, H. J. (1999). Regulation of midline development by antagonism of lefty and nodal signaling. *Development*, 126(14), 3253–3262.
- [25] Boyden, E. S., Zhang, F., Bamberg, E., Nagel, G., & Deisseroth, K. (2005). Millisecond-timescale, genetically targeted optical control of neural activity. *Nature Neuroscience*, 8(9), 1263.

- [26] Brodsky, M. (2018). Turing-like patterns can arise from purely bioelectric mechanisms. *bioRxiv*, (pp. 336461).
- [27] Brownell, W. E., Qian, F., & Anvari, B. (2010). Cell membrane tethers generate mechanical force in response to electrical stimulation. *Biophysical journal*, 99(3), 845–852.
- [28] Bub, G., Shrier, A., & Glass, L. (2002). Spiral wave generation in heterogeneous excitable media. *Physical Review Letters*, 88(5), 058101.
- [29] Bub, G., Shrier, A., & Glass, L. (2005). Global organization of dynamics in oscillatory heterogeneous excitable media. *Physical Review Letters*, 94(2), 028105.
- [30] Buckley, C. E., Moore, R. E., Reade, A., Goldberg, A. R., Weiner, O. D., & Clarke, J. D. W. (2016). Reversible Optogenetic Control of Subcellular Protein Localization in a Live Vertebrate Embryo. *Developmental Cell*, 36(1), 117–126.
- [31] Burridge, P. W., Keller, G., Gold, J. D., & Wu, J. C. (2012). Production of de novo cardiomyocytes: Human pluripotent stem cell differentiation and direct reprogramming. *Cell Stem Cell*, 10(1), 16–28. J1: Cell Stem Cell.
- [32] Burton, R. A., Klimas, A., Ambrosi, C. M., Tomek, J., Corbett, A., Entcheva, E., & Bub, G. (2015). Optical control of excitation waves in cardiac tissue. *Nature photonics*, 9(12), 813.
- [33] Butterweck, A., Gergs, U., Elfgang, C., Willecke, K., & Traub, O. (1994). Immunochemical characterization of the gap junction protein connexin<sub>45</sub> in mouse kidney and transfected human hela cells. *The Journal of membrane biology*, 141(3), 247–256.
- [34] Buzsáki, G. (2006). *Rhythms of the Brain*. Oxford University Press.
- [35] Buzsáki, G. & Moser, E. I. (2013). Memory, navigation and theta rhythm in the hippocampal-entorhinal system. *Nature Neuroscience*, 16(2), 130–138.
- [36] Cabo, C., Pertsov, A. M., Baxter, W. T., Davidenko, J. M., Gray, R. A., & Jalife, J. (1994). Wave-front curvature as a cause of slow conduction and block in isolated cardiac muscle. *Circulation research*, 75(6), 1014–1028.
- [37] Calderón, J. C., Bolaños, P., & Caputo, C. (2014). The excitation–contraction coupling mechanism in skeletal muscle. *Biophysical reviews*, 6(1), 133–160.
- [38] Carballo, G. B., Honorato, J. R., de Lopes, G. P. F., & Spohr, T. C. L. d. S. e. (2018). A highlight on Sonic hedgehog pathway. *Cell Communication and Signaling*, 16(1), 11.
- [39] Cardin, J. A., Carlén, M., Meletis, K., Knoblich, U., Zhang, F., Deisseroth, K., Tsai, L.-H., & Moore, C. I. (2009). Driving fast-spiking cells induces gamma rhythm and controls sensory responses. *Nature*, 459(7247), 663–667.

- [40] Cervera, J., Alcaraz, A., & Mafe, S. (2014). Membrane potential bistability in nonexcitable cells as described by inward and outward voltage-gated ion channels. *The Journal of Physical Chemistry B*, 118(43), 12444–12450.
- [41] Cervera, J., Alcaraz, A., & Mafe, S. (2016). Bioelectrical signals and ion channels in the modeling of multicellular patterns and cancer biophysics. *Scientific reports*, 6, 20403.
- [42] Cervera, J., Manzanares, J. A., & Mafe, S. (2015). Electrical coupling in ensembles of nonexcitable cells: modeling the spatial map of single cell potentials. *The Journal of Physical Chemistry B*, 119(7), 2968–2978.
- [43] Chal, J., Al Tanoury, Z., Hestin, M., Gobert, B., Aivio, S., Hick, A., Cherrier, T., Nesmith, A. P., Parker, K. K., & Pourquié, O. (2016). Generation of human muscle fibers and satellite-like cells from human pluripotent stem cells in vitro. *Nature protocols*, 11(10), 1833.
- [44] Chemla, S. & Chavane, F. (2010). Voltage-sensitive dye imaging: Technique review and models. *Journal of Physiology-Paris*, 104(1), 40–50.
- [45] Chen, K. H., Boettiger, A. N., Moffitt, J. R., Wang, S., & Zhuang, X. (2015). Spatially resolved, highly multiplexed RNA profiling in single cells. *Science*, 348(6233), aaa6090.
- [46] Chen, T.-W., Wardill, T. J., Sun, Y., Pulver, S. R., Renninger, S. L., Baohan, A., Schreiter, E. R., Kerr, R. A., Orger, M. B., Jayaraman, V., Looger, L. L., Svoboda, K., & Kim, D. S. (2013). Ultra-sensitive fluorescent proteins for imaging neuronal activity. *Nature*, 499(7458), 295–300.
- [47] Chen, Y. & Schier, A. F. (2002). Lefty Proteins Are Long-Range Inhibitors of Squint-Mediated Nodal Signaling. *Current Biology*, 12(24), 2124–2128.
- [48] Cherry, E. M. & Fenton, F. H. (2004). Suppression of alternans and conduction blocks despite steep apd restitution: electrotonic, memory, and conduction velocity restitution effects. *American journal of physiology. Heart and circulatory physiology*, 286(6), H2332–41.
- [49] Chien, M.-P., Werley, C. A., Farhi, S. L., & Cohen, A. E. (2015). Photostick: a method for selective isolation of target cells from culture. *Chemical Science*, 6(3), 1701–1705.
- [50] Chifflet, S., Hernández, J. A., & Grasso, S. (2005). A possible role for membrane depolarization in epithelial wound healing. *American Journal of Physiology-Cell Physiology*, 288(6), C1420–C1430.
- [51] Chow, B. Y., Han, X., Dobry, A. S., Qian, X., Chuong, A. S., Li, M., Henninger, M. A., Belfort, G. M., Lin, Y., Monahan, P. E., & Boyden, E. S. (2010). High-performance genetically targetable optical neural silencing by light-driven proton pumps. *Nature*, 463(7277), 98–102.

- [52] Clay, J. R. & Shrier, A. (1999). On the role of subthreshold dynamics in neuronal signaling. *Journal of theoretical biology*, 197(2), 207–216.
- [53] Clayton, R., Bernus, O., Cherry, E., Dierckx, H., Fenton, F., Mirabella, L., Panfilov, A., Sachse, F. B., Seemann, G., & Zhang, H. (2011). Models of cardiac tissue electrophysiology: progress, challenges and open questions. *Progress in biophysics and molecular biology*, 104(1-3), 22–48.
- [54] Cohen, A. E. (2004). *Nanoscale mechanics*.
- [55] Colatsky, T., Fermini, B., Gintant, G., Pierson, J. B., Sager, P., Sekino, Y., Strauss, D. G., & Stockbridge, N. (2016). The comprehensive in vitro proarrhythmia assay (cipa) initiative — update on progress. ID: 271243.
- [56] Constantin, B. & Cronier, L. (2000). Involvement of gap junctional communication in myogenesis. *International Rev. Cytol.*, 196, 1–65.
- [57] Coombes, S. (2005). Waves, bumps, and patterns in neural field theories. *Biological Cybernetics*, 93(2), 91–108.
- [58] Cornwell, M., Vangala, M., Taing, L., Herbert, Z., Köster, J., Li, B., Sun, H., Li, T., Zhang, J., & Qiu, X. (2018). Viper: Visualization pipeline for rna-seq, a snakemake workflow for efficient and complete rna-seq analysis. *BMC bioinformatics*, 19(1), 135.
- [59] Courtemanche, M., Glass, L., & Keener, J. P. (1993). Instabilities of a propagating pulse in a ring of excitable media. *Physical Review Letters*, 70(14), 2182.
- [60] Crill, W. E. (1996). Persistent sodium current in mammalian central neurons. *Annual Review of Physiology*, 58(1), 349–362.
- [61] Cross, M. & Greenside, H. (2009). *Pattern formation and dynamics in nonequilibrium systems*. Cambridge University Press.
- [62] Cross, M. H., Cross, P., & Brinster, R. (1973). Changes in membrane potential during mouse egg development. *Developmental biology*, 33(2), 412–416.
- [63] Crunelli, V., Tóth, T. I., Cope, D. W., Blethyn, K., & Hughes, S. W. (2005). The ‘window’-type calcium current in brain dynamics of different behavioural states. *The Journal of physiology*, 562(1), 121–129.
- [64] Cytrynbaum, E. & Keener, J. P. (2002). Stability conditions for the traveling pulse: Modifying the restitution hypothesis. *Chaos: An Interdisciplinary Journal of Nonlinear Science*, 12(3), 788–799.

- [65] Dahal, G. R., Pradhan, S. J., & Bates, E. A. (2017). Inwardly rectifying potassium channels influence drosophila wing morphogenesis by regulating dpp release. *Development*, 144(15), 2771–2783.
- [66] Dana, H., Mohar, B., Sun, Y., Narayan, S., Gordus, A., Hasseman, J. P., Tsegaye, G., Holt, G. T., Hu, A., Walpita, D., et al. (2016). Sensitive red protein calcium indicators for imaging neural activity. *Elife*, 5, e12727.
- [67] Dascal, N. (2001). Ion-channel regulation by g proteins. *Trends in Endocrinology & Metabolism*, 12(9), 391–398.
- [68] Datlinger, P., Rendeiro, A. F., Schmidl, C., Krausgruber, T., Traxler, P., Klughammer, J., Schuster, L. C., Kuchler, A., Alpar, D., & Bock, C. (2017). Pooled CRISPR screening with single-cell transcriptome readout. *Nature Methods*, 14(3), 297–301.
- [69] de Lacy Costello, B., Toth, R., Stone, C., Adamatzky, A., & Bull, L. (2009). Implementation of glider guns in the light-sensitive belousov-zhabotinsky medium. *Physical Review E*, 79(2), 026114.
- [70] Deglincerti, A., Croft, G. F., Pietila, L. N., Zernicka-Goetz, M., Siggia, E. D., & Brivanlou, A. H. (2016). Self-organization of the *in vitro* attached human embryo. *Nature*, 533(7602), 251–254.
- [71] Denning, C., Borgdorff, V., Crutchley, J., Firth, K. S., George, V., Kalra, S., Kondrashov, A., Hoang, M. D., Mosqueira, D., & Patel, A. (2016). Cardiomyocytes from human pluripotent stem cells: from laboratory curiosity to industrial biomedical platform. *Biochimica et Biophysica Acta (BBA)-Molecular Cell Research*, 1863(7), 1728–1748.
- [72] Dixit, A., Parnas, O., Li, B., Chen, J., Fulco, C. P., Jerby-Arnon, L., Marjanovic, N. D., Dionne, D., Burks, T., Raychowdhury, R., Adamson, B., Norman, T. M., Lander, E. S., Weissman, J. S., Friedman, N., & Regev, A. (2016). Perturb-Seq: Dissecting Molecular Circuits with Scalable Single-Cell RNA Profiling of Pooled Genetic Screens. *Cell*, 167(7), 1853–1866.e17.
- [73] Dobin, A., Davis, C. A., Schlesinger, F., Drenkow, J., Zaleski, C., Jha, S., Batut, P., Chaisson, M., & Gingeras, T. R. (2013). Star: ultrafast universal rna-seq aligner. *Bioinformatics*, 29(1), 15–21.
- [74] Donoghue, M., Wakimoto, H., Maguire, C. T., Acton, S., Hales, P., Stagliano, N., Fairchild-Huntress, V., Xu, J., Lorenz, J. N., Kadambi, V., et al. (2003). Heart block, ventricular tachycardia, and sudden death in ace2 transgenic mice with downregulated connexins. *Journal of molecular and cellular cardiology*, 35(9), 1043–1053.
- [75] Draper, M. & Mya-Tu, M. (1959). A comparison of the conduction velocity in cardiac tissues of various mammals. *Experimental physiology*, 44(1), 91–109.

- [76] Du, D. T., Hellen, N., Kane, C., & Terracciano, C. M. (2015). Action potential morphology of human induced pluripotent stem cell-derived cardiomyocytes does not predict cardiac chamber specificity and is dependent on cell density. *Biophysical journal*, 108(1), 1–4.
- [77] Duan, L., Hope, J., Ong, Q., Lou, H.-Y., Kim, N., McCarthy, C., Acero, V., Lin, M. Z., & Cui, B. (2017). Understanding CRY2 interactions for optical control of intracellular signaling. *Nature Communications*, 8(1).
- [78] Dubrulle, J., Jordan, B. M., Akhmetova, L., Farrell, J. A., Kim, S.-H., Solnica-Krezel, L., & Schier, A. F. (2015). Response to Nodal morphogen gradient is determined by the kinetics of target gene induction. *eLife*, 4, e05042.
- [79] Durant, F., Bischof, J., Fields, C., Morokuma, J., LaPalme, J., Hoi, A., & Levin, M. (2019). The Role of Early Bioelectric Signals in the Regeneration of Planarian Anterior/Posterior Polarity. *Biophysical Journal*, 116(5), 948–961.
- [80] Echebarria, B. & Karma, A. (2002). Instability and spatiotemporal dynamics of alternans in paced cardiac tissue. *Physical Review Letters*, 88(20), 208101.
- [81] Einthoven, W. (1912). The different forms of the human electrocardiogram and their signification. *The Lancet*.
- [82] Eisner, D. A., Caldwell, J. L., Kistamás, K., & Trafford, A. W. (2017). Calcium and excitation-contraction coupling in the heart. *Circulation research*, 121(2), 181–195.
- [83] Elowitz, M. B. & Leibler, S. (2000). A synthetic oscillatory network of transcriptional regulators. *Nature*, 403(6767), 335.
- [84] Emiliani, V., Cohen, A. E., Deisseroth, K., & Häusser, M. (2015). All-optical interrogation of neural circuits. *Journal of Neuroscience*, 35(41), 13917–13926.
- [85] Ernst, S. G. (1997). A Century of Sea Urchin Development. *Integrative and Comparative Biology*, 37(3), 250–259.
- [86] Fan, L. Z., Kheifets, S., Böhm, U. L., Piatkevich, K. D., Wu, H., Parot, V., Xie, M. E., Boyden, E. S., Takesian, A. E., & Cohen, A. E. (2019). All-optical electrophysiology reveals excitation, inhibition, and neuromodulation in cortical layer I. *bioRxiv*, (pp. 614172).
- [87] Farhi, S. L., Parot, V. J., Grama, A., Yamagata, M., Abdelfattah, A. S., Adam, Y., Lou, S., Kim, J. J., Campbell, R. E., Cox, D. D., & Cohen, A. E. (2019). Wide-area all-optical neurophysiology in acute brain slices. *Journal of Neuroscience*, (pp. 0168–19).
- [88] Farrell, J. A., Wang, Y., Riesenfeld, S. J., Shekhar, K., Regev, A., & Schier, A. F. (2018). Single-cell reconstruction of developmental trajectories during zebrafish embryogenesis. *Science*, 360(6392), eaar3131.

- [89] Fast, V. G. & Kléber, A. G. (1997). Role of wavefront curvature in propagation of cardiac impulse. *Cardiovascular research*, 33(2), 258–271.
- [90] Fast, V. G. & Kléber, A. G. (1995). Cardiac tissue geometry as a determinant of unidirectional conduction block: assessment of microscopic excitation spread by optical mapping in patterned cell cultures and in a computer model. *Cardiovascular research*, 29(5), 697–707.
- [91] Fauny, J.-D., Thisse, B., & Thisse, C. (2009). The entire zebrafish blastula-gastrula margin acts as an organizer dependent on the ratio of Nodal to BMP activity. *Development*, 136(22), 3811–3819.
- [92] Feldman, B., Dougan, S. T., Schier, A. F., & Talbot, W. S. (2000). Nodal-related signals establish mesendodermal fate and trunk neural identity in zebrafish. *Current biology: CB*, 10(9), 531–534.
- [93] Feldman, B., Gates, M. A., Egan, E. S., Dougan, S. T., Rennebeck, G., Sirotkin, H. I., Schier, A. F., & Talbot, W. S. (1998). Zebrafish organizer development and germ-layer formation require nodal-related signals. *Nature*, 395(6698), 181–185.
- [94] FitzHugh, R. (1961). Impulses and Physiological States in Theoretical Models of Nerve Membrane. *Biophysical Journal*, 1(6), 445–466.
- [95] Frame, L. H. & Simson, M. B. (1988). Oscillations of conduction, action potential duration, and refractoriness. a mechanism for spontaneous termination of reentrant tachycardias. *Circulation*, 78(5), 1277–1287.
- [96] Friedland, A. E., Lu, T. K., Wang, X., Shi, D., Church, G., & Collins, J. J. (2009). Synthetic gene networks that count. *Science*, 324(5931), 1199–1202.
- [97] Fyhn, M., Molden, S., Witter, M. P., Moser, E. I., & Moser, M.-B. (2004). Spatial representation in the entorhinal cortex. *Science (New York, N.Y.)*, 305(5688), 1258–1264.
- [98] Gallaher, J., Bier, M., & van Heukelom, J. S. (2010). First order phase transition and hysteresis in a cell's maintenance of the membrane potential—an essential role for the inward potassium rectifiers. *Biosystems*, 101(3), 149–155.
- [99] Galvani, L. (1791). D viribus electricitatis in motu musculari : Commentarius. *Bologna: Tip. Istituto delle Scienze*.
- [100] Gardner, T. S., Cantor, C. R., & Collins, J. J. (2000). Construction of a genetic toggle switch in escherichia coli. *Nature*, 403(6767), 339.
- [101] Gellens, M. E., George, A. L., Chen, L., Chahine, M., Horn, R., Barchi, R. L., & Kallen, R. G. (1992). Primary structure and functional expression of the human cardiac tetrodotoxin-insensitive voltage-dependent sodium channel. *Proceedings of the National Academy of Sciences*, 89(2), 554–558.

- [102] Glass, L., Guevara, M. R., Shrier, A., & Perez, R. (1983). Bifurcation and chaos in a periodically stimulated cardiac oscillator. *Physica D: Nonlinear Phenomena*, 7(1-3), 89–101.
- [103] Glass, L., Nagai, Y., Hall, K., Talajic, M., & Nattel, S. (2002). Predicting the entrainment of reentrant cardiac waves using phase resetting curves. *Physical Review E*, 65(2), 021908.
- [104] Gong, Y., Huang, C., Li, J. Z., Grewe, B. F., Zhang, Y., Eismann, S., & Schnitzer, M. J. (2015). High-speed recording of neural spikes in awake mice and flies with a fluorescent voltage sensor. *Science*, 350(6266), 1361–1366.
- [105] Govorunova, E. G., Sineshchekov, O. A., Janz, R., Liu, X., & Spudich, J. L. (2015). Natural light-gated anion channels: A family of microbial rhodopsins for advanced optogenetics. *Science*, 349(6248), 647–650.
- [106] Govorunova, E. G., Sineshchekov, O. A., Li, H., Janz, R., & Spudich, J. L. (2013). Characterization of a highly efficient blue-shifted channelrhodopsin from the marine alga *Platymonas subcordiformis*. *The Journal of Biological Chemistry*, 288(41), 29911–29922.
- [107] Green, J. B. & Sharpe, J. (2015). Positional information and reaction-diffusion: two big ideas in developmental biology combine. *Development*, 142(7), 1203–1211.
- [108] Gritsman, K., Talbot, W. S., & Schier, A. F. (2000). Nodal signaling patterns the organizer. *Development*, 127(5), 921–932.
- [109] Grusch, M., Schelch, K., Riedler, R., Reichhart, E., Differ, C., Berger, W., Ingles-Prieto, A., & Janovjak, H. (2014). Spatio-temporally precise activation of engineered receptor tyrosine kinases by light. *The EMBO Journal*, 33(15), 1713–1726.
- [110] Guevara, M., Ward, G., Shrier, A., & Glass, L. (1984). Electrical alternans and period doubling bifurcations. *IEEE Comp. Cardiol*, 562, 167–170.
- [111] Guntas, G., Hallett, R. A., Zimmerman, S. P., Williams, T., Yumerefendi, H., Bear, J. E., & Kuhlman, B. (2015). Engineering an improved light-induced dimer (iLID) for controlling the localization and activity of signaling proteins. *Proceedings of the National Academy of Sciences*, 112(1), 112–117.
- [112] Guo, T., Al Abed, A., Lovell, N. H., & Dokos, S. (2011). Parameter fitting using multiple datasets in cardiac action potential modeling. *Conference proceedings: ... Annual International Conference of the IEEE Engineering in Medicine and Biology Society. IEEE Engineering in Medicine and Biology Society. Annual Conference*, 2011, 158–161.
- [113] Gurdon, J., Tiller, E., Roberts, J., & Kato, K. (1993). A community effect in muscle development. *Current biology*, 3(1), 1–11.

- [114] Habib, N., Avraham-Davidi, I., Basu, A., Burks, T., Shekhar, K., Hofree, M., Choudhury, S. R., Aguet, F., Gelfand, E., Ardlie, K., Weitz, D. A., Rozenblatt-Rosen, O., Zhang, F., & Regev, A. (2017). Massively parallel single-nucleus RNA-seq with DroNc-seq. *Nature Methods*, 14(10), 955–958.
- [115] Harvey, S. A. & Smith, J. C. (2009). Visualisation and Quantification of Morphogen Gradient Formation in the Zebrafish. *PLOS Biology*, 7(5), e1000101.
- [116] Heintz, U. & Schlichting, I. (2016). Blue light-induced LOV domain dimerization enhances the affinity of Aureochrome 1a for its target DNA sequence. *eLife*, 5.
- [117] Hibino, H., Inanobe, A., Furutani, K., Murakami, S., Findlay, I., & Kurachi, Y. (2010). Inwardly rectifying potassium channels: their structure, function, and physiological roles. *Physiological Reviews*, 90(1), 291–366.
- [118] Hille, B. (2001). *Ion channels of excitable membranes*, volume 507. Sunderland, MA: Sinauer.
- [119] Hirn, C., Shapovalov, G., Petermann, O., Roulet, E., & Ruegg, U. T. (2008). Nav1.4 Deregulation in Dystrophic Skeletal Muscle Leads to Na<sup>+</sup> Overload and Enhanced Cell Death. *The Journal of General Physiology*, 132(2), 199–208.
- [120] Hochbaum, D. R., Zhao, Y., Farhi, S. L., Klapoetke, N., Werley, C. A., Kapoor, V., Zou, P., Kralj, J. M., Maclaurin, D., Smedemark-Margulies, N., Saulnier, J. L., Boulting, G. L., Straub, C., Cho, Y. K., Melkonian, M., Wong, G. K.-S., Harrison, D. J., Murthy, V. N., Sabatini, B. L., Boyden, E. S., Campbell, R. E., & Cohen, A. E. (2014). All-optical electrophysiology in mammalian neurons using engineered microbial rhodopsins. *Nature Methods*, 11(8), 825–833.
- [121] Hodgkin, A. L. & Huxley, A. F. (1952). A quantitative description of membrane current and its application to conduction and excitation in nerve. *The Journal of Physiology*, 117(4), 500–544.
- [122] Hoekstra, M., Mummery, C. L., Wilde, A. A., Bezzina, C. R., & Verkerk, A. O. (2012). Induced pluripotent stem cell derived cardiomyocytes as models for cardiac arrhythmias. *Front Physiol*, 3. ID: Hoekstra2012.
- [123] Hoffman, B. F., DE Carvalho, A. P., Mello, W. C., & Cranefield, P. F. (1959). Electrical activity of single fibers of the atrioventricular node. *Circulation research*, 7(1), 11–18.
- [124] Hsu, H., Huang, E., Yang, X.-c., Karschin, A., Labarca, C., Figl, A., Ho, B., Davidson, N., & Lester, H. (1993). Slow and incomplete inactivations of voltage-gated channels dominate encoding in synthetic neurons. *Biophysical journal*, 65(3), 1196–1206.
- [125] Huang, Y.-L., Walker, A. S., & Miller, E. W. (2015). A Photostable Silicon Rhodamine Platform for Optical Voltage Sensing. *Journal of the American Chemical Society*, 137(33), 10767–10776.

- [126] Hughes, S. W., Cope, D. W., Toth, T. I., Williams, S. R., & Crunelli, V. (1999). All thalamocortical neurones possess a t-type calcium 'window' current that enables the expression of bistability-mediated activities. *The Journal of physiology*, 517(3), 805–815.
- [127] Hume, J. & Uehara, A. (1985). Ionic basis of the different action potential configurations of single guinea-pig atrial and ventricular myocytes. *The Journal of physiology*, 368(1), 525–544.
- [128] Hwang, B., Lee, J. H., & Bang, D. (2018). Single-cell RNA sequencing technologies and bioinformatics pipelines. *Experimental & Molecular Medicine*, 50(8), 1–14.
- [129] Inaba, M., Yamanaka, H., & Kondo, S. (2012). Pigment Pattern Formation by Contact-Dependent Depolarization. *Science*, 335(6069), 677–677.
- [130] Iwashita, M., Watanabe, M., Ishii, M., Chen, T., Johnson, S. L., Kurachi, Y., Okada, N., & Kondo, S. (2006). Pigment Pattern in jaguar/obelix Zebrafish Is Caused by a Kir7.1 Mutation: Implications for the Regulation of Melanosome Movement. *PLOS Genetics*, 2(11), e197.
- [131] Izhikevich, E. M. (2007). *Dynamical Systems in Neuroscience*. MIT press.
- [132] Izquierdo, E., Quinkler, T., & Renzis, S. D. (2018). Guided morphogenesis through optogenetic activation of Rho signalling during early Drosophila embryogenesis. *Nature Communications*, 9(1), 2366.
- [133] Jaitin, D. A., Weiner, A., Yofe, I., Lara-Astiaso, D., Keren-Shaul, H., David, E., Salame, T. M., Tanay, A., van Oudenaarden, A., & Amit, I. (2016). Dissecting Immune Circuits by Linking CRISPR-Pooled Screens with Single-Cell RNA-Seq. *Cell*, 167(7), 1883–1896.e15.
- [134] Jiruska, P., Curtis, M. d., Jefferys, J. G. R., Schevon, C. A., Schiff, S. J., & Schindler, K. (2013). Synchronization and desynchronization in epilepsy: controversies and hypotheses. *The Journal of Physiology*, 591(4), 787–797.
- [135] Johnson, H. E., Goyal, Y., Pannucci, N. L., Schüpbach, T., Shvartsman, S. Y., & Toettcher, J. E. (2017). The Spatiotemporal Limits of Developmental Erk Signaling. *Developmental Cell*, 40(2), 185–192.
- [136] Johnson, H. E. & Toettcher, J. E. (2019). Signaling Dynamics Control Cell Fate in the Early Drosophila Embryo. *Developmental Cell*, 48(3), 361–370.e3.
- [137] Jongsma, H. J. & Wilders, R. (2000). Gap junctions in cardiovascular disease. *Circulation research*, 86(12), 1193–1197.
- [138] Jun, J. J., Steinmetz, N. A., Siegle, J. H., Denman, D. J., Bauza, M., Barbarits, B., Lee, A. K., Anastassiou, C. A., Andrei, A., Aydın, F., Barbic, M., Blanche, T. J., Bonin, V., Couto, J., Dutta, B., Gratiy, S. L., Gutnisky, D. A., Häusser, M., Karsh, B., Ledochowitsch, P., Lopez,

- C. M., Mitelut, C., Musa, S., Okun, M., Pachitariu, M., Putzeys, J., Rich, P. D., Rossant, C., Sun, W.-l., Svoboda, K., Carandini, M., Harris, K. D., Koch, C., O’Keefe, J., & Harris, T. D. (2017). Fully integrated silicon probes for high-density recording of neural activity. *Nature*, 551(7679), 232–236.
- [139] Kaberniuk, A. A., Shemetov, A. A., & Verkhusha, V. V. (2016). A bacterial phytochrome-based optogenetic system controllable with near-infrared light. *Nature Methods*, 13(7), 591–597.
- [140] Kalderon, N., Epstein, M. L., & Gilula, N. B. (1977). Cell-to-cell communication and myogenesis. *The Journal of cell biology*, 75(3), 788–806.
- [141] Kaplan, D. T., Clay, J. R., Manning, T., Glass, L., Guevara, M. R., & Shrier, A. (1996). Sub-threshold dynamics in periodically stimulated squid giant axons. *Physical Review Letters*, 76(21), 4074.
- [142] Karakikes, I., Ameen, M., Termglinchan, V., & Wu, J. C. (2015). Human induced pluripotent stem cell-derived cardiomyocytes: Insights into molecular, cellular, and functional phenotypes. *Circulation research*, 117(1), 80–88. JI: Circ Res.
- [143] Karma, A. (1993). Spiral breakup in model equations of action potential propagation in cardiac tissue. *Physical review letters*, 71(7), 1103.
- [144] Karma, A. (1994). Electrical alternans and spiral wave breakup in cardiac tissue. *Chaos: An Interdisciplinary Journal of Nonlinear Science*, 4(3), 461–472.
- [145] Kawakami, K., Asakawa, K., Hibi, M., Itoh, M., Muto, A., & Wada, H. (2016). Gal4 Driver Transgenic Zebrafish: Powerful Tools to Study Developmental Biology, Organogenesis, and Neuroscience. *Advances in Genetics*, 95, 65–87.
- [146] Kawano, F., Suzuki, H., Furuya, A., & Sato, M. (2015). Engineered pairs of distinct photo-switches for optogenetic control of cellular proteins. *Nature Communications*, 6(1).
- [147] Keener, J. P. (1986). A geometrical theory for spiral waves in excitable media. *SIAM Journal on Applied Mathematics*, 46(6), 1039–1056.
- [148] Keith, A. & Flack, M. (1907). The form and nature of the muscular connections between the primary divisions of the vertebrate heart. *Journal of anatomy and physiology*, 41(Pt 3), 172.
- [149] Kennedy, M. J., Hughes, R. M., Peteya, L. A., Schwartz, J. W., Ehlers, M. D., & Tucker, C. L. (2010). Rapid blue light induction of protein interactions in living cells. *Nature methods*, 7(12), 973–975.
- [150] Kim, S. S., Rouault, H., Druckmann, S., & Jayaraman, V. (2017). Ring attractor dynamics in the *Drosophila* central brain. *Science*, 356(6340), 849–853.

- [151] Kirkton, R. D. & Bursac, N. (2011). Engineering biosynthetic excitable tissues from unexcitable cells for electrophysiological and cell therapy studies. *Nature communications*, 2, 300.
- [152] Klapoetke, N. C., Murata, Y., Kim, S. S., Pulver, S. R., Birdsey-Benson, A., Cho, Y. K., Morimoto, T. K., Chuong, A. S., Carpenter, E. J., Tian, Z., Wang, J., Xie, Y., Yan, Z., Zhang, Y., Chow, B. Y., Surek, B., Melkonian, M., Jayaraman, V., Constantine-Paton, M., Wong, G. K.-S., & Boyden, E. S. (2014). Independent optical excitation of distinct neural populations. *Nature Methods*, 11(3), 338–346.
- [153] Klein, A., Mazutis, L., Akartuna, I., Tallapragada, N., Veres, A., Li, V., Peshkin, L., Weitz, D., & Kirschner, M. (2015). Droplet Barcoding for Single-Cell Transcriptomics Applied to Embryonic Stem Cells. *Cell*, 161(5), 1187–1201.
- [154] Ko, H., Cossell, L., Baragli, C., Antolik, J., Clopath, C., Hofer, S. B., & Mrcic-Flogel, T. D. (2013). The emergence of functional microcircuits in visual cortex. *Nature*, 496(7443), 96–100.
- [155] Koller, M. L., Riccio, M. L., & Jr, R. F. G. (1998). Dynamic restitution of action potential duration during electrical alternans and ventricular fibrillation. *American Journal of Physiology-Heart and Circulatory Physiology*, 275(5), H1635–H1642.
- [156] Kondo, S. & Miura, T. (2010). Reaction-diffusion model as a framework for understanding biological pattern formation. *Science*, 329(5999), 1616–1620.
- [157] Konig, S., Hinard, V., Arnaudeau, S., Holzer, N., Potter, G., Bader, C. R., & Bernheim, L. (2004). Membrane hyperpolarization triggers myogenin and myocyte enhancer factor-2 expression during human myoblast differentiation. *The Journal of biological chemistry*, 279(27), 28187–28196.
- [158] Kopan, R. & Ilagan, M. X. G. (2009). The Canonical Notch Signaling Pathway: Unfolding the Activation Mechanism. *Cell*, 137(2), 216–233.
- [159] Kralj, J. M., Douglass, A. D., Hochbaum, D. R., Maclaurin, D., & Cohen, A. E. (2012). Optical recording of action potentials in mammalian neurons using a microbial rhodopsin. *Nature Methods*, 9(1), 90–95.
- [160] Kralj, J. M., Hochbaum, D. R., Douglass, A. D., & Cohen, A. E. (2011). Electrical Spiking in "Escherichia coli" Probed with a Fluorescent Voltage-Indicating Protein. *Science*, 333(6040), 345–348.
- [161] Kruse, M., Schulze-Bahr, E., Corfield, V., Beckmann, A., Stallmeyer, B., Kurtbay, G., Ohmert, I., Schulze-Bahr, E., Brink, P., & Pongs, O. (2009). Impaired endocytosis of the ion channel trpm4 is associated with human progressive familial heart block type i. *The Journal of clinical investigation*, 119(9), 2737–2744.

- [162] Kuhnert, L. (1986). A new optical photochemical memory device in a light-sensitive chemical active medium. *Nature*, 319(6052), 393.
- [163] Lancaster, M. A., Renner, M., Martin, C.-A., Wenzel, D., Bicknell, L. S., Hurles, M. E., Homfray, T., Penninger, J. M., Jackson, A. P., & Knoblich, J. A. (2013). Cerebral organoids model human brain development and microcephaly. *Nature*, 501(7467), 373–379.
- [164] Langlois, S., Cowan, K. N., Shao, Q., Cowan, B. J., & Laird, D. W. (2008). Caveolin-1 and-2 interact with connexin43 and regulate gap junctional intercellular communication in keratinocytes. *Molecular biology of the cell*, 19(3), 912–928.
- [165] Law, R. & Levin, M. (2015). Bioelectric memory: modeling resting potential bistability in amphibian embryos and mammalian cells. *Theoretical Biology and Medical Modelling*, 12(1), 22.
- [166] Levin, M. (2002). Isolation and community: a review of the role of gap-junctional communication in embryonic patterning. *Journal of Membrane Biology*, 185(3), 177–192.
- [167] Li, Y. & Bennett, D. J. (2003). Persistent sodium and calcium currents cause plateau potentials in motoneurons of chronic spinal rats. *Journal of neurophysiology*, 90(2), 857–869.
- [168] Lin, J. Y., Knutsen, P. M., Muller, A., Kleinfeld, D., & Tsien, R. Y. (2013). ReaChR: a red-shifted variant of channelrhodopsin enables deep transcranial optogenetic excitation. *Nature Neuroscience*, 16(10), 1499–1508.
- [169] Lindemans, F. W. & Denier van der Gon, J. J. (1978). Current thresholds and liminal size in excitation of heart muscle. *Cardiovascular research*, 12(8), 477–485.
- [170] Liu, J., Bijlenga, P., Fischer-Lougheed, J., Occhiodoro, T., Kaelin, A., Bader, C. R., & Bernheim, L. (1998). Role of an inward rectifier k current and of hyperpolarization in human myoblast fusion. *The Journal of physiology*, 510(2), 467–476.
- [171] Llinás, R. R. (2003). The contribution of santiago ramon y cajal to functional neuroscience. *Nature Reviews Neuroscience*, 4(1), 77.
- [172] Long, S., Ahmad, N., & Rebagliati, M. (2003). The zebrafish nodal-related gene southpaw is required for visceral and diencephalic left-right asymmetry. *Development*, 130(11), 2303–2316.
- [173] Love, M. I., Huber, W., & Anders, S. (2014). Moderated estimation of fold change and dispersion for rna-seq data with deseq2. *Genome biology*, 15(12), 550.
- [174] L. Oliveira, B., Guo, Z., & L. Bernardes, G. J. (2017). Inverse electron demand Diels–Alder reactions in chemical biology. *Chemical Society Reviews*, 46(16), 4895–4950.

- [175] Macosko, E., Basu, A., Satija, R., Nemes, J., Shekhar, K., Goldman, M., Tirosh, I., Bialas, A., Kamitaki, N., Martersteck, E., Trombetta, J., Weitz, D., Sanes, J., Shalek, A., Regev, A., & McCarroll, S. (2015). Highly Parallel Genome-wide Expression Profiling of Individual Cells Using Nanoliter Droplets. *Cell*, 161(5), 1202–1214.
- [176] Mahn, M., Gibor, L., Patil, P., Malina, K. C.-K., Oring, S., Printz, Y., Levy, R., Lampl, I., & Yizhar, O. (2018). High-efficiency optogenetic silencing with soma-targeted anion-conducting channelrhodopsins. *Nature Communications*, 9(1), 4125.
- [177] Marder, E. & Bucher, D. (2001). Central pattern generators and the control of rhythmic movements. *Current Biology*, 11(23), R986–R996.
- [178] Marino, S., Hogue, I. B., Ray, C. J., & Kirschner, D. E. (2008). A methodology for performing global uncertainty and sensitivity analysis in systems biology. *Journal of theoretical biology*, 254(1), 178–196.
- [179] Markson, J. S. & Elowitz, M. B. (2014). Synthetic biology of multicellular systems: new platforms and applications for animal cells and organisms. *ACS Synthetic Biology*, (pp. 875–876).
- [180] Martyn, I., Kanno, T. Y., Ruzo, A., Siggia, E. D., & Brivanlou, A. H. (2018). Self-organization of a human organizer by combined Wnt and Nodal signalling. *Nature*, 558(7708), 132.
- [181] Massagué, J. (2012). TGF $\beta$  signalling in context. *Nature Reviews Molecular Cell Biology*, 13(10), 616–630.
- [182] McKenna, A., Findlay, G. M., Gagnon, J. A., Horwitz, M. S., Schier, A. F., & Shendure, J. (2016). Whole-organism lineage tracing by combinatorial and cumulative genome editing. *Science*, 353(6298), aaf7907.
- [183] McLellan, M. A., Rosenthal, N. A., & Pinto, A. R. (2017). Cre-loxP-Mediated Recombination: General Principles and Experimental Considerations. *Current Protocols in Mouse Biology*, 7(1), 1–12.
- [184] McNamara, H. M., Dodson, S., Huang, Y.-L., Miller, E. W., Sandstede, B., & Cohen, A. E. (2018). Geometry-Dependent Arrhythmias in Electrically Excitable Tissues. *Cell Systems*, 7(4), 359–370.e6.
- [185] McNamara, H. M., Salegame, R., Tanoury, Z. A., Xu, H., Begum, S., Ortiz, G., Pourquie, O., & Cohen, A. E. (2019). Bioelectrical signaling via domain wall migration. *bioRxiv*, (pp. 570440).
- [186] McNamara, H. M., Zhang, H., Werley, C. A., & Cohen, A. E. (2016). Optically Controlled Oscillators in an Engineered Bioelectric Tissue. *Physical Review X*, 6(3), 031001.

- [187] Milo, R. & Phillips, R. (2015). *Cell Biology by the Numbers*. Garland Science.
- [188] Mines, G. R. (1913). On dynamic equilibrium in the heart. *The Journal of physiology*, 46(4-5), 349–383.
- [189] Mines, G. R. (1914). On circulating excitations in heart muscle and their possible relation to tachycardia and fibrillation. *Trans R Soc Can*, 8, 43–52.
- [190] Mobasher, A., Lewis, R., Ferreira-Mendes, A., Rufino, A., Dart, C., & Barrett-Jolley, R. (2012). Potassium channels in articular chondrocytes. *Channels*, 6(6), 416–425.
- [191] Moffitt, J. R., Bambah-Mukku, D., Eichhorn, S. W., Vaughn, E., Shekhar, K., Perez, J. D., Rubinstein, N. D., Hao, J., Regev, A., Dulac, C., & Zhuang, X. (2018). Molecular, spatial, and functional single-cell profiling of the hypothalamic preoptic region. *Science*, 362(6416), eaau5324.
- [192] Moffitt, J. R., Hao, J., Bambah-Mukku, D., Lu, T., Dulac, C., & Zhuang, X. (2016). High-performance multiplexed fluorescence in situ hybridization in culture and tissue with matrix imprinting and clearing. *Proceedings of the National Academy of Sciences*, 113(50), 14456–14461.
- [193] Montague, T. G. & Schier, A. F. (2017). Vg1-Nodal heterodimers are the endogenous inducers of mesendoderm. *eLife*, 6, e28183.
- [194] Mordwinkin, N. M., Burridge, P. W., & Wu, J. C. (2013). A review of human pluripotent stem cell-derived cardiomyocytes for high-throughput drug discovery, cardiotoxicity screening, and publication standards. *Journal of cardiovascular translational research*, 6(1), 22–30.
- [195] Moreno, A., Rook, M., Fishman, G., & Spray, a. C. (1994). Gap junction channels: distinct voltage-sensitive and-insensitive conductance states. *Biophysical journal*, 67(1), 113–119.
- [196] Moses, J. E. & Moorhouse, A. D. (2007). The growing applications of click chemistry. *Chemical Society Reviews*, 36(8), 1249–1262.
- [197] Muller, P., Rogers, K. W., Jordan, B. M., Lee, J. S., Robson, D., Ramanathan, S., & Schier, A. F. (2012). Differential Diffusivity of Nodal and Lefty Underlies a Reaction-Diffusion Patterning System. *Science*, 336(6082), 721–724.
- [198] Nagai, Y., González, H., Shrier, A., & Glass, L. (2000). Paroxysmal starting and stopping of circulating waves in excitable media. *Physical review letters*, 84(18), 4248.
- [199] Nagel, G., Szellas, T., Huhn, W., Kateriya, S., Adeishvili, N., Berthold, P., Ollig, D., Heegemann, P., & Bamberg, E. (2003). Channelrhodopsin-2, a directly light-gated cation-selective membrane channel. *Proceedings of the National Academy of Sciences of the United States of America*, 100(24), 13940–13945.

- [200] Nagumo, J., Arimoto, S., & Yoshizawa, S. (1962). An active pulse transmission line simulating nerve axon. *Proceedings of the IRE*, 50(10), 2061–2070.
- [201] Nakai, J., Ohkura, M., & Imoto, K. (2001). A high signal-to-noise Ca<sup>2+</sup> probe composed of a single green fluorescent protein. *Nature Biotechnology*, 19(2), 137.
- [202] Ng, S. Y., Wong, C. K., & Tsang, S. Y. (2010). Differential gene expressions in atrial and ventricular myocytes: insights into the road of applying embryonic stem cell-derived cardiomyocytes for future therapies. *American journal of physiology. Cell physiology*, 299(6), C1234–49.
- [203] Nguyen, Q.-T., Schroeder, L. F., Mank, M., Muller, A., Taylor, P., Griesbeck, O., & Kleinfeld, D. (2010). An in vivo biosensor for neurotransmitter release and in situ receptor activity. *Nature neuroscience*, 13(1), 127.
- [204] Nitsan, I., Drori, S., Lewis, Y. E., Cohen, S., & Tzllil, S. (2016). Mechanical communication in cardiac cell synchronized beating. *12*, 472.
- [205] Noble, D. (1962). A modification of the Hodgkin—Huxley equations applicable to Purkinje fibre action and pacemaker potentials. *The Journal of Physiology*, 160(2), 317–352.
- [206] Nolasco, J. & Dahlen, R. W. (1968). A graphic method for the study of alternation in cardiac action potentials. *Journal of applied physiology*, 25(2), 191–196.
- [207] Noszticzius, Z., Horsthemke, W., McCormick, W., Swinney, H. L., & Tam, W. (1987). Sustained chemical waves in an annular gel reactor: a chemical pinwheel. *Nature*, 329(6140), 619.
- [208] Novick, A. & Weiner, M. (1957). Enzyme induction as an all-or-none phenomenon. *Proceedings of the National Academy of Sciences of the United States of America*, 43(7), 553–566.
- [209] O’Hara, T., Virág, L., Varró, A., & Rudy, Y. (2011). Simulation of the undiseased human cardiac ventricular action potential: model formulation and experimental validation. *PLoS computational biology*, 7(5), e1002061.
- [210] Oka, Y. & Sato, T. N. (2015). Whole-mount single molecule fish method for zebrafish embryo. *Scientific reports*, 5, 8571.
- [211] O’Keefe, J. (1976). Place units in the hippocampus of the freely moving rat. *Experimental Neurology*, 51(1), 78–109.
- [212] Onsager, L. (1944). Crystal statistics. i. a two-dimensional model with an order-disorder transition. *Physical Review*, 65(3-4), 117.
- [213] Ornitz, D. M. & Itoh, N. (2015). The Fibroblast Growth Factor signaling pathway.

- [214] Ozbudak, E. M., Thattai, M., Lim, H. N., Shraiman, B. I., & Van Oudenaarden, A. (2004). Multistability in the lactose utilization network of *Escherichia coli*. *Nature*, 427(6976), 737.
- [215] Packer, A. M., Russell, L. E., Dagleish, H. W. P., & Häusser, M. (2015). Simultaneous all-optical manipulation and recording of neural circuit activity with cellular resolution *in vivo*. *Nature Methods*, 12(2), 140–146.
- [216] Pai, V. P., Pietak, A., Willocq, V., Ye, B., Shi, N.-Q., & Levin, M. (2018). HCN2 Rescues brain defects by enforcing endogenous voltage pre-patterns. *Nature Communications*, 9(1), 1–15.
- [217] Park, J., Werley, C. A., Venkatachalam, V., Kralj, J. M., Dib-Hajj, S. D., Waxman, S. G., & Cohen, A. E. (2013). Screening fluorescent voltage indicators with spontaneously spiking hek cells. *PLoS one*, 8(12), e85221.
- [218] Petersen, C. C. (2017). Whole-Cell Recording of Neuronal Membrane Potential during Behavior. *Neuron*, 95(6), 1266–1281.
- [219] Piatkevich, K. D., Jung, E. E., Straub, C., Linghu, C., Park, D., Suk, H.-J., Hochbaum, D. R., Goodwin, D., Pnevmatikakis, E., Pak, N., Kawashima, T., Yang, C.-T., Rhoades, J. L., Shemesh, O., Asano, S., Yoon, Y.-G., Freifeld, L., Saulnier, J. L., Riegler, C., Engert, F., Hughes, T., Drobizhev, M., Szabo, B., Ahrens, M. B., Flavell, S. W., Sabatini, B. L., & Boyden, E. S. (2018). A robotic multidimensional directed evolution approach applied to fluorescent voltage reporters. *Nature chemical biology*, 14(4), 352–360.
- [220] Pietak, A. & Levin, M. (2017). Bioelectric gene and reaction networks: computational modelling of genetic, biochemical and bioelectrical dynamics in pattern regulation. *Journal of the Royal Society, Interface*, 14(134), 10.1098/rsif.2017.0425.
- [221] Pitcairn, E., Harris, H., Epiney, J., Pai, V. P., Lemire, J. M., Ye, B., Shi, N.-Q., Levin, M., & McLaughlin, K. A. (2017). Coordinating heart morphogenesis: A novel role for hyperpolarization-activated cyclic nucleotide-gated (HCN) channels during cardiogenesis in *Xenopus laevis*. *Communicative & Integrative Biology*, 10(3), e1309488.
- [222] Pourbadie, H. G. & Sayyah, M. (2018). Optogenetics: Control of Brain Using Light. *Iranian Biomedical Journal*, 22(1), 4–5.
- [223] Protze, S. I., Liu, J., Nussinovitch, U., Ohana, L., Backx, P. H., Gepstein, L., & Keller, G. M. (2017). Sinoatrial node cardiomyocytes derived from human pluripotent cells function as a biological pacemaker. *Nature biotechnology*, 35(1), 56–68.
- [224] Proulx, A., Merrifield, P. A., & Naus, C. C. (1997). Blocking gap junctional intercellular communication in myoblasts inhibits myogenin and *mrf4* expression. *Developmental genetics*, 20(2), 133–144.

- [225] Pudasaini, A., El-Arab, K. K., & Zoltowski, B. D. (2015). LOV-based optogenetic devices: light-driven modules to impart photoregulated control of cellular signaling. *Frontiers in Molecular Biosciences*, 2.
- [226] Purnick, P. E. & Weiss, R. (2009). The second wave of synthetic biology: from modules to systems. *Nature reviews Molecular cell biology*, 10(6), 410.
- [227] Qin, D., Xia, Y., & Whitesides, G. M. (2010). Soft lithography for micro-and nanoscale patterning. *Nature protocols*, 5(3), 491.
- [228] Qu Zhilin, Garfinkel Alan, Chen Peng-Sheng, & Weiss James N. (2000). Mechanisms of Discordant Alternans and Induction of Reentry in Simulated Cardiac Tissue. *Circulation*, 102(14), 1664–1670.
- [229] Ramón y Cajal, S. (1928). Degeneration and regeneration of the nervous system.
- [230] Rodriques, S. G., Stickels, R. R., Goeva, A., Martin, C. A., Murray, E., Vanderburg, C. R., Welch, J., Chen, L. M., Chen, F., & Macosko, E. Z. (2019). Slide-seq: A scalable technology for measuring genome-wide expression at high spatial resolution. *Science*, 363(6434), 1463–1467.
- [231] Roes, S. D., Borleffs, C. J., van der Geest, R. J., Westenberg, J. J., Marsan, N. A., Kaandorp, T. A., Reiber, J. H., Zeppenfeld, K., Lamb, H. J., de Roos, A., Schalij, M. J., & Bax, J. J. (2009). Infarct tissue heterogeneity assessed with contrast-enhanced mri predicts spontaneous ventricular arrhythmia in patients with ischemic cardiomyopathy and implantable cardioverter-defibrillator. *Circulation. Cardiovascular imaging*, 2(3), 183–190.
- [232] Rogers, K. W., Lord, N. D., Gagnon, J. A., Pauli, A., Zimmerman, S., Aksel, D. C., Reyon, D., Tsai, S. Q., Joung, J. K., & Schier, A. F. (2017a). Nodal patterning without lefty inhibitory feedback is functional but fragile. *Elife*, 6, e28785.
- [233] Rogers, K. W., Lord, N. D., Gagnon, J. A., Pauli, A., Zimmerman, S., Aksel, D. C., Reyon, D., Tsai, S. Q., Joung, J. K., & Schier, A. F. (2017b). Nodal patterning without Lefty inhibitory feedback is functional but fragile. *eLife*, 6.
- [234] Rohr, S., Kucera, J. P., Fast, V. G., & Kléber, A. G. (1997). Paradoxical improvement of impulse conduction in cardiac tissue by partial cellular uncoupling. *Science*, 275(5301), 841–844.
- [235] Sako, K., Pradhan, S., Barone, V., Inglés-Prieto, P., Müller, P., Ruprecht, V., Čapek, D., Galande, S., Janovjak, H., & Heisenberg, C.-P. (2016). Optogenetic Control of Nodal Signaling Reveals a Temporal Pattern of Nodal Signaling Regulating Cell Fate Specification during Gastrulation. *Cell Reports*, 16(3), 866–877.
- [236] Sakurai, T., Mihaliuk, E., Chirila, F., & Showalter, K. (2002). Design and control of wave propagation patterns in excitable media. *Science*, 296(5575), 2009–2012.

- [237] Satija, R., Farrell, J. A., Gennert, D., Schier, A. F., & Regev, A. (2015). Spatial reconstruction of single-cell gene expression data. *Nature biotechnology*, 33(5), 495.
- [238] Schwindt, P. C. & Crill, W. E. (1995). Amplification of synaptic current by persistent sodium conductance in apical dendrite of neocortical neurons. *Journal of neurophysiology*, 74(5), 2220–2224.
- [239] Sharma, A., Wu, J. C., & Wu, S. M. (2013). Induced pluripotent stem cell-derived cardiomyocytes for cardiovascular disease modeling and drug screening. *Stem Cell Research Therapy*, 4(6), 150. ID: Sharma2013.
- [240] Shen, M. M. & Schier, A. F. (2000). The EGF-CFC gene family in vertebrate development. *Trends in Genetics*, 16(7), 303–309.
- [241] Shiferaw, Y. & Karma, A. (2006). Turing instability mediated by voltage and calcium diffusion in paced cardiac cells. *Proceedings of the National Academy of Sciences of the United States of America*, 103(15), 5670–5675.
- [242] Shrier, A., Dubarsky, H., Rosengarten, M., Guevara, M. R., Nattel, S., & Glass, L. (1987). Prediction of complex atrioventricular conduction rhythms in humans with use of the atrioventricular nodal recovery curve. *Circulation*, 76(6), 1196–1205.
- [243] Silverman, M. E., Grove, D., & Upshaw, C. B. (2006). Why Does the Heart Beat? The Discovery of the Electrical System of the Heart. *Circulation*.
- [244] Solnica-Krezel, L. & Sepich, D. S. (2012). Gastrulation: making and shaping germ layers. *Annual Review of Cell and Developmental Biology*, 28, 687–717.
- [245] Spemann, H. & Mangold, H. (1924). über Induktion von Embryonalanlagen durch Implantation artfremder Organisatoren. *Archiv für mikroskopische Anatomie und Entwicklungsmechanik*, 100(3), 599–638.
- [246] Stoeckius, M., Hafemeister, C., Stephenson, W., Houck-Loomis, B., Chattopadhyay, P. K., Swerdlow, H., Satija, R., & Smibert, P. (2017). Simultaneous epitope and transcriptome measurement in single cells. *Nature Methods*, 14(9), 865–868.
- [247] Sultan, M., Schulz, M. H., Richard, H., Magen, A., Klingenhoff, A., Scherf, M., Seifert, M., Borodina, T., Soldatov, A., Parkhomchuk, D., et al. (2008). A global view of gene activity and alternative splicing by deep sequencing of the human transcriptome. *Science*, 321(5891), 956–960.
- [248] Sundelacruz, S., Levin, M., & Kaplan, D. L. (2009). Role of membrane potential in the regulation of cell proliferation and differentiation. *Stem cell reviews and reports*, 5(3), 231–246.

- [249] Swartz, B. E. (1998). The advantages of digital over analog recording techniques. *Electroencephalography and Clinical Neurophysiology*, 106(2), 113–117.
- [250] Tang, Q., Tsytsarev, V., Frank, A., Wu, Y., Chen, C.-w., Erzurumlu, R. S., & Chen, Y. (2016). *In Vivo* Mesoscopic Voltage-Sensitive Dye Imaging of Brain Activation. *Scientific Reports*, 6, 25269.
- [251] Tecott, L., Shtrom, S., & Julius, D. (1995). Expression of a serotonin-gated ion channel in embryonic neural and nonneural tissues. *Molecular and Cellular Neuroscience*, 6(1), 43–55.
- [252] ten Tusscher, K. H. W. J., Noble, D., Noble, P. J., & Panfilov, A. V. (2004). A model for human ventricular tissue. *American Journal of Physiology-Heart and Circulatory Physiology*, 286(4), H1573–H1589.
- [253] ten Tusscher, K. H. W. J. & Panfilov, A. V. (2006). Alternans and spiral breakup in a human ventricular tissue model. *American Journal of Physiology. Heart and Circulatory Physiology*, 291(3), H1088–1100.
- [254] Tian, L., Hires, S. A., Mao, T., Huber, D., Chiappe, M. E., Chalasani, S. H., Petreanu, L., Akerboom, J., McKinney, S. A., Schreiter, E. R., Bargmann, C. I., Jayaraman, V., Svoboda, K., & Looger, L. L. (2009). Imaging neural activity in worms, flies and mice with improved GCaMP calcium indicators. *Nature Methods*, 6(12), 875–881.
- [255] Tischer, D. & Weiner, O. D. (2014). Illuminating cell signalling with optogenetic tools. *Nature reviews Molecular cell biology*, 15(8), 551.
- [256] Todhunter, M. E., Jee, N. Y., Hughes, A. J., Coyle, M. C., Cerchiari, A., Farlow, J., Garbe, J. C., LaBarge, M. A., Desai, T. A., & Gartner, Z. J. (2015). Programmed synthesis of three-dimensional tissues. *Nature methods*, 12(10), 975.
- [257] Toettcher, J. E., Gong, D., Lim, W. A., & Weiner, O. D. (2011). Light control of plasma membrane recruitment using the phy-pif system. *Methods in enzymology*, 497, 409–423.
- [258] Tononi, G., Sporns, O., & Edelman, G. M. (1994). A measure for brain complexity: relating functional segregation and integration in the nervous system. *Proceedings of the National Academy of Sciences*, 91(11), 5033–5037.
- [259] Trapnell, C., Williams, B. A., Pertea, G., Mortazavi, A., Kwan, G., Van Baren, M. J., Salzberg, S. L., Wold, B. J., & Pachter, L. (2010). Transcript assembly and quantification by rna-seq reveals unannotated transcripts and isoform switching during cell differentiation. *Nature biotechnology*, 28(5), 511.
- [260] Turing, A. M. (1952). The Chemical Basis of Morphogenesis. *Philosophical Transactions of the Royal Society of London. Series B, Biological Sciences*, 237(641), 37–72.

- [261] van Boxtel, A. L., Economou, A. D., Heliot, C., & Hill, C. S. (2018). Long-Range Signaling Activation and Local Inhibition Separate the Mesoderm and Endoderm Lineages. *Developmental Cell*, 44(2), 179–191.e5.
- [262] van den Heuvel, M. P. & Hulshoff Pol, H. E. (2010). Exploring the brain network: A review on resting-state fMRI functional connectivity. *European Neuropsychopharmacology*, 20(8), 519–534.
- [263] Varghese, A., TenBroek, E. M., Coles Jr, J., & Sigg, D. C. (2006). Endogenous channels in hek cells and potential roles in hcn ionic current measurements. *Progress in biophysics and molecular biology*, 90(1-3), 26–37.
- [264] Wang, G. K., Russell, C., & Wang, S.-Y. (2004). State-dependent block of voltage-gated na<sup>+</sup> channels by amitriptyline via the local anesthetic receptor and its implication for neuropathic pain. *Pain*, 110(1-2), 166–174.
- [265] Wang, Y., Mi, J., Lu, K., Lu, Y., & Wang, K. (2015). Comparison of gating properties and use-dependent block of nav1. 5 and nav1. 7 channels by anti-arrhythmics mexiletine and lidocaine. *PLoS One*, 10(6), e0128653.
- [266] Warmflash, A., Sorre, B., Etoc, F., Siggia, E. D., & Brivanlou, A. H. (2014). A method to recapitulate early embryonic spatial patterning in human embryonic stem cells. *Nature Methods*, 11(8), 847–854.
- [267] Watanabe, M., Iwashita, M., Ishii, M., Kurachi, Y., Kawakami, A., Kondo, S., & Okada, N. (2006). Spot pattern of leopard Danio is caused by mutation in the zebrafish connexin41.8 gene. *EMBO Reports*, 7(9), 893.
- [268] Wei, S. & Wang, Q. (2018). Molecular regulation of Nodal signaling during mesendoderm formation. *Acta Biochimica et Biophysica Sinica*, 50(1), 74–81.
- [269] Weiss, J. N., Garfinkel, A., Karagueuzian, H. S., Qu, Z., & Chen, P.-S. (1999). Chaos and the transition to ventricular fibrillation: a new approach to antiarrhythmic drug evaluation. *Circulation*, 99(21), 2819–2826.
- [270] Weiss, J. N., Karma, A., Shiferaw, Y., Chen, P.-S., Garfinkel, A., & Qu, Z. (2006). From pulsus to pulseless: the saga of cardiac alternans. *Circulation research*, 98(10), 1244–1253.
- [271] Werley, C. A., Chien, M.-P., & Cohen, A. E. (2017a). Ultrawidefield microscope for high-speed fluorescence imaging and targeted optogenetic stimulation. *Biomedical optics express*, 8(12), 5794–5813.
- [272] Werley, C. A., Chien, M.-P., Gaublomme, J., Shekhar, K., Butty, V., Yi, B. A., Kralj, J. M., Bloxham, W., Boyer, L. A., Regev, A., & Cohen, A. (2017b). Geometry-dependent functional changes in ipsc-derived cardiomyocytes probed by functional imaging and rna sequencing. *PLoS one*, 12(3), e0172671.

- [273] Whitman, M. (2001). Nodal Signaling in Early Vertebrate Embryos: Themes and Variations. *Developmental Cell*, 1(5), 605–617.
- [274] Wolpert, L. (1969). Positional information and the spatial pattern of cellular differentiation. *Journal of theoretical biology*, 25(1), 1–47.
- [275] Wussling, M., Scheufler, K., Schmerling, S., & Drygalla, V. (1997). Velocity-curvature relationship of colliding spherical calcium waves in rat cardiac myocytes. *Biophysical journal*, 73(3), 1232–1242.
- [276] Wybo, W. A. M., Torben-Nielsen, B., Nevian, T., & Gewaltig, M.-O. (2019). Electrical Compartmentalization in Neurons. *Cell Reports*, 26(7), 1759–1773.e7.
- [277] Xu, P., Qiao, K., & Stephanopoulos, G. (2017). Engineering oxidative stress defense pathways to build a robust lipid production platform in *Yarrowia lipolytica*. *Biotechnology and Bioengineering*, 114(7), 1521–1530.
- [278] Xu, P.-F., Houssin, N., Ferri-Lagneau, K. F., Thisse, B., & Thisse, C. (2014). Construction of a Vertebrate Embryo from Two Opposing Morphogen Gradients. *Science*, 344(6179), 87–89.
- [279] Yamamoto, W., Asakura, K., Ando, H., Taniguchi, T., Ojima, A., Uda, T., Osada, T., Hayashi, S., Kasai, C., Miyamoto, N., Tashibu, H., Yoshinaga, T., Yamazaki, D., Sugiyama, A., Kanda, Y., Sawada, K., & Sekino, Y. (2016). Electrophysiological characteristics of human ipsc-derived cardiomyocytes for the assessment of drug-induced proarrhythmic potential. *PLOS ONE*, 11(12), e0167348.
- [280] Yan, L., Chen, J., Zhu, X., Sun, J., Wu, X., Shen, W., Zhang, W., Tao, Q., & Meng, A. (2018). Maternal Huluwa dictates the embryonic body axis through  $\beta$ -catenin in vertebrates. *Science*, 362(6417), eaat1045.
- [281] Yang, X., Pabon, L., & Murry, C. E. (2014). Engineering adolescence: maturation of human pluripotent stem cell-derived cardiomyocytes. *Circulation research*, 114(3), 511–523.
- [282] Ye, L., Zimmermann, W.-H., Garry, D. J., & Zhang, J. (2013). Patching the heart: cardiac repair from within and outside. *Circulation research*, 113(7), 922–932.
- [283] Zaglia, T., Pianca, N., Borile, G., Da Broi, F., Richter, C., Campione, M., Lehnart, S. E., Luther, S., Corrado, D., Miquerol, L., et al. (2015). Optogenetic determination of the myocardial requirements for extrasystoles by cell type-specific targeting of channelrhodopsin-2. *Proceedings of the National Academy of Sciences*, 112(32), E4495–E4504.
- [284] Zeldovich, Y. & Frank-Kamenetskii, D. (1938). Theory of flame propagation. *Zh.Fiz.Khim*, 12, 100.
- [285] Zemelman, B. V., Lee, G. A., Ng, M., & Miesenböck, G. (2002). Selective photostimulation of genetically chARGed neurons. *Neuron*, 33(1), 15–22.

- [286] Zemelman, B. V., Nesnas, N., Lee, G. A., & Miesenbock, G. (2003). Photochemical gating of heterologous ion channels: remote control over genetically designated populations of neurons. *Proceedings of the National Academy of Sciences of the United States of America*, 100(3), 1352–1357.
- [287] Zeng, W. & Glass, L. (1996). Statistical properties of heartbeat intervals during atrial fibrillation. *Physical Review E*, 54(2), 1779–1784.
- [288] Zhang, F., Wang, L.-P., Brauner, M., Liewald, J. F., Kay, K., Watzke, N., Wood, P. G., Bamberg, E., Nagel, G., Gottschalk, A., & Deisseroth, K. (2007). Multimodal fast optical interrogation of neural circuitry. *Nature*, 446(7136), 633–639.
- [289] Zhang, H., Reichert, E., & Cohen, A. E. (2016). Optical electrophysiology for probing function and pharmacology of voltage-gated ion channels. *eLife*, 5, e15202.
- [290] Zhang, J., Talbot, W. S., & Schier, A. F. (1998). Positional Cloning Identifies Zebrafish one-eyed pinhead as a Permissive EGF-Related Ligand Required during Gastrulation. *Cell*, 92(2), 241–251.
- [291] Zhang, Z., Zhao, Z., Liu, Y., Wang, W., Wu, Y., & Ding, J. (2013). Kinetic model of nav1.5 channel provides a subtle insight into slow inactivation associated excitability in cardiac cells. *PLoS one*, 8(5), e64286.
- [292] Zhu, H., Scharnhorst, K. S., Stieg, A. Z., Gimzewski, J. K., Minami, I., Nakatsuji, N., Nakano, H., & Nakano, A. (2017). Two dimensional electrophysiological characterization of human pluripotent stem cell-derived cardiomyocyte system. *Scientific Reports*, 7, 43210.
- [293] Zou, P., Zhao, Y., Douglass, A. D., Hochbaum, D. R., Brinks, D., Werley, C. A., Harrison, D. J., Campbell, R. E., & Cohen, A. E. (2014). Bright and fast multicoloured voltage reporters via electrochromic FRET. *Nature Communications*, 5, 4625.



**T**HIS THESIS WAS TYPESET using L<sup>A</sup>T<sub>E</sub>X, originally developed by Leslie Lamport and based on Donald Knuth's T<sub>E</sub>X. The body text is set in 11 point Egenolff-Berner Garamond, a revival of Claude Garamont's humanist typeface. The above illustration, "Science Experiment 02", was created by Ben Schlitter and released under [CC BY-NC-ND 3.0](#). A template that can be used to format a PhD thesis with this look and feel has been released under the permissive MIT (X11) license, and can be found online at [github.com/suchow/Dissertate](https://github.com/suchow/Dissertate) or from its author, Jordan Suchow, at [suchow@post.harvard.edu](mailto:suchow@post.harvard.edu).